Contribution to the manufacturing and the understanding of the thermal behaviour of capillary structures dedicated to Loop Heat Pipes

Rémi Giraudon

N° d'ordre NNT : 2018LYSEI003

THESE de DOCTORAT DE L'UNIVERSITE DE LYON
opérée au sein de
L'Institut National des Sciences Appliquées de Lyon

Ecole Doctorale N° ED 162
(Mécanique, Énergétique, Génie Civil, Acoustique)

Spécialité: Thermique et Energétique :

Soutenue publiquement le 15/01/2018, par :
Rémi Giraudon

Contribution to the manufacturing and the understanding of the thermal behaviour of capillary structures dedicated to Loop Heat Pipes

Devant le jury composé de :

BERTIN Yves	Professeur (PPRIME, ENSMA, Poitiers)	Président
BERTRAND Ghislaine	Professeur (CIRIMAT, INP, Toulouse)	Rapporteur
PRAT Marc	Directeur de Recherche (IMFT, Toulouse)	Rapporteur
LAUNAY Stéphane	Maître de Conférences (IUTSI, Aix Marseille Université)	Examinateur
SARTRE Valérie	Maître de Conférences, HDR (CETHIL, INSA Lyon)	Directrice de thèse
LIPS Stéphane	Maître de Conférences (CETHIL, INSA Lyon)	Directeur de thèse
GREMILLARD Laurent	Directeur de Recherche (MATEIS, INSA Lyon)	Directeur de thèse

Thèse préparée dans le cadre d'un partenariat entre le Centre d'Énergétique et de Thermique de Lyon (CETHIL - UMR5008 - INSA de Lyon) et le laboratoire Matériaux, Ingénierie et Sciences (MATEIS - UMR5510 – INSA de Lyon)

Département FEDORA – INSA Lyon - Ecoles Doctorales – Quinquennal 2016-2020

SIGLE	ECOLE DOCTORALE	NOM ET COORDONNEES DU RESPONSABLE
CHIMIE	**CHIMIE DE LYON** **http://www.edchimie-lyon.fr** Sec : Renée EL MELHEM Bat Blaise Pascal 3e etage secretariat@edchimie-lyon.fr Insa : R. GOURDON	M. Stéphane DANIELE Institut de Recherches sur la Catalyse et l'Environnement de Lyon IRCELYON-UMR 5256 Équipe CDFA 2 avenue Albert Einstein 69626 Villeurbanne cedex directeur@edchimie-lyon.fr
E.E.A.	**ELECTRONIQUE, ELECTROTECHNIQUE, AUTOMATIQUE** **http://edeea.ec-lyon.fr** Sec : M.C. HAVGOUDOUKIAN Ecole-Doctorale.eea@ec-lyon.fr	M. Gérard SCORLETTI Ecole Centrale de Lyon 36 avenue Guy de Collongue 69134 ECULLY Tél : 04.72.18 60.97 Fax : 04 78 43 37 17 Gerard.scorletti@ec-lyon.fr
E2M2	**EVOLUTION, ECOSYSTEME, MICROBIOLOGIE, MODELISATION** **http://e2m2.universite-lyon.fr** Sec : Sylvie ROBERJOT Bât Atrium - UCB Lyon 1 04.72.44.83.62 Insa : H. CHARLES secretariat.e2m2@univ-lyon1.fr	M. Fabrice CORDEY CNRS UMR 5276 Lab. de géologie de Lyon Université Claude Bernard Lyon 1 Bât Géode 2 rue Raphaël Dubois 69622 VILLEURBANNE Cédex Tél : 06.07.53.89.13 cordey@ univ-lyon1.fr
EDISS	**INTERDISCIPLINAIRE SCIENCES-SANTE** **http://www.edisslyon.fr** Sec : Sylvie ROBERJOT Bât Atrium - UCB Lyon 1 04.72.44.83.62 Insa : M. LAGARDE secretariat.ediss@univ-lyon1.fr	Mme Emmanuelle CANET-SOULAS INSERM U1060, CarMeN lab, Univ. Lyon 1 Bâtiment IMBL 11 avenue Jean Capelle INSA de Lyon 696621 Villeurbanne Tél : 04.72.68.49.09 Fax :04 72 68 49 16 Emmanuelle.canet@univ-lyon1.fr
INFOMATHS	**INFORMATIQUE ET MATHEMATIQUES** **http://edinfomaths.universite-lyon.fr** Sec :Renée EL MELHEM Bat Blaise Pascal, 3e étage Tél : 04.72. 43. 80. 46 Fax : 04.72.43.16.87 infomaths@univ-lyon1.fr	M. Luca ZAMBONI Bâtiment Braconnier 43 Boulevard du 11 novembre 1918 69622 VILLEURBANNE Cedex Tél :04 26 23 45 52 zamboni@maths.univ-lyon1.fr
Matériaux	**MATERIAUX DE LYON** **http://ed34.universite-lyon.fr** Sec : Marion COMBE Tél:04-72-43-71-70 –Fax : 87.12 Bat. Direction ed.materiaux@insa-lyon.fr	M. Jean-Yves BUFFIERE INSA de Lyon MATEIS Bâtiment Saint Exupéry 7 avenue Jean Capelle 69621 VILLEURBANNE Cedex Tél : 04.72.43 71.70 Fax 04 72 43 85 28 Ed.materiaux@insa-lyon.fr
MEGA	**MECANIQUE, ENERGETIQUE, GENIE CIVIL, ACOUSTIQUE** http://edmega.universite-lyon.fr/ Sec : Marion COMBE Tél:04-72-43-71-70 –Fax : 87.12 Bat. Direction mega@insa-lyon.fr	M. Philippe BOISSE INSA de Lyon Laboratoire LAMCOS Bâtiment Jacquard 25 bis avenue Jean Capelle 69621 VILLEURBANNE Cedex Tél : 04.72 .43.71.70 Fax : 04 72 43 72 37 Philippe.boisse@insa-lyon.fr
ScSo	**ScSo*** **http://ed483.univ-lyon2.fr/** Sec : Viviane POLSINELLI Brigitte DUBOIS Insa : J.Y. TOUSSAINT Tél : 04 78 69 72 76 viviane.polsinelli@univ-lyon2.fr	M. Christian MONTES Université Lyon 2 86 rue Pasteur 69365 LYON Cedex 07 Christian.montes@univ-lyon2.fr

*ScSo : Histoire, Géographie, Aménagement, Urbanisme, Archéologie, Science politique, Sociologie, Anthropologie

“ *Is í ding di féin a scoileann an dair* ” Irish proverb

Tenter de rendre heureux ses proches, et faire de la recherche sont deux activités similaires. Ce sont des travaux qui, en un sens, ne sont jamais terminés et qui demandent une remise en question permanente afin de ne pas finir par échouer.

Remerciements

Je tiens à saluer la mémoire de Stéphane Launay qui aurait dû être présent ce 15 janvier pour faire partie du jury. Le destin en a voulu autrement, mais Stéphane était dans toutes les têtes aujourd'hui.

15 janvier 2018, ca y est, la thèse est enfin soutenue. Que de chemin parcouru pour en arriver là. Et ce chemin, je ne l'ai parcouru seul. Même si aujourd'hui, c'est moi qui me suis présenté seul devant le jury, j'ai été accompagné et aidé au jour le jour. Pas une seule fois, Laurent, Stéphane ou Valérie ne m'ont laissé seul face aux problèmes rencontrés. Les réunions très régulières ont toujours été source d'inspiration pour moi. Ils ont suivi ce travail avec beaucoup de rigueur et d'intérêt ce qui m'a permis de systématiquement avancer. J'en profite pour remercier Eric, Damien, Jérôme et Florian, tous du labo Matéis, pour avoir grandement participé à la thèse en apportant leur point de vue sur la partie sciences des matériaux. Je remercie également Marian pour la formation accélérée sur la science des données qui a montré tout son intérêt lorsque le nombre de tests est trop grand. A l'heure de me remémorer ces innombrables tests effectués, ma pensée s'oriente naturellement vers l'Atelier. Chaque demande, urgente ou non a été traitée dans des délais, prévenant tout stress. Avec Christophe, les conversations sont du type :

-J'ai besoin de ça dans trois semaines au plus tard, c'est possible tu penses ?
-Pas de soucis, je pense y arriver en deux.

Et seulement une semaine plus tard, la pièce arrive ! Mais s'il traite si bien les demandes, c'est qu'il est entouré des très compétents Nicolas, Xavier et avant ça Joël qui sont remerciés tout autant. J'en profite pour glisser un petit mot de remerciements également à Anthony et Serge qui m'ont permis d'utiliser mes bancs d'essais avec des logiciels d'acquisition performants. Je n'oublie pas non plus Antoine dont l'énergie débordante m'a permis d'avancer sereinement, sachant qu'il n'était jamais loin en cas de pépin. Si la thèse a pu être menée à son terme, c'est également grâce à l'activité du secrétariat qui gère toute la partie non scientifique et qui permet le plus souvent aux doctorants de se concentrer sur d'autres choses. En ce qui me concerne, j'ai principalement été épaulé par Florence et Maryline mais Christine, Silas, Rémy, Corinne, Nazaré ou encore Sophie ont à l'occasion su me dépanner et je les associe à ces remerciements. On a souvent tendance à dire « ma thèse », mais en ce qui me concerne, j'ai plutôt eu l'impression d'être au cœur d'un projet collectif où beaucoup ont apporté une ou plusieurs pièces.

Merci à Ghislaine Bertrand, Marc Prat et Yves Bertin pour avoir accepté du juger ce travail parfois éloigné de leurs thématiques de recherches respectives. Vos remarques, tant via le rapport, que le jour de la soutenance ont été très constructives et ont permis des discussions intéressantes.

Mais assez parlé boulot, j'ai également passé du temps au labo à ne pas travailler et pendant ces périodes j'ai trouvé des collègues qui sont devenus des copains et on n'a jamais donné notre part au chien quand il s'est agi de s'amuser un bon coup. Que ce soit à la coinche, au foot ou à la K-fête, j'ai passé du très bon temps avec vous tous, Aurélia, Quentin, Thibault, Sandra, Adrien, Eloïse, Martin, Loïc, Damien, Nicolas, David, Thomas, Bus, Ghady, Julie, Kevin, Léon, Etienne.

Parmi toutes ces personnes, je sors du lot Damien et Olivier. J'ai beaucoup aimé votre rapport à la science et au travail de recherche. Vous m'avez mis le pied à l'étrier en me donnant les bons filons (80 trèfle par exemple). Surtout, vous m'avez ouvert les portes de votre groupe de potes qui sont tout aussi excellents que vous (et oui les Vieux Michels, je parle de vous). Et ça, c'est inestimable. Des Rouies à

la Pendine, de MRoc à Puy-Saint-Vincent, passer du temps dans les montagnes et ailleurs avec vous a été, et sera toujours un grand bonheur.

Une thèse est certes un travail, mais également une épreuve et un peu un accomplissement personnel. C'est donc assez difficile de débrancher complètement. Mais j'ai eu la chance d'atterrir à l'AS Caluire en septembre 2015 pour faire un peu de sport. J'y ai trouvé des personnes aux qualités humaines incroyables qui m'ont vraiment aidé à me détendre notamment en troisième année de thèse. Les moments passés avec Clément le coach, Jordan la loco, Etienne le dénivelateur, Lucas l'insalien, Nico le jeune, Nico le vieux, Robin le gibbon, Clémence la steepleuse, Laetitia la maman, David le marathonien, Dany l'infatigable, mais aussi Mathilde, Marcel, Anatole, Mathieu, Nicolas. On retourne à Vic dès que possible mais cette fois, on sort pas le vendredi soir !

Mais je n'oublie pas les copains avec lesquels les parties de walou, de FIFA, de belote, de wist, de bombu, de limite limite, de pérudo, de molkky, de pétanque s'enchaînent sans qu'on se lasse. Maxou, Jerem, Baz, Simon, Max, Nana et Fanny, ne changez rien, vous êtes tous parfaits mais y en a un qui est con ! Merci, De nada !

Un petit coucou aux Nantais, ces vieux amigos que j'ai plaisir à revoir à chaque retour sur Nantes. Je connais certains d'entre vous depuis 20 ans (oui Yoyo, rappelle-toi le CE1 !), et c'est cool de garder cette amitié malgré la distance et la faible fréquence de mes retours…

Je n'oublie pas Margot qui depuis de nombreuses années absorbe mes plaintes quelles qu'elles soient ! Les discussions sur d'innombrables sujets, intimes ou non, sérieux ou non, et ton avis bien souvent pertinent m'ont été et continue de m'être très précieux.

Enfin, même s'ils n'ont pas vraiment aidé à la réalisation de cette thèse, je veux remercier ma petite famille dans son ensemble pour son soutien dans toutes les situations possibles et imaginables. Je vous admire tous les quatre pour différentes raisons : Alice, pour ta capacité à tout surmonter malgré une énorme sensibilité, Camille pour tes convictions inébranlables et ton énergie à les défendre sans jamais donner de leçons, et les deux vieux (bim dans la tête) pour votre recette de cuisine. On vous a imposé 3 ingrédients à ajouter au fur et à mesure que vous concoctiez le plat (en 89, 91 puis 95). Vous avez su surveiller la cuisson et remuer un peu (parfois beaucoup !) quand il le fallait pendant toutes ces années et aujourd'hui, ça m'a l'air plutôt réussi. Papa, tu disais que tu avais appris à faire la cuisine en regardant, ta mère faire ; si un jour j'ai l'occasion, je n'oublierai pas ce conseil et tacherai de faire aussi bien que vous l'avez fait avec nous.

Résumé

Contribution à la fabrication et la compréhension du comportement thermique de structures capillaires optimisées pour les boucles diphasiques à pompage thermo-capillaire

Les boucles diphasiques à pompage thermo-capillaire de type LHP (pour Loop Heat Pipe, en anglais), dont le fonctionnement s'apparente à celui d'un caloduc, permettent un transfert de chaleur particulièrement efficace et entièrement passif entre une source chaude et une source froide. Ce transfert s'effectue au moyen d'un fluide diphasique, mû grâce à la force motrice capillaire générée par un matériau poreux contenu dans l'évaporateur/réservoir de la LHP. Outre son rôle de barrière hydraulique entre les phases liquide et vapeur, ce matériau doit assurer une fonction de barrière thermique afin de favoriser l'évaporation du liquide. L'aptitude du matériau à remplir ses fonctions dépend étroitement de sa microstructure, elle-même liée à la méthode de fabrication. Dès lors, l'objectif de la thèse est d'associer la science des matériaux à celle de la thermique, pour améliorer les procédures de fabrication de structures capillaires existantes ou tester de nouvelles méthodes, et aboutir à des structures dont les caractéristiques sont en adéquation avec celles qui sont recherchées.

Au cours de ce travail, un modèle analytique est développé afin de simuler le comportement thermo-hydraulique d'une LHP munie de structures poreuses mono- et bicouches. L'intégration d'une seconde couche poreuse permet de limiter le flux de fuite par conduction à travers son épaisseur, tout en assurant un bon transfert de chaleur vers les interfaces liquide-vapeur, et ainsi favoriser l'évaporation. Une étude paramétrique est menée afin de connaître l'influence des caractéristiques hydrauliques et thermiques (conductivité thermique, perméabilité, porosité, rayon de pore) de chacune des deux couches sur les performances de la LHP, et de déterminer les valeurs optimales de ces caractéristiques.

Sur la base de ces résultats, de nombreux échantillons poreux en cuivre et en zircone, de forme cylindrique, ont été fabriqués, par frittage de poudres ou par une technique de freeze casting. Dans le but de comprendre l'influence des paramètres de frittage (pression de formation, masse de poudre frittée, temps et température de frittage) sur les caractéristiques des structures poreuses, un plan d'expérience a été suivi pour les échantillons en cuivre. Des structures bicouches ont également été réalisées, par dépôt d'une fine couche d'or sur certains échantillons en zircone, ou par superposition d'une couche de zircone et d'une couche de cuivre.

Un premier banc d'essais a été conçu et réalisé, qui permet de mesurer successivement le rayon de pore effectif et la perméabilité des structures capillaires obtenues. Les mesures de perméabilité montrent que les protocoles de fabrication des échantillons en cuivre sont plus reproductibles que ceux des échantillons en zircone. Les résultats obtenus grâce au plan d'expérience montrent que la pression de formation de la pastille poreuse est le paramètre le plus influent sur la perméabilité et le rayon de pores tandis que la masse de poudre frittée a une influence significative sur l'épaisseur de la pastille. La température et la durée de frittage ont une influence bien moindre.

Un second banc d'essais, dont la géométrie et le fonctionnement reproduisent ceux d'un évaporateur/réservoir de LHP, et intégrant successivement les différents échantillons fabriqués, permet de mesurer le coefficient d'échange thermique de l'évaporateur et de détecter le flux thermique maximal correspondant à l'assèchement partiel de la structure capillaire. Il s'avère que ces paramètres dépendent fortement des caractéristiques hydrodynamiques et géométriques de la structure, en particulier de son état de surface, sa perméabilité et son rayon de pores. L'existence d'un interstice entre la surface de l'échantillon et la paroi ailetée de l'évaporateur favorise l'évacuation de la vapeur et retarde ainsi

l’apparition de l’assèchement. Si cet échantillon est constitué de zircone, l’adjonction d’un revêtement en or permet une meilleure homogénéisation en température, donc une initiation plus tardive des premières bulles de vapeur. Un matériau poreux perméable permet la dissipation de fortes densités de flux thermiques, car le liquide percole plus facilement à travers lui. Une comparaison du flux maximal mesuré avec les limites de fonctionnement théoriques montre qu’un échantillon peu perméable est susceptible d’atteindre la limite capillaire alors qu’un échantillon très perméable atteindrait la limite d’ébullition. Toutefois, les tendances observées différent fortement selon le fluide utilisé (eau ou pentane). Le pentane permet d’obtenir des coefficients d’échanges plus élevés que l’eau grâce à sa forte mouillabilité. Le nombre de tests et de paramètres étant très élevé, une approche statistique par arbre de décision a été mise en œuvre. Elle confirme la forte influence du fluide, de l’état de surface et du rayon des pores sur le coefficient d’échange thermique.

Mots-clés : loop heat pipe, structure capillaire, frittage, freeze casting, caractérisation hydrodynamique, caractérisation thermique

Abstract

Contribution to the manufacturing and the understanding of the thermal behaviour of capillary structures dedicated to Loop Heat Pipes

The capillary pumped loops (CPL) or loop heat pipes (LHP), whom the operating principle is similar to classic heat pipes, enable an efficient heat transfer between a hot source and a cold source without additional energy sources. Indeed, a porous structure provides a capillary force that enables a two-phase fluid to circulate around the loop, transferring the heat from the evaporator to the condenser. The porous structure acts as a hydraulic barrier between the two phases and as a thermal barrier enabling the liquid evaporation. The ability of the capillary structure to fulfil its mission depends on its microstructure, and thus on the manufacturing process. Therefore, the objective of the present thesis is to join the thermal sciences with the material sciences in order to improve the existing manufacturing procedure or even to test new ones. It aims at obtaining capillary structures corresponding to heat transfer applications.

During this work, an analytical model is developed in order to simulate the thermo-hydraulic behaviour of LHPs with different capillary structures (mono and multi layers). The integration of a second layer enables to decrease the heat lost by conduction through its thickness, while ensuring a high heat transfer to the liquid-vapour interface where the evaporation takes place. A parametric study is conducted in order to analyse the influence of the thermo-hydraulic characteristics (thermal conductivity, permeability, porosity, pore radius) of each layer on the thermal performance of the LHP, and in order to determine the optimum wick characteristics.

Based on these results, many porous samples are manufactured by sintering or freeze casting of copper and zirconia powders. One of the objectives is to understand the influence of the manufacturing parameters (forming pressure, mass of sintered copper, sintering time and sintering temperature) on the samples characteristics. In this purpose, a design of experiment is proposed for the manufacturing of the copper samples. Another objective is to manufacture multi-layer structures. Moreover, the co-sintering of two layers and the coating of a thin gold layer on zirconia samples is done in order to obtain bi-layer wicks.

A first test bench has been designed in order to successively determine the permeability and the effective pore radius of the capillary structures. The reproducibility of the manufacturing protocol has been studied and showed that the copper enables to obtain more reproducible characteristics than zirconia. The results obtained by means of the design of experiment show that the forming pressure has a significant influence on the permeability and the effective pore radius whereas the mass of sintered powder has an influence on the thickness. The sintering time and sintering temperature have not significant influences on the samples characteristics.

A second test bench, whom the geometry and the operating principle reproduce the ones of an evaporator/reservoir of a LHP, is designed in order to determine the evaporator heat transfer coefficient and the maximum heat load that the capillary structure can evacuate, before the occurrence of an operating limit due to partial dry-out. The values significantly depend on the hydrodynamic and topographic characteristics of the porous structure, especially its permeability, its pore radius and its surface quality. The presence of a gap between the porous structure and the evaporator fins makes easier the removal of the vapour and pushes back the occurrence of a dry-out. The addition of a gold layer on a zirconia sample enables a spreading effect of the heat, and delay the occurrence of the nucleation. A porous structure with a high permeability enables the management of high heat loads since the percolation through the wick is made easier. The theoretical study of the operating limits shows that a

structure with a low permeability has more chance to reach the capillary limit than a structure with a high permeability which reaches the boiling limit. However, the observed trends significantly differ depending on the working fluid (water or pentane). Pentane enables to reach higher heat transfer coefficient due to its high wettability. The high number of tests and parameters has enabled a statistical approach by means of a decision tree method. It confirms that the fluid, the surface quality and the pore radius have a significant influence on the heat transfer coefficient.

Key-words: loop heat pipe, capillary structure, sintering, freeze casting, hydrodynamic characterisation, thermal characterisation

Contents

Résumé 7
Abstract 9
Contents 11
List of figures 15
List of tables 20
Nomenclature 21
Introduction 25
Chapter I Introduction to the fundamental concepts of the heat and mass transfer in a LHP ... 29
I.1 Description of a loop heat pipe and its operating principle 30
I.1.1 Description of the components of a LHP 30
I.1.2 Thermodynamic cycle of a LHP 33
I.1.3 Characterisation of the LHP performance 36
I.1.4 Selection of the working fluid 40
I.1.5 Selection of the material used to manufacture the wick 43
I.1.6 Selection of the material/working fluid couple 47
I.2 Thermo-hydraulic behaviour of a LHP porous medium 50
I.2.1 Description of the hydrodynamic characteristics of a porous wick 50
I.2.2 Thermal behaviour of a porous wick in contact with the evaporator wall 53
I.2.3 Development of advanced porous medium 57
I.2.4 Conclusion 62
I.3 Evaporator modelling 63
I.3.1 Model of heat transfer within the porous medium 63
I.3.2 Model of evaporation at the wick surface 64
I.3.3 Models of the whole evaporator 64
I.3.4 Model of evaporator coupled to the LHP 69
I.4 Conclusion 72
Chapter II Theoretical study of a bi-layer wick performance 73
II.1 Development of the LHP model 74
II.1.1 Equations of the model 74
II.1.2 Solving procedure 76
II.1.3 Description of the reference LHP 77
II.1.4 Results in standard conditions 78
II.1.5 Validity of the isothermal condition at the interface of the wick layers 79
II.2 Parametric study 81

II.2.1 Characterisation of the performance of a LHP with a bilayer wick 82
II.2.2 Influence of the thickness and thermal conductivity 84
II.2.3 Influence of the permeability 86
II.2.4 Influence of the porosity 87
II.2.5 Influence of the pore radius 88
II.2.6 Influence of the working fluid 90
II.2.7 Conclusion 91
Chapter III Manufacturing of the wicks 93
III.1 Methods to manufacture porous structures 94
III.1.1 Partial Sintering of powder 94
III.1.2 Freeze casting 99
III.1.3 Other methods 101
III.2 Manufacturing of the wick bottom layer 103
III.2.1 Pulsed Electric Current Sintering of copper wires 103
III.2.2 Partial sintering of copper powder 104
III.3 Manufacturing of the wick top layer 107
III.3.1 Freeze casting of zirconia powder 108
III.3.2 Partial sintering of zirconia powder 110
III.4 Manufacturing of a bilayer wick 111
III.4.1 Co-sintering of the two layers 112
III.4.2 Coating of a gold film on the top layer 112
III.5 Geometrical characterisation of the manufactured samples 113
III.5.1 Determination of the mass and the volume of the sample 113
III.5.2 Topographical characterisation 114
III.5.3 Microscopic characterisation 115
III.6 Conclusion 117
Chapter IV Hydrodynamic characterisation 119
IV.1 State-of-the-art of the hydrodynamic characterisation methods 120
IV.1.1 Determination of the permeability 120
IV.1.2 Determination of the effective pore radius 121
IV.2 Experimental apparatus and procedures 123
IV.2.1 Experimental apparatus 123
IV.2.2 Saturation of the wick 124
IV.2.3 Determination of the permeability 124
IV.2.4 Determination of the effective pore radius 127
IV.3 Results and discussions 129

IV.3.1 Reproducibility of the protocols 129
IV.3.2 Influence of the sintering parameters on the copper sample characteristics 131
IV.3.3 Presentation of the hydrodynamic characteristics of the zirconia samples 132
IV.3.4 Comparison with the literature 134
IV.4 Conclusion 135
Chapter V Thermal characterisation of the porous wick 137
V.1 State-of-the-art of the test benches 138
V.2 Description of the experimental apparatus and the procedures 140
V.2.1 Description of the experimental apparatus 140
V.2.2 Description of the experimental procedures 142
V.3 Theoretical study of the wick operating limits 144
V.3.1 Prediction of the capillary limit 144
V.3.2 Prediction of the boiling limit 145
V.4 Influence of the test bench parameters on the wick thermal behaviour 146
V.4.1 Reproducibility of the thermal characterisation 146
V.4.2 Influence of the saturation temperature 146
V.4.3 Influence of the hydrostatic pressure 148
V.4.4 Influence of the oxidation of the evaporator 148
V.4.5 Influence of the pressure applied on the back face of the evaporator 148
V.4.6 Influence of the addition of a top layer 149
V.4.7 Conclusion 150
V.5 In-depth investigation of the thermal behaviour of wicks used as a bottom layer 151
V.5.1 Influence of the surface quality 151
V.5.2 Influence of the hydrodynamic characteristics of the wick 156
V.5.3 Comparison of the results obtained with water and pentane 161
V.5.4 Statistical analysis of the parameters influence on the heat transfer coefficient 161
V.6 Conclusion 165
Conclusion 167
References 171
Appendix A Effective thermal conductivity correlations 179
Appendix B Detailed expression of the coefficients defined in the Siedel analytical study 181
Appendix C Characterisation by mercury intrusion 185
Appendix D Characteristics of the capillary structures 186

List of figures

Figure 0-1 : Microprocessor transistor counts between 1971 and 2011 and Second Moore's law [2] . 25
Figure 0-2 : Schematic of a capillary heat pipe (Bonjour *et al.* [3]). 26
Figure 0-3 : Schematic of a loop heat pipe, Siedel [4] 26
Figure 0-4: Expected flowchart of the PhD thesis 27
Figure I-1 : Schematic of a classic LHP (Siedel *et al.* [8]) 30
Figure I-2 : schematic of a LHP (a) and a CPL (b), Butler *et al.* [13] 31
Figure I-3 : Schematic of a flat evaporator (adapted from Singh *et al.* [14]) 31
Figure I-4 : Schematic of a cylindrical evaporator (adapted from Kaya and Goldak [11]) 31
Figure I-5 : Schematic of a cylindrical evaporator and focus on the meniscus (Cimbala *et al.* [17]) 32
Figure I-6: P-T diagram of a LHP operating cycle 34
Figure I-7: Saturation curve of water 35
Figure I-8: Schematic of the liquid location inside the LHP according to its operating mode, Launay *et al.* [5] 37
Figure I-9: Typical shapes of LHP operating curves, Launay *et al.* [5] 37
Figure I-10: Operating domain of the working fluid in the P-T diagram (Coquard [41]) 40
Figure I-11 : Comparison of the various working fluid properties at a temperature of 20 °C 42
Figure I-12: Occurrence of the utilisation of each working fluids in the experimental studies published between 1998 and 2010 (Launay and Vallée [18]) 43
Figure I-13: Saturation curves of standard fluids for LHP 43
Figure I-14: Occurrence of the various wick materials in the experimental studies of LHP published between 1998 and 2010 44
Figure I-15: Melting temperatures of various polymers, metals and ceramics 44
Figure I-16 : Thermal expansion coefficients of various polymers, metals and ceramics (Lide [46]).. 45
Figure I-17: Thermal conductivities of various polymers, metals and ceramics, Touloukian ([47]–[49]) 45
Figure I-18 : Comparison of material prices (industrie.com [50], Les Echos [51], january 2016) 46
Figure I-19 : Contact angles measurements (Extrand and Kumagai [93]) 49
Figure I-20: Static, advancing and receding contact angles of water on various materials (when several authors investigated the same contact angle, the average value is plotted). 49
Figure I-21 : Tortuosity of a porous structure 51
Figure I-22 : Permeability of a sintered wick calculated with different correlations 52
Figure I-23 : Permeability versus the porosity (powder sphere radius equal to 2.5 µm) 52
Figure I-24 : Permeability versus the pore radius (porosity equal to 40 %) 53
Figure I-25 : Pore radius versus the porosity for various samples 53
Figure I-26 : Evolution of the evaporator heat transfer coefficient as a function of the heat flux density and the saturation temperature (Zhao and Liao [38]) 54
Figure I-27: Evaporator heat transfer coefficient as a function of the heat flux density and the elevation (Delil and Baturkin [109]) 55
Figure I-28 : Various classic groove designs (Choi *et al.* [112]) 56
Figure I-29 : New groove design (Choi *et al.* [112]) 56
Figure I-30: Influence of a gap between the wick and the evaporator fins (Schertzer *et al.* [111]) 56
Figure I-31: Change in the average heated surface temperature with heat flux for a gap of (a) □ 0 µm, Δ 100 µm, + 200 µm, ◊ 300 µm, x 400 µm, and (b) ○ 600 µm, Δ 700 µm, x 1000 µm (Khammar *et al.* [110]) 57
Figure I-32: Schematic of the evaporator at the start-up (adapted from Platel *et al.* [113]) 57

Figure I-33 : Schematic of the dry-out mechanism in a monoporous wick (adapted from Lin *et al.* [115]) 58
Figure I-34 : Schematic of the evaporation mechanism for a bi porous wick (Lin *et al.* [115]) 58
Figure I-35 : Schematic structure of a bimodal porous medium for a bidispersed wick (a) and a biporous wick (b). The arrows indicate the flow paths (Mottet and Prat [120] adapted from Rasor and Desplat [121]) 59
Figure I-36 : Microscopic view of a bi-modal porous medium with a SEM, Yeh *et al.* [116] 59
Figure I-37 : Pore size distribution of a monoporous and a biporous wick (Yeh *et al.* [116]) 59
Figure I-38 : Schematic of porous media with the bidispersed structure: (a) bidispersed porous medium; (b) equilateral triangular pattern of three clusters; (c) equilateral triangular pattern inside a cluster; (d) square pattern inside a cluster (Yu and Cheng [122]) 60
Figure I-39: Schematic of the menisci in a "real" porous structure when the maximum capillary pressure is reached 61
Figure I-40 : Comparison of LHP performance for monoporous, biporous and double-layer wicks (Wu *et al.* [119]) 62
Figure I-41 : Schematic of a multi-layer wick (Xu *et al.* [128]) 62
Figure I-42 : Thermal resistance as a function of the mass flow rate (e_w = 6 mm, S_w = 12.5 cm²) 64
Figure I-43: Schematic of the pore geometry used by Zhao and Liao [108] 65
Figure I-44 : Heat transfer coefficient versus heat flux density (Zhao and Liao [108]) 66
Figure I-45 : Schematic of the vapour zone by Demidov and Yatsenko [138] 66
Figure I-46 : Schematic of the model developed by Figus *et al.* [114] 67
Figure I-47 : Example of results obtained by Figus *et al.* [114] 67
Figure I-48 : Pore network representation of porous microstructure (Mottet *et al.* [29]) 68
Figure I-49 : Schematic of discrete liquid-vapour interfaces in the pore network (Mottet *et al.* [29]) . 68
Figure I-50 : Development of a two-phase zone under the evaporator fins (Mottet *et al.* [29]) 69
Figure I-51: Schematic of the modelled LHP (a) and the nodal network (b): Siedel *et al.* [4], [141]... 70
Figure I-52: Schematic of the 2D analytical model domain (Siedel [4]) 71
Figure I-53 : Influence of λ_{eff} on T_e (adapted from Siedel [4]) 71
Figure I-54: Influence of λ_{eff} on the heat flux distribution if Q_{in} = 50 W (Siedel [4]) 72
Figure II-1: Schematic of the complete LHP 74
Figure II-2: Schematic of the 2D analytical model domain 74
Figure II-3 : Solving procedure of the model 77
Figure II-4: Results of the analytical model in standard conditions (Table II-3) 78
Figure II-5: Schematic of the discretization 80
Figure II-6: Example of temperature field inside the wick in a case of a valid isothermal boundary condition 81
Figure II-7: Example of temperature field inside the wick in the case of a non-valid isothermal boundary condition 81
Figure II-8: Evolution of the pressures inside the porous medium (Q_{in} = 50 W, $r_{p,top}$ = 25 µm) 83
Figure II-9 : Evolution of the pressures inside the porous medium (Q_{in} = 100 W, $r_{p,\,top}$ = 25 µm) 83
Figure II-10 : Influence of top layer thickness and thermal conductivity on the global thermal resistance 84
Figure II-11: Influence of the top layer thickness and thermal conductivity on the operating limits ... 85
Figure II-13 : Influence of the bottom layer thickness and thermal conductivity on the global thermal resistance 85
Figure II-12: Schematic of the heat transfer in the bottom layer between the evaporator fins and the fluid 86

Figure II-14: Influence of the bottom layer thickness and thermal conductivity on the operating limits 86
Figure II-15: Influence of the bottom and top layer permeability on the thermal resistance 87
Figure II-16 : Influence of the bottom and top layer permeability on the operating limits 87
Figure II-17 : Influence of the porosity on the global thermal resistance 88
Figure II-18: Influence of the bottom and top layer porosity on the operating limits 88
Figure II-19: Influence of the top and bottom layer pore radius on the thermal resistance..... 89
Figure II-20 : Influence of versus the top layer pore radius on the operating limits 89
Figure II-21 : Influence of the bottom layer pore radius on the operating limits 90
Figure II-22 : Influence of the working fluid on the global thermal resistance..... 90
Figure III-1 : Competition between two mechanisms : Sintering and grain growth (adapted from Bernache-Assolant [146])..... 94
Figure III-2 : Schematic of the wick before (left) and after the sintering (right), Déjou [147]..... 95
Figure III-3 : Schematic of Spark Plasma Sintering (Khor *et al.* [148]), illustrated on hollow spheres random compacts..... 96
Figure III-4 : Distribution of the powder particles in the green compact (a) and interconnected porosity formed in the sintered wick (Samanta *et al.* [152]) 97
Figure III-5 : Pore radius (r_p) of experimental LHP wicks versus the powder radius (r_s)..... 98
Figure III-6: Evolution of the porosity of nickel samples as a function of the sintering temperature... 98
Figure III-7 : Schematic of a freeze casting system (Wegst *et al.* [156])..... 100
Figure III-8 : Schematic diagram of the ice templating process (adapted from Bouville [157]) 100
Figure III-9 : Cross sectional of ice templated ceramic samples including various additives (Bouville [157])..... 101
Figure III-10 : Schematic of robocasting technique (Saiz *et al.* [162])..... 102
Figure III-11 : Typical processing methods for the production of macroporous ceramics 103
Figure III-12: Pictures of the porous structure after PECS 104
Figure III-13: Particle size distribution of the copper power used for sintering 104
Figure III-14: Schematic of the method to obtain a flat disk shaped porous copper..... 105
Figure III-15: Temperature profile of the muffle furnace during the copper powder sintering 105
Figure III-16: Picture of the bottom layer (a) and XRD scan (b) 106
Figure III-17: Picture of a failed sintering process..... 106
Figure III-18: Particle size distribution of the zirconia powder 108
Figure III-19: Schematic of the freeze caster 108
Figure III-20: Example of pressure and temperature profiles used for freeze casting 109
Figure III-21: SEM pictures of a freeze casted samples..... 109
Figure III-22: Temperature profile of the muffle furnace during the zirconia powder sintering 110
Figure III-23: SEM pictures of the sample Zi-sin-5-a..... 111
Figure III-24: Pore size distribution of the nylon powder..... 111
Figure III-25: Schematic of the method to obtain a bi-layer wick 112
Figure III-26: Schematic arrangement of the gas ion and evaporation sources in a vacuum chamber 113
Figure III-27: Examples of topography analysis by confocal microscopy (profile (a, d) and complete surface (b, e)) and with pressure paper (c, f) of the side A of sample Cu-sin-7-c (a, b, c) and the side B of sample Cu-sin-2-c (d, e, f) 115
Figure III-28: XRCT of the sample Ni-sin-x (a) and microscopy of the sample Cu-sin-3-a (b)..... 115
Figure III-29: XRCT of a porous sample with large pores (2D and 3D views of the sample Ni-sin-x) 116
Figure III-30: SEM view of the sample Cu-sin-6-b 116

Figure IV-1: Experimental apparatus to measure the permeability using a constant pressure reservoir (Singh *et al.* [169]) 120
Figure IV-2: Experimental set up to measure the permeability by NMR (Looyestijn *et al.* [170]) 121
Figure IV-3 : Schematic of the test benches for effective pore radius measurements (Holley and Faghri [171]) 121
Figure IV-4: Experimental apparatus designed to perform the bubble point testing (Singh *et al.* [7]) 122
Figure IV-5: U-tube bubble point testing system (Singh *et al.* [169]) 123
Figure IV-6: Schematic of the experimental setup 124
Figure IV-7: Schematic of the experimental procedure used to saturate the wick with liquid..... 124
Figure IV-8 : Schematic of the successive steps enabling to measure the permeability 125
Figure IV-9: Example of experimental data enabling to determine the permeability (Cu-sin-7-c) 126
Figure IV-10: Comparison between the permeabilities measured with pentane and with water 127
Figure IV-11 : Schematic of the successive steps enabling to measure the effective pore radius..... 127
Figure IV-12: Example of minimum meniscus radius determination (sample Cu-sin-5-a). 128
Figure IV-13: Contact angle of water (a) and pentane (b) on oxidised copper, and water (c) and pentane on standard copper (c) 129
Figure IV-14: Hydrodynamic characteristics of samples obtained with the same protocol 130
Figure IV-15: Porosity and mechanical resistance of the zirconia samples as a function of the percentage of PFA 133
Figure IV-16: Experimental permeability versus theoretical permeability calculated with the Kozeny-Carman and Rumpf-Gupte correlations..... 135
Figure V-1 : Schematic of the experimental set up used by Zhao and Liao ([38], [108])..... 138
Figure V-2: Schematic of the experimental set up used by Khammar *et al.* [110] 139
Figure V-3: Schematic of the experimental apparatus used by Delil and Baturkin [109]..... 139
Figure V-4 : Evolution of the vapour zone up to the breakthrough (Mottet *et al.* [29])..... 140
Figure V-5 : Schematic of the experimental apparatus 141
Figure V-6 : Evaporator design (Siedel [4])..... 141
Figure V-7: Example of thermal behaviour (sample Cu-sin4-a, water, 50 °C)..... 143
Figure V-8: Evaporator superheat in the presence (a) and in the absence (b) of a hysteresis (Cu-sin-2-c) 143
Figure V-9: Schematic of the meniscus motion depending on the heat load 144
Figure V-10: Test of reproducibility on the sample Cu-sin-5-a (water, T_{sat} = 50 °C) 146
Figure V-11: Influence of the saturation temperature on the thermal performance (Cu-sin-3-a, water) 147
Figure V-12: Influence of the hydrostatic pressure with sample Cu-sin-3-a (water, T_{sat} =50 °C) 148
Figure V-13: Influence of the chemical surface quality of the evaporator with sample Cu-sin-6-c (water, T_{sat} =50 °C)..... 149
Figure V-14: Influence of the pressure applied on the back face of the evaporator (sample Cu-sin-4-a, pentane, T_{sat} = 40 °C)..... 149
Figure V-15: Heat transfer coefficient as a function of the heat load applied to a bi-layer wick as well as to the copper layer alone 150
Figure V-16: Confocal microscopy of the sample Cu-sin-7-c 152
Figure V-17: Influence of the surface quality on the thermal performance 153
Figure V-18: Schematic of the different contact configurations between the porous wick and the evaporator wall..... 154
Figure V-19: Schematic of the boiling dynamics at the vicinity of an evaporator fin 154
Figure V-20: Comparison of the thermal performance before and after the coating 155
Figure V-21: Heat transfer coefficient as a function of the heat load for each sample with water 156

Figure V-22: $Q_{opt,exp}$ as a function of $Q_{opt,th}$ with water 157
Figure V-23: $\Delta T_{sh,max,exp}$ as a function of $\Delta T_{sh,max,th}$ with water (r_n = 3.6 µm) 158
Figure V-24: Pictures obtained with optical microscopy 158
Figure V-25: Heat transfer coefficient as a function of the heat load for each sample with pentane .. 159
Figure V-26: $Q_{opt,exp}$ as a function of $Q_{opt,th}$ with pentane 160
Figure V-27: Experimental maximum superheat as a function of the effective pore radius 160
Figure V-28: Comparison of the thermal performance of the samples with water and pentane 161
Figure V-29: Decision tree enabling the prediction of the heat transfer coefficient 164
Figure V-30: Decision tree enabling the prediction of the heat transfer coefficient with water 165
Figure A-1: Effective thermal conductivities calculated with λ_l = 0.6 W/m.K and λ_{mat} = 380 W/m.K 180
Figure B-1: Schematic of the 2D analytical model domain and boundary conditions 181
Figure B-2: Geometrical parameters enabling the resolution of the analytical model 182
Figure C-1: Example of curves enabling the determination of the porous medium characteristics 185

List of tables

Table I-1 : Classification of the condenser technologies (adapted from Launay and Vallée [18]) 33
Table I-2: Analytical expressions of the operating temperature, Launay *et al.* [5] 38
Table I-3: Operating temperature range for various working fluids (Faghri [42]) 41
Table I-4: Environmental and safety properties of various working fluids 41
Table I-5: Properties of usual working fluids at 20 °C 42
Table I-6: Advantages and drawbacks of metallic wicks 46
Table I-7 : Advantages and drawbacks of polymer wicks 47
Table I-8: Advantages and drawbacks of ceramic wicks 47
Table I-9 : Chemical compatibility between various fluids and materials 48
Table I-10: Studies investigating the wettability of water on various materials 50
Table I-11: Thermal characterisation of porous structures 55
Table I-12 : Comparison of porous samples permeabilities (Chen *et al.* [123]) 60
Table I-13: Characteristics of the LHP for the parametric study performed by Siedel [4] 70
Table II-1 : Nodal network equations of Siedel [4] and the present model 75
Table II-2: Output data of the model 76
Table II-3 : Definition of the standard LHP for the parametric study 78
Table II-4 : Maximum heat loads of various working fluids 91
Table II-5 : Optimum wick characteristics 91
Table III-1 : Effect of the sintering parameters on the wick characteristics. A “plus”, for positive, means that the effect corresponds to the objective of the manufacturer (high porosity and small pore radius) 99
Table III-2: Sintering parameters of the design of experiment 107
Table III-3: Manufacturing protocols of the copper samples obtained by sintering 107
Table III-4: Manufacturing protocols by freeze casting 110
Table III-5: Manufacturing protocols of zirconia samples by sintering 111
Table IV-1: Hydrodynamic characteristics of the manufactured samples 131
Table IV-2: Influence of the sintering parameters on the wick characteristics 132
Table IV-3: Hydrodynamic characteristics of the zirconia samples 133
Table V-1: Influence of the saturation temperature on the theoretical limits (Cu-sin-3-a, water) 147
Table V-2: Results of thermal characterisation of the bilayer wick, and the copper layer alone (water, T_{sat} = 50 °C, H_l = 3.9 cm) 150
Table V-3: Surface quality of the samples manufactured following the design of experiment 151
Table V-4: Characteristics of the sample Cu-sin-7-c after each surface treatment (pentane, T_{sat} = 40 °C, H_l = 3.9 cm) 153
Table V-5: Results of characterisation of the two zirconia samples used to test the coating 155
Table V-6: Results of thermal characterisation with water (T_{sat} = 50 °C, H_l = 3.9 cm, side A) 157
Table V-7: Results of thermal characterisation with pentane (T_{sat} = 40 °C, H_l = 3.9 cm, side A) 159
Table V-8: Test parameters enabling the estimation of the heat transfer coefficient 163
Table B-1: k_n coefficients (Siedel [4]) 182
Table C-1: Comparison between the porosity and permeability obtained with mercury intrusion and with the test benches used in this thesis 185
Table D-1: Characteristics of the manufactured porous samples 186

Nomenclature

Latin symbols

a, a_0, a_1	length (k_n coefficients, Appendix B)	m
a_{ev}	accommodation coefficient	-
b	length (k_n coefficients, Appendix B)	m
B	length ratio (k_n coefficients, Appendix B)	-
c, c_0, c_1	length (k_n coefficients, Appendix B)	m
C	length ratio (k_n coefficients, Appendix B)	-
c_p	specific heat	$J.kg^{-1}.K^{-1}$
d, d_0	length (k_n coefficients, Appendix B)	m
D	length ratio (k_n coefficients, Appendix B)	-
d	diameter	m
e	thickness	m
g	specific free energy	J/kg
g	gravitational acceleration	$m.s^{-2}$
H	height	m
h	heat transfer coefficient	$W.m^{-2}.K^{-1}$
h_{lv}	enthalpy of vaporisation	$J.kg^{-1}$
I	electrical current	A
i, j	finite element increment	
J	mechanical equivalent of heat	$kg.m.kcal^{-1}$
k_n	n^{th} analytical model coefficient	-
k_{hfs}	heat flux sensor sensitivity	
K	permeability	m²
L	length	m
l	width	m
m, n	Fourier series increment (k_n coefficients, Appendix B)	
M, N	line and column numbers of the discretisation matrix	
$\bar{M}$	molar mass	$kg.mol^{-1}$
m	mass	kg
$\dot{m}$	mass flow rate	$kg.s^{-1}$
n	iteration increment	-
Nb	Number of merit	-
P	pressure	Pa
Q	heat flux	W
R	thermal resistance	$K.W^{-1}$
$\bar{R}$	universal gas constant	$J.K^{-1}.mol^{-1}$
r	radius	m
S	cross-sectional area, or surface	m²
T	temperature	K

t	time	s
U	voltage	V
u	velocity	$m.s^{-1}$
$\dot{V}$	volumetric flow rate	$m^3.s^{-1}$
V	volume	m^3
x,y,z	axis coordinates	m

Greek Symbols

α	regular pressure losses coefficient	-
β	singular pressure losses coefficient	-
Δ	difference	-
δ	film thickness	
ε	porosity	-
λ	thermal conductivity	$W.m^{-1}.K^{-1}$
μ	dynamic viscosity	Pa.s
η	pore depth (Zhao and Liao [107])	m
ϕ	heat flux density	$W.m^{-2}$
ρ	density	$kg.m^{-3}$
σ	surface tension	$N.m^{-1}$
θ	angle	rad
τ	constant of time	s
ξ	tortuosity	-

Subscripts

0	initial
2φ	two-phase
δ	thin film
∞	infinity, at the very end of the experiment
a	advancing
amb	ambient
b	evaporator body
bot	bottom layer
c	condenser, condensation
ci	cumulative intrusion
cont	contact
cap	capillary
Darcy	Darcy
e	evaporator

eff	effective
elec	electrical
eq	equilibrium
ev	evaporation
exp	experimental
ext	external
f	forming
fin	fins
gap	gap
gr	vapour grooves
hfs	heat flux sensor
hl	heat leaks
hs	hydrostatic
i, j	control volume increment
i	inner, inlet, internal
in	input
interconnection	interconnection
L	liquid line
l	liquid
loss	heat losses by the back face of the evaporator
LHP	loop heat pipe
m	meniscus
mat	material
min	minimum
max	maximum
n	nucleation
NCG	non-condensable gases
o	outer, outlet
opt	optimum
p	pore
p	plate (only when associated with θ)
pentane	pentane
r	reservoir of the LHP
r	receding (only when associated with θ)
res	reservoir of the test bench
real	real
s	powder particle
s	static (only when associated with θ)
sat	saturation
sen	sensible
sh	superheat

sin	sintering
sink	heat sink
straight	straight
sub	subcooling
th	theoretical
top	top layer
tot	total
tube	tube
V	vapour line
v	vapour
vt	vapour tube
w	wick
water	water
wall	evaporator wall
wp	pore wall
we	wick, evaporator side

Non Dimensional Numbers

$Bi = \frac{Lh}{\lambda}$	Biot number
$Re = \frac{\rho u d}{\mu}$	Reynolds number
$Pe = \frac{\rho u L c_p}{\lambda}$	Peclet number

Introduction

The thermal management takes more and more place in many industrial sectors, especially in the telecom and computer industries (hardware), where the density of electronic components increases constantly. In 1965, Gordon Moore predicted (first Moore's Law [1]) the every year doubling in the number of components per integrated circuit during a decade. In 1975, he readjusted his forecast (second Moore's law [2]), saying that the number of transistors on a microprocessor will double every two year (Figure 0-1). This prediction has been verified up to 2010 where constructors faced cooling problems. The simultaneous power increase of computers and their dimension decrease leads to heat flux densities never encountered before. Moreover, the size of the classical cooling systems using a finned heat sink and a fan must be reduced and thus, the cooling capacity decreases as well.

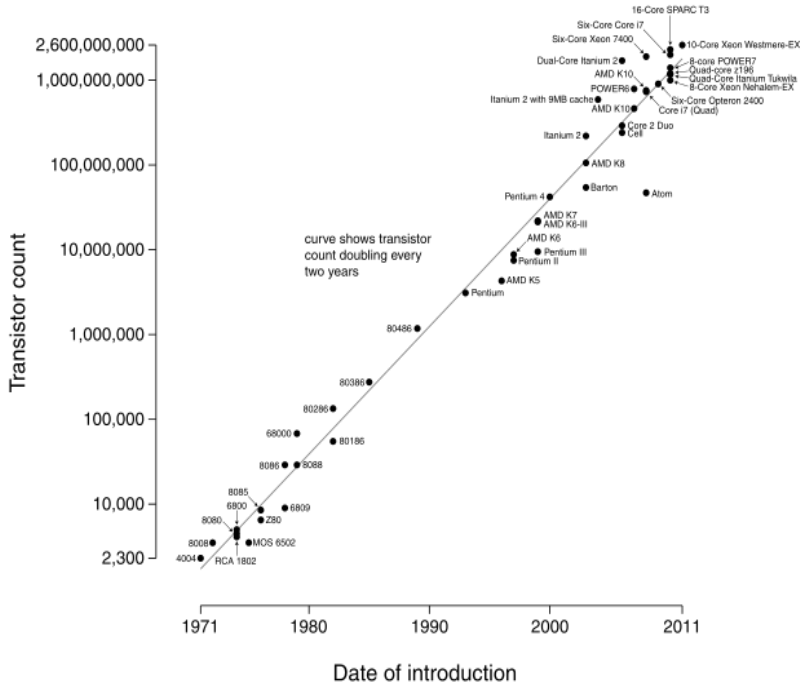

Figure 0-1 : Microprocessor transistor counts between 1971 and 2011 and Second Moore's law [2]

Thus, more performant cooling systems, usually based on liquid-vapour phase change phenomena, must be developed to answer these issues. Some of these devices use heat pipe technologies to transfer the heat from a very confined space to a location where space is available for the heat sink.

A heat pipe is a close tight envelope filled with a two-phase fluid at liquid-vapour equilibrium (Figure 0-2). The heat flux supplied at one end, called evaporator, enables to evaporate the liquid phase. The vapour flows to the other end, which is cooled and where it condenses. A capillary structure pumps the liquid back to the evaporator. Thus, this system is passive since there is no mechanical pump to ensure the circulation of the fluid. The absence of pump is a major advantage since it decreases the mass, the system complexity and the failure risk (less vibrations).

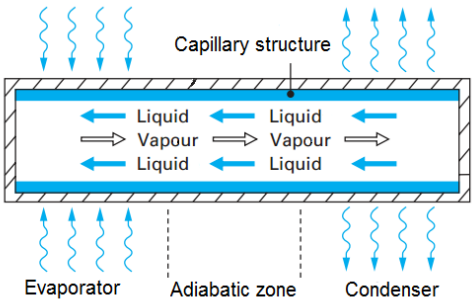

Figure 0-2 : Schematic of a capillary heat pipe (Bonjour *et al.* [3]).

However, heat flux densities transferred by traditional capillary heat pipes are generally limited, especially over long distances, due to operating limits inherent to the presence of a wick covering the whole internal surface of the device. Loop heat pipes (LHPs) are less sensible to this limit. A LHP operates similarly to a classic heat pipe. The main difference is that the wick is only located in the evaporator region (Figure 0-3). Furthermore, the vapour and the liquid lines are separated, avoiding the interactions between both phases that flow in opposite directions.

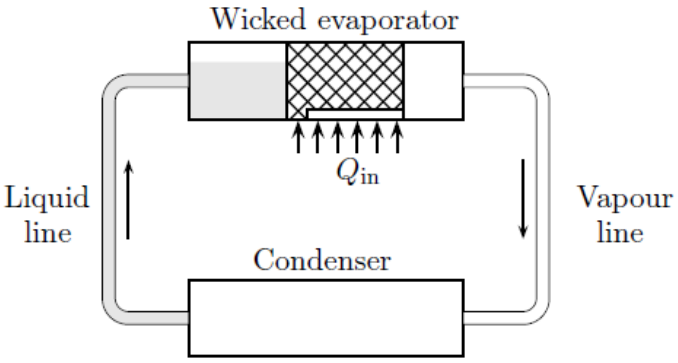

Figure 0-3 : Schematic of a loop heat pipe, Siedel [4]

The first LHP was developed to cool electronic components in spatial applications. Nowadays, two-phase loops are already implemented in industrial systems and especially the Capillary Pumped Loop for Integrated Power (CPLIP) whose operating principle is the same than in a LHP. They are used to evacuate the heat generated by railway inverters. Even if LHPs start to be commercialised, the physical mechanisms governing their operation are not fully understood and many researchers work on the improvement of their thermal performance. The CETHIL laboratory is involved in this research area for a dozen of years. In 2006, during the European project COSEE[2], Launay *et al.* [5] developed a simplified analytical model in order to facilitate the design of LHPs. In 2010, the laboratory worked together with the ATHERM Company, in the framework of the SYSHANG[3] project to manufacture the first LHP dedicated to avionic applications. Hodot [6] tested the thermal behaviour of this LHP submitted to an acceleration field. More recently, in the framework of the PRIMAE[4] project, the CETHIL patented an

[2]COSEE: Cooling Of Seat Electronic box and cabin Equipment, European FP6-Project AST5-CT-2006-030800

[3]SYSHANG: SYStème à cHANGement de phase

[4]PRIMAE: Packaging of futuRe Integrated ModulAr Electronics, European Commission Grant Agreement FP7-265416-Primae – www.primae.org

adsorption-based antifreeze solution enabling a LHP to operate with water as the working fluid. During his PhD thesis, Siedel [4] developed a complete analytical model to accurately predict the heat and mass transfer inside a LHP.

However, since visual observation inside the evaporator of a LHP is difficult, the fine comprehension of the phenomena acting in its capillary structure remains nowadays an issue. Moreover, these phenomena are strongly coupled to those operating in the other parts of the loop. Thus, there is a need of experimental test benches decoupling the evaporator from the rest of the loop and enabling the analysis of its hydrodynamic and thermal behaviours.

The performance of the evaporator is closely linked to the wick characteristics, depending itself on its manufacturing process. Thus, the design and manufacturing of porous materials suitable for LHPs requires a collaborative work between material science and thermal science laboratories. The specific development of manufacturing procedures, using classical techniques like sintering or non-classical techniques like freeze casting or robocasting, is expected to enhance the heat transfer capacity of the LHPs. Thereby, the CETHIL laboratory and the MATEIS laboratory joined forces to build the 2MATHER[5] project, which was funded by the Carnot Institute "Ingéniere @ Lyon" in 2015.

The present PhD thesis, which is part of this project, intends developing manufacturing techniques of capillary structures specifically dedicated to LHP applications. It also aims to better understand the link between the manufacturing parameters and the wick characteristics. An original approach, presented in Figure 0-4, will be developed to reach these objectives.

In a first step, the search of optimum wick characteristics will be undertaken, using a refined model describing the heat and mass transfer inside the LHP evaporator, coupled to a complete model of the system that provide realistic boundary conditions. In a second step, classical manufacturing techniques of porous materials (sintering) will be adapted to obtain the required characteristics while specific manufacturing methods (freeze casting) will be developed. The consecutive characterisation of the manufactured porous samples will highlight the effect of manufacturing parameters on these characteristics, and thus, helps to adjust these parameters and to improve the theoretical model. The in-situ testing of a capillary structure inside a LHP is the last step of this approach, but it is outside the scope of the present work.

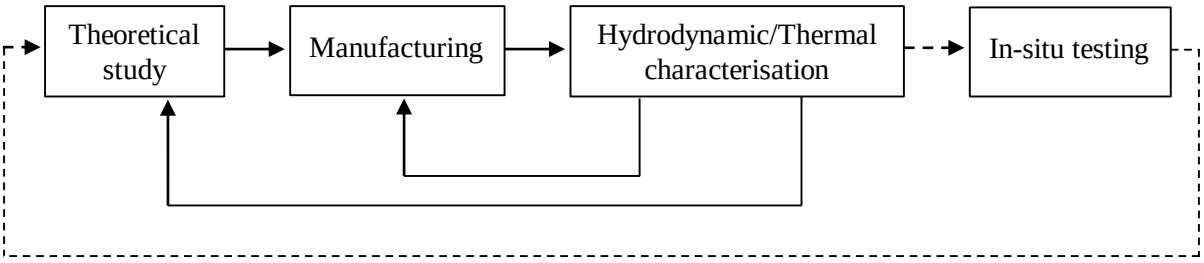

Figure 0-4: Expected flowchart of the PhD thesis

[5]2MATHER: MAtériaux poreux structures pour le MAnagement THERmique

This thesis is organised as follows:

- The Chapter 1 aims at providing the fundamental concepts of the physics involved in a LHP. It describes its operating principle, especially inside the capillary structure, and models describing the operation of a LHP evaporator are detailed.

- The Chapter 2 presents the model used in the present study in order to understand the influence of various types of capillary structures dedicated to LHPs. An extensive parametric analysis is conducted to find the optimum characteristics of the porous medium.

- The Chapter 3 proposes a state-of-the-art of the methods enabling to manufacture a porous medium. Then, it details the manufacturing processes used in this thesis: partial sintering, freeze casting and coating. It describes the characterisation of the capillary structures in terms of geometry, surface quality and pores architecture.

- The Chapter 4 deeply investigates various test benches found in the literature enabling to characterise the hydrodynamic behaviour of porous samples. It justifies the choice of an experimental apparatus specifically dedicated to this study. The experimental set up enabling to determine the permeability and the effective pore radius of porous samples is described in this chapter. The results are discussed in terms of reproducibility and compared to the literature. Moreover, the influence of the manufacturing parameters on the hydrodynamic characteristics is investigated.

- The Chapter 5 proposes a state-of-the-art of various test benches intended to investigate the heat and mass transfer in LHP evaporators. It enables the manufacturing of an experimental apparatus specifically designed to answer the objectives of this thesis. The influence of the capillary structure characteristics on the heat transfer coefficient and the operating limits is investigated. The results are discussed in a way to understand the physical mechanisms acting inside the porous structure.

Chapter I Introduction to the fundamental concepts of the heat and mass transfer in a LHP

This chapter aims at providing the necessary background to understand the motivations of the present thesis. The fundamental concepts of the fluid flow and two-phase heat transfer in a capillary structure integrated in the environment of a LHP evaporator are presented, based on a literature study covering the experimental as well as the theoretical works performed by scientists in the field of LHPs.

In a first part, the operating principle of a LHP is summarised and its various components are described. Methods enabling to characterise the global performance of a LHP are presented. The types of fluids and wicks generally used in these devices are detailed, as well as the criteria leading to the selection of a fluid / wick material couple.

In a second part, an emphasis is put on the capillary structure. Since it is a key component of LHPs its characteristics have a significant influence on the operating limits and on the thermal performance of the system.

Finally, various models predicting the thermo-hydraulic behaviour of a porous medium, a wick/evaporator and a complete LHP are presented.

I.1 Description of a loop heat pipe and its operating principle

In this section, the LHP components and operating principles are thoroughly described in order to give a better understanding of the environment in which the capillary structures that will be manufactured and characterised throughout this PhD work are studied. Indeed, the physical phenomena occurring inside the wick are strongly coupled to the whole system operation.

A LHP is a closed tight device using liquid-vapour phase change to transfer high heat fluxes from a heat source to a heat sink with small temperature differences. The working fluid, at liquid-vapour equilibrium state, evaporates in the evaporator where a heat load is applied. Then, it flows through the vapour line to the condenser where it goes back to liquid state. The liquid flows back to the evaporator through the liquid line. The pumping force is provided by a wick located in the evaporator. Contrarily to thermosiphons and flat heat pipes, the vapour phase and the liquid phase are not in the same channel (Figure I-1). Thus, at high heat fluxes, the LHP is less concerned by interactions between the liquid phase flow and the vapour phase flow than a classic heat pipe where there is a unique channel (Singh *et al.* [7]).

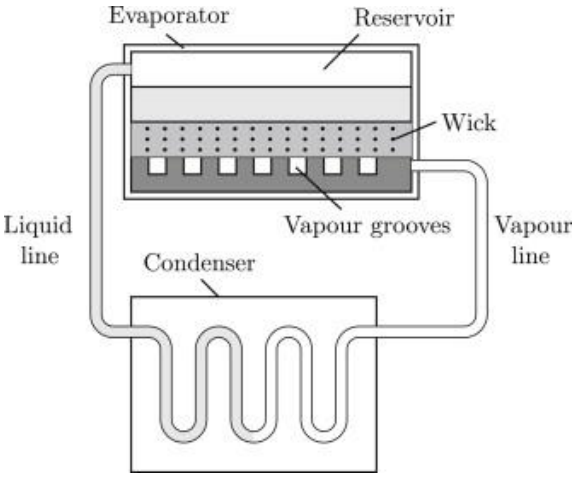

Figure I-1 : Schematic of a classic LHP (Siedel *et al.* [8])

I.1.1 Description of the components of a LHP

A typical LHP includes four main components: the evaporator, the reservoir or compensation chamber, the transport lines and the condenser. A short description of each one and an explanation of their operating principles is provided hereafter. For more information about the components, the reader can refer to the works of Singh *et al.* [7], Ku [9], Maydanik [10] and Siedel [4].

I.1.1.1 Description of the evaporator / reservoir

The evaporator/reservoir is the key component of a LHP. Contrarily to a capillary pumped loop (CPL), in which the reservoir is connected to the liquid line (Figure I-2, b), the LHP has a reservoir integrated into the evaporator casing (Figure I-2, a). This casing can be flat shaped (Figure I-3) or of cylindrical design (Figure I-4), depending on the application and the operating pressure. It includes a wick, in closed contact to the internal wall and a set of vapour grooves that can be arranged inside either the casing or the wick. Various groove designs have been proposed in order to decrease the thermal resistance in the evaporator, for example by Singh *et al.* [7], Kaya and Goldak [11] or Altman *et al.* [12].

The reservoir, filled by the returning subcooled liquid, absorbs the variation of liquid volume inside the LHP when submitted to variable operating conditions. In a flat evaporator, the reservoir is usually located above the wick so that the liquid can directly percolate through it. In a cylindrical evaporator, the primary wick, designed of the shape of a hollow cylinder, is often fed by a concentric secondary

wick occupying all the evaporator/reservoir length. The liquid flows through the wick, which acts as a capillary pump. It evaporates at the contact of the wick with the internal casing, heated by the external heat source. The vapour is removed through the vapour grooves to the vapour line.

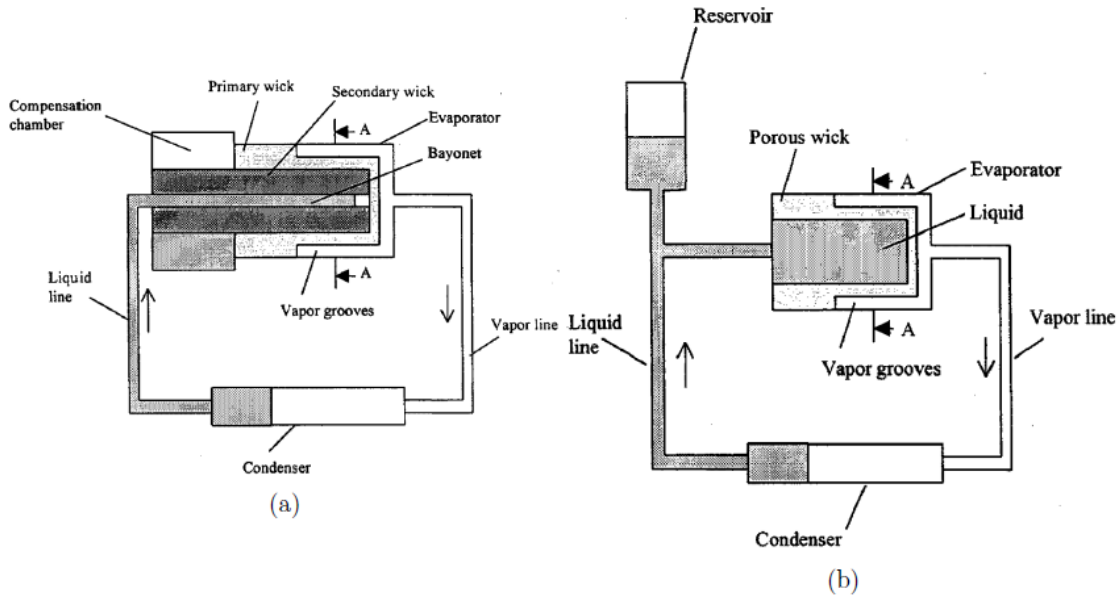

Figure I-2 : schematic of a LHP (a) and a CPL (b), Butler *et al.* [13]

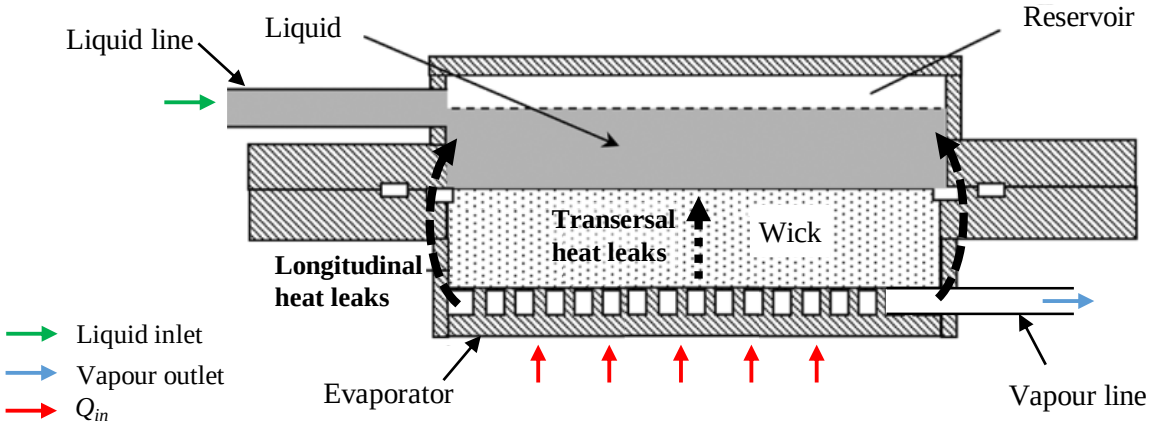

Figure I-3 : Schematic of a flat evaporator (adapted from Singh *et al.* [14])

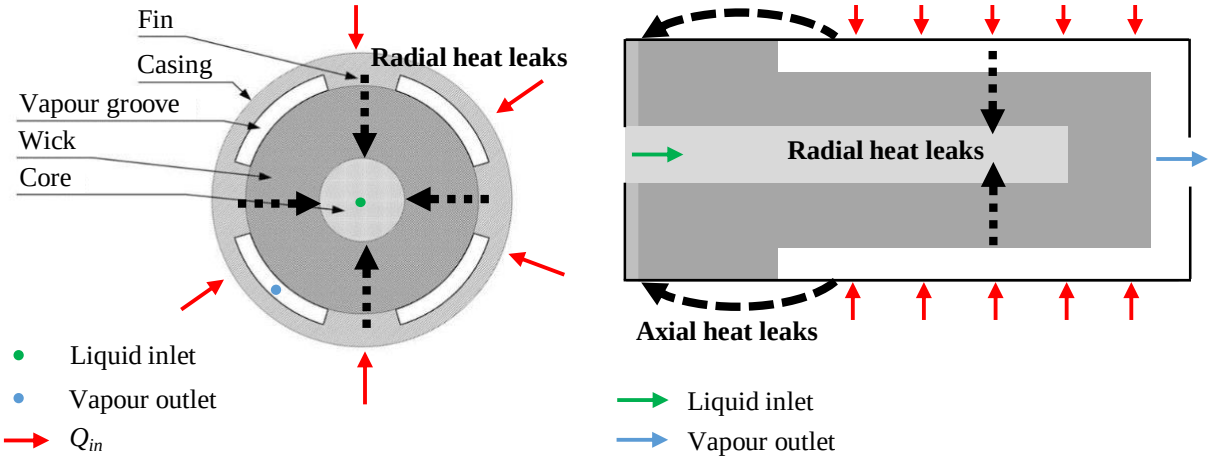

Figure I-4 : Schematic of a cylindrical evaporator (adapted from Kaya and Goldak [11])

The evaporator must transfer the largest possible part of the applied heat load Q_{in} to the working fluid in order to evaporate it. The heat not transferred to the fluid is called heat leak or parasitic heat flux (Figure I-3 and Figure I-4). The parasitic heat flux goes to the reservoir through different ways. The heat leaks going from the evaporator to the reservoir through the wick are called transversal or radial heat leaks for a flat or a cylindrical evaporator respectively. The heat leaks going from the evaporator to the reservoir through the evaporator casing are called longitudinal or axial heat leaks for a flat or a cylindrical evaporator respectively.

The heat leaks help the LHP to start up, by heating the fluid located in the reservoir when the heat load is applied. This is the major advantage of a LHP compared to a CPL, which requires the pre-heating of the compensation chamber before the start-up. However, after the start-up stage, the heat leaks must be as low as possible. Indeed, they decrease the performance of the system by increasing the reservoir temperature. According to Wang *et al.* [15], the flat evaporator enables a better contact between the wick and the evaporator due to the flat interface. However, it suffers from more heat leaks.

When the fluid evaporates, an interface between the vapour and liquid phases is created in the wick (Figure I-5). The curvature of this interface leads to a pressure difference between the vapour and the liquid. This phenomenon is described by the Young-Laplace equation:

$$\Delta P_{cap} = P_v - P_l = \frac{2\sigma}{r_m} \tag{I-1}$$

where ΔP_{cap} is the capillary pressure, P_v the vapour pressure, P_l the liquid pressure, σ the surface tension of the working fluid, r_m the meniscus radius of curvature.

The capillary pressure acts as a pump and enables the working fluid to circulate around the loop by compensating the pressure losses. When the heat load increases, the pressure losses increase and the meniscus radius decreases to keep an equilibrium.

In the case of a cylindrical evaporator, the wick may include two different structures: the primary and the secondary wicks (Figure I-5). The role of the secondary wick is to bring the working fluid to the primary wick and to avoid a local dry out. It has to be sufficiently permeable to spread the fluid in the primary wick, whereas the latter should have small pores to provide a high capillary pressure.

In most of the cylindrical LHP designs, a bayonet extends the liquid line to feed the end of the evaporator core opposite to the reservoir with cold liquid, avoiding the occurrence of superheated regions (Figure I-5). The role of the bayonet is more deeply analysed by Hodot [6] and Soler [16].

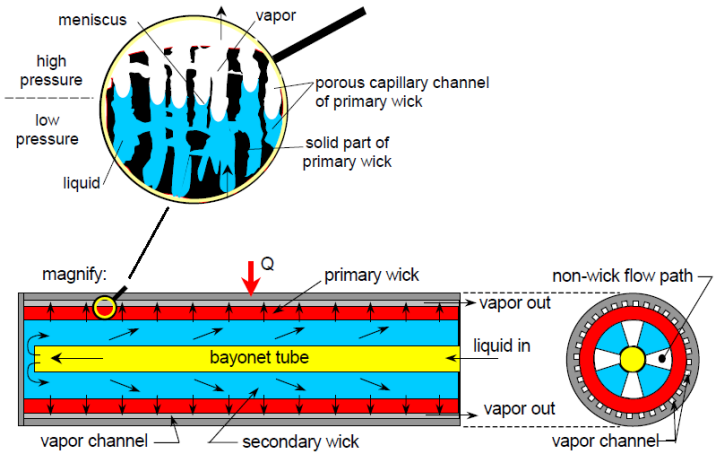

Figure I-5 : Schematic of a cylindrical evaporator and focus on the meniscus (Cimbala *et al.* [17])

I.1.1.2 Description of the transport lines

There are two transport lines. The first one enables the vapour to flow from the grooves to the condenser and is called "vapour line". The second one, located between the condenser and the reservoir is called "liquid line" as it enables the liquid supplied by the vapour condensation to return to the reservoir. Generally, the lengths of the transport lines depend on the position of the evaporator and the condenser. The line diameters have to be chosen by the designer. They are usually close to the capillary length of the fluid. For the fluids used in heat pipes, Launay and Vallée [18] report line diameters ranging from 1.2 to 6.35 mm. The vapour density being very small compared to the liquid density, the designer usually tries to have a larger diameter for the vapour line in order to reduce the velocity and thus, the pressure losses in the vapour line. However, it complicates the integration of the LHP in its environment.

The fluid flowing along the lines is not necessarily in a single phase. Depending on many parameters, especially the ambient temperature, condensation can occur in the vapour line and evaporation in the liquid line. In order to visualise the fluid flow inside the transport lines, Cimbala *et al.* [17] used a neutron radiographic system and Siedel [4] used transport lines made of glass.

I.1.1.3 Description of the condenser

The condenser enables to transfer the heat from the working fluid to the heat sink. A performant design is essential to ensure a low thermal resistance. Launay and Vallée [18] have identified many condenser technologies found in experimental works in the literature. They proposed the classification presented in Table I-1.

Table I-1 : Classification of the condenser technologies (adapted from Launay and Vallée [18])

Condensation cross-section	Thermal link between the working fluid and the cooling fluid	Modes of external heat transfer
• Circular • Annular	• plate heat exchanger • finned heat exchanger • tube-in-tube heat exchanger	• air forced convection • air natural convection • liquid forced convection • radiative heat transfer

In most applications, the condenser is subjected to natural or forced convection with the outside air that constitutes the heat sink. The heat sink temperature has a strong influence on the LHP operation, as it will be later explained in Section I.1.3.2.

A as conclusion, the wicks specifically dedicated to LHP applications have various designs and functions. The characteristics of these wicks must be adapted to the following specific functions: transport of liquid, capillary pumping, heat transfer and vapour removal. A great care must be put on the choice of the parameters of the porous structure as it influences the LHP performance. These parameters are closely linked to the manufacturing methods developed to obtain the porous structures. A part of the present work will be focused on the link between manufacturing and wick characteristics (Chapter III and Chapter IV).

The following part will give a different light in the role played by the wick in the LHP operation by considering the thermodynamic cycle of the working fluid flowing around the loop.

I.1.2 Thermodynamic cycle of a LHP

The working fluid flow in a LHP can be described by means of its thermodynamic cycle in a pressure-temperature diagram. Several authors, including Maydanik [10], Launay *et al.* [19], Siedel [4] and Ku [9] described the thermodynamic cycle of a LHP but there are some differences between their works.

An example of such a cycle is presented on Figure I-6. Two saturation curves are represented, the first one corresponding to the saturation state of a flat interface and the second one corresponding to the saturation state of a curved spherical interface having a curvature radius equal to r_m. The difference between the two curves is given by the Laplace-Young equation (Eq. (I-1)).

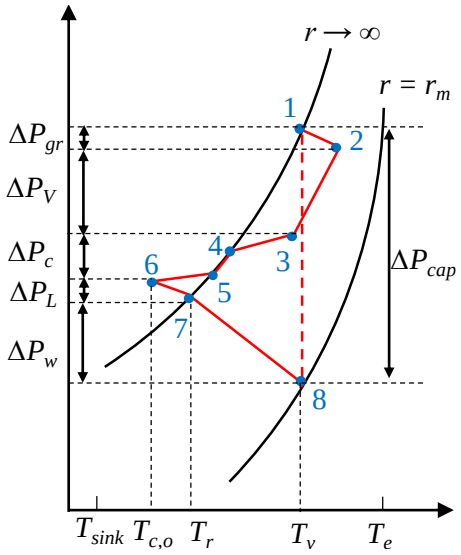

Figure I-6: P-T diagram of a LHP operating cycle

The thermodynamic cycle can be described as follows:

From 1 to 2: the vapour flows from the wick to the outlet of the evaporator through the grooves. The grooves induce small pressure drops and the vapour is slightly superheated. The associated pressure losses are ΔP_{gr}. The maximum temperature of the working fluid is the evaporator temperature T_e.

From 2 to 3: the vapour flows from the outlet of the evaporator to the inlet of the condenser. The major part of the pressure drops occurs in this vapour line and are called ΔP_V. Indeed, the vapour velocity is higher than in any other parts of the LHP due to the small density of the vapour ρ_v. According to Maydanik [10], the LHP operates better if the temperature in the vapour line is constant. It avoids any superheat or early condensation in the vapour line. However, particularly at small mass flow rates, temperature variations may occur, depending on the heat exchanges with the ambience. Thus, the ambient temperature and the thermal conductivity of the transport lines affect the vapour temperature.

From 3 to 4: the superheated vapour enters the condenser and its temperature decreases to the saturation temperature.

From 4 to 5: the saturated vapour condenses until being entirely liquid.

From 5 to 6: the liquid is subcooled until reaching the end of the condenser. The temperature of the fluid at the condenser outlet $T_{c,o}$ may be different from the heat sink temperature T_{sink} if the heat load is high or if the condenser is too short. At steady state, the liquid subcooling ensures the thermal balance of the reservoir by compensating the heat leaks from the evaporator to the reservoir.

The pressure losses in the entire condenser (from 3 to 6) ΔP_c are generally small (Maydanik [10]).

From 6 to 7: the liquid flows from the end of the condenser to the reservoir where it reaches a thermal equilibrium state (7). In general, the pressure drops in the liquid line ΔP_L are small due to the small velocity of the liquid compared to the vapour velocity. Depending on the heat load, the heat sink

temperature, the ambient temperature and the liquid line insulation, the temperature may vary along the liquid line.

From 7 to 8: the liquid percolates through the wick. The associated pressure drops ΔP_w mainly depends on the wick permeability which is affected by the pore radius and the porosity. The temperature increases as the fluid gets closer to the evaporator.

From 8 to 1: a pressure jump ΔP_{cap} occurs at the meniscus interface where the evaporation takes place. ΔP_{cap} is the capillary force provided to overcome the pressure losses due to the circulation of the working fluid along the LHP. The temperature of the working fluid is assumed to be constant and equal to the vapour temperature T_v.

A high *dP/dT* slope is preferred concerning the saturation curve. Indeed, it enables to obtain a smaller temperature difference between the reservoir and the evaporator for the same ΔP_{cap}. That can be explained by means of the saturation curve of water shown in Figure I-7. It shows that the *dP/dT* slope increases with an increasing temperature. Thereby, to overcome the same pressure difference between the reservoir and the evaporator, the temperature difference is smaller if the *dP/dT* slope is higher. For example, if ΔP = 0.2 bar and the temperature T_r of the liquid/vapour interface in the reservoir is 35 °C, the one of the interface in the wick T_v must reach 65 °C whereas if T_r = 83 °C, T_v must be of 91 °C.

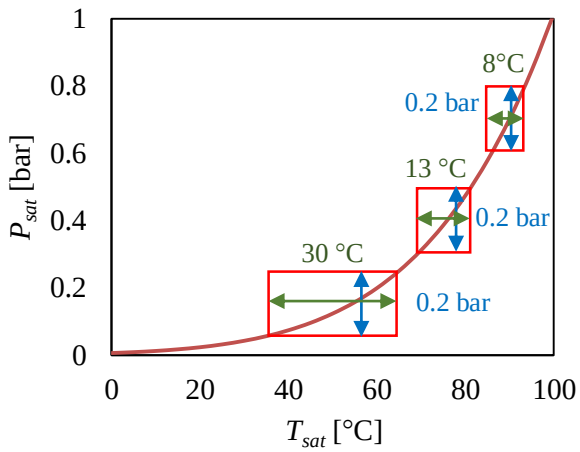

Figure I-7: Saturation curve of water

According to Maydanik [10], there are three main conditions for the LHP to operate:

- At the start up, a sufficient temperature difference must exist between the evaporator and the reservoir to overcome the pressure losses in the loop except the wick. A thermodynamic relationship expresses this condition:

$$\left(\frac{\partial P}{\partial T}\right)_T \Delta T_{1-7} = \Delta P_{1-7} \tag{I-2}$$

- The maximum capillary pressure $\Delta P_{cap,max}$ that the capillary structure can sustain must be sufficient to overcome the pressure losses in the whole loop:

$$\Delta P_{cap,max} > \Delta P_{gr} + \Delta P_V + \Delta P_c + \Delta P_L + \Delta P_w + \Delta P_{hs} \tag{I-3}$$

$$\Delta P_{cap,max} = \frac{2\sigma}{r_{m,min}} \quad \text{(I-4)}$$

where $r_{m,min}$ is the minimum possible radius of curvature of the liquid-vapour interface in the wick. It depends on the pore radius distribution and on the wettability of the fluid on the pore wall (See Section I.1.6.2 and Section I.2.3.1) and ΔP_{hs} is the hydrostatic pressure if there is an elevation difference $\Delta H_{c\text{-}e}$ between the evaporator and the condenser.

$$\Delta P_{hs} = (\rho_l - \rho_v) g \Delta H_{c-e} \quad \text{(I-5)}$$

where g is the gravitational acceleration and ρ_l the liquid density.

- The subcooling $\Delta T_{5\text{-}6}$ must be sufficient to avoid boiling in the liquid line:

$$\left(\frac{\partial P}{\partial T}\right)_T \Delta T_{5-6} > \Delta P_{5-6} \quad \text{(I-6)}$$

In conclusion, this part highlights that the wick characteristics, and particularly the pore radius and the permeability, strongly affect the thermodynamic cycle of the LHP, since the capillary pumping pressure as well as the pressure drops between the reservoir and the evaporator are linked to these characteristics.

I.1.3 Characterisation of the LHP performance

This part describes two ways to characterise the LHP performance at steady-state, for a normal operation of this system, i.e. after start-up and when the operating limits are not reached. These methods use temperature values at key points of the LHP that can be experimentally measured or determined by a model. The first one is to estimate the global thermal resistance of the LHP, whereas the second one consists of plotting the operating curve. Finally, the operating limits that are likely to be reached in a LHP are presented.

I.1.3.1 Thermal resistances

This is usual in the literature to estimate the steady state LHP performance using its global thermal resistance R_{LHP}:

$$R_{LHP} = \frac{T_e - T_c}{Q_{in}} \quad \text{(I-7)}$$

where T_c is the condenser temperature and Q_{in} is the applied heat load.

This global thermal resistance does not provide the location of the various temperature drops in the LHP. That is why Launay *et al.* [19] separated the global thermal resistance in two, the resistance of the evaporator R_e (Eq. (I-8)) and the resistance of the condenser R_c (Eq. (I-9)):

$$R_e = \frac{T_e - T_v}{Q_{in}} \quad \text{(I-8)}$$

$$R_c = \frac{T_v - T_c}{Q_{in}} \quad \text{(I-9)}$$

Depending on the studies, T_c can be considered as the temperature of the fluid inside the condenser tube, as the temperature of the condenser wall or even as the heat sink temperature. Both the condenser wall and the fluid inside the condenser tube may be subjected to high temperature gradients, leading to

difficulties to define a single temperature value. That's why, the heat sink temperature is most often considered. However, major differences exist between these approaches. Indeed, the external thermal resistance between the condenser wall and the heat sink is preponderant over the internal resistance due to condensation.

I.1.3.2 Operating modes

Another way to estimate the LHP performance is to study the evolution of the operating temperature as a function of the applied heat load, called the operating curve of the LHP. Generally, the operating temperature is considered to be the reservoir temperature (Launay *et al.* [5], Ku [9]). This approach enables to distinguish the different operating modes. According to several authors, there are two distinct operating modes called Variable Conductance Mode (VCM) and Fixed Conductance Mode (FCM). Especially, Launay *et al.* [5] deeply described these two modes.

The LHP operates at VCM when the liquid exits the condenser at a temperature close to the heat sink temperature. It occurs when the condenser is long enough to subcool the liquid (Figure I-8), mainly for low heat loads. The LHP operates at FCM when the two phase length $L_{2\phi}$ is close to the condenser length (Figure I-8). In this mode, the operating temperature increases linearly with respect to the heat load.

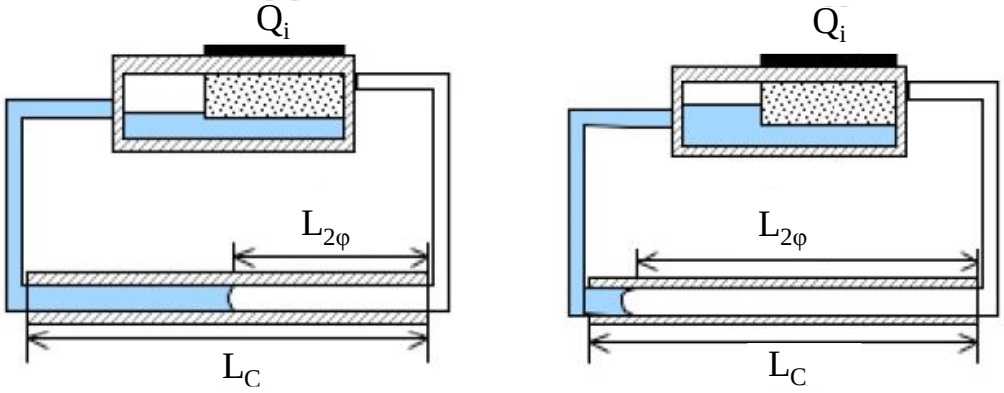

Figure I-8: Schematic of the liquid location inside the LHP according to its operating mode, Launay *et al.* [5]

Figure I-9 shows two different types of operating curves. According to Launay and Vallée [18], if the difference between the heat sink temperature and the ambient temperature is large, a U-shaped curve is expected. Indeed, at low heat loads, the fluid velocity in the liquid line is low and its temperature increases by heat exchange with the ambience. When the heat load increases, the fluid flows faster, its temperature gets closer to the one of the heat sink. Thus, the returning liquid cools the reservoir. The liquid temperature increases at high heat loads when the condenser is not long enough to cool the fluid down to T_{sink}. If the heat sink temperature is close to the ambient temperature, a flattened curve is expected at low heat loads, then the operating temperature increases similarly to the previous case.

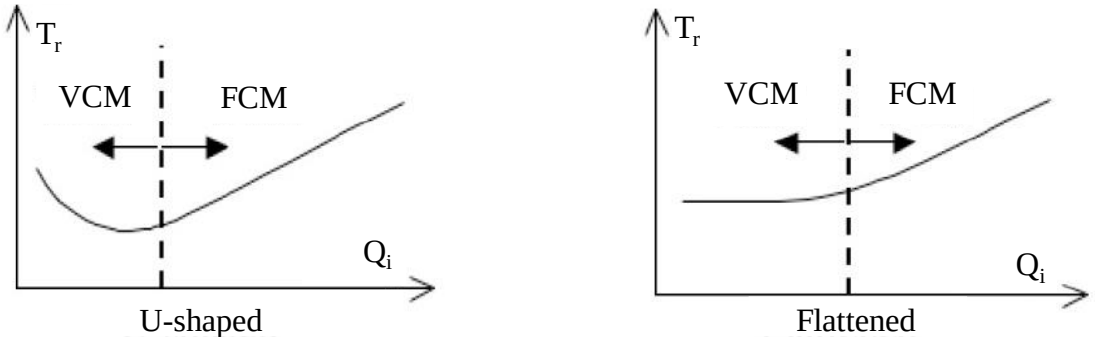

Figure I-9: Typical shapes of LHP operating curves, Launay *et al.* [5]

Launay *et al.* [5] developed an analytical model based on the energy balance in the different components of the LHP. This closed form analytical model gives different expressions of the operating temperature for the two modes of LHP steady-state operation (Table I-2). h_{lv}, c_{pl} are the enthalpy of vaporisation and the specific heat of the fluid; R_e, R_{wall}, R_{amb}, and R_w are the thermal resistances of the evaporator, the evaporator wall, the ambiance and the wick respectively; h_L, h_c and h_{sub} are the convective heat transfer coefficients between the liquid line and the fluid, the condenser tube and the condensing or subcooled fluid, respectively; d_L and L_L are the diameter and the length of the liquid line; d_c and L_c are the diameter and the length of the condenser; and T_{amb} is the ambient temperature.

Table I-2: Analytical expressions of the operating temperature, Launay *et al.* [5]

Mode	Expression of the operating temperature	
VCM	$T_r = \dfrac{T_{sink} + \dfrac{h_{lv}}{c_{p,l}}\left[\dfrac{R_e}{R_{wall}} + \dfrac{T_{amb}}{R_{amb}Q_{in}}\right] + (T_{amb} - T_{sink})\left(1 - exp\left(\dfrac{\pi d_L L_L h_L h_{lv}}{Q_{in} c_{p,l}}\right)\right)}{1 - \left[\dfrac{1}{\rho_v c_{p,l}}\left(\dfrac{1}{R_w} + \dfrac{1}{R_{wall}}\right)(\Delta P_V + \Delta P_L - \rho_l g \Delta H_{c-e}) - \dfrac{h_{lv}}{R_{amb} c_{p,l}}\right]\dfrac{1}{Q_{in}}}$	(I-10)
FCM	$T_r = T_{sink} + \dfrac{Q_{in}}{\pi d_c L_c h_c}\dfrac{\left(1 + \dfrac{R_e}{R_{wall}}\dfrac{h_c}{h_{sub}}\right)}{1 + \dfrac{R_e}{R_{wall}}}$	(I-11)

In VCM, the operating curve is governed by the heat transfer in the evaporator/reservoir while in FCM, it is governed by the heat transfer in the condenser. The main drawback of this model is the necessity to estimate R_e which depends on the material used for the casing and the wick, on the grooves and porous structure design, particularly on the contact between them and on the presence or not of dry-out zones. It is necessary to better understand the phenomena involved at this place to correctly estimate R_e. This is one of the objective of the present study.

For deeper explanations and descriptions about the operating curves, it is interesting to refer to the works of Maydanik [20], Chen [21], Boo and Chung [22] and Riehl and Dutra [23]. It emerges from these works that whatever the way used to determine the LHP performance, the wick thermal characteristics are determinant. Thus, it is necessary to have a better knowledge on them. The thermal resistance characterising the performance of the evaporator will be used as the main parameter in the experimental study (Chapter V).

I.1.3.3 Operating limits

The good operation of a LHP is summarised by Mr David Antoniuk: "No bubble… no trouble". Indeed, phenomena like the development of a vapour blanket near the evaporator or the boiling inside the porous structure have a strong influence on the thermo-hydrodynamic behaviour of the wick. The emergence of vapour inside the capillary structure, experimentally observed by Cimbala *et al.* [17] using neutron radiography, may reveal the occurrence of boiling or the capillary limit which are the most likely to occur in a LHP. These limits must be detected to correctly design a LHP depending on the application and to predict the performance of this cooling device. However, the detection of one or the other limit remains an issue nowadays since it is experimentally difficult to perform visualisations within the wick.

This part provides a description of the physical phenomena associated to the boiling and capillary limits. Some correlations are proposed to predict their occurrence. Even if the correlations are too general to give accurate results (Adkins and Dykhuizen [24]), they enable to understand the phenomena.

To go further, the reader can refer to the works of Siedel [4], Launay *et al.* [19], Hamdan *et al.* [25] and Chuang [26].

Boiling limit

In LHPs, boiling is expected to occur at the interface between the envelope and the capillary wick (Mishkinis and Ochterbeck [27]). It may also occur in the wick, leading to the dry out by destroying the menisci. This is due to the NCGs entrapped in microscopic cavities, playing the role of nucleation sites. Kaya and Goldak [11] explained that the presence of vapour or NCGs trapped in small cavities may lead to early boiling inside the wick, at small superheats ΔT_{sh}. After the evacuation of all the NCGs present in the device, purification of the fluid or after the improvement of the wick/fin interface, the superheat required to initiate boiling increases. It can reach 200 K, based on the work of Stralen *et al.* [28]. In their experiments, boiling was not observed if a good contact was ensured between the wick and the envelope.

In order to predict the boiling limit of their LHP, Kaya and Goldak [11] estimated that nucleation occurs at superheat of 4 K. Mottet *et al.* [29] used the same value. Dhir *et al.* [30] gives an expression to predict the superheat of boiling incipience $\Delta T_{sh,max}$ as a function of the pressure of the non-condensable gas P_{NCG}:

$$\Delta T_{sh,max} = T_l - T_{sat} = \frac{\left(\frac{2\sigma}{r_p} - P_{NCG}\right) T_{sat}}{\rho_v h_{lv}} \tag{I-12}$$

where T_{sat} is the saturation temperature and r_p the pore radius of the wick. Mishkinis and Ochterbeck [27], Peterson [31] and Dunn and Reay [32] used another expression, proposed by Chi [33]:

$$\Delta T_{sh,max} = T_l - T_{sat} = \frac{2\sigma T_{sat}}{\rho_v h_{lv}} \left(\frac{1}{r_n} - \frac{1}{r_p}\right) \tag{I-13}$$

where r_n is the bubble nucleation radius. A method to determine the nucleation radius is proposed in Section V.3.2. This limit cannot be easily calculated since the nucleation radius is unknown. Mishkinis and Ochterbeck [27] estimate that this expression is valid only if there are NCGs entrapped in the wick and proposed another method to determine $\Delta T_{sh,max}$ based on the Kwak model ([34], [35]): the surface energy for vapour bubble formation is assigned as the energy required to detach a cluster composed of activated molecules. If the number of molecules in the cluster overcomes the critical one in given conditions, the vapour bubble growth may also be predicted by this theory. The Kwak model is more realistic than the classical models of Chi [33] and Dhir *et al.* [30], and it has a larger validity range. The classical models underestimate the critical nucleation rate compared to the results experimentally observed.

Cimbala *et al.* [17] showed, by means to visualisation by neutron radiography, that the dry-out could occur in the primary wick, decreasing drastically the LHP performance.

Capillary limit

Nagano and Ku [36], Ku [9], Maydanik [10] and Santos *et al.* [37] experimentally and theoretically investigated the capillary limit, arising when the maximum capillary pressure $\Delta P_{cap,max}$ becomes lower than the pressures losses around the loop. Compared to classical heat pipes, the heat flux corresponding to the capillary limit of a LHP is higher due to the confinement of the wick in the evaporator section (Singh *et al.* [7]). Indeed, in a classical heat pipe, the capillary structure is located all along the pipe which increases the pressure losses.

In the literature, it is generally considered that when the heat flux exceeds the maximum value allowing the pressure balance expressed by Eq. (I-3) to be respected, a dry-out region is formed and the LHP finds a new equilibrium (Zhao and Liao [38]). This will be discussed in more details in the Section I.3. The LHP operation is possible until the dry-out region reaches the reservoir. In this situation, the hydraulic barrier is broken, leading to the inability of the wick to ensure its role.

I.1.4 Selection of the working fluid

This section presents a non-exhaustive study of the influence of the working fluid on the LHP operation, extracted from the works of Launay *et al.* [19], Siedel [4], Hoang *et al.* [39] and Kaya and Ku [40]. The mentioned authors propose more complete studies (effect of the fluid charge, for example). This section gives the main criteria to correctly choose the working fluid.

I.1.4.1 Temperature range

The temperature range in which the working fluid can operate is the most important criterion to choose a fluid. According to Coquard [41], the operating area of a LHP usually lies between the triple point and the critical point of the working fluid, as shown in Figure I-10.

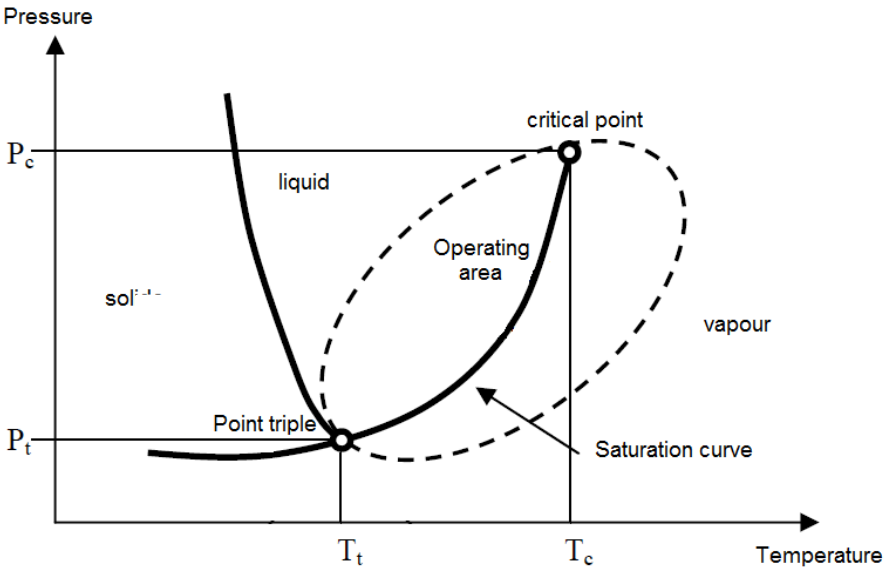

Figure I-10: Operating domain of the working fluid in the P-T diagram (Coquard [41])

However, in practice, the temperature range is not so large because the performance and the design of the LHP are strongly affected close to the limits. The low temperature limit is usually due to a too low absolute vapour pressure. According to Kaya and Ku [40], it limits the maximum pressure drops that the LHP can overcome. The high temperature limit is due to a too high vapour pressure, which induces an unacceptable casing thickness to sustain the resulting mechanical stresses. Faghri [42] has studied the influence of the operating temperature range on the choice of working fluid. Table I-3 summarises his work.

I.1.4.2 Environment and safety

The environment and safety criteria must be taken into account when selecting a fluid for a given application. Some fluids having a high Ozone Depletion Potential (ODP) or a high Global Warming Potential (GWP) must be avoided when possible. In most applications, the use of toxic, flammable and environmentally harmful fluids are strictly regulated. Table I-4 presents the environmental and safety properties of various working fluids in the low temperature range. Most of the following values come from Hodot [6] who worked on the safety characteristics of various fluids suitable for avionics.

Table I-3: Operating temperature range for various working fluids (Faghri [42])

Working fluid	Operating temperature range [°C]	Classified temperature application
Helium	-271 to -269	Cryogenic
Hydrogen	-259 to -242	
Neon	-246 to -236	
Nitrogen	-203 to -170	
Argon	-189 to -157	
Oxygen	-200 to -154	
Krypton	-157 to -113	
Ammonia	-60 to 100	Low temperature
Pentane	-20 to 120	
Freon 113	-10 to 100	
Acetone	0 to 120	
Water	30 to 200	
Mercury	150 to 650	Medium temperature
Sulphur	257 to 674	
Sodium	600 to 1200	High temperature
Lithium	1000 to 1800	
Silver	1800 to 2300	

Table I-4: Environmental and safety properties of various working fluids

Fluid	ODP	GWP	Flammability
Water	0	*	-
Methanol	0	2.8	flammable
Acetone	0	0.5	-
Ammonia	0	0	flammable between 15 % and 28 % in air
Pentane	0	<11	flammable
R134a	0	1430	-
R245fa	0	8000	flammable

*Water has a global warming potential but it is naturally present in the atmosphere.

I.1.4.3 Thermo-hydraulic characteristics of the working fluid

The working fluid has a strong impact on the LHP performance. Launay *et al.* [19] published an in-depth study of the influence of the working fluid on the LHP operation.

In order to choose the most efficient fluid with respect to the application, Launay *et al.* [43] worked on different fluidic criteria to determine figures of merit for LHPs. These criteria come from the minimisation of the term which depends on the fluid properties in the expression of the operating temperature previously presented (Table I-2).

For example, the figure of merit *Nb1* is determined in VCM, if the heat leaks through the wick are much lower than the heat leaks through the wall:

$$Nb1 = \frac{c_{p,l}}{h_{lv}} \tag{I-14}$$

The same method is applied for each domain of validity. The figures of merit are computed for ammonia, acetone, methanol, ethanol, water and FC72. The numbers of merit can easily be determined for many fluids in order to know which fluid provides the best thermohydraulic behaviour. The results obtained with this method by Launay *et al.* [43] show that the fluid must exhibit a high surface tension, a high specific heat, a high enthalpy of vaporisation and low liquid and vapour viscosities, μ_l and μ_v.

Based on these results, a fast method is proposed here to select a suitable working fluid at a given operating temperature. The previous thermohydraulic characteristics at 20 °C (Table I-5) as well as the

thermal conductivity of the fluid λ_l are plotted for various fluids in a radar chart, except the vapour viscosity which undergoes very few variations from a fluid to another one. Ammonia properties are taken as a reference because it is a very usual working fluid in LHPs. When the value of a parameter is larger than one, it means that the fluid is better than ammonia regarding this parameter. Thereby, a fluid with a large pentagon surface area (Figure I-11) should be performant. Figure I-11 shows that water and ammonia are the most performant working fluids in LHPs, followed by propylene. For the other fluids, the pentagon areas are significantly smaller.

Table I-5: Properties of usual working fluids at 20 °C

Fluid	**σ (mN/m)**	**c_{pl} (J/kg/K)**	**h_{lv} (kj/kg)**	**μ_l (10^{-4} Pa.s)**	**μ_v (10^{-6} Pa.s)**	**λ_l (W/m/K)**
Water	72.9	4 182	2 454	10	8.9	0.602
Methanol	22.7	2 460	1 185	5.8	9.5	0.204
Ethanol	22.7	2 404	1 007	12	8.4	0.179
Acetone	20.0	2 158	548	3.2	8.2	0.18
Ammonia	33.0	4 752	1 189	1.38	9.9	0.491
R134a	12.0	1 404	182	2.1	11.5	0.083
Pentane	16.0	2 293	370	2.2	6.8	0.113
Propylene	41.9	2 423	439	0.9	-	0.200

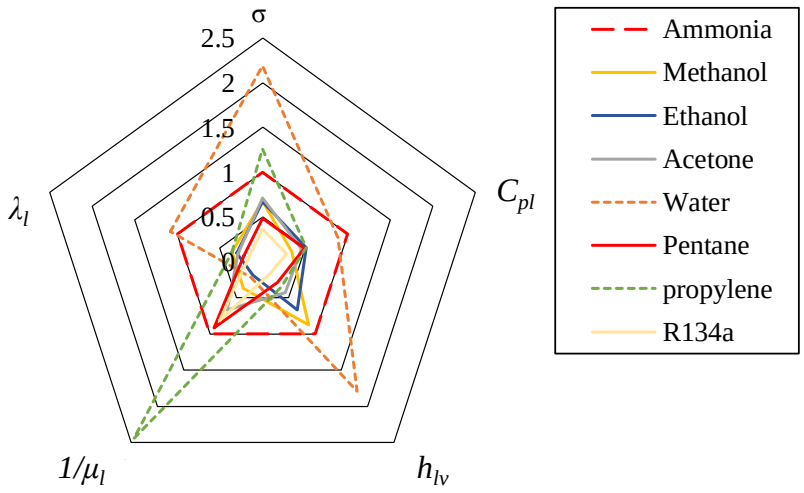

Figure I-11 : Comparison of the various working fluid properties at a temperature of 20 °C

Launay and Vallée [18] made an extensive literature review of the fluids used in LHPs between 1998 and 2010. Figure I-12 shows the occurrence of the various fluids in the 55 available studies. One can note that ammonia and water are the most used fluids which is in good accordance with the previous analysis.

Historically, ammonia was used in a lot of spatial applications. However, its use on Earth is presently limited due to its toxicity. Water is a convenient fluid because it is available, cheap, and harmless but it subjected to freezing at low temperatures and it is not chemically compatible with some usual materials (Section I.1.6.1). Thus, authors like Boo and Chung [22] used acetone, ethanol and methanol in LHPs. According to their work, at low heat loads, acetone allows better performance whereas at high heat loads, methanol would be the best fluid. The transition heat load depends on the geometry.

Finally, the *dP/dT* slope is an important parameter that must be taken into account, as explained in Section I.1.2. Figure I-13 shows the saturation curves of the most used fluids in LHPs. It shows that the *dP/dT* slope is higher for ammonia than for any other fluids. That can explain why ammonia has been so much used. Water has the lowest *dP/dT* slope making it difficult to be used at low temperatures.

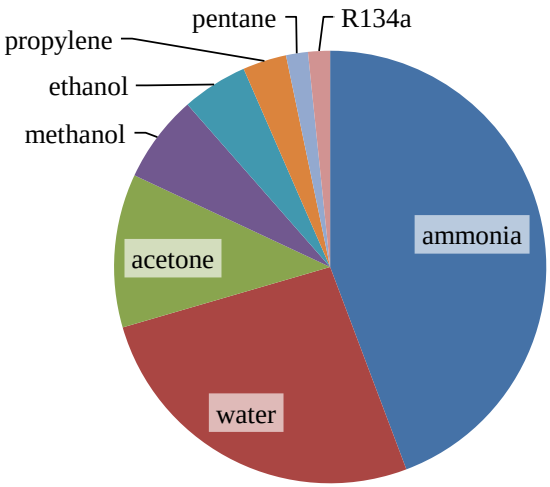

Figure I-12: Occurrence of the utilisation of each working fluids in the experimental studies published between 1998 and 2010 (Launay and Vallée [18])

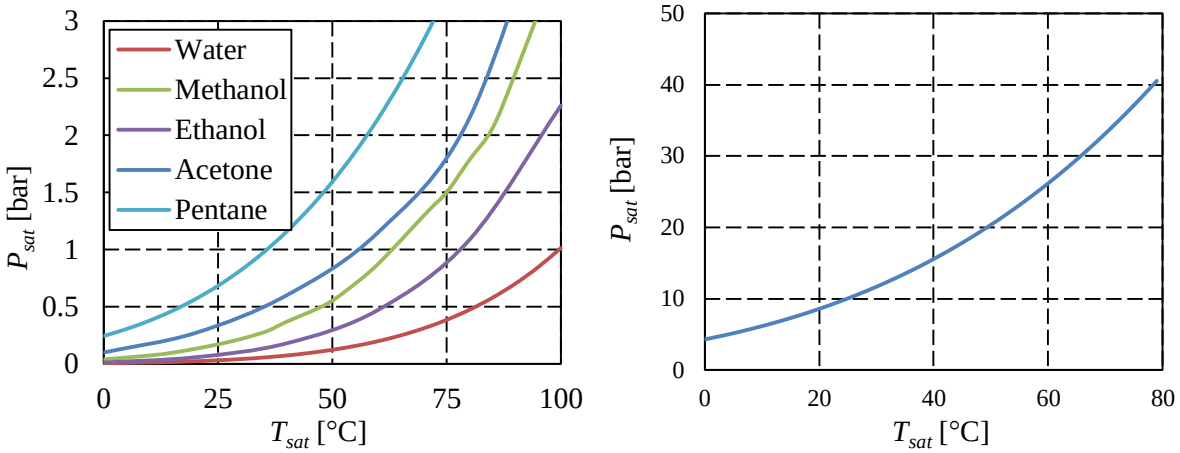

a) Low *dP/dT* slope b) High *dP/dT* slope: Ammonia

Figure I-13: Saturation curves of standard fluids for LHP

For more information about the effect of the working fluid, one can refer to the works of Siedel [4] and Mishkinis *et al.* [44]. In conclusion, the thermal performance of the LHP strongly depends on the fluid. That's why it must be chosen with due care. The fluid selection is an important aspect to consider in the frame of this work because, as it will be explained later, there are strong interactions between the fluid and the wick material (Section I.1.6).

I.1.5 Selection of the material used to manufacture the wick

Among all the wick characteristics, only the material properties are studied hereafter. The other characteristics are presented in Section I.2.1. The choice of the manufacturing parameters, and especially the type of powder, is presented in the Chapter III.

According to Baumann and Rawal [45], the wick material has a strong influence on the LHP performance. Several criteria are observed when choosing a wick material: thermal expansion, mechanical resistance, temperature range, thermal conductivity, availability and cost. Launay and Vallée [18] listed the various wick materials used in 55 experimental studies published between 1998 and 2010. Figure I-14 summarises the results of this review. 89 % of the wicks are made of metallic materials but ceramics (silica) and plastics (PE, PP, PTFE) are used more and more (2 % and 9 % respectively).

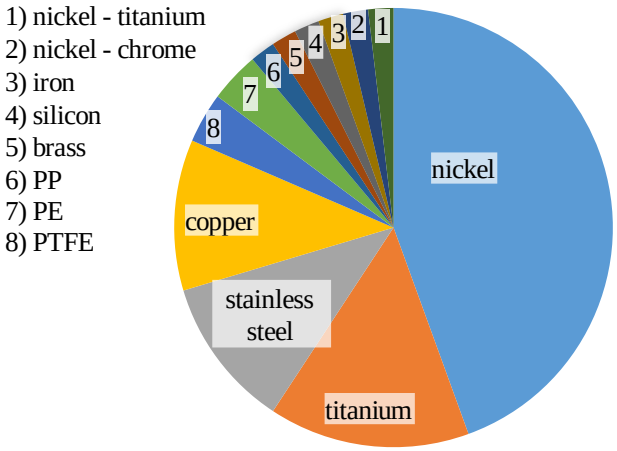

Figure I-14: Occurrence of the various wick materials in the experimental studies of LHP published between 1998 and 2010

The first criterion of selection of a wick material is the operating temperature range. The melting temperature of the material must be higher than the maximum temperature expected to be reached inside the wick. Figure I-15 shows the melting temperature of several materials suitable for LHP wicks. However, the maximum allowable temperature is lower than the melting temperature, since some of these materials and mainly the polymers lose their rigidity before reaching their melting temperature. The polymers cannot be used at high temperatures whereas most ceramics and metals can all operate at temperature higher than 500 °C.

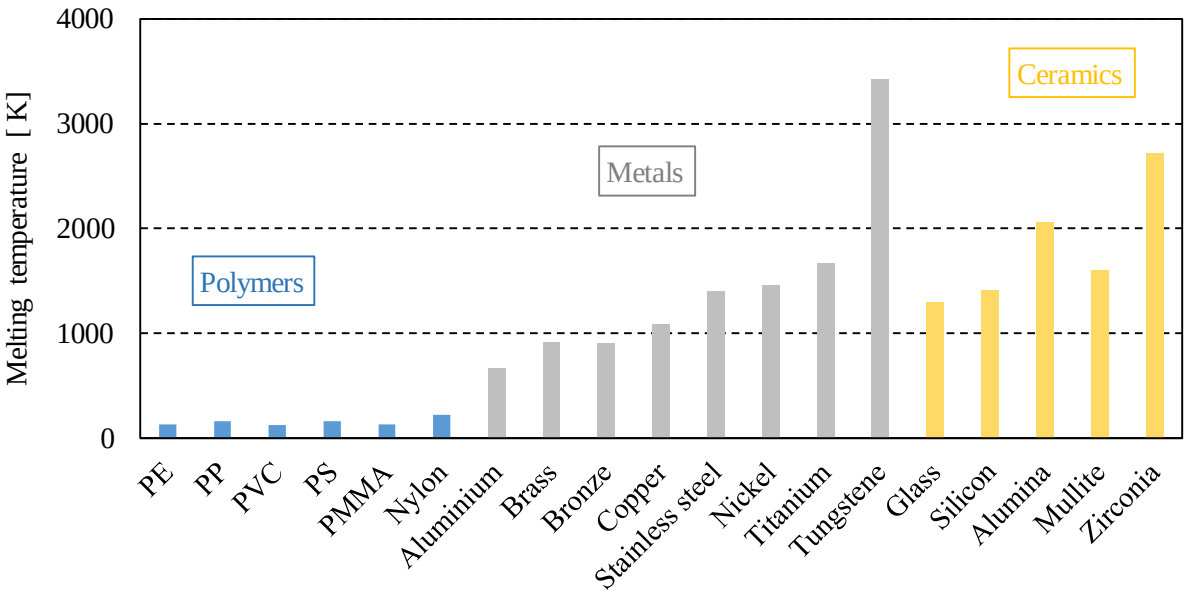

Figure I-15: Melting temperatures of various polymers, metals and ceramics

The choice of the wick material may depend on the thermal expansion coefficient. Indeed, it is usual to choose a material having a thermal expansion close to the one of the casing material since large differences lead to strong mechanical stresses. This parameter is quantified for many materials in Figure I-16, showing that the thermal expansion coefficient is larger for polymers than for ceramics and metals.

The thermal conductivity of a material must be taken into account. A conductive porous material improves the heat transfer to the evaporative interface but leads to higher heat leaks. Thus, in the case of a monolayer wick, a trade-off must be found. Figure I-17 shows the thermal conductivity of several materials. The polymers have thermal conductivities lower than 0.5 W/m.K whereas metals as well as

silicon have high thermal conductivities. The thermal conductivity of ceramics ranges from 1 to 10 W/m.K. According to Singh *et al.* [7] nickel offers the best trade-off in order to keep the heat leaks at a reasonable level and to properly transfer the heat flux to the fluid.

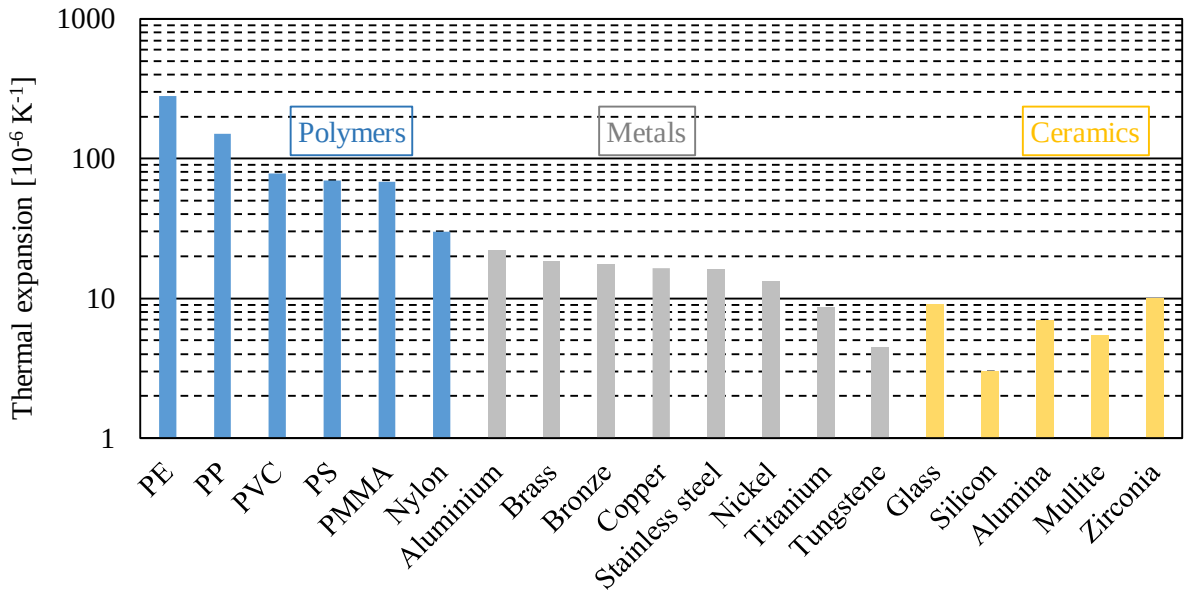

Figure I-16 : Thermal expansion coefficients of various polymers, metals and ceramics (Lide [46])

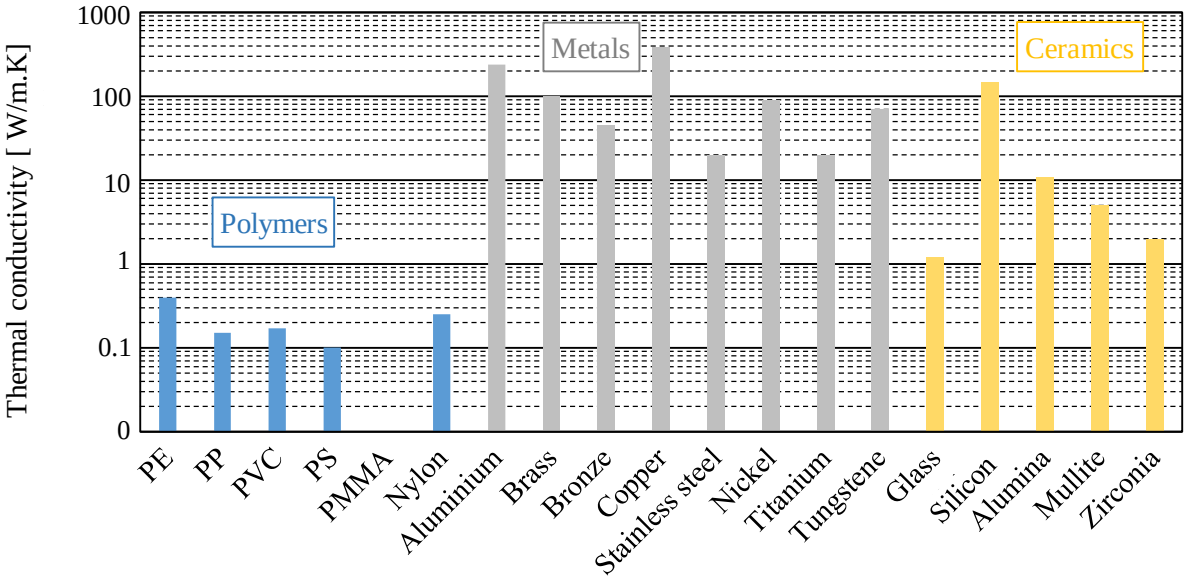

Figure I-17: Thermal conductivities of various polymers, metals and ceramics, Touloukian ([47]–[49])

The availability and the cost must be taken into account when choosing a material (Figure I-18). The best trade-off between price and physical characteristics must be searched. The prices listed in this figure are an order of magnitude of the real prices, since they change every day as well as the dollar/euro conversion. Metals are more expensive than ceramics or plastics. Moreover, their price increases more and more. That's why, nickel, which is used in many applications, is now replaced by cheaper materials in applications for which the cost is an important criterion. The evolution of the materials and their manufacturing processes may lead to reconsideration of the materials used nowadays.

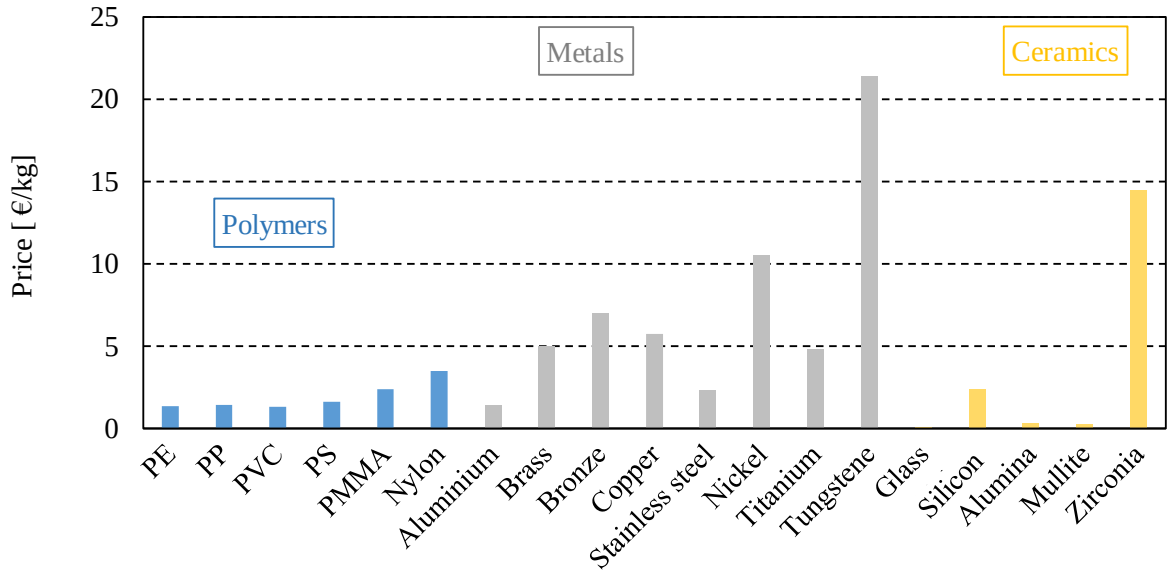

Figure I-18 : Comparison of material prices (industrie.com [50], Les Echos [51], january 2016)

The advantages and drawbacks of the various materials are summarised in the following. They are proposed by researchers having experimentally tested various materials in a LHP.

Metallic wicks

The advantages and drawbacks of metallic wicks are detailed in Table I-6. According to Singh *et al.* [7] nickel is massively used in LHP applications with monoporous wicks for three mains reasons. Firstly, as explained previously, it offers a good trade-off in terms of thermal conductivity. Secondly, it is easy to manufacture with high porosity and fine pore size. Finally, it is available in high assay level at reasonable cost. Other metallic wicks are also often used because they can operate at very high operating temperatures. According to Singh *et al.* [7], for very high temperatures (above 200 °C) stainless steel is preferred to copper as the materials should not have any galvanic potential. In some studies, other metals were tested, even metallic alloys like bronze (Albertin *et al.* [52]).

Table I-6: Advantages and drawbacks of metallic wicks

Advantages	Drawbacks
• Mechanical resistance • Large temperature range • Low thermal expansion • Easily sinterable	• High cost • High weight

Polymer wicks

Even if metallic wicks are usual, several authors tested other materials, especially polymers, in order to enhance the thermal performance of the LHP. The advantages and drawbacks of polymer wicks are detailed in Table I-7. Riehl and Dutra [23], Bai *et al.* [53] and Bazzo and Riehl [54] used polyethylene (PE) wicks. Boo and Chung [22] tested a polypropylene (PP) wick because it has better thermal characteristics than PE. Nagano and Nagai [55] and Kobayashi *et al.* [56] used a polytetrafluorethylene (PTFE or Teflon®) wick. Polymer wicks may be efficient, however, the maximum temperature they can support and the problems of chemical compatibility significantly reduce the conditions in which they can operate.

Table I-7 : Advantages and drawbacks of polymer wicks

Advantages	Drawbacks
• High processability • Low weight • Easy to assemble • Low cost	• Temperature limitations (low melting temperature and large thermal expansion) • Chemical compatibility • Wettability with the working fluid • Shrinkage/creep • Durability against space radiation. Indeed, plastics are more sensitive to irradiation than metals. This has to be taken into account in space applications.

Ceramic wicks

Other authors tried ceramics as wick material. For example, Xu *et al.* [57] used Ti_3AlC_2 and Berti *et al.* [58] used mullite and alumina. They both conclude that ceramics were an efficient alternative to metal wicks. LHPs also accept porous silica glasses (Silk and Myre [59]), carbon foams (Silk and Myre [60]) and biomorphous silicon carbide (Weisenseel *et al.* [61]) as a material for the capillary structure. In order to further investigate the ceramics tested in LHPs, the reader can refer to the works of Pastukhov and Maydanik [62], Santos *et al.* [63] and Reimbrecht [64]. Hammel *et al.* [65] details various advantages of the ceramic materials over other materials such as polymers and metals. The advantages and drawbacks of ceramic wicks are summarised in Table I-8.

Table I-8: Advantages and drawbacks of ceramic wicks

Advantages	Drawbacks
• Hardness • Chemical inertness • Thermal shock resistance • Corrosion and wear resistance • Low density	• Brittleness

Other materials

It is important to keep one mind open when choosing the wick material. For example, biomaterial have already been used to design wicks. Indeed, Putra *et al.* [66] have tested the collaria (a biomaterial) in a LHP evaporator.

In conclusion, the selection of the wick must meet a great number of requirements, which are not always compatible to each other. Thus, in the case of a single layer of porous material, trade-offs must be done so that the wick is able to fulfil its different functions. Some researchers tried to improve the wick characteristics by superimpose two layers with different materials or by sintering two different materials together. This will be discussed later in Section I.2.3.2.

I.1.6 Selection of the material/working fluid couple

In a heat pipe, two physical phenomena linked to the interaction between the solid material of the LHP and the working fluid has to be taken into account: the wettability of the liquid on the solid material and the chemical compatibility between this two phases.

I.1.6.1 Material/working fluid compatibility

The couple material/working fluid has a strong impact on the LHP performance. Indeed, the chemical incompatibility between the material and the fluid is a source of misoperations. It can generate non-condensable gases (NCGs). In every case, the presence of NCGs decreases the LHP performance. According to Ku [9], there are at least four destinations for the NCGs:

- They can reach the reservoir and remain inside it as they cannot flow through the wick.
- They can be stored at the condenser. Indeed, the temperature is low and they cannot leave it as they don't condense themselves.
- They can be absorbed by the working fluid and circulate around the loop.
- They can be adsorbed by the envelope or wick materials.

Table I-9 summarises the work of Mishkinis *et al.* [44] and Hodot [6] who tried to inventory the compatibility of various fluids and materials. Each cell gives the compatibility between a material and a fluid according to several authors. The letters give the compatibility according to several authors and the cell colour sums up the point of views of the authors having worked with this material/fluid couple. For example, three authors have studied the compatibility of nickel and ethanol. According to them, this couple has an excellent compatibility [13M], a probable compatibility [23M] and a non-compatibility for a long period of use [10H]. Thus, the cell colour is grey because there is a conflict between these different authors.

Table I-9 : Chemical compatibility between various fluids and materials

A , A-	Excellent compatibility	A	Excellent compatibility
AB, A, A-	Probable compatibility	A-	Probable compatibility
A to B	Conflict between two or more authors	AB	Probable incompatibility
AB, B, B+	Probably incompatible	B+	Incompatibility for a long period of use and above 125 °C
B, B+	Incompatible	B	Incompatibility

	Nickel	Hastelloy	Titanium	Copper	SS316	SS304	Bronze	Aluminium
Ethanol	**A** [67] **AB** [68] **B+** [44]	**A** [69]–[71][72]	**A** [70], [71]	**A** [34][60]	**A** [69]–[73]	**A** [69]–[71] [72][67] **A-**[74][75]	**A** [70], [71] **B** [74][75]	**A**[72] **A-**[72][70], [71] **B** [67]
Methanol	**A**[74][42] [74][67] **A-**[32][75] **B+** [44] **B** [76]	**A** [69] [70], [71]	**A** [71] **A-**[69] [70]	**A** [42], [32], [74] [75] [77] [67] **A-**[70],[78]	**A** [69]–[73][74]	**A** [69]–[71][72] [74][67] **A-**[74][75] [79][80][81] **AB**[82]	**A** [70], [71]	**A** [70] **A-**[73][71] **B** [42][32] [74][75]
Acetone	**A** [67] **A-**[32] **AB** [83] [84] **B+** [44]	**A** [69]–[71][72]	**A** [69] [60][61]	**A** [70][42] [32][74] [83] [77] [67]	**A** [69][73] [60][61] [74] [74][67] **A-**[72][42] [32][75] **AB** [83] **B** [81]	**A** [69][70], [71][74] [42][74][67] **A-**[72][32], [75] **AB** [81]	**A** [72][60] [61]	**A** [73][60][61] [42][74][67] **A-**[72][32] [75][85] **AB** [81]
Ammonia	**A** [74][42][32]	**A** [69]–[71] [72] **A-**[70]	**A-**[69], [71] **B+**[70]	**B** [86], [42], [32]	**A** [72] [69] [86] [73] [42], [32] [70], [71]	**A** [72], [86], [70], [71] [42], [74] [32] **A-**[69]	**B** [72], [70], [71]	**A** [[86], [70] [74] [42], [32] **A-**[72][73][71]
Toluene	**AB** [68]	**A** [69]–[71] [72]	**A**[69], [70], [71] **A-**[75]	**A** [70]	**A** [69]–[73]	**A** [69]–[71] [72] **A-**[87]	**A** [72], [70], [71]	**A** [72], [73], [70], [71]] **A-**[87] **B** [74]
Water	**A** [74] [42] [74][67] **A-**[32] **AB** [75] **B+** [88] **B** [89] [76]	**A** [72], [69], [70]	**A** [42], [32], [74] [75] [77] **A-**[90] **B** [89]	**A** [42], [32], [74][75] [77] **A-**[70]	**A** [69]–[73], [74] [67] **A-**[74][75] **B+**[91] [92] **B** [89]	**A** [69]–[71] [72][74] [67] **A-**[74][75]	**A** [72], [70], [71]	**A** [72], [70] **A-**[73][71] **B** [42][32][74] [75] [76][67], [89]

In conclusion, water seems to offer a good trade-off between performance and hazardous issues. This fluid is neither toxic nor expensive. Moreover, it is perfectly compatible with hastelloy, copper, stainless steel (according to 17 studies against 3) and bronze. Thus, in the experimentations presented in the Chapters IV and V, this fluid will be used.

I.1.6.2 Wettability of the fluid on the wall

The wettability of the fluid on the wall affects the contact angle. A non-wetting fluid exhibits a large contact angle that can drastically decrease the capillary force and thus, the LHP performance. Indeed, the maximum capillary pressure that the wick can sustain depends on the minimum contact angle θ_{min} between the fluid and the pore wall. The lower is the minimum contact angle, the higher the maximum capillary pressure:

$$\Delta P_{cap,max} = \frac{2\sigma}{r_p} cos\theta_{min} \tag{I-15}$$

The menisci are not static since the interface, submitted to evaporation and continuously supplied with the percolating liquid, may move inside the porous medium. Thus, a dynamic contact has to be considered. Figure I-19 explains the measurement method of the different angles: a droplet is deposed on a plate that is progressively inclined. The static contact angle θ_s is measured when the plate is at horizontal position whereas the receding contact angle θ_r and advancing contact angle θ_a are measured at the maximum inclination of the plate θ_p for which the droplet remains immobile.

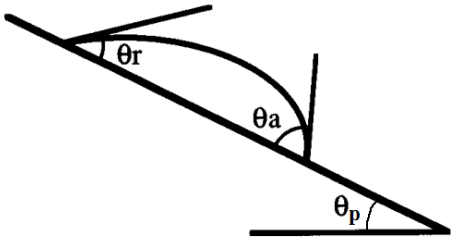

Figure I-19 : Contact angles measurements (Extrand and Kumagai [93])

Figure I-20 shows the advancing, receding and static contact angle measurements of water on various materials extracted from various studies. Letters are set at the top of each value in order to identify the authors who have measured the contact angle (Table I-10). It shows that the contact angle is very large for polymers whereas it is small for ceramics. It means that the effective pore radius will be smaller and thus, the capillary pressure will be higher if the wick is made of a ceramic material.

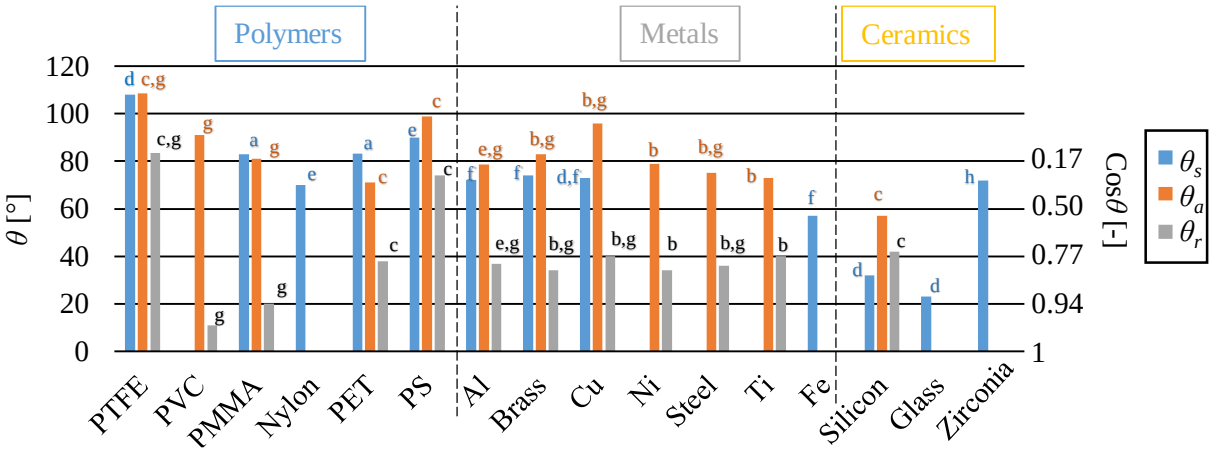

Figure I-20: Static, advancing and receding contact angles of water on various materials (when several authors investigated the same contact angle, the average value is plotted).

Table I-10: Studies investigating the wettability of water on various materials

Authors	Corresponding letter on Figure I-20
Extrand and Kumagai [93]	a
Faghri and Zhang [94]	b
Rafiee [95]	c
Kwok and Neumann [96]	d
Erbil *et al.* [97]	e
Majid [98]	f
Espagon *et al.* [99]	g
Gonzalez-Martin *et al.* [100]	h

In conclusion, the whole operation of the LHP is significantly affected by modifications of the wick characteristics both in terms of hydrodynamic behaviour and thermal performance. This section has shown the interest of working with various materials depending on the constraints and on the applications. The material sciences is expected to enable the development of porous structures specifically dedicated to LHPs.

I.2 Thermo-hydraulic behaviour of a LHP porous medium

The first section of this work has shown that the wick is a key element of a LHP. Thus, it is of interest to focus on this component. According to Launay and Vallée [18], physical mechanisms act together at different scales in the wick:

- Wettability and evaporation in thin films (1 µm)
- Heat transfer and capillary pumping in a porous medium (1-10 µm)
- Permeability through a porous medium (1-10 mm)

The LHP performance, and especially the evaporator one, are greatly dependent on the efficiency of these mechanisms. Conversely, they may be altered in particular operating conditions, leading to the occurrence of an operating limit of the system. It is obvious that the wick parameters have a significant influence on these phenomena. Thus, this section aims to describe the wick thermo-hydraulic behaviour, then details the influence of the wick parameters on it. The case of a monoporous wick is firstly detailed with various approaches. The hydrodynamic behaviour of a fluid inside a porous medium, the thermal mechanisms involved in such a medium and the interaction of this medium with the evaporator wall are discussed. Finally, the opportunity to develop advanced porous media enabling to enhance the evaporator performance is investigated.

I.2.1 Description of the hydrodynamic characteristics of a porous wick

The main hydrodynamic characteristics of a porous medium are the permeability K, the porosity ε and the tortuosity ζ. A state-of-the-art of the test benches enabling the determination of these characteristics is presented in the Chapter IV. The permeability, characterising the ability of a porous medium to be crossed by a fluid, has a direct influence on the capillary limit. Indeed, the pressure losses through the wick, which are a part of the total pressure losses around the loop, are inversely proportional to the permeability, according to the Darcy law:

$$\Delta P_w = \frac{\mu_l e_w u_l}{K} \tag{I-16}$$

Where e_w is the wick thickness and u_l the liquid velocity. An increasing permeability decreases the pressures losses and shifts the occurrence of the capillary limit to higher heat fluxes. The permeability depends on the two other hydrodynamic characteristics. The porosity represents the void fraction inside a porous structure:

$$\varepsilon = 1 - \frac{m_w}{\rho_{mat} V_w} \tag{I-17}$$

where m_w is the mass of the wick, V_w the volume of the wick and ρ_{mat} the density of the material of the wick. A porosity is closed if there is no interconnections between the pore whereas if the porosity is open, the capillary structure is a pore network. The permeability is often higher if the porosity is open.

The tortuosity ξ is the ratio between the real path of the liquid L_{real} percolating inside the pores and the straight length $L_{straight}$ (Figure I-21):

$$\xi = \frac{L_{real}}{L_{straight}} \tag{I-18}$$

The higher the tortuosity, the lower the permeability, partly because it increases the pressure losses.

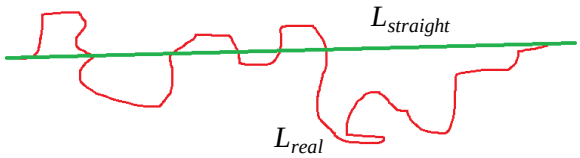

Figure I-21 : Tortuosity of a porous structure

There is no analytical model enabling to determine these characteristics. However, various semi-empirical relationships between them exist in the literature. For the case of a porous medium made of spherical particles, Kozeny-Carman [101] proposed a semi-empirical correlation, based on the Poiseuille model [102] which considers a fluid flow through a capillary tube. It enables to estimate the permeability as follows:

$$K = \frac{d_s^2 \varepsilon^3}{180(1-\varepsilon)^2} \tag{I-19}$$

where d_s is the powder particles diameter of the porous structure. This equation is valid with the assumptions that the pores are interconnected and randomly distributed.

In 1976, Chi [33] proposed to modify the Kozeny-Carman equation into Eq. (I-20), which better fits with sintered capillary structures:

$$K = \frac{d_s^2 \varepsilon^3}{150(1-\varepsilon)^2} \tag{I-20}$$

Rumpf and Gupte [103] proposed a correlation based on dimensional analysis in order to study the dependence of the permeability on the porosity using a uniform package of spherical particles:

$$K = \frac{\varepsilon^{5.5} d_s^2}{5.6} \tag{I-21}$$

In 1988, Du Plessis and Masliyah [104] proposed a new mathematical model for a laminar flow through a rigid isotropic and consolidated porous medium:

$$K = \frac{d_s^2 \varepsilon}{41(1-\varepsilon)^{\frac{4}{3}}}\left[1-(1-\varepsilon)^{\frac{1}{3}}\right]\left[1-(1-\varepsilon)^{\frac{2}{3}}\right] \quad \text{(I-22)}$$

Figure I-22 shows that the permeability correlations follow the same trends but a constant gap of around one order of magnitude exists between the correlations based on the Kozeny equation ((I-19) and (I-20)) and the others ((I-21) and (I-22)).

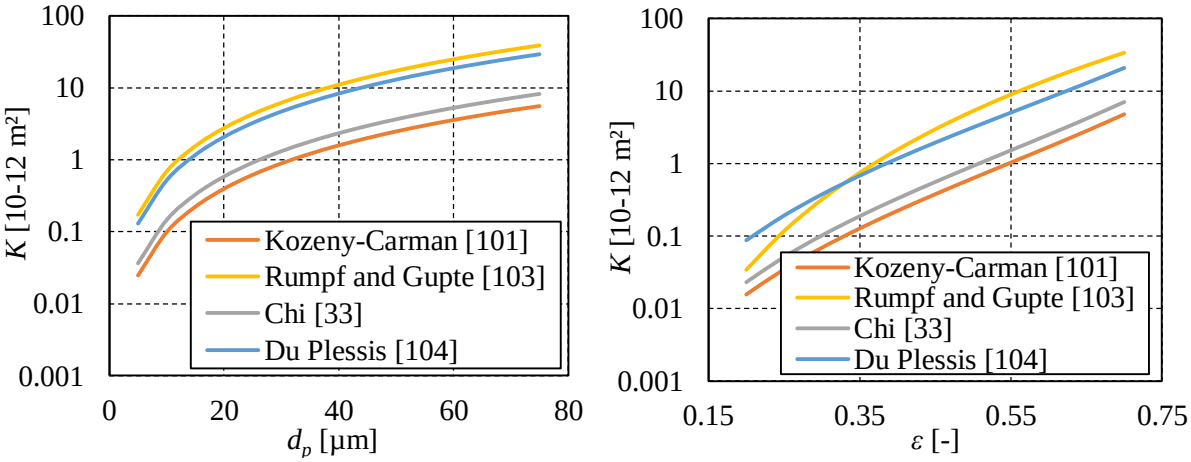

a) Plotted with $\varepsilon = 0.4$ b) Plotted with $d_s = 15$ µm

Figure I-22 : Permeability of a sintered wick calculated with different correlations

Unfortunately, all these correlations suffer from large inaccuracies and may be far from the measured permeability by a factor 10. That is why, many researchers prefer performing their own measurements. Figure I-23 shows the evolution of the permeability versus the porosity for various experimental works of the literature. Two studies propose surprising results which are surrounded in Figure I-23. Firstly, the samples of Deng *et al.* [105] have a decreasing permeability for an increasing porosity. Secondly, Li *et al.* [106] are lower by a factor 100 and 1000 than the predictions. The other data roughly follows the trends of the correlations and differ by a factor 10 or less from the correlations.

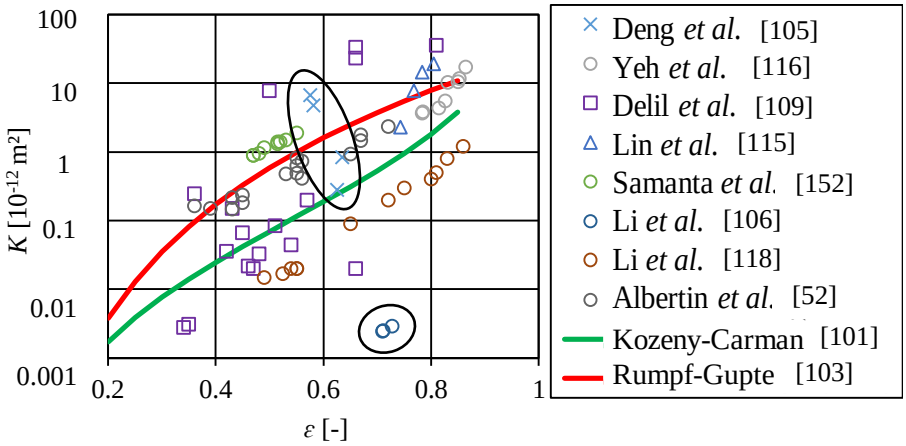

Figure I-23 : Permeability versus the porosity (powder sphere radius equal to 2.5 µm)

Figure I-24 shows the evolution of the permeability versus the pore radius. The data seem to follow the trends of the correlations. However, it is not evident for small pore radii. These results confirm that using the correlations is of interest in order to roughly predict the permeability but to accurately know this characteristic, it is preferable to experimentally determine it (See Section IV.1).

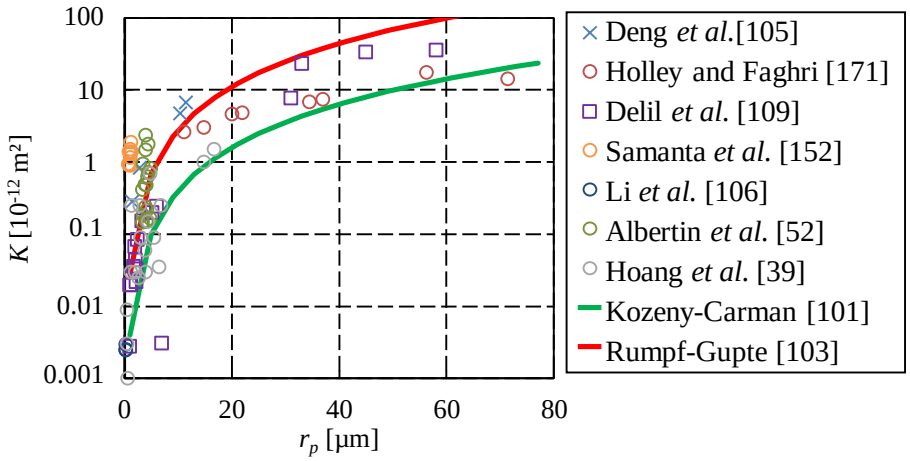

Figure I-24 : Permeability versus the pore radius (porosity equal to 40 %)

In theory, there is no interdependence between the porosity and the pore radius. However, it is difficult to manufacture a wick with a small pore radius and a high porosity. Figure I-25 shows the pore radius as a function of the porosity, for various porous structures used in the literature. Even if the trend is not obvious, it is possible to see that the higher the porosity, the higher the pore radius.

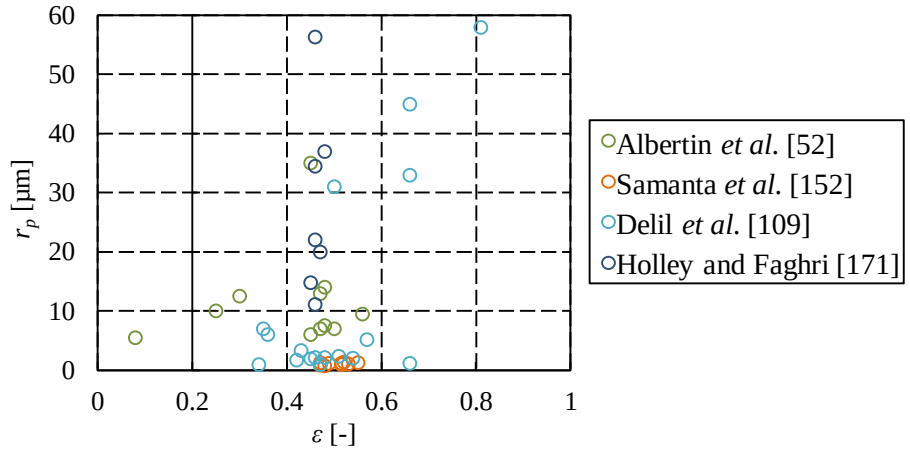

Figure I-25 : Pore radius versus the porosity for various samples

Hoang *et al.* [107] observed in the literature a large scattering of the permeabilities and of the porosities for a considered pore radius. According to Launay and Vallée [18], this dispersion could be due to the material or the manufacturing process. The porous medium is often assumed to be homogeneous, with identical pore sizes, whereas it is never the case in reality. However, a single value of pore radius is considered in the correlations. According to the definition given to this radius that may vary from one author to another (effective pore radius, median pore radius, average pore radius…), and to the type of experimental method and statistical treatment used to obtain the pore radius, this value may differ even for a given porous wick. Thus, clarifications must be brought on the different definitions of the pore radius that may be considered (See Section I.2.3.1).

I.2.2 Thermal behaviour of a porous wick in contact with the evaporator wall

A wick must provide the capillary pressure enabling the fluid to circulate around the loop by means of suitable hydrodynamic characteristics but it also needs to ensure a good heat transfer from the evaporator to the fluid. That is why, authors like Zhao and Liao ([38], [108]) experimentally investigated the heat transfer coefficient h_e while decoupling the evaporator and the rest of the loop. In this case the definition of the heat transfer coefficient is:

$$h_e = \frac{Q_{in}}{T_e - T_{sat}} \tag{I-23}$$

Some authors define the evaporator temperature as the vapour temperature $T_{v,e}$ inside the grooves, other define it as the fin temperature T_{fin} and finally, it can be defined as the temperature of the copper block $T_{e,wall}$. It is generally accepted that the saturation temperature is taken at the reservoir, in the liquid $T_{l,r}$ or the vapour phase $T_{v,r}$. Generally speaking, the heat transfer coefficient is studied by increasing step by step the heat load. A state-of-the-art of the test benches enabling the determination of the heat transfer coefficient is presented in Chapter V.

Zhao and Liao [38] explained that for low and moderate heat fluxes, bubbles and liquid coexist in the porous wick. With an increasing heat load, the two-phase zone shrinks vertically while it expands laterally. The bubble growth-collapse cycle and the number of isolated bubbles in this zone increases. These phenomena lead to an increase of the heat transfer coefficient. Beyond a certain heat flux called the critical heat flux (CHF), the bubbles coalesce immediately after being generated close to the heated surface. When a continuous vapour film is formed, the heat transfer coefficient drastically decreases.

The heat transfer coefficient and the CHF are higher if the liquid temperature at the inlet of the wick increases, as shown in Figure I-26, because the two-phase zone near the heated surface is wider. In contrast, the heat transfer coefficient and the CHF are lower if an adverse hydrostatic pressure exists because the liquid supply becomes more difficult.

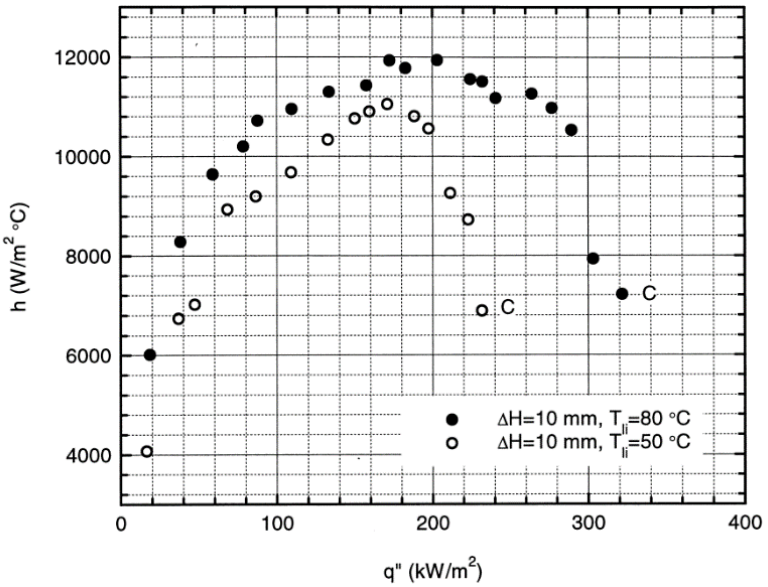

Figure I-26 : Evolution of the evaporator heat transfer coefficient as a function of the heat flux density and the saturation temperature (Zhao and Liao [38])

The same behaviour is observed by Delil and Baturkin [109]. Figure I-27 shows the heat transfer coefficient obtained with various anti-gravity heights. The three curves follow the same trend. The heat transfer coefficient increases with an increasing heat load. It reaches a maximum at the CHF, and then it decreases. As expected, an increasing height of anti-gravity head decreases the thermal performance. The authors tested various porous structures in order to investigate the influence of the wick characteristics.

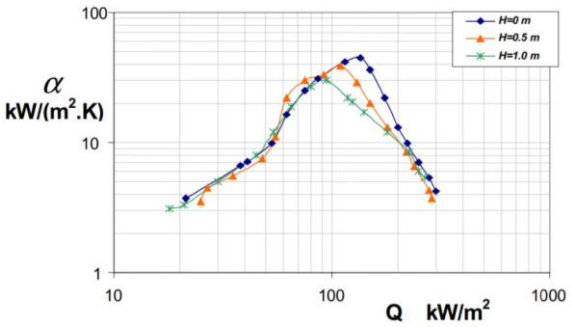

Figure I-27: Evaporator heat transfer coefficient as a function of the heat flux density and the elevation (Delil and Baturkin [109])

In practice, very few studies dealing quantitatively with the thermal characterisation of a porous wick in contact with an evaporator wall are available in the literature. Table I-11 presents results of the thermal characterisation of various porous structures. The heat transfer coefficients are given at the CHF. Due to different experimental conditions and porous structures, a large scattering of the values is observed. Moreover, there are various definitions of the temperature difference enabling the determination of the heat transfer coefficient. It leads to large differences the h_e values since the thermal resistances taken into account largely differ. Apart from Zhao and Liao [108], authors did not try to link the CHF with the occurrence of an operating limit.

Table I-11: Thermal characterisation of porous structures

Authors	Year	CHF (W/m²)	h_e (W/m².K)	Definition of ΔT
Zhao and Liao [38]	2000	180 000	10 300	$T_{fin} - T_{v,r}$
Zhao and Liao [108]	2000	200 000	12 000	$T_{fin} - T_{v,r}$
Khammar *et al.* [110]	2014	58 300	2 400	$T_{wall,e} - T_{sat,r}$
Schertzer *et al.* [111]	2006	220 000	7000	$T_{wall,e} - T_{sat,r}$
Delil and Baturkin [109]	2002	135 000	45 000	$T_{v,e} - T_{l,r}$
Delil and Baturkin [109]	2002	60 000	69 000	$T_{v,e} - T_{l,r}$

The contact surface between the wick and evaporator internal wall has a major influence on the evaporator thermal performance. It should facilitate transmission of the heat flux and enable a large evaporation surface area and an easy evacuation of the vapour to the vapour grooves. A good trade-off has to be found between the surface area in contact with the wall and the one in contact with the vapour grooves.

The vapour grooves design may affect the evaporation surface area. The grooves can be engraved into the wick (Figure I-28 a) or into the evaporator wall (Figure I-28 b). In the former design, the evaporation surface area is expected to increase. However, in the literature, it is possible to find studies showing that one or the other configuration provides the highest thermal performance. Thus the question of the best configuration is still open.

Choi *et al.* [112] proposed to interpenetrate the wick with the evaporator wall (Figure I-29) in order to increase their contact surface area. With the proposed design, they found a large enhancement of the evaporator thermal conductance and lower operating temperatures.

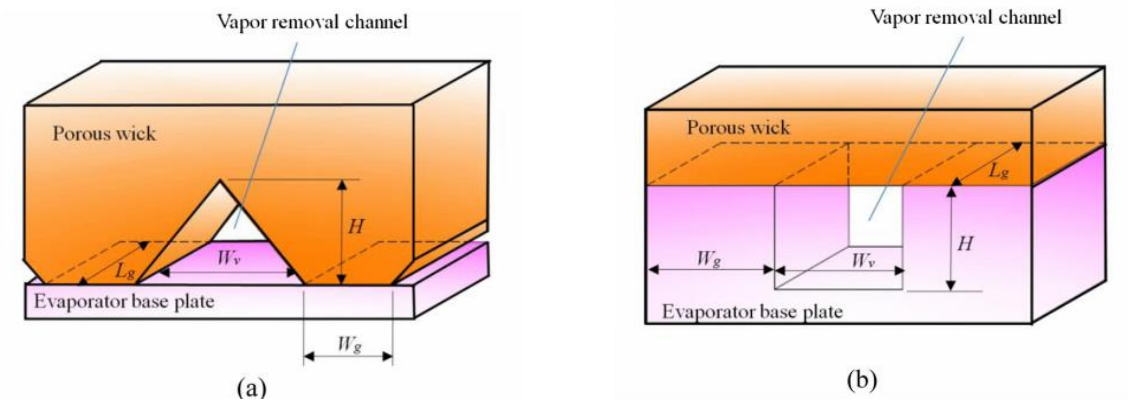

Figure I-28 : Various classic groove designs (Choi *et al.* [112])

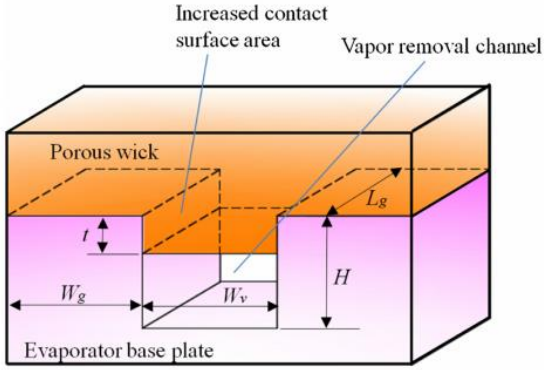

Figure I-29 : New groove design (Choi *et al.* [112])

Schertzer *et al.* [111] studied the influence of a gap between the finned evaporator and the porous wick on the heat and mass transfer. They showed that increasing the gap size d_{gap} up to 500 µm had a positive influence on the heat transfer coefficient (Figure I-30).

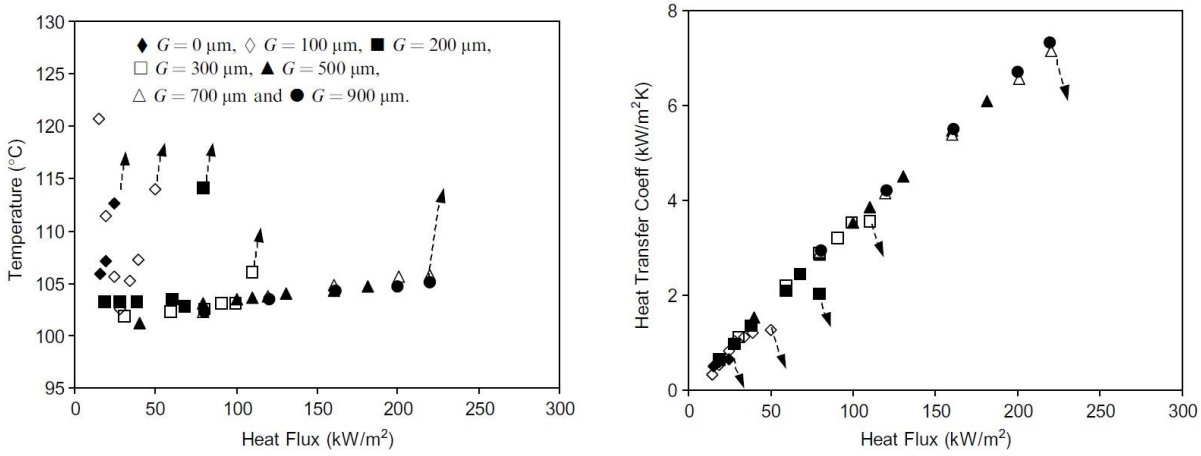

a) Space averaged evaporator temperature b) Average heat transfer coefficient

Figure I-30: Influence of a gap between the wick and the evaporator fins (Schertzer *et al.* [111])

The presence of a gap changes the evaporation dynamics. Below 200 µm, a vapour pocket builds up beneath the porous medium before leaving the evaporator through the grooves. Above 200 µm, the vapour leaves easily the region between the evaporator wall and the porous medium. In this study, the transition gap has the same size as the pore size. It could indicate that the gap must always be larger than the pore size of the porous structure. Khammar *et al.* [110] also found that the presence of a gap enables to increase the maximum heat load. They showed that 600 µm is the optimum gap enabling the vapour

to leave the grooves without increasing the thermal resistance (Figure I-31). However, in their study, they didn't link the transition gap to the pore radius.

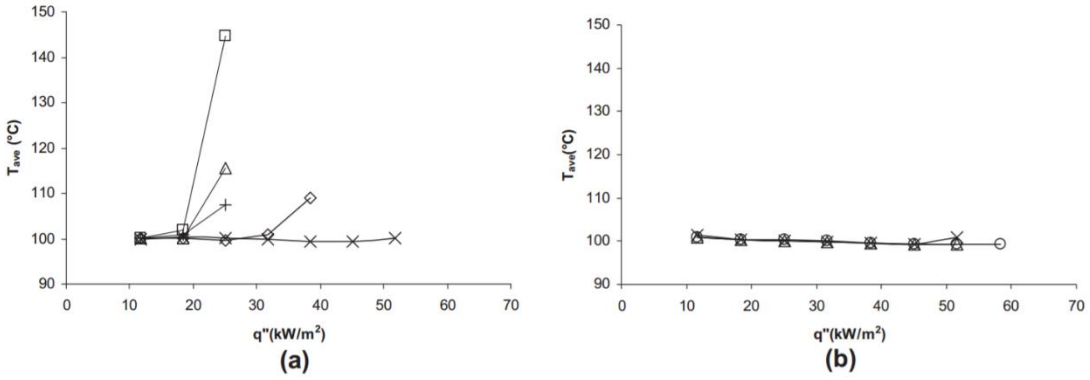

Figure I-31: Change in the average heated surface temperature with heat flux for a gap of (a) □ 0 µm, Δ 100 µm, + 200 µm, ◊ 300 µm, x 400 µm, and (b) ○ 600 µm, Δ 700 µm, x 1000 µm (Khammar *et al.* [110])

The physical explanation of the existence of a transition gap was proposed by Platel *et al.* [113]. At start-up, if the grooves are full of liquid (Figure I-32), the vapour formed under the fin is evacuated by the channel having the largest diameter, for which it is easier to overcome the capillary pressure difference. If the pore diameter is larger than the gap, the wick dry out occurs. Figus *et al.* [114] numerically studied the influence of a thin gap between the fin and the wick. Like the previous authors, they showed that this gap enables the vapour to leave more easily the grooves, reducing significantly the evaporator temperature. However, further studies are still required to fully understand the role of such a gap depending on the operating parameters.

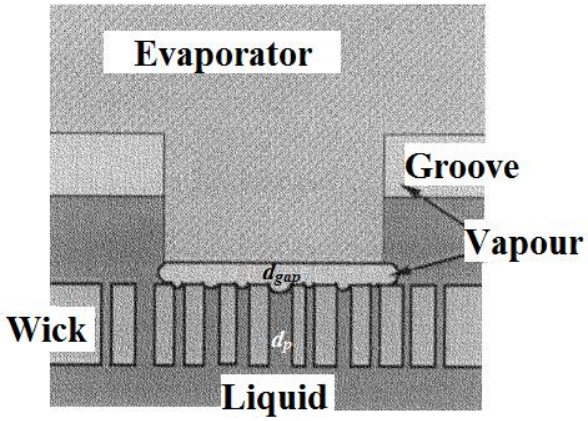

Figure I-32: Schematic of the evaporator at the start-up (adapted from Platel *et al.* [113])

I.2.3 Development of advanced porous medium

The behaviour of a fluid inside a porous medium as well as the occurrence of a vapour blanket depends on the pore radius. In the case of a monoporous, the pore size distribution is centred on a single value, whereas this is not the case for heterogeneous porous media. Many types of advanced capillary structures can be found with different pore size distributions. This section presents and describes the various porous structures encountered in the literature.

I.2.3.1 Biporous and bidispersed structures

The wicks of the first LHPs were monoporous. These wicks are easy to manufacture but do not avoid the formation of a vapour blanket near the evaporator at high heat fluxes (Figure I-33). Indeed, since the

pores are small in order to ensure a high capillary pressure, the vapour cannot easily leave the wick. At very high applied heat load, the vapour blanket reaches the reservoir and prevents the LHP operation.

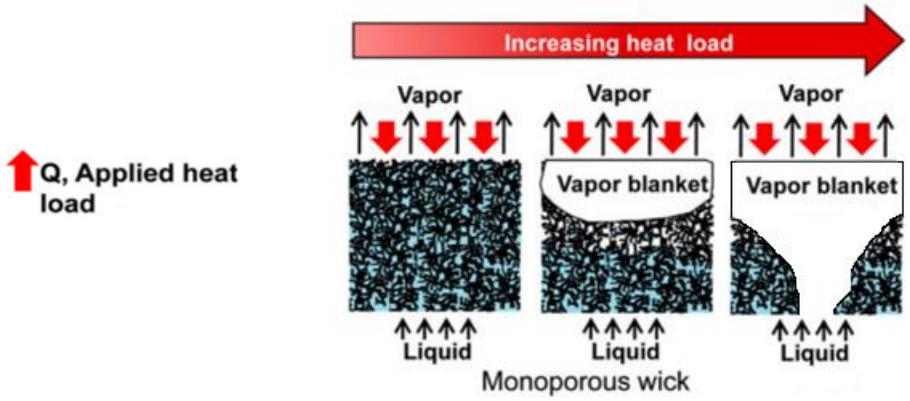

Figure I-33 : Schematic of the dry-out mechanism in a monoporous wick (adapted from Lin *et al.* [115])

The drawbacks of monoporous structures explain why several authors has manufactured biporous and bidispersed wicks also called bimodal porous media: Yeh *et al.* ([116], [117]), Li *et al.* [118], Putra *et al.* [66] and Wu *et al.* [119] among others. These types of wick have the particularity to be composed by both small and large pores. The liquid flows up to the heating wall through the small pores which provide the capillary force and the vapour leaves more easily the wick through the large pores.

Figure I-34 shows the evaporation mechanism in a biporous wick. As the heat load increases, the meniscus recedes in the wick, but without creating any vapour blanket. Thereby, the CHF is higher for a biporous wick than for a monoporous wick. Moreover, the permeability can increase without losing the capillary pumping force provided by the small pores.

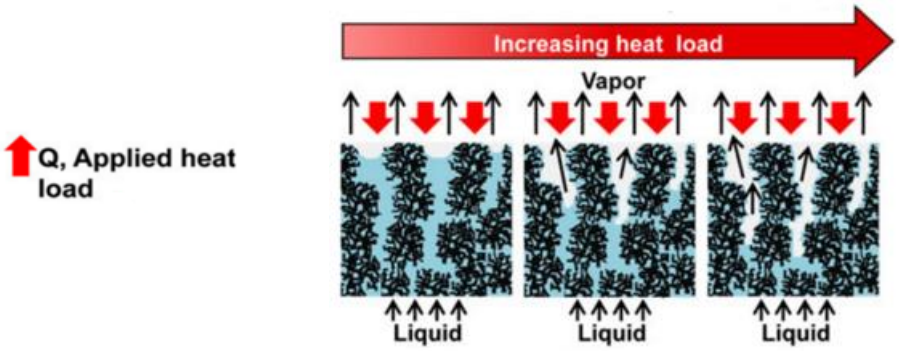

Figure I-34 : Schematic of the evaporation mechanism for a bi porous wick (Lin *et al.* [115])

The advantages and drawbacks of bidispersed and biporous wicks are the same. Only the manufacturing method changes as explained by Mottet and Prat [120]. A bidispersed wick is manufactured by sintering particles already porous (Figure I-35 a) whereas a biporous wick is manufactured by sintering together small powder particles and large pore former particles. The pore former is vaporised before the complete sintering so that it creates larger pores in the porous structure (Figure I-35 b). A microscopic view obtained with a SEM enables to confirm the presence of different pore sizes (Figure I-36). The methods of manufacturing are largely explained in Chapter III.

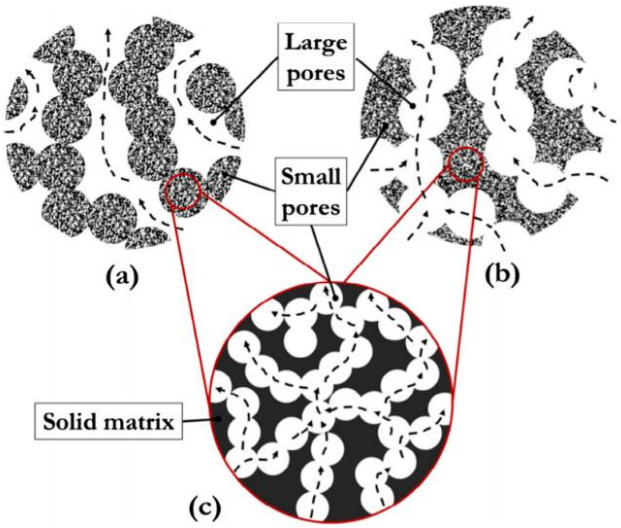

Figure I-35 : Schematic structure of a bimodal porous medium for a bidispersed wick (a) and a biporous wick (b). The arrows indicate the flow paths (Mottet and Prat [120] adapted from Rasor and Desplat [121])

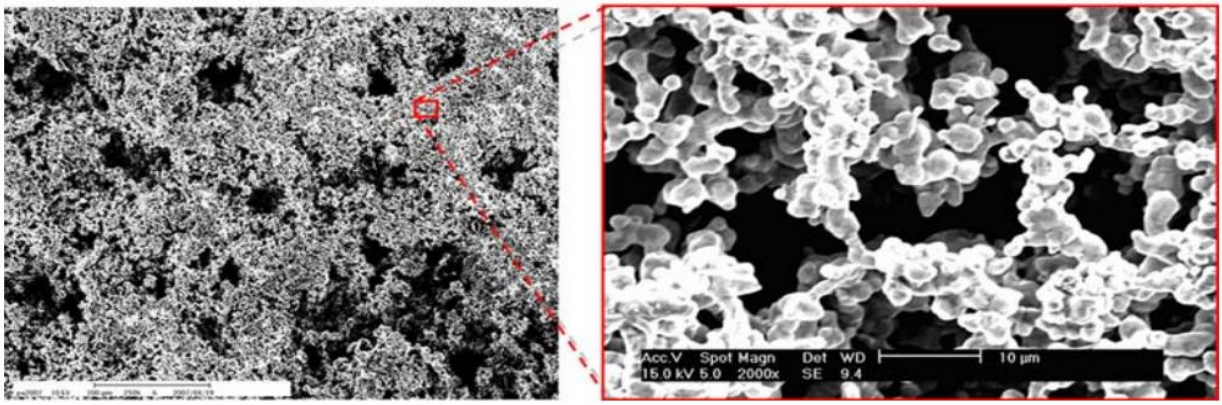

Figure I-36 : Microscopic view of a bi-modal porous medium with a SEM, Yeh *et al.* [116]

Figure I-37 shows an example of pore size distribution of a monoporous and a biporous wick. The curve of the biporous wick has two local maxima (6 µm for the small pores and 25 µm for the channels) whereas the curve of the monoporous wick has only one (10 µm).

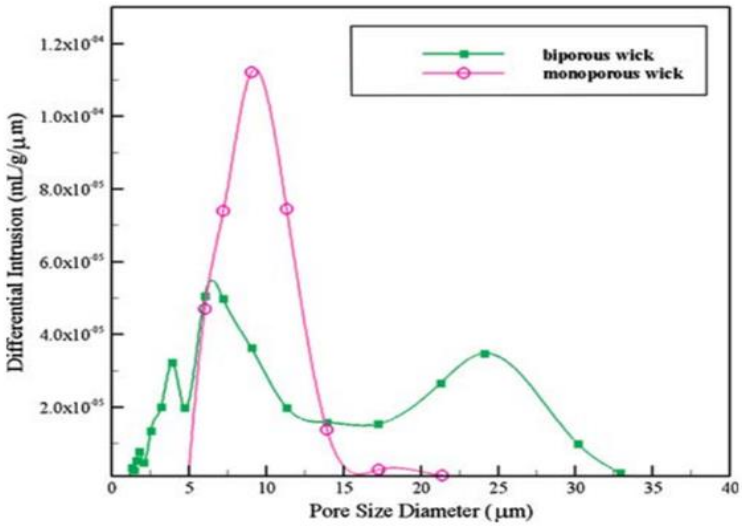

Figure I-37 : Pore size distribution of a monoporous and a biporous wick (Yeh *et al.* [116])

An example of structure of a bidispersed wick is detailed by Cheng and Yu [122]. Such a porous medium is composed of large clusters themselves composed of microporous media (Figure I-38). This type of wick can exhibit a large permeability (Table I-12). Indeed, the permeability of a monodispersed wick increases by a factor 8.3, 11.5 and 21.1 when using macro-pores of 200, 400 and 800 µm respectively. Moreover, the permeability of a monodispersed wick with 800 µm pore diameter is only 1.07 times larger than a bidispersed wick with 800 µm macro-pores and 80 µm micro-pores. The capillary pressure will be ten times higher for the bidispersed wick than for the monodispersed because its micro-pores are ten times smaller. The main problem of biporous and bidispersed wicks is their brittleness. Indeed, a structure with large pores is mechanically less resistant than a monoporous wick. However, bidispersed wicks are of great interest for LHP applications.

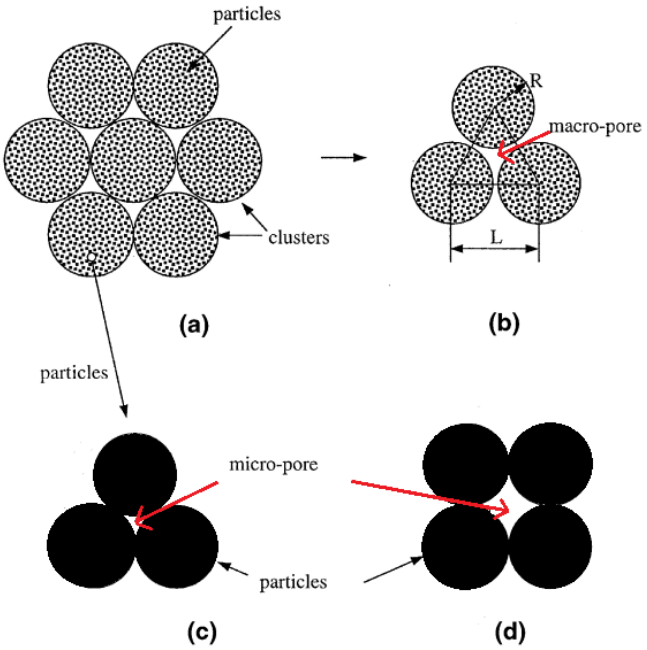

Figure I-38 : Schematic of porous media with the bidispersed structure: (a) bidispersed porous medium; (b) equilateral triangular pattern of three clusters; (c) equilateral triangular pattern inside a cluster; (d) square pattern inside a cluster (Yu and Cheng [122])

Table I-12 : Comparison of porous samples permeabilities (Chen *et al.* [123])

Samples	Micro pore diameter [µm]	Macro pore diameter	K [10^{-10} m²]
1	80	Mono-dispersed	0.267
2	800	Mono-dispersed	6.035
3	80	200	2.235
4	80	400	3.078
5	80	800	5.642

When considering that kind of porous wick with a given pore size distribution, the definition of the pore radius needs to be detailed. According to the Laplace-Young equation, the maximum capillary pressure is reached at first in the largest pore (depicted on the left of Figure I-39). The minimum meniscus radius $r_{m,min}$ is expressed by:

$$r_{m,min} = \frac{2\sigma}{\Delta P_{cap,max}} \tag{I-24}$$

The minimum radius depends on the wettability of the fluid on the pore wall. This results in a contact angle between the liquid-vapour interface and the solid wall, that can be experimentally determined (Section IV.2.4). In the large pore of Figure I-39, the contact angle θ_{min} has reached its minimum value whereas in the other pores, the meniscus radius can further decreases since θ_{min} has not be reached. The largest pore radius is called the effective pore radius $r_{p,eff}$ in the following of this work. The relationship between $r_{p,eff}$ and $r_{m,min}$ is:

$$r_{p,eff} = r_{m,min} cos\theta_{min} \tag{I-25}$$

θ_{min} will be simply noted θ.

The mean pore radius r_p results from an arithmetic averaging of the n pore radii of the structure (Figure I-39). It is determined as follows:

$$r_p = \frac{1}{n}\sum_{1}^{n} r_{p,n} \tag{I-26}$$

In practice, all the pore radii cannot be measured, especially inside the capillary structure. The method to measure r_p is detailed in the Section III.5.3.

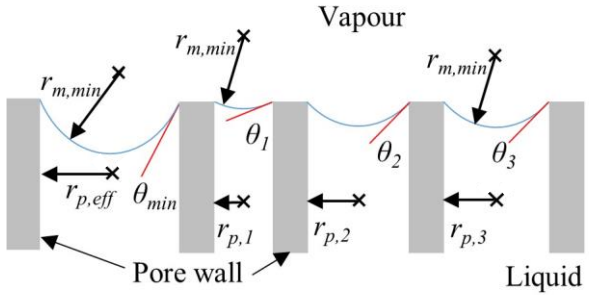

Figure I-39: Schematic of the menisci in a "real" porous structure when the maximum capillary pressure is reached

I.2.3.2 Multi-layer structures

Multi-layer structures can be used to answer the mechanical strength problems. Such structures are frequently used in cylindrical LHP evaporators (see Section I.1.1.1): a secondary wick was added in series to the main wick by several authors including Pastukhov *et al.*([124], [62]), Van Oost *et al.* [125] and Ogushi *et al.* [126]. The secondary wick can also act as a thermal barrier (Fershtater and Maydanik [127]) and reduce the heat leaks to the reservoir. When using a secondary wick, this one must exhibit a high permeability to limit the pressure losses and a low thermal conductivity to limit the heat leaks to the reservoir.

Wu *et al.* [119] developed a double layer cylindrical wick. The outer wick (or primary wick) is biporous to enable the evacuation of the vapour and to provide a high capillary pressure. The inner wick (or secondary wick) is monoporous to provide good mechanical strength. This kind of wick can increase the performance of the LHP compared to a biporous and a monoporous wick. Indeed, the heat load corresponding to the maximum allowable evaporator temperature is higher and the global thermal resistance R_{LHP} is lower (Figure I-40).

Recently, Xu *et al.* [128] investigated a multi-layer wick for a flat disk-shape evaporator. Figure I-41 presents the design of such a wick. It is composed by three layers having a diameter of 68 mm and a thickness of 2 mm. The vapour grooves are located in the high thermally conductive primary wick in order to avoid the conductive thermal resistance of the evaporator fins. This wick is biporous to avoid

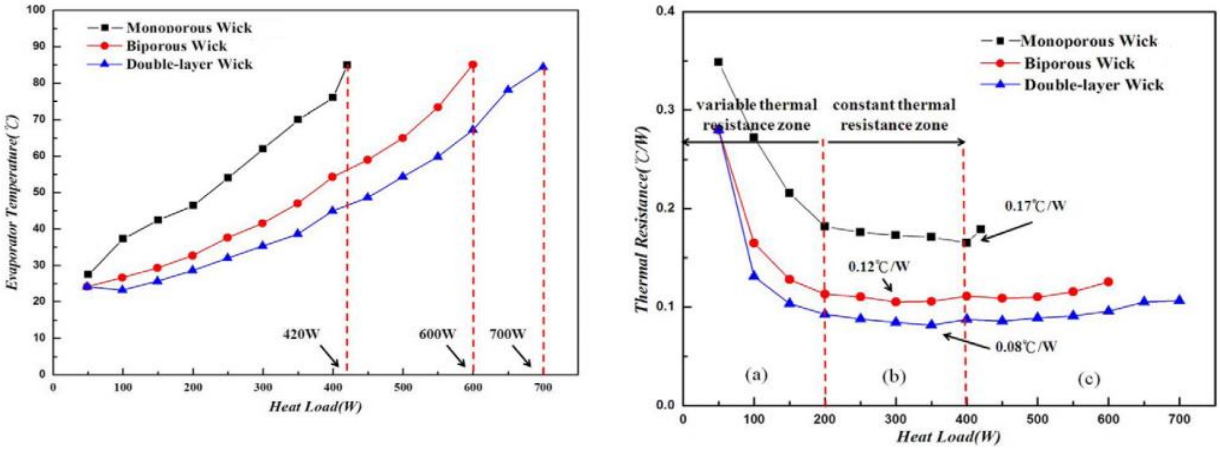

Figure I-40 : Comparison of LHP performance for monoporous, biporous and double-layer wicks (Wu *et al.* [119])

the formation of a vapour blanket, as explained before. The role of the secondary monoporous wick (average powder diameter of 149 µm) is to supply the primary wick with liquid. It has a high thermal conductivity in order to spread the heat to the incoming liquid. The third wick, of low thermal conductivity, acts as a thermal and hydraulic barrier. The average pore size of this wick is of 20 µm. With such a wick, the LHP performance are improved and it significantly reduces the time needed to reach a steady state. Moreover, it decreases the evaporator wall superheat from 20 to 50 K.

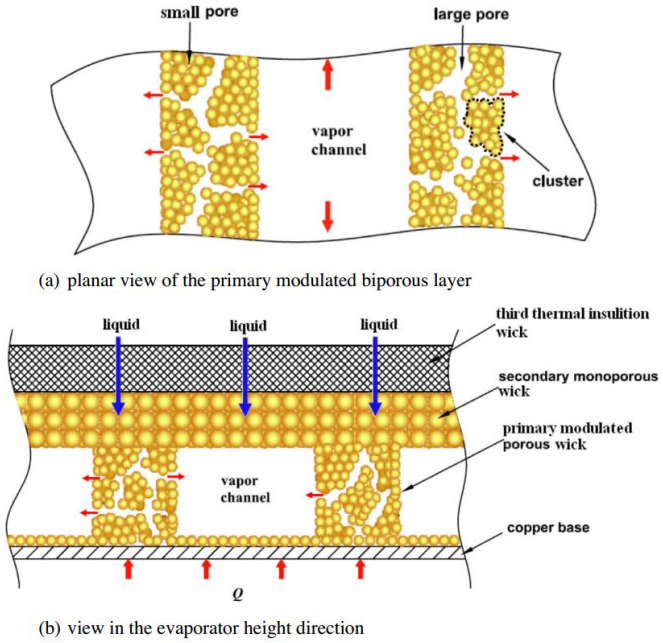

Figure I-41 : Schematic of a multi-layer wick (Xu *et al.* [128])

I.2.4 Conclusion

In conclusion, the hydrodynamic characteristics, the quality of the contact between the wick and the evaporator wall, and the pore size distribution have an influence on the heat and mass transfer inside the LHP evaporator and on the occurrence of the operating limits. Biporous and bidispersed wicks enable to delay the development of the vapour blanket but may create structural brittleness. Multi-layer mono/bi porous wicks seem to be able to solve these issues. Predicting the wick characteristics leading to the

highest performance is one of the objectives of this work as well as manufacturing and testing these porous structures. The Chapter II and the Chapter III aim at fulfilling these purposes.

To the literature, most experimental works investigating the heat transfer coefficient of a LHP evaporator as a function of the heat load showed that the curves present a maximum value, corresponding to the best evaporator performance. Very few authors compared the corresponding heat flux to the theoretical capillary or boiling limits of a LHP. Thus, it is difficult to estimate if one or the other limit is reached. This work will be conducted in the Chapter V of the present thesis.

I.3 Evaporator modelling

Many researchers developed numerical or analytical models in order to understand and predict the evaporator thermal and hydrodynamic behaviours. This section successively investigates the models of heat transfer inside the porous medium, at the interface between the wick and the evaporator wall and at the scale of the complete LHP.

I.3.1 Model of heat transfer within the porous medium

In order to model the heat transfer inside a porous medium crossed by a fluid in motion, an equivalent thermal resistance is determined. It depends on the fluid properties, the fluid velocity, the porous structure and the wick material.

To this purpose, an effective thermal conductivity λ_{eff} of the porous medium is considered. It is the thermal conductivity of an equivalent homogeneous and isotropic solid material. It depends on the solid material and the fluid but as the fluid conductivity is usually small compared to the solid one, λ_{eff} mainly depends on the microstructure of the solid particle matrix, which affects the conductive heat path. λ_{eff} plays an important role in the evaporator operation: it affects the heat transfer from the fins to the evaporating interface, as well as the heat leaks through the wick. A lot of correlations are reported in the literature in order to estimate this parameter, each one having its own assumptions (Appendix A). Thus, the accurate prediction of the effective thermal conductivity of a porous medium is still a challenge. In this thesis, the Alexander's correlation [129] is used. Indeed, this correlation is used in many studies: Bazzo and Riehl [54], Singh [130], and Li and Peterson [131] among others.

In the case of a flat wick saturated with liquid, a wick thermal resistance R_w can be determined following a classical method which considers a conductive model:

$$R_w = \frac{e_w}{\lambda_{eff} S_w} \tag{I-27}$$

where S_w is the wick cross sectional area. This conductive model is only reliable for wicks of high thermal conductivity and for low mass flow rates, for which the Peclet number P_e is small:

$$Pe = \frac{\rho_l c_{p,l} e_w u_l}{\lambda_{eff}} \tag{I-28}$$

Hamdan *et al.* [132] said that for thick wicks with low thermal conductivity (large Peclet number), the convective heat transfer in not negligible compared to the conductive one. The thermal resistance taking into account a convecto-conductive heat transfer is given by Launay *et al.* [5]:

$$R_w = \frac{exp\left(\frac{\dot{m} c_{p,l}}{\lambda_{eff} S_w} e_w\right) - 1}{\dot{m} c_{p,l}} \tag{I-29}$$

where $\dot{m}$ is the fluid mass flow rate. Figure I-42 shows the thermal resistance versus the mass flow rate of water for a high and a low effective thermal conductivity. For high thermal conductivity, the

convecto-conductive model is not necessary. Indeed, the thermal resistance increases of only 3 % if the mass flow rate increases from 0 to 6.10^{-5} kg/s. Contrariwise, for low thermal conductivity it seems essential to take convection into account as the thermal resistance increases of 130 % in the same conditions.

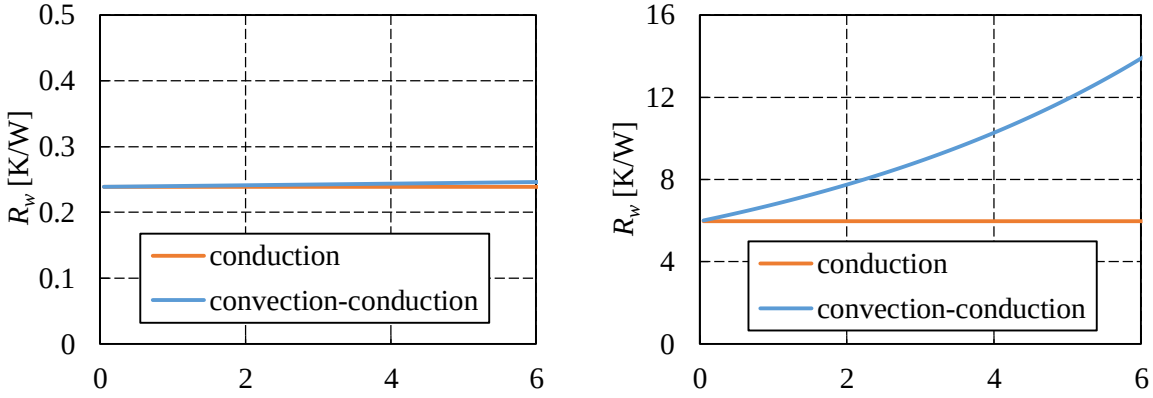

a) λ_{eff} = 20 W/m/K b) λ_{eff} = 0.8 W/m/K

Figure I-42 : Thermal resistance as a function of the mass flow rate (e_w = 6 mm, S_w = 12.5 cm²)

I.3.2 Model of evaporation at the wick surface

This section proposes a review of various models in order to study the heat and mass transfer during the liquid evaporation at the interface between the wick and the evaporator wall.

The heat transfer coefficient of the evaporator depends on the heat transfer coefficient of evaporation h_{ev} itself. In the case of a saturated wick (small heat loads). Carey [133] suggests a heat transfer coefficient using the kinetic theory of gases:

$$h_{ev} = \frac{2a_{ev}}{2-a_{ev}} \frac{\rho_v h_{lv}^2}{T_{sat}} \left(\frac{2\pi \bar{R} T_{sat}}{\bar{M}} \right)^{-0.5} \left(1 - \frac{P_{sat}}{2\rho_v h_{lv}} \right) \quad \text{(I-30)}$$

where $\bar{M}$ is the molar mass and $\bar{R}$ is the gas constant. Morooka *et al.* [134] proposed the following equation to estimate the heat transfer coefficient of evaporation:

$$h_{ev} = \frac{1}{\left(\frac{1.18 d_p}{2\lambda_e} + \left(1 - \frac{\rho_v}{\rho_l} \right) \frac{T_v \sqrt{2\pi \bar{R} T_v} a_{ev}}{J \rho_v a_{ev} {h_{lv}}^2} \right)} \quad \text{(I-31)}$$

where J is the mechanical equivalent of heat. One can note that these expressions depend on a_{ev} which is the one dimensional accommodation coefficient. Eames *et al.* [135] proposed a review of the accommodation coefficient for water and their results show a large range lying from 0.01 to 1. Despite this wide range, the value of the resulting heat transfer coefficient of evaporation corresponds to a negligible thermal resistance compared to thermal resistances due to convective and conductive phenomena. Thus, these models need to be extended to take into account the global behaviour of the fluid in the porous medium.

I.3.3 Models of the whole evaporator

In order to take into account the global behaviour of the fluid in a LHP evaporator, a lot of numerical studies consider a small element of the evaporator including half of a vapour groove and half of a fin. Thus, these models do not take into account the heat leaks through the evaporator wall. For example,

Cao and Faghri [136] studied both analytically and numerically the steady-state heat and mass transfer in the wick assuming that it is saturated in liquid. Analytical solutions for liquid pressures, velocities and temperatures in a homogeneous porous structure are determined. They also proposed a three dimensional model [137], solving the conservation equations inside the wick, the vapour groove and the wall. Their results show that the pressure drops in the wick and the vapour grooves are relatively small compared to the capillary pumping pressure. Thus, a two-dimensional modelling neglecting the vapour flow and the heat transfer in the groove is generally sufficiently accurate.

Zhao and Liao [108] proposed a complete model of the heat transfer in a single pore. It takes into account the heat transfer coefficient of evaporation and the disjoining pressure P_d, which is due to the Van Der Waals forces when evaporation in thin films takes place. The temperature T_δ and the pressure P_δ at the thin film interface are given by the two following equations:

$$P_\delta(\eta) = P_{sat}(T_\delta)\exp\left(\frac{P_\delta(\eta) - P_{sat}(T_\delta) + P_d(\eta) - \frac{2\sigma}{r_m}}{\rho_l \bar{R} T_\delta(\eta)}\right) \tag{I-32}$$

$$T_\delta(\eta) = T_{wp} + \frac{\delta_l(\eta)}{\lambda_l}\frac{2a_{ev}}{2-a_{ev}}\frac{h_{lv}}{\sqrt{2\pi\bar{R}}}\left(\frac{P_{sat}(T_v)}{\sqrt{T_v}} - \frac{P_\delta(\eta)}{T_\delta(\eta)}\right) \tag{I-33}$$

where δ is the thin film thickness at a pore depth η (Figure I-43). T_{wp} is the pore wall temperature. These equations are coupled with an energy balance equation where the heat flux transferred by conduction from the pore solid wall to the interface is equal to the heat flux transferred by evaporation:

$$\frac{\dot{m} h_{lv} \pi r_{p,eff}^2}{\varepsilon} = \int_{\eta_0}^{\eta_b} \frac{T_{wp} - T_\delta(\eta)}{\delta_l(\eta)} 2\pi r(\eta) d\eta \tag{I-34}$$

This enables to calculate T_{wp} and finally, the heat transfer coefficient $h_{e,th}$:

$$h_{e,th} = \frac{Q_{in}}{T_{wp} - T_v} \tag{I-35}$$

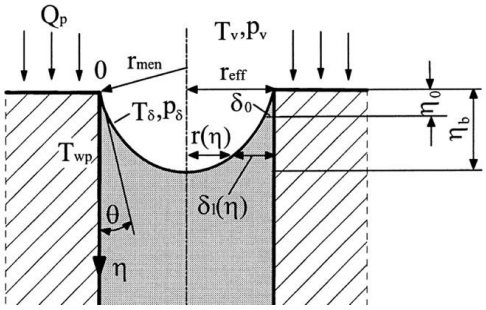

Figure I-43: Schematic of the pore geometry used by Zhao and Liao [108]

They proposed two models depending on the heat load. For lower heat loads than the CHF, the triple points are located at the wick surface. For heat loads higher than the CHF, they introduced a two-phase zone under the fin. The maximum heat flux is reached when this zone becomes full of vapour. According to their study, the CHF corresponds to the capillary limit. That was confirmed by an experimental study (Figure I-44), in which they observed that, at small and moderate heat fluxes, the wick is fully saturated. Around the CHF, a vapour zone starts to grow. Beyond the maximum heat flux, the temperature of the heated zone increases dramatically and the test has to be stopped. At this stage, there is no liquid anymore near the heated surface.

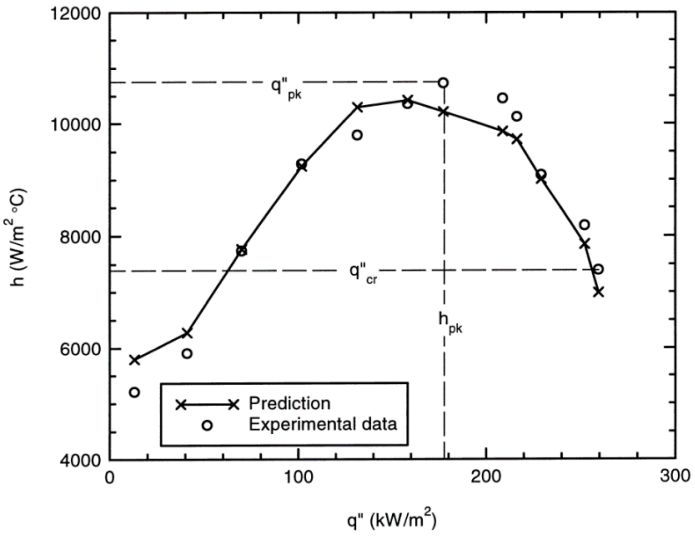

Figure I-44 : Heat transfer coefficient versus heat flux density (Zhao and Liao [108])

Demidov and Yatsenko [138] computed the equations of conservation to determine the expansion of a vapour zone under the heated fin when the heat load increases (Figure I-45 a). Two important assumptions are made. First, they assumed that there exists a superheated vapour zone in the vicinity of the heated wall while the wick is saturated by a subcooled liquid elsewhere. They further assumed that, when the vapour zone do not exceed the heated surface, there would be a liquid meniscus near the corners formed by the lateral sides of the heating fins and the top surface of the porous structure. On the other hand, when the vapour zone expands beyond the surface of the heated wall, this liquid meniscus would disappear. They concluded that at low heat loads, a stable vapour zone may exist under the fin. When the surface area of this zone exceeds the one of the heated input element (HIE) as shown in Figure I-45 (b), a further increase in the heat load leads to an expansion of the dried zone into the capillary structure. This is consistent with the results of Zhao and Liao [108]. They also demonstrated that the presence of liquid menisci would greatly enhance the evaporative heat flux.

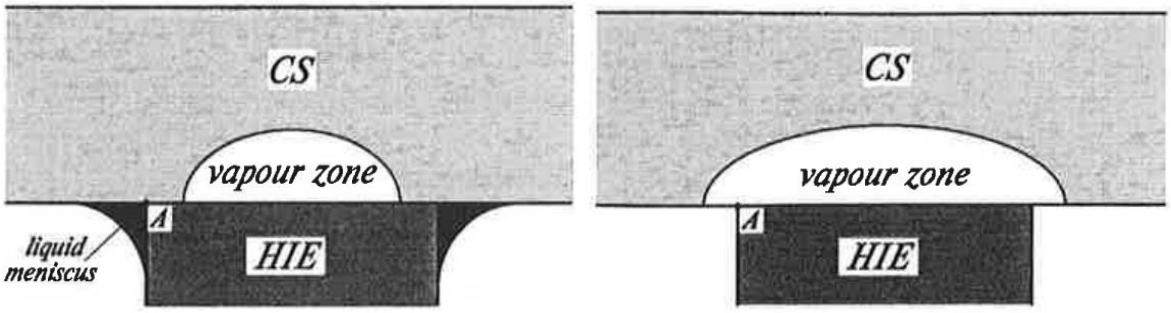

a) Low heat load b) High heat load

Figure I-45 : Schematic of the vapour zone by Demidov and Yatsenko [138]

Kaya and Goldak [11] numerically studied the heat and mass transfer inside a capillary evaporator in the same zone. They used the finite element method to solve the equations of continuity, energy and the Darcy equation:

$$\nabla . u = 0 \tag{I-36}$$

$$u = -\frac{K}{\mu_l}\nabla P \tag{I-37}$$

$$\rho c_{p,l}\nabla(u.T) = \lambda_{eff}\nabla^2 T \tag{I-38}$$

They considered two cases: one of a fully saturated wick and the other at high heat loads, when a vapour region takes place inside the wick. At high heat fluxes, the fluid velocity is much higher at the triple line between the solid wall, the vapour and the liquid phases. At moderate heat fluxes, the velocity is almost the same all along the wick-grooves interface.

Figus *et al.* [114] numerically simulated the heat and mass transfer in an element of symmetry of the evaporator (Figure I-46 a). Their model results from a coupling of a pore network model and a thermal network model. Pores and throats are linked together (Figure I-46 b). The mass, momentum and energy balance equations are solved using a technique similar to a standard finite volume technique.

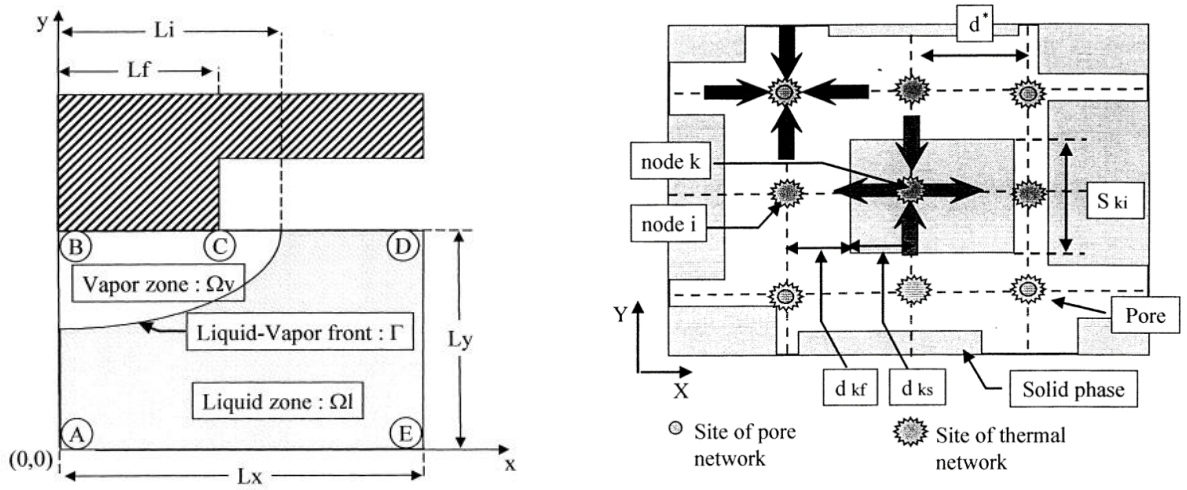

a) Global modelled area b) Focus on the pore network

Figure I-46 : Schematic of the model developed by Figus *et al.* [114]

They simulated various heat loads to obtain temperature and pressure profiles in the porous medium as shown in Figure I-47. It allows to track the evolution of the vapour zone inside the wick. They proposed similar conclusions than Demidov and Yatsenko [138] about the evolution of this zone. The vapour zone firstly develops at the vicinity of the evaporator fin, then penetrates into the wick with a fractal type interface.

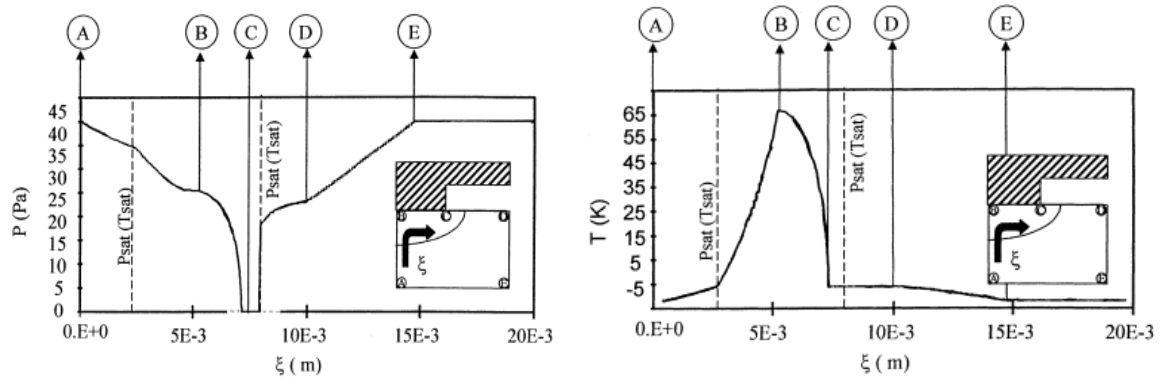

a) Pressure profile b) Temperature profile

Figure I-47 : Example of results obtained by Figus *et al.* [114]

Coquard [41] and Mottet [139] improved the model of Figus *et al.* [114]. They used various pore sizes (Figure I-48) and distributions. In this case, the size of the throats is randomly distributed between a minimum and a maximum value according to a given probability distribution function.

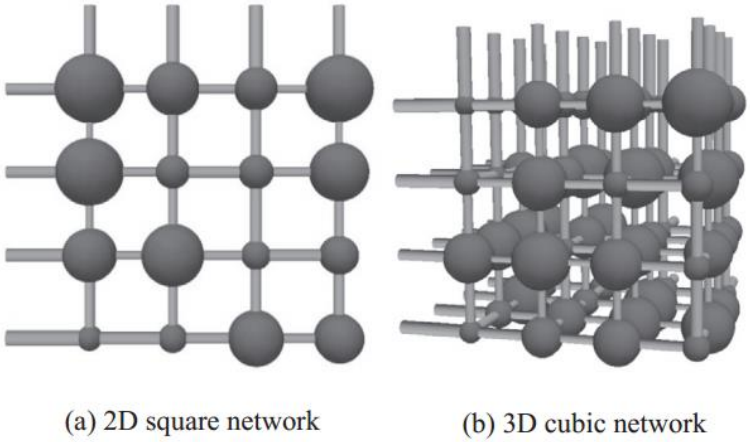

Figure I-48 : Pore network representation of porous microstructure (Mottet *et al.* [29])

The equations governing the heat and mass transfer are discretised. The vapour penetrates the pore step by step until reaching a pressure equilibrium between the liquid and the vapour phases (Figure I-49). There are two conditions leading to an invasion of a pore by the vapour. Firstly, it occurs if the pressure jump across a meniscus exceeds the maximum capillary pressure at this throat. Secondly, it occurs at any place in the capillary structure where the temperature of the liquid exceeds the vapour temperature by at least 4 K, because of nucleation.

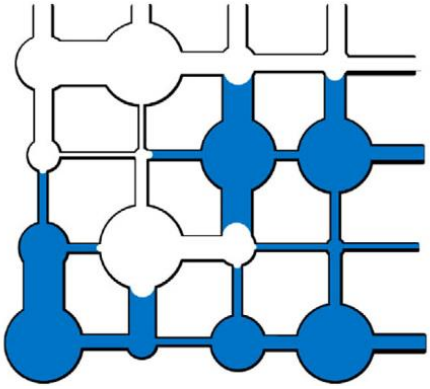

Figure I-49 : Schematic of discrete liquid-vapour interfaces in the pore network (Mottet *et al.* [29])

The major part of the investigation in 2D reports either a liquid phase (low heat loads) or a vapour phase (high heat loads) under the evaporator fin. However, Mottet *et al.* [29] has conducted the same work in three dimensions and found different results. The 3D simulation tends to prove that, at moderate heat fluxes, the pocket near the evaporator is not only made of vapour but composed by two phases (Figure I-50). This configuration leads to the best evaporator performance as the conductance between the fin and the groove is maximum. It tends to prove that, similarly to the results of Demidov and Yatsenko [138], the maximum heat flux is reached when the whole heated area is dried . Moreover, it is in good accordance with the results of Zhao and Liao [108] who showed that around the CHF, a two-phase zone is present under the fin.

As a conclusion, it is of interest to study the physical phenomena at a local scale in order to predict the occurrence of the limits. However, the previous models are not designed to understand the influence of the wick characteristics on the global LHP performance since the investigation is performed with an evaporator element decoupled from the rest of the LHP. In the present study, one of the objectives is to integrate an evaporator model inside a global LHP model.

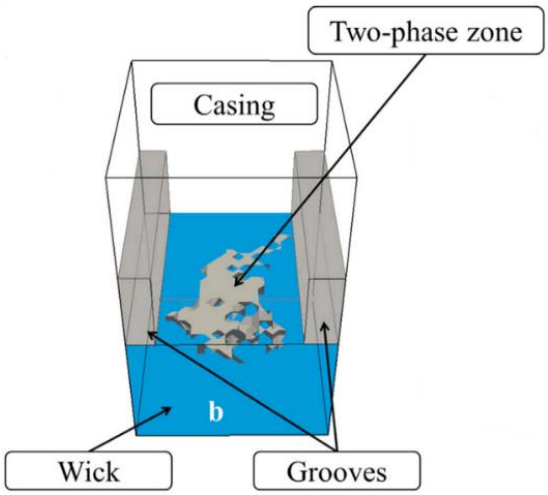

Figure I-50 : Development of a two-phase zone under the evaporator fins (Mottet *et al.* [29])

I.3.4 Model of evaporator coupled to the LHP

Only one model is presented in this section, the objective of this work being not to perfectly predict the performance of a LHP but to find the trends enabling the determination of a porous material leading to an improvement of the LHP performance. To this purpose, the extension of an existing model, such as the one developed by Siedel [4], is sufficient. However, for an in-depth investigation of the global LHP models, the reader can refer to the survey of the steady-state LHP models which was recently performed by Siedel [140].

Siedel [4] developed a nodal model which considers a monolayer and monoporous wick that enables to investigate the influence of the wick characteristics on the LHP performance. It also enables to study the heat flux distribution as well as the temperature field inside the wick. A schematic of the modelled LHP with the various nodes is shown in Figure I-51. The nodal network of the complete LHP is based on a combination of energy balance equations for each component of the LHP. $T_{r,i}$, $T_{c,o}$ and T_{ext} are the temperature at the reservoir inlet, condenser outlet and of the ambience, respectively. The heat flux transferred to the wick is called Q_w. The part of Q_w transferred to the fluid and enabling the evaporation is called Q_{ev}. The parasitic heat flux transferred to the reservoir through the wick is the subtraction of Q_{ev} to Q_w. The parasitic heat flux transferred to the reservoir through the evaporator body is called Q_b. The LHP is performant if Q_{ev} is high and the parasitic heat fluxes are low. Thus, a part of the condenser length should be used to subcool the returning liquid.

The various characteristics of the LHP with a flat-disk shaped evaporator and the test conditions of the model are described in Table I-13.

In order to precisely describe the heat and mass transfer inside the evaporator casing / porous wick assembly, two analytical models were developed by Siedel [4] and integrated to the nodal network. Based on Fourier series expansion, these analytical models describe the temperature fields in the wick and the evaporator casing. Figure I-52 shows the schematic of the 2D model domain of the wick. A small element is considered at the evaporator centre, constituted by half a groove and half a fin. The side walls of this zone are not affected by the boundary effects, so that adiabatic conditions can be considered, due to the symmetries. In this model, the boundary condition are T_r, T_e, and T_v at the top, bottom left and bottom right of the domain, respectively (Figure I-52).

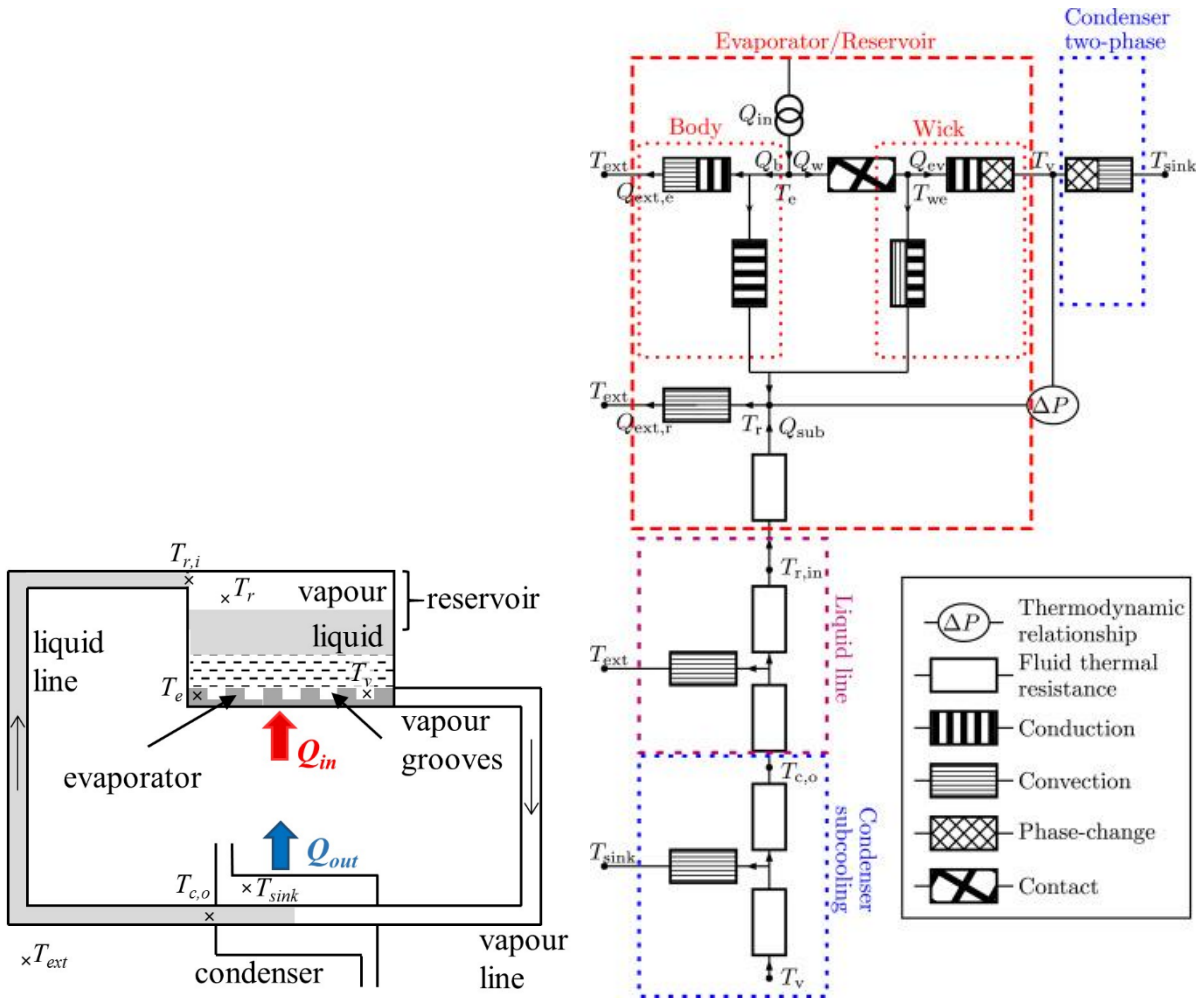

a) Schematic of the LHP b) Nodal network

Figure I-51: Schematic of the modelled LHP (a) and the nodal network (b): Siedel *et al.* [4], [141]

Table I-13: Characteristics of the LHP for the parametric study performed by Siedel [4]

Operating conditions			**Evaporator parameters**		
Heat load	Q_{in}	50 W	Wick thickness	e_w	3 mm
Heat sink temperature	T_{sink}	20 °C	Evaporator diameter	d_e	41 mm
Ambient temperature	T_{amb}	22 °C	Reservoir height	H_r	10 mm
	Fluid	Water	Evaporator body thickness	e_b	3 mm
	Position	Horizontal	Evaporator body thermal conductivity	$\lambda_{mat,b}$	26 W/m.K
Transport line parameters			Contact resistance	$R_{cont,e}$	1×10^{-4} K.m²/W
Transport lines length	L_{V+L}	200 mm	Groove width	l_{gr}	1 mm
Condenser length	L_c	100 mm	**Other parameters**		
Transport lines thermal conductivities	λ_V λ_L	1 W/m.K	Heat sink heat transfer	h_{sink}	2000 W/m².K
Transport lines inner and outer diameter	$d_{L,i}$/ $d_{L,o}$ $d_{V,i}$ / $d_{V,o}$	2 / 2.4 mm	Accommodation coefficient	a_{ev}	0.1

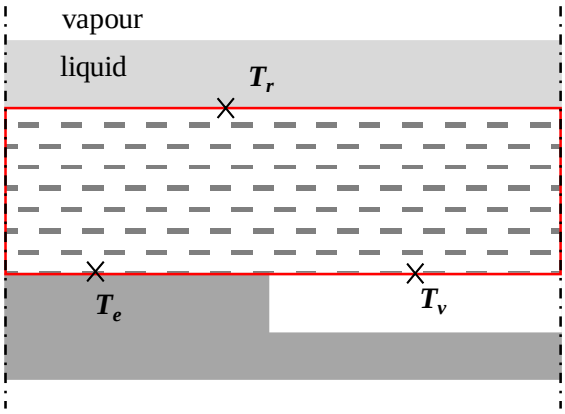

Figure I-52: Schematic of the 2D analytical model domain (Siedel [4])

A parametric study has been performed on several parameters. Only the effect of the effective thermal conductivity of the wick is reported here. Figure I-53 shows the influence of λ_{eff} on the evaporator temperature for various heat loads. The performance of the LHP is maximum if T_e is minimum. At 50 W, T_e is minimum if λ_{eff} is of 3 W/m.K.

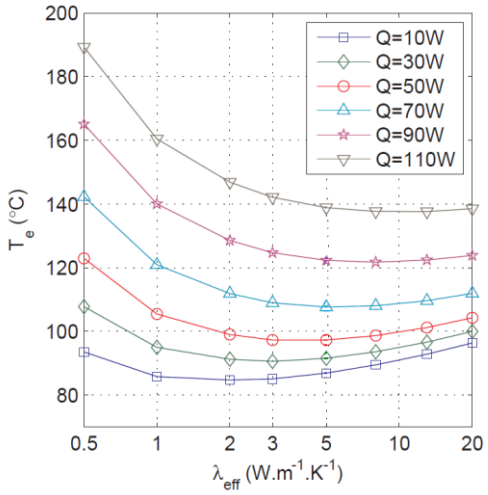

Figure I-53 : Influence of λ_{eff} on T_e (adapted from Siedel [4])

Figure I-54 presents the heat flux distribution at 50 W. It shows that the heat flux Q_{ev} enabling the evaporation of the fluid reaches a maximum when λ_{eff} is around 3 W/m.K. This optimum can be explained by the fact that a wick having a high thermal conductivity increases the parasitic heat flux through the wick (as shown in Figure I-54 by the continuous increase of the term (Q_w - Q_{ev}) at the detriment of Q_{ev}. However, a wick having a low thermal conductivity decreases both Q_w and the heat flux transferred to the liquid-vapour interfaces. This result is consistent with the study of the evaporator temperature at the same heat load. Even if the minimum T_e depends on the heat loads, it always exists an optimum λ_{eff}.

These results show that an optimisation of the LHP performance is possible by an adequate design of the wick. The wick layer in contact with the vapour grooves should have a high thermal conductivity to easily transfer the heat flux to the interface, whereas the layer in contact with the reservoir should have a low thermal conductivity to limit the parasitic heat flux. The bi-layer wick, studied by Wu *et al.* [119] and Xu *et al.* [128] among others, seems to be a suitable design able to increase the system performance. That is why, the objective of this PhD work is focused on the manufacturing, characterisation and testing of such a wick design with two layers.

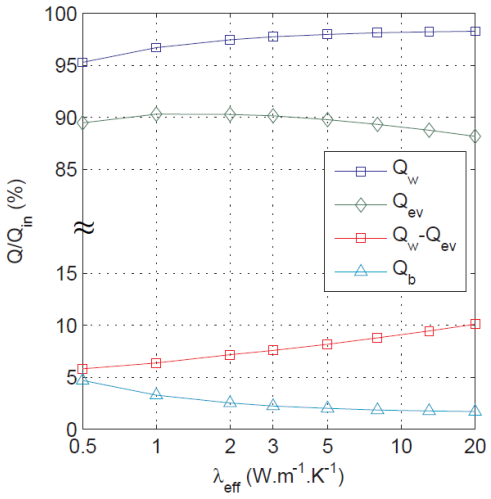

Figure I-54: Influence of λ_{eff} on the heat flux distribution if Q_{in} = 50 W (Siedel [4])

In conclusion, the several models previously described have two interests: firstly, understanding and predicting the limit of a capillary structure dedicated to LHPs, and secondly, improving the porous structure to push back the occurrence of the operating limits.

I.4 Conclusion

The capillary structure inserted in a LHP has to fulfil various functions. It builds up a hydraulic barrier between the liquid flowing from the reservoir and the vapour escaping to the vapour line. It also builds up a thermal barrier, in order to reduce the heat leaks which tend to increase the operating temperature. The selection of the wick parameters - pore radius, porosity, permeability, thermal conductivity … - has therefore a great importance, since they directly affect these functions.

The capillary structure performance are usually described by the evolution of the heat transfer coefficient as a function of the heat flux. This curve exhibits a maximum, beyond which the heat transfer mechanisms inside the wick are modified. Some authors describe the appearance of a two-phase zone under the heated fins, followed by a dry-out if the heat flux further increases. This phenomenon is associated to the capillary limit.

Most of the wicks presently manufactured are made of mono porous sintered metallic powder. However, some studies have shown the interest of ceramic as a wick material. Bi porous or bi dispersed structures have been manufactured and have proven their ability to retard the development of a dry-out zone, but they suffer from brittleness. It seems that bi-layers wicks could solve this issue.

Some LHP evaporator models identified in the literature assume a saturated wick whereas others assume a vapour zone inside the capillary structure. The objectives of these models are to understand the thermo-hydraulic phenomena governing the evaporator behaviour and to better understand the development of dry-out zones. Moreover, the models help to improve the properties of the porous structure. The probable interest of a two-layer capillary structure, including a material with a high thermal conductivity to transfer the heat to the liquid-vapour interface, and a material with a low thermal conductivity to limit the parasitic heat fluxes, is confirmed. Thereby, a predictive model of a bilayer wick will be developed in Chapter II.

Chapter II Theoretical study of a bi-layer wick performance

This chapter aims at theoretically investigating the thermal performance of a LHP, as a function of the capillary wick parameters. Simulations performed by Siedel [4] on a monolithic wick showed that a wick with two different layers could improve the thermal performance by decreasing the heat leaks and improving the heat transfer from the evaporator to the fluid.

Thus, in a first step, the analytical model developed by Siedel is extended to predict the operation of a LHP equipped with such a wick. In a second step, an extensive parametric study is performed to determine the wick characteristics leading to the most efficient LHP operation. They will be considered as the specifications for the manufacturing processes presented in Chapter III.

II.1 Development of the LHP model

The model enabling the numerical study of the heat and mass transfer in a wick designed for LHP is presented in this section. The modification of the Siedel's model [4] is explained to integrate two porous layers having different thermo-hydrodynamic properties. Then, the solving procedure leading to a thermal and hydrodynamic steady state solution is detailed. Finally, the LHP taken as a reference and the results in standard conditions are presented, and the method enabling to check the validity of the solution is described.

II.1.1 Equations of the model

The present model is briefly described, by focusing on the specificities brought by the addition of a supplementary layer in the wick. Figure II-1 shows a schematic of the complete LHP equipped with a bi-layer wick. The top layer has a low thermal conductivity in order to keep the parasitic heat flux at a low level, whereas the bottom layer has a high thermal conductivity in order to transfer the heat to the evaporating interface.

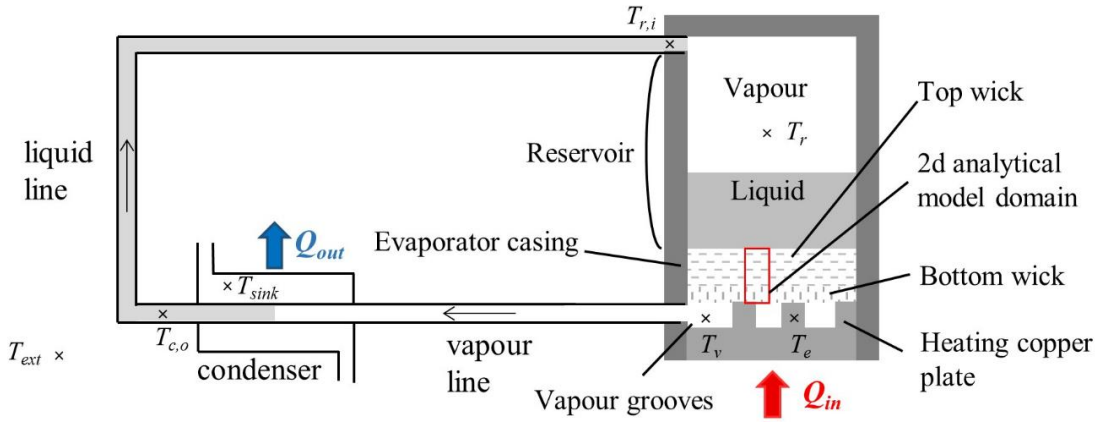

Figure II-1: Schematic of the complete LHP

Figure II-2 shows the schematic of the 2D model domain of the wick in the Siedel's model and in the present one. The same small element is considered at the evaporator centre and the same adiabatic conditions are assumed at the side walls of this zone. In the present model, the boundary condition on the upper side of the bottom layer becomes the contact temperature between the two layers T_{cont} (Figure II-2 b) instead of the reservoir temperature T_r in Siedel's model (Figure II-2 a). It is assumed to be an isothermal boundary condition. This assumption will be discussed in Section II.1.5. The boundary conditions at the bottom of the domain remains the same. The heat transfer in the top layer is modelled by a thermal resistance $R_{w,top}$ considering that the heat transfer is due to both 1D conduction and convection phenomena (Eq.(I-29)).

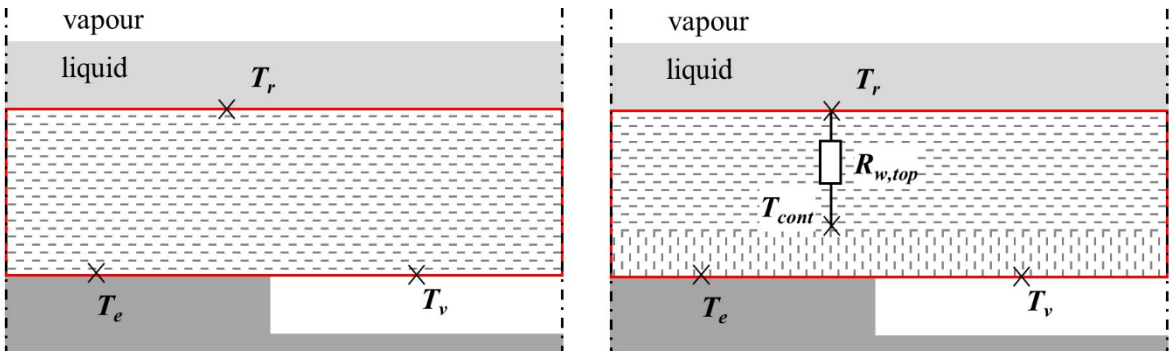

a) Siedel's model [4] b) Present model

Figure II-2: Schematic of the 2D analytical model domain

The equations of the nodal network are presented in Table II-1. It is similar to the one presented in Figure I-51except that there is one more node inside the porous structure. A single column in Table II-1 means that the same equation is used in both models. Otherwise, in the left part of this table, one can find the equations of the Siedel's model and in the right part, the present model equations are detailed. It can be seen that the major part of the equations remains the same in both models. The k_n coefficients, in equations (II-10) to (II-15), are detailed in the Appendix B. They result from the resolution of the two analytical models of heat and mass transfer inside the wick and inside the evaporator casing. The fourteen unknowns included in these fourteen equations are described in Table II-2. They are the output data of this model. The input data are mainly the heat load Q_{in}, the heat sink temperature T_{sink}, the ambient temperature T_{amb}, the fluid thermophysical properties, and the LHP characteristics (the reservoir surface S_r, the external and internal condenser diameters $d_{c,o}$ and $d_{c,i}$).

Table II-1 : Nodal network equations of Siedel [4] and the present model

Siedel's model [4]	Present model	
$Q_b + Q_w = Q_{in}$		(II-1)
$Q_w = \frac{S_w}{R_{cont,e}}(T_e - T_{we})$		(II-2)
$Q_{sub} + Q_{ext,e} + Q_{ext,r} + Q_{sen} + Q_{ev} = Q_{in}$		(II-3)
$Q_{sen} = \dot{m}_l c_{pl}(T_v - T_r)$		(II-4)
$Q_{sub} = \dot{m}_l c_{pl}(T_r - T_{r,i})$		(II-5)
$Q_{ext,r} = h_{ext} S_r (T_r - T_{ext})$		(II-6)
$T_v - T_r = \frac{T_v(1/\rho_v - 1/\rho_l)}{h_{lv}}(\Delta P_v + \Delta P_l - (\rho_l - \rho_v) g \Delta H_{c-e} + P_{NCG})$		(II-7)
$T_{c,o} = T_{sink} + (T_v - T_{sink}) exp\left(\frac{-\pi(L_c - L_{2\varphi})}{\dot{m}_l c_{p,l}\left(\frac{1}{(d_{c,i} h_L)} + \frac{1}{(h_{sink} d_{c,o})} + \frac{\ln\left(\frac{d_{c,o}}{d_{c,i}}\right)}{2\lambda_L} \right)} \right)$		(II-8)
$T_{r,i} = T_{ext} + (T_{c,o} - T_{ext}) exp\left(\frac{-\pi d_{L,i} L_L}{\dot{m}_l c_{p,l}\left(1/h_L + d_{L,i}/(h_{ext} d_{L,o}) + \frac{\ln\left(\frac{d_{c,o}}{d_{c,i}}\right)}{2\lambda_L} \right)} \right)$		(II-9)

$Q_w = k_1 T_r + k_2 T_v + k_3 T_{we}$ (II-10)	$Q_w = k_1 T_{cont} + k_2 T_v + k_3 T_{we}$ (II-11)
$Q_{ev} = k_4 T_r + k_5 T_v + k_6 T_{we}$ (II-12)	$Q_{ev} = k_4 T_{cont} + k_5 T_v + k_6 T_{we}$ (II-13)
$Q_b = k_7 T_r + k_8 T_e + k_9$ (II-14)	
$Q_{ext,e} = k_{10} T_r + k_{11} T_e + k_{12}$ (II-15)	
No top layer	$Q_{ev} - Q_w = \frac{T_{cont} - T_r}{R_{w,top}}$ (II-16)

Table II-2: Output data of the model

Heat fluxes		Temperatures	
Q_{ev}	heat flux transferred by latent heat to the fluid	T_v	vapour temperature
Q_{sen}	sensible heat transferred to the fluid	T_r	reservoir temperature
$Q_{ext,r}$	heat losses of the reservoir to the ambiance	$T_{r,i}$	fluid temperature at the end of the liquid line
$Q_{ext,e}$	heat losses of the evaporator body to the ambiance	$T_{c,o}$	fluid temperature at the end of the condenser
Q_{sub}	heat flux necessary to subcool the returning liquid	T_{we}	temperature at the contact of the wick and the evaporator
Q_w	heat flux transferred to the wick	T_e	evaporator temperature
Q_b	heat flux transferred to the evaporator body	T_{cont}	temperature at the interface between the two layers of the wick

II.1.2 Solving procedure

The solving procedure is presented in Figure II-3. Iterations have to be performed on the vapour temperature since the fluid properties and the heat transfer coefficient between the transport lines and the liquid h_L or the condensing vapour h_c depend on this temperature. The mass flow rate is also initialised assuming that 80 % of Q_{in} is transferred to the fluid by evaporation. These parameters being initialised, the condensation heat transfer coefficient h_c, the thermophysical properties and the pressure drops of the fluid in the various LHP elements can be determined, then the two-phase length in the condenser and the k_n coefficients. Then, the model is run and the vapour temperature T_v^{n+1}, calculated at the $(n+1)$ iteration, is compared to the previous value T_v^n. If the convergence criterion is satisfied, the procedure stops. Otherwise, T_v^{n+1} and Q_{ev} are used to calculate the thermophysical properties and the mass flow rate at $(n+1)$ and the procedure starts again.

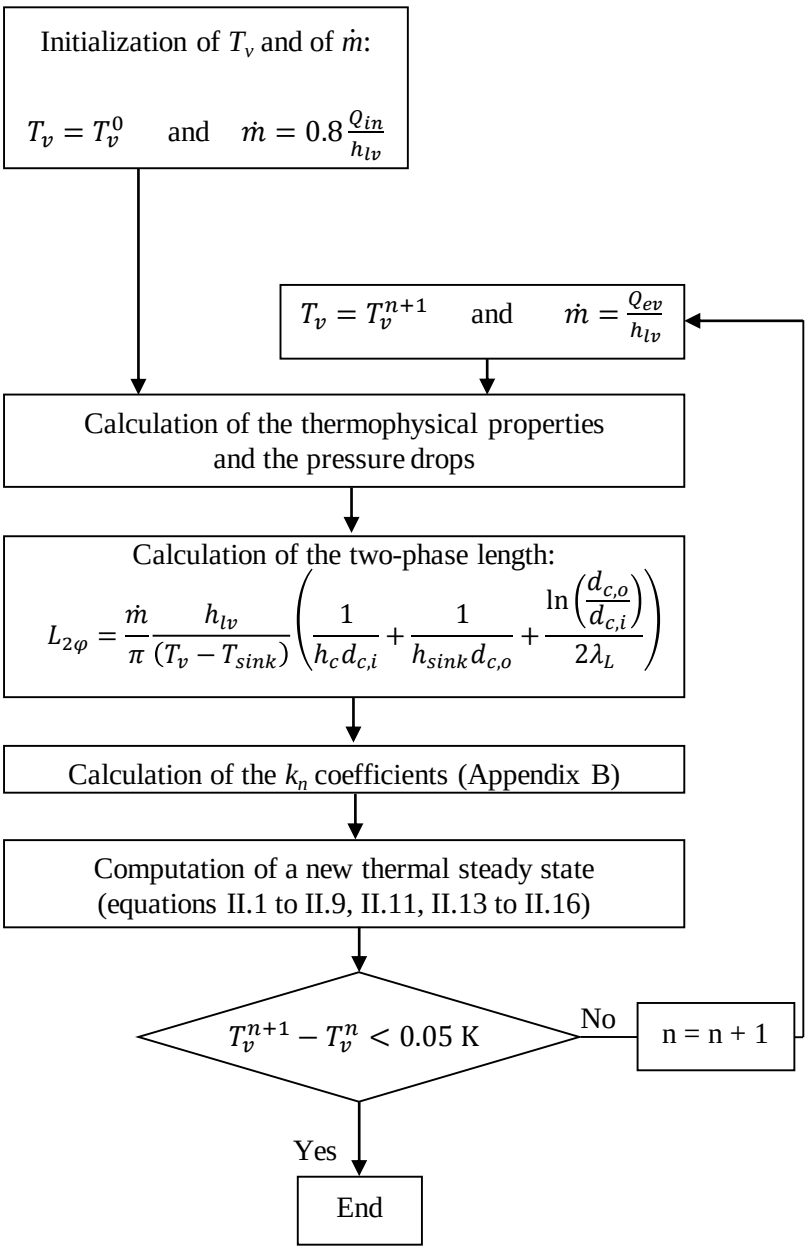

Figure II-3 : Solving procedure of the model

II.1.3 Description of the reference LHP

The parametric study is conducted with a standard LHP having a flat-disk shaped evaporator equipped with a bilayer wick as shown in Figure II-1. The main geometrical parameters correspond to the experimental LHP of Siedel [4] described in Table II-3, where $r_{p,top}$ and $r_{p,bot}$ are the top radius of the top and the bottom layer, ε_{top} and ε_{bot} are the porosity of the top and the bottom layer, $e_{w,top}$ and $e_{w,bot}$ are the thickness of the top and the bottom layer, $\lambda_{mat,top}$ and $\lambda_{mat,bot}$ are the thermal conductivity of the top and bottom layer material, K_{top} and K_{bot} are the permeability of the top and bottom layer and l_{fin} is the fin width. Water is used as working fluid. A 12 mm thick bilayer wick is considered. The values of the wick parameters are examples found in the literature for a copper bottom layer (Deng *et al.* [105], Becker *et al.* [142], Albertin *et al.* [52]) and a ceramic top layer (Xu *et al.* [57]).

Table II-3 : Definition of the standard LHP for the parametric study

Operating conditions		**Wick parameters (top layer)**		**Evaporator / reservoir parameters**	
Q_{in}	30 W	$r_{p,\,top}$	15 µm	a_{ev}	0.6
T_{sink}	15°C	ε_{top}	0.45	P_{NCG}	0 Pa
T_{amb}	25°C	$e_{w,top}$	10 mm	d_e	40 mm
Fluid	Water	$\lambda_{mat,top}$	1 W/m.K	H_r	20 mm
Position	Horizontal	K_{top}	1.8×10^{-12} m²	e_b	3 mm
h_{sink}	600 W/m².K	**Wick parameters (bottom layer)**		λ_b	0.25 W/m.K
Transport line parameters				$R_{cont,e}$	3×10^{-4} Km²/W
L_V	685 mm	$r_{p,\,bot}$	5 µm	l_{gr}	2 mm
L_c	250 mm	ε_{bot}	0.45	l_{fin}	2 mm
L_L	245 mm	$e_{w,bot}$	2 mm		
λ_{wall}	1 W/m.K	$\lambda_{mat,bot}$	400 W/m.K		
$d_{i,L}$ / $d_{o,L}$ $d_{i,V}$ / $d_{o,V}$	2 / 6 mm	K_{bot}	2.0×10^{-13} m²		

In each simulation presented in the Section II.2, only one parameter varies, the others being fixed at the reference value. For example, if the influence of the top layer thickness is studied, all the other parameters have the value of Table II-3 and the top layer thickness varies in the investigated range.

II.1.4 Results in standard conditions

The model is run in the standard conditions described in Table II-3. Figure II-4 (a) shows the evolution of the evaporator temperature and the reservoir temperature as a function of the heat load. It shows that the two operating modes also exist with a bi-layer wick. The LHP operates at the variable conductance mode up to 30 W and at fixed conductance mode for higher heat loads (See Section I.1.3.2). The evaporator temperature is about 80 °C at 60 W leading to a global thermal resistance of about 1 K/W which is relatively low considering that it takes into account the contact resistance between the wick and the evaporator as well as the thermal resistance at the condenser. Figure II-4 (b) shows the heat flux distribution as a function of the heat load. The part Q_w of the heat load Q_{in} reaching the wick is about 90 % whatever the heat load. Moreover, the major part of this heat flux is used to evaporate the fluid. Indeed, Q_{ev} is slightly lower than Q_w. In the present example, the heat leaks through the wick are relatively low compared to the results of Siedel [4] presented in the Section I.3.

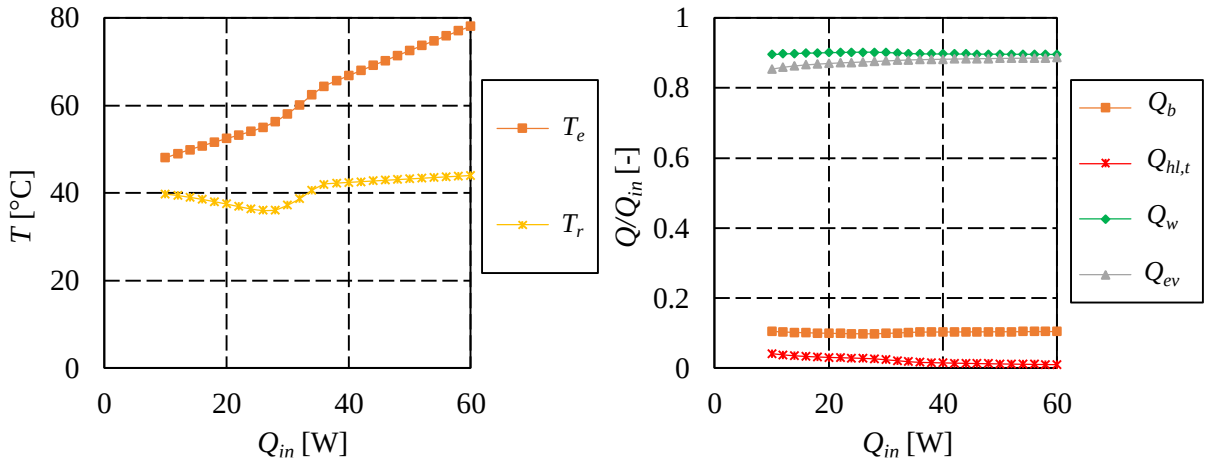

a) Evaporator wall and reservoir temperatures b) Heat fluxes distribution in the evaporator

Figure II-4: Results of the analytical model in standard conditions (Table II-3)

II.1.5 Validity of the isothermal condition at the interface of the wick layers

In Section II.1.1, an isothermal boundary condition at the interface between the two layers is assumed. The present section aims at checking the validity of this assumption, by performing several simulations of the heat transfer inside the bi-layer wick with two different models and various parameters. Once the solution of the analytical model described in the Section II.1.1 is obtained, a numerical model is run to compare both solutions.

The numerical model determines the temperature field inside the wick. At first approximation, the heat transfer by convection is neglected in order to simplify the equations, since the mass flow rate in the investigated heat load range is relatively low. Moreover, the effective thermal conductivity of both layers enables this assumption (Figure I-42). The numerical model uses the same 2D domain (Figure II-5 a) than the analytical model, with the same symmetries and thus, the same adiabatic conditions. The boundary conditions at the top and the bottom of the domain (T_r, T_{we} and T_v) are calculated with the analytical model and are an input data of the numerical model. It is important to note that the numerical model of the heat transfer inside the porous wick cannot replace the analytical model in the nodal network because it needs the solution of the analytical model to be run.

The numerical model uses the finite volume method to compute the temperature field inside the porous medium. Figure II-5 (a) shows the discretization of the domain where *i* and *j* detect the control volume along the *x* and *y* axis of the domain respectively. A temperature $T_{i,j}$ and a thermal conductivity $\lambda_{i,j}$ are affected to each control volume. The domain of simulation has a width equal to $l_{gr}/2 + l_{fin}/2$ and a height equal to $e_{w,top} + e_{w,bot}$. It is divided in $M \times N$ control volumes leading to:

$$\Delta x = \frac{l_{gr} + l_{fin}}{2N} \tag{II-17}$$

$$\Delta y = \frac{e_{w,top} + e_{w,bot}}{2M} \tag{II-18}$$

where Δx and Δy are the dimensions of a control volume. The contact between the two layers is assumed to be without any thermal resistance. Each control volume i,j of the network receives four heat fluxes Q from the neighbouring control volumes (Figure II-5 b):

$$Q_{x-,i,j} = (T_{i,j-1} - T_{i,j})\left(\frac{1}{\frac{\Delta x}{2\Delta y \lambda_{i,j-1}} + \frac{\Delta x}{2\Delta y \lambda_{i,j}}}\right) \tag{II-19}$$

$$Q_{x+,i,j} = (T_{i,j+1} - T_{i,j})\left(\frac{1}{\frac{\Delta x}{2\Delta y \lambda_{i,j+1}} + \frac{\Delta x}{2\Delta y \lambda_{i,j}}}\right) \tag{II-20}$$

$$Q_{y+,i,j} = (T_{i-1,j} - T_{i,j})\left(\frac{1}{\frac{\Delta y}{2\Delta x \lambda_{i-1,j}} + \frac{\Delta y}{2\Delta x \lambda_{i,j}}}\right) \tag{II-21}$$

$$Q_{y-,i,j} = (T_{i+1,j} - T_{i,j})\left(\frac{1}{\frac{\Delta y}{2\Delta x \lambda_{i+1,j}} + \frac{\Delta y}{2\Delta x \lambda_{i,j}}}\right) \tag{II-22}$$

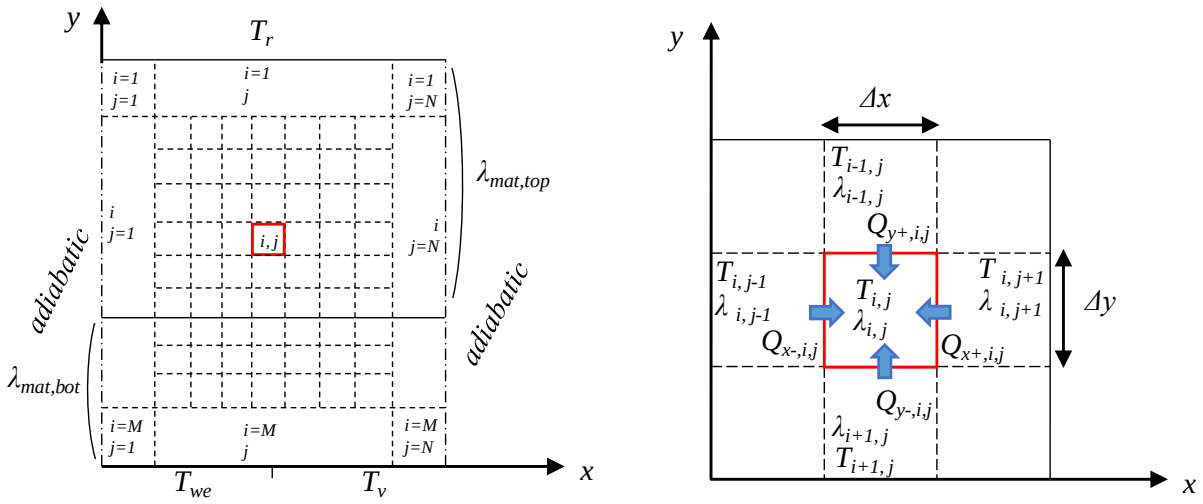

a) Domain of simulation b) Control volume

Figure II-5: Schematic of the discretization

The heat flux balance in the control volume leads to:

$$Q_{x-,i,j} + Q_{x+,i,j} + Q_{y+,i,j} + Q_{y-,i,j} = 0 \quad \text{(II-23)}$$

This equation is true while the control volume is not at an extremity of the domain of simulation. In this case, one or two heat fluxes are modified by an adiabatic condition (Q = 0) or by a Dirichlet condition (modification of the neighbour temperature). This equation is developed for each control volume in a square matrix [A] having a side size M×N:

$$[A] \times [T] = [B] \quad \text{(II-24)}$$

where [T] is the matrix of the control volume temperatures and [B] is the matrix of the boundary conditions. The system is solved with a MATLAB code as follows:

$$[T] = [B] \setminus [A] \quad \text{(II-25)}$$

Figure II-6 shows the temperature fields obtained at 30 W with both models, in the reference case. A relatively good accordance can be observed between the two temperature fields and the contact between the two layers matches to an isothermal line, meaning that the assumption of an isothermal boundary condition at the interface between the two layers is correct.

However, it exists some sets of wick parameters for which the temperature fields determined with the numerical model and with the analytical model differ to each other. For example, the temperature field shown in Figure II-7 is obtained at 30 W, with a thinner bottom layer having a lower thermal conductivity than the bottom layer of the wick used to obtain the temperature field shown in Figure II-6. Using the numerical model, the isotherm lines cross the interface between the two layers, meaning that the assumption of an isothermal boundary condition at the interface between the two layers is not valid. In this case, the analytical solution cannot be trusted.

Many simulations were performed, and have shown that, if the bottom layer has a high thermal conductivity, the isotherm distortion only occurs in a very thin layer, at the vicinity of the heated wall. Considering that, in the following part of this work, the bottom layer will have a high thermal conductivity, in order to transfer the heat in the x direction to the evaporating interface, the assumption of a 1D heat transfer in the y direction through the top layer is validated.

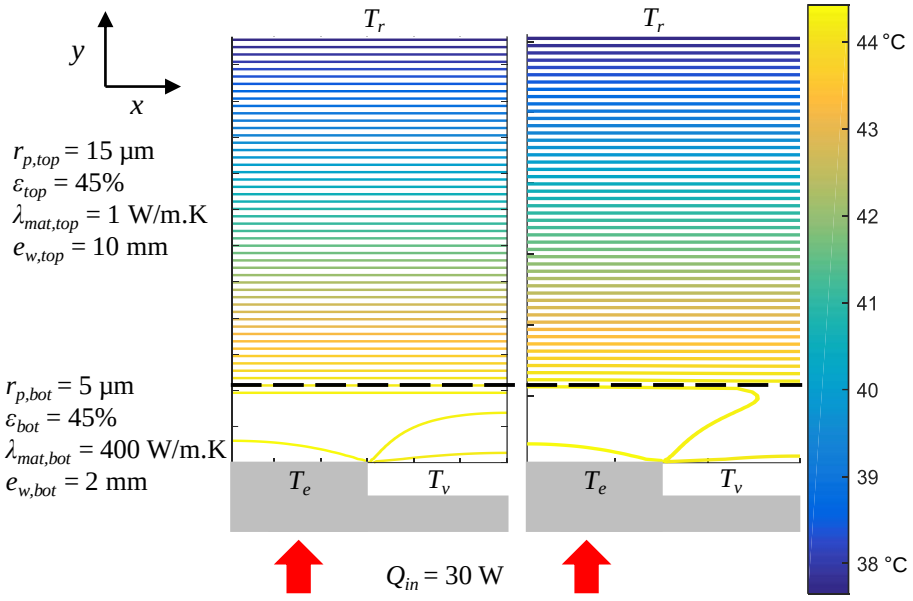

a) Analytical solution b) Numerical simulation

Figure II-6: Example of temperature field inside the wick in a case of a valid isothermal boundary condition

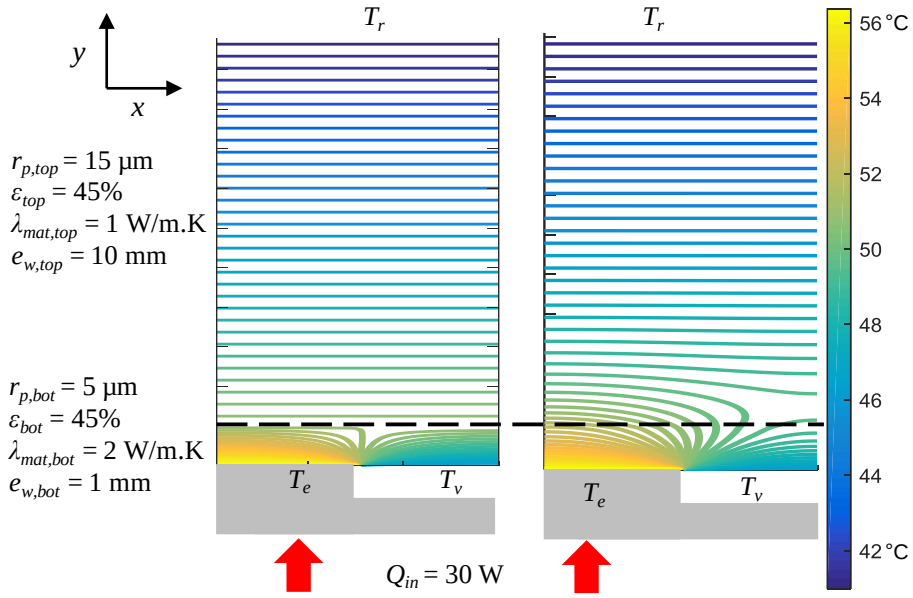

a) Analytical solution b) Numerical simulation

Figure II-7: Example of temperature field inside the wick in the case of a non-valid isothermal boundary condition

II.2 Parametric study

This section presents the results of the parametric study performed with the model previously described. Its main objective is to facilitate the choice of the manufacturing parameters by targeting the wick characteristics leading to the best thermal and hydrodynamic performance.

In a first part the methods to characterise the LHP performance are described. Then, the influence of the thickness, the material thermal conductivity, the porosity, the permeability and the pore radius of each layer on them is described as well as the influence of the working fluid.

II.2.1 Characterisation of the performance of a LHP with a bilayer wick

In this section, the choice has been made to investigate the global thermal resistance R_{LHP}, the boiling limit and the capillary limit. The methodology is the same as described in Section I.1.3, the double layer only induces specificities concerning the boiling limit that will be detailed hereafter.

The global thermal resistance, determined with equation (I-7), is a very usual parameter, since it can be easily compared to experimental data, or to values available in the literature.

In order to study the occurrence of the capillary limit, the input heat load is increased step by step in the model until the condition expressed by Eq. (I-3) is not respected anymore.

In a LHP, the working fluid is at saturation inside the reservoir and at the surface of the wick in contact with the vapour grooves. If the fluid superheat inside the capillary structure overcomes a value determined with Eq.(I-13), boiling may occur. This phenomenon must be avoided because it prevents the LHP to properly operate as the bubbles may block the liquid return paths, leading to a dry out (Chuang [26]). Thus, it is of interest to study the conditions that lead to the risk of boiling. It is assumed that it boiling cannot occur as long as the liquid is subcooled inside the wick structure. Indeed, the nucleation does not start if the superheat is too small, but determining this value require the knowledge of the nucleation radius (Eq.(I-13)).

According to Stephan [143], in the case of a spherical bubble having a radius r_m, the vapour and liquid phase saturation pressures ($P_{sat,v}$ and $P_{sat,l}$) differ from the saturation pressure of a plane interface P_{sat}:

$$P_{sat,v}(T_{sat}, r_m) = P_{sat}(T) - \frac{\rho_v}{\rho_l - \rho_v}\frac{2\sigma}{r_m} \tag{II-26}$$

$$P_{sat,l}(T_{sat}, r_m) = P_{sat}(T) - \frac{\rho_l}{\rho_l - \rho_v}\frac{2\sigma}{r_m} \tag{II-27}$$

It is assumed that ρ_v is negligible compared to ρ_l. Furthermore, the calculation is performed for bubbles of the largest possible size, since the superheat required to generate a bubble decreases with its size. Since in a porous medium, the bubble radius cannot exceed the pore radius ($r_m = r_p$), the previous equations become:

$$P_{sat,v}\left(T_{sat}, r_p\right) \approx P_{sat}(T) \tag{II-28}$$

$$P_{sat,l}\left(T_{sat}, r_p\right) \approx P_{sat}(T) - \frac{2\sigma}{r_p} \tag{II-29}$$

Figure II-8 illustrates the evolution of the pressure of the liquid P_l along the fluid flow in a bilayer wick as well as the saturation pressure of the vapour and liquid corresponding to the temperature of the liquid inside the wick ($T_{l,xw}$) at 50 W and with a top pore radius equal to 25 µm. The rest of the parameters used to obtain Figure II-8 are detailed in Table II-3. $r_{p,top}$ is large to keep the permeability at a high level whereas $r_{p,bot}$ is small to increase the capillary pumping. As the liquid gets closer to the evaporator wall, its temperature increases. It leads to an increase of $P_{sat,v}$ and $P_{sat,l}$. The sudden drop of $P_{sat,l}$ at the interface between the two layers is due to the change of pore radius. At last, P_l decreases along the wick because of the pressure drops. This decrease is very small and not noticeable on the curve as the permeability of both layers is high. At any time, the pressure of the liquid must be higher than the saturation pressure of the liquid in order to avoid the boiling risk. Boiling is expected to occur in the top layer, close to the contact between the two layers, where the difference of pressure between the liquid and its saturation

temperature is minimum (circle in Figure II-8). Indeed, the pore radius is large since it is the top layer. Moreover, the temperature is high since it is close to the evaporator wall. It leads to a relatively high saturation pressure. At last, the pressure of the liquid is low because it has flowed through a large part of the wick.

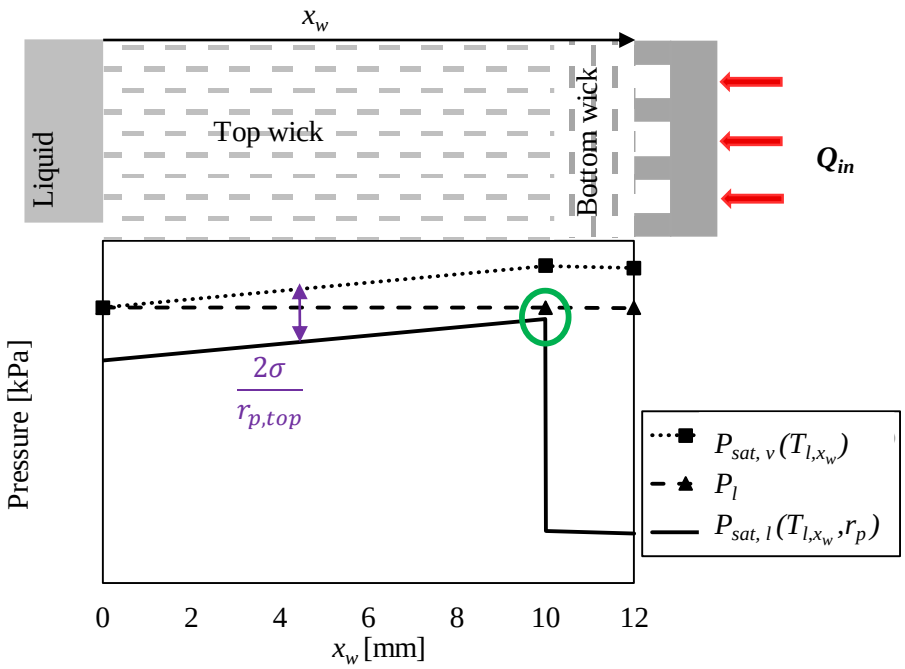

Figure II-8: Evolution of the pressures inside the porous medium (Q_{in} = 50 W, $r_{p,top}$ = 25 µm)

An example of situation for which boiling is likely to occur is shown in Figure II-9. As compared to the previous simulation, the heat flux has been increased to 100 W. Inside the highlighted zone, the pressure of the liquid is lower than the saturation pressure and boiling could start. It can be noted that if the pressure drops through the top layer increase, the boiling risk is reached at a lower heat load.

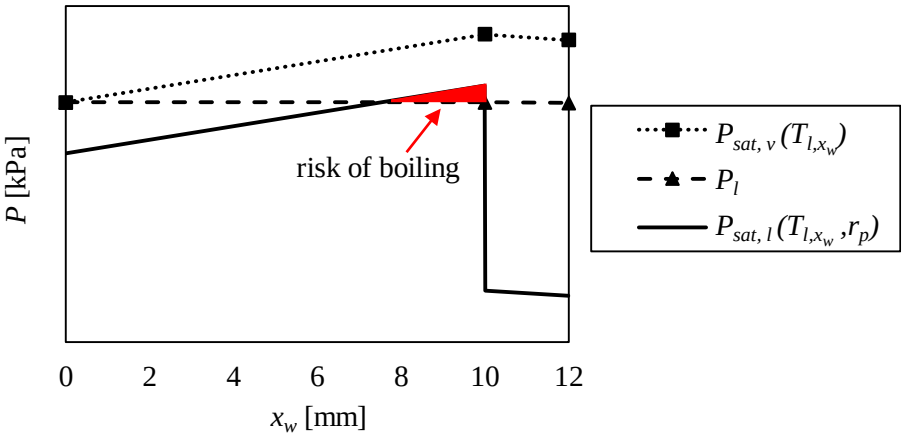

Figure II-9 : Evolution of the pressures inside the porous medium (Q_{in} = 100 W, $r_{p,top}$ = 25 µm)

The method to determine the boiling limit is similar to the one determining the capillary limit, previously described. The input heat load is increased in the model while the following condition expressed remains false:

$$P_{cont,l} > P_{sat,v}(T)\big|_{cont} - \frac{2\sigma}{r_{p,top}} \qquad \text{(II-30)}$$

where $P_{cont,l}$ is the liquid pressure at the contact between the two layers. The lowest heat load leading to a boiling risk is called the boiling limit.

In the following parts, the influence of each investigated parameter on the thermal performance and the occurrence of the operating limits is described.

II.2.2 Influence of the thickness and thermal conductivity

In this section, the results are presented as a function of the bulk material thermal conductivity. In the model, the correlation of Alexander [129] is used to obtain the effective thermal conductivity of the porous structure. This correlation has been taken among many other correlations (Appendix A) and the results presented hereafter could slightly differ with another correlation, but the trends would remain the same.

$$\lambda_{eff} = \lambda_l \left(\frac{\lambda_{mat}}{\lambda_l}\right)^{(1-\varepsilon)^{0,59}} \tag{II-31}$$

II.2.2.1 Influence of the top layer properties

Figure II-10 shows the prediction of the global thermal resistance as a function of the top layer thickness for four different thermal conductivities. For a constant bottom layer thickness, an increase of the thickness of the top layer decreases R_{LHP}. However, this decrease is more significant for small thicknesses. Figure II-10 also shows that the top layer material has an influence. An increasing thermal conductivity increases R_{LHP}. This phenomenon is particularly true if the thermal conductivity is higher than 1 W/m.K. These results are explained by a decrease of the heat leaks if $e_{w,top}$ increases or if $\lambda_{mat,top}$ decreases. It leads to an increase of the evaporation heat flux Q_{ev}. As Q_{ev} increases, the evaporator temperature decreases, decreasing the thermal resistance.

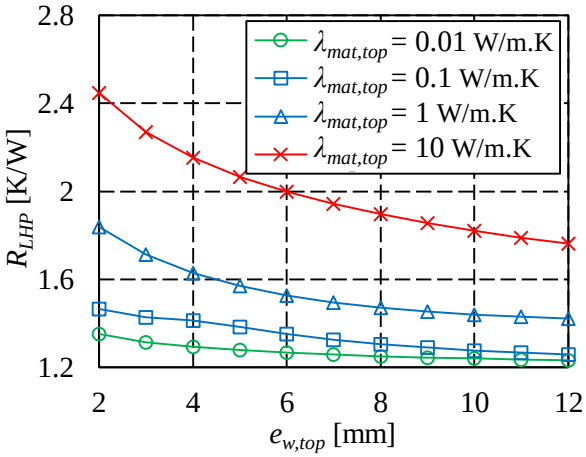

Figure II-10 : Influence of top layer thickness and thermal conductivity on the global thermal resistance

Figure II-11 (a) shows the influence of $e_{w,top}$ on the operating limits. An increasing $e_{w,top}$ decreases both the capillary and the boiling limits meaning that a thin layer can operate at a higher maximum heat flux than a thick layer. Indeed, a thick wick increases the pressure drops, decreasing both the capillary limit (Eq.(I-3)) and the boiling limit (Eq.(II-30)). Figure II-11 (b) also shows the influence of $\lambda_{mat,top}$ on the operating limits. An increasing $\lambda_{mat,top}$ increases both the capillary and the boiling limits. It can be explained by a change of the fluid properties. Indeed, an increasing $\lambda_{mat,top}$ increases the LHP thermal resistance and thus, the vapour temperature, leading to a lower fluid viscosity. The resulting lower pressure drops increase the operating limits.

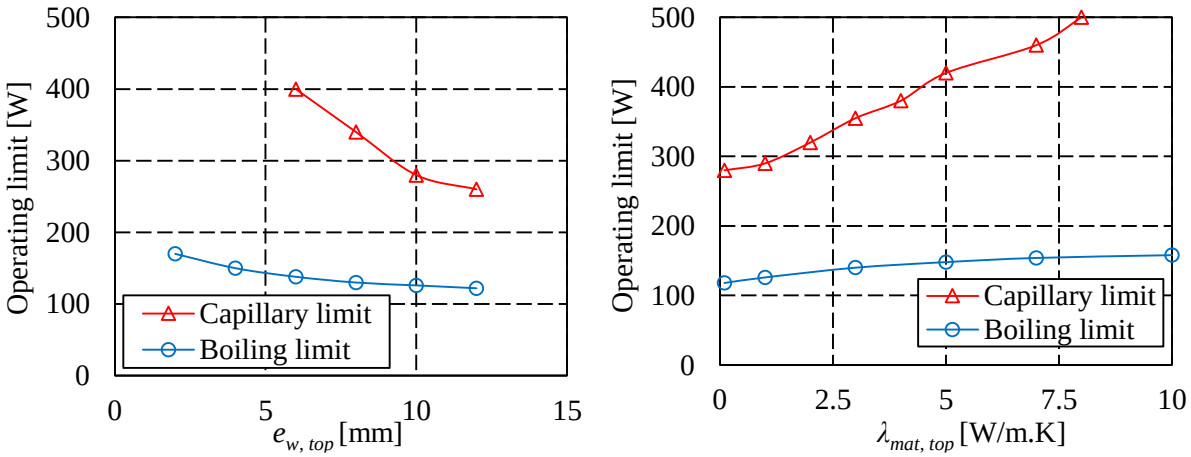

a) Thickness b) Thermal conductivity

Figure II-11: Influence of the top layer thickness and thermal conductivity on the operating limits

These results mean that a trade-off must be found both on the thickness and the thermal conductivity of the top layer. In the perspective of a future wick manufacturing, the targeted range for $e_{w,top}$ lies between 5 and 10 mm and the targeted range for $\lambda_{mat,top}$ lies between 0.5 and 2 W/m².K. These ranges provide a thermal resistance lower than 1.6 K/W without decreasing too much the operating limits.

II.2.2.2 Influence of the bottom layer properties

Figure II-12 shows the influence of the bottom layer thermal conductivity $\lambda_{mat,bot}$ and thickness $e_{w,bot}$ on the global thermal resistance R_{LHP}. It is clear that, for a fixed top layer thickness, the bottom layer thickness has almost no influence on the global thermal resistance. Indeed, the major part of the heat flux is transferred close to the evaporator fin whereas only a minor part reaches the meniscus at the centre of the vapour groove (Figure II-13). This result would be different if the accommodation coefficient, defined in Section I.3.2, would be very low. The heat flux would need a larger surface to be evacuated and thus, it would be spreaded up to the centre of the grooves.

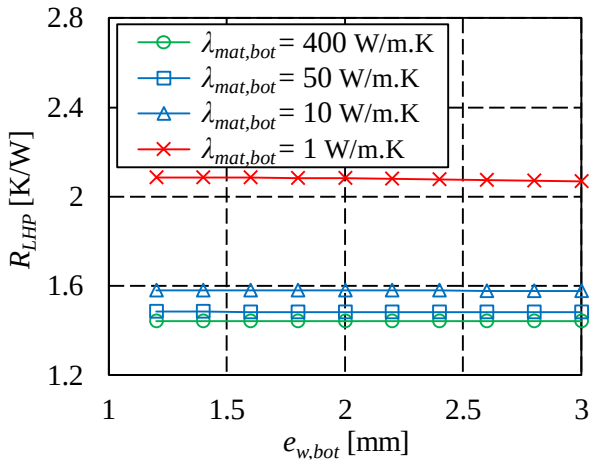

Figure II-12 : Influence of the bottom layer thickness and thermal conductivity on the global thermal resistance

In the studied case, it is not necessary to increase the thickness of the layer having a high thermal conductivity. Thus, the thickness of the samples that will be manufactured must be reduced as much as possible in order to decrease the pressure losses through the porous wick while keeping a sufficient mechanical strength. Moreover, the whole wick thickness is usually limited because in the context of most applications the LHP is integrated in an environment with space constraints. As the bottom layer

thickness has a negligible influence on the thermal performance, it should be as thin as possible in order to decrease the dimensions of the evaporator. For the same reason, the thermal conductivity of the bottom layer material has a small influence on R_{LHP}, especially if it is higher than 10 W/m.K. As a consequence, the bottom layer thermal conductivity must remain higher than 10 W/m.K in order to enhance the heat transfer between the evaporator wall and the menisci where the evaporation takes place.

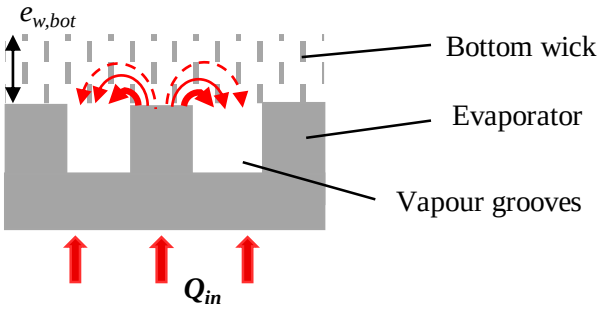

Figure II-13: Schematic of the heat transfer in the bottom layer between the evaporator fins and the fluid

Figure II-14 shows the influence of $e_{w,bot}$ (a) and $\lambda_{mat,bot}$ (b) on the operating limits. The influence of $e_{w,bot}$ is negligible. Indeed, the large part of the pressure drops in the wick is due to the top layer which is thicker. Thus, an increasing $e_{w,bot}$ only slightly decreases the capillary limit. Moreover, the boiling risk concerning the top layer, a variation of the bottom layer thickness does not change the boiling limit.

Figure II-14 also shows that $\lambda_{mat,bot}$ has almost no influence on the capillary limit. This results was expected since the thermal conductivity has no influence on the hydrodynamic operation. An increasing thermal conductivity increases the boiling limit but beyond 100 W/m.K, it has no longer influence. As observed in Figure II-12, R_{LHP} increases with a decreasing thermal conductivity. It means that the evaporator temperature increases, leading to an increase of the boiling risk. Thus a material having a thermal conductivity higher than 100 W/m.K should be preferred for the bottom layer.

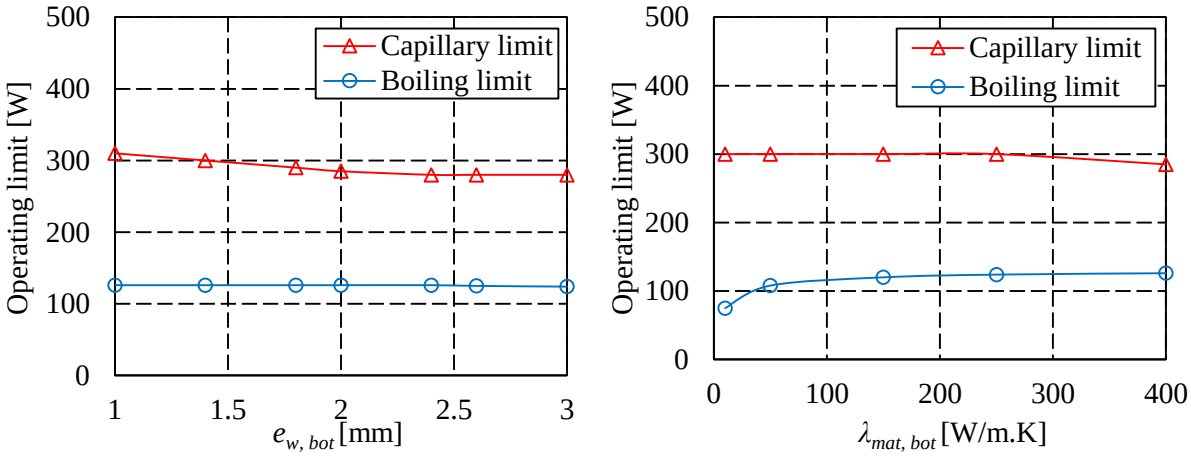

Figure II-14: Influence of the bottom layer thickness and thermal conductivity on the operating limits

II.2.3 Influence of the permeability

Figure II-15 shows the influence of the bottom layer permeability K_{bot} as well as the top layer permeability K_{top} on the global thermal resistance. It is clear that neither K_{top} nor K_{bot} have an influence on R_{LHP}. Indeed, the permeability mainly affects the hydrodynamic operation.

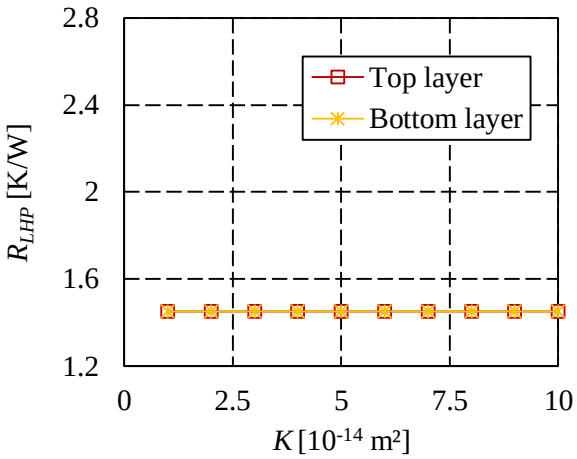

Figure II-15: Influence of the bottom and top layer permeability on the thermal resistance

Figure II-16 shows the operating limits as a function of K_{bot} (a) and K_{top} (b). K_{bot} has no influence on the boiling limit but a too low permeability can reduce drastically the capillary limit. Indeed, decreasing the permeability leads to an increase of the pressure drops along the wick and thus, the capillary limit is reached at a lower heat load. Thus, K_{bot} must remain above 2×10^{-14} m². Beyond this value, the pressure losses through the porous wick become negligible compared to the pressure losses of the rest of the loop and especially in the vapour line where the fluid velocity is maximum.

For the same reason, an increasing K_{top} increases the capillary limit (Figure II-16 b). It is also observed that a decrease of K_{top} decreases the boiling limit particularly if it is lower than 5×10^{-14} m². Indeed, the pressure of the liquid inside the wick decreases for a decreasing K_{top} and it becomes lower than the saturation pressure of the liquid at a lower heat load. It means that increasing K_{top} beyond this threshold will not improve the LHP performance.

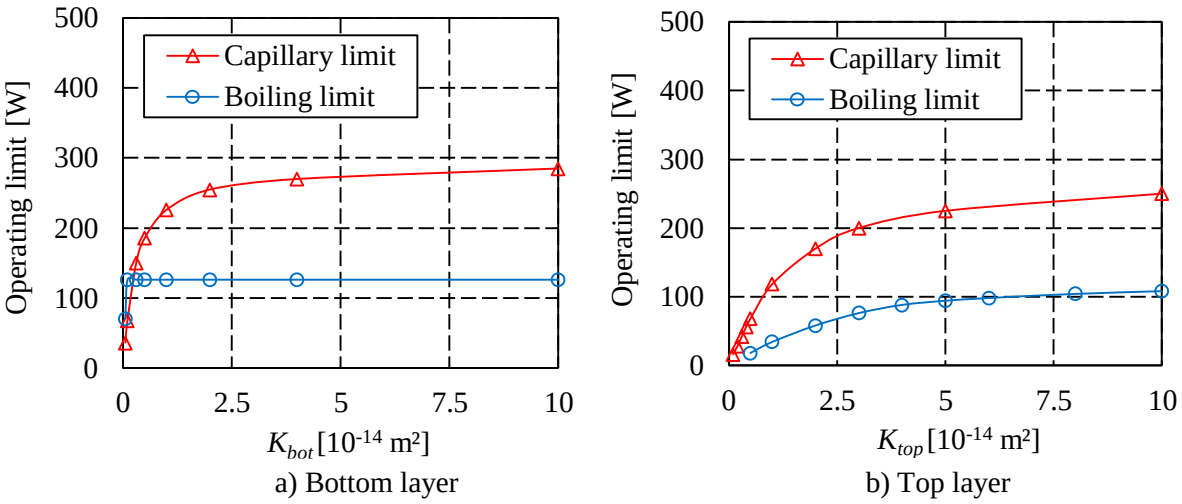

Figure II-16 : Influence of the bottom and top layer permeability on the operating limits

II.2.4 Influence of the porosity

Figure II-17 shows the prediction of the global thermal resistance versus the bottom and top layers porosities, ε_{bot} and ε_{top} respectively. The porosity can influence the LHP operation since it modifies the thermal resistance of the layers. Indeed, the effective thermal conductivity of both layers depends on the porosity (Eq. (II-31)). Figure II-17 shows that the porosity of both layers has no influence on the thermal performance. Concerning the top layer, the values of $\lambda_{mat,top}$ and λ_l are close together. It means that the effective thermal conductivity of the top layer does not depend on the porosity (according to (II-31), λ_{eff}

$= \lambda_l = \lambda_{mat,top}$). Concerning the bottom layer, the previous sections highlighted the low influence of the thermal conductivity and the permeability on R_{LHP}. Thus, it was expected that the porosity, which only affects these two parameters (Eq. (II-31) and (I-19) respectively), has no influence on R_{LHP} either.

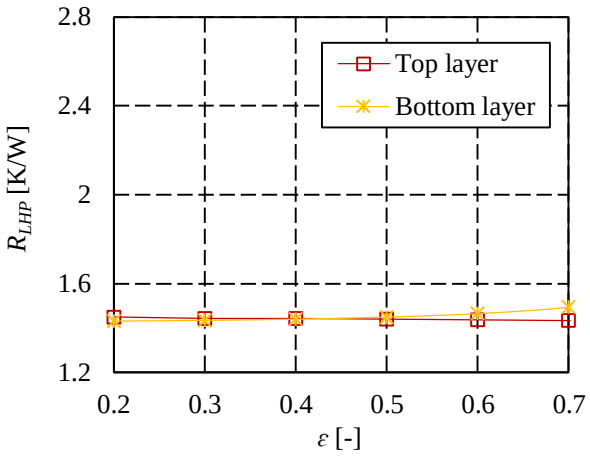

Figure II-17 : Influence of the porosity on the global thermal resistance

Figure II-18 shows the influence of the top and bottom layers porosities on the operating limits. Neither ε_{bot} nor ε_{top} have a significant influence on the boiling limit. Indeed, these parameters mainly change the hydrodynamic operation. However, too low values of ε_{bot} and ε_{top} decrease the capillary limit. Indeed, reducing the porosity decreases the permeability and so, increases the pressure drops, leading to an early occurrence of the capillary limit. Thus, after the manufacturing stage, the top layer porosity should remain above 30 % and the bottom one above 37 %.

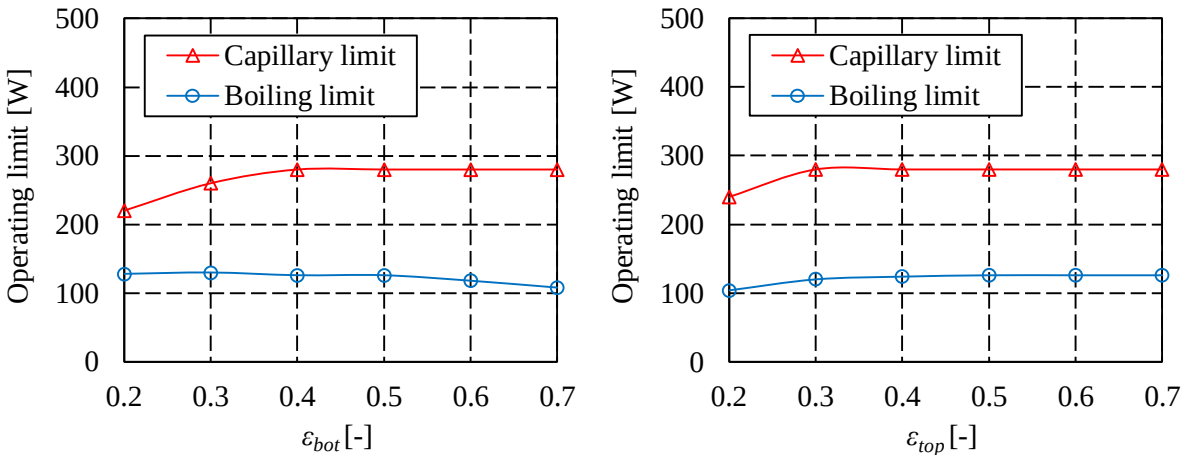

a) Bottom layer b) Top layer

Figure II-18: Influence of the bottom and top layer porosity on the operating limits

II.2.5 Influence of the pore radius

Figure II-19 shows the influence of the top layer pore radius $r_{p,top}$ and bottom layer pore radius $r_{p,bot}$ on the global thermal resistance R_{LHP}. The global thermal resistance is independent of these two parameters. Indeed, they don't modify the thermal properties of the wick.

Figure II-20 shows the boiling and capillary limits as a function of the top layer pore radii. The results show that the boiling limit is the limiting phenomenon for large pore radii. As expected, the maximum heat load is low with a large top layer pore radius. Indeed, an increasing pore radius leads to an increase

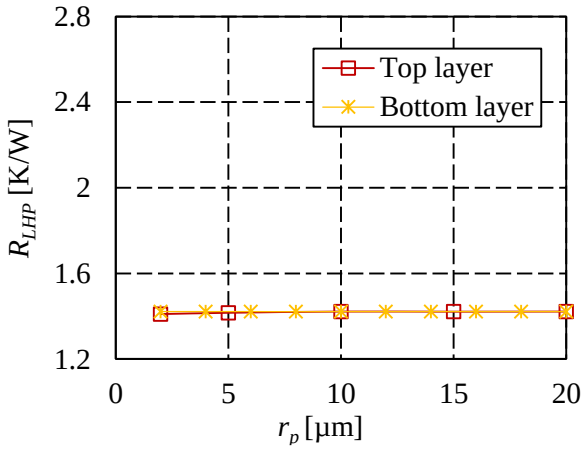

Figure II-19: Influence of the top and bottom layer pore radius on the thermal resistance

of the liquid saturation pressure (Eq. (II-29)) which can more easily reach the pressure of the liquid. A too small $r_{p,top}$ also decreases the boiling limit because a low permeability of the porous medium decreases the liquid pressure below the saturation pressure. At the same time, a too small pore radius reduces the capillary limit since it reduces the permeability (Eq. (I-19)). An optimum value is reached at a $r_{p,top}$ value of about 5 µm. However, it seems reasonable to target a larger pore radius for two reasons. The first one is that the capillary limit is determined in the case of a perfectly pure fluid. However, if some impurities are present in the fluid, the small pores could be obstructed. The second reason is that the capillary limit is determined in the case of an isotropic porous medium. However, the real porous media have a pore radius distribution which depends on the quality of the metallic powder and on the manufacturing process. A variation of the pore size, even a small one, could drastically decrease the limits under the optimum value. On the contrary, an increase of several microns of the pore size has a small influence if the pore size is beyond the optimum. A top pore radius lying between 5 and 10 µm seems to be an interesting trade-off.

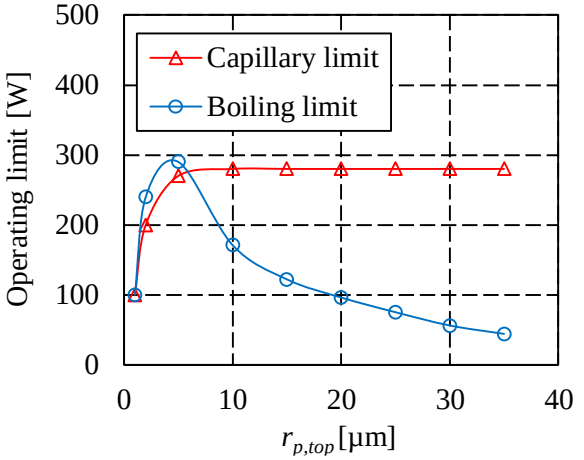

Figure II-20 : Influence of the top layer pore radius on the operating limits

Figure II-21 shows the evolution of the boiling and capillary limits as a function of the bottom layer pore radius $r_{p,bot}$. This parameter does not have any influence on the boiling limit. Indeed, as explained before, boiling is expected to occur inside the top layer close to the interface between the two layers because $r_{p,top}$ is usually larger than $r_{p,bot}$. However, it has a large influence on the capillary limit. An increasing pore radius increases the permeability and decreases the pressure losses. At the same time, it decreases the maximum capillary pressure (Eq. (I-24). These two opposite tendencies lead to the existence of an optimum value of the pore radius for which the capillary limit is maximum. Figure II-21

shows that this optimum is between 0.5 and 0.8 µm. It means that the closer is the pore radius from this range, the higher is the capillary limit. For similar reasons as before, a targeted range varying between 2 and 10 µm is chosen in the present study. Indeed, it enables to evacuate more than 10 W/cm² (125 W for an evaporator having a diameter of 40 mm) without any risks.

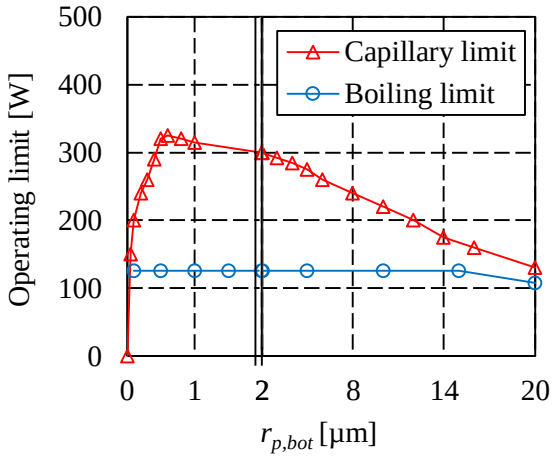

Figure II-21 : Influence of the bottom layer pore radius on the operating limits

II.2.6 Influence of the working fluid

Figure II-22 shows the influence of the working fluid on the global thermal resistance of the LHP. At low heat loads, the smallest value of R_{LHP} is reached with ammonia whereas the greatest one is obtained with water. Indeed, at low heat loads, the LHP operation is optimum with a fluid having a high *dP/dT* slope (Section I.1.2 and I.1.4.2). At high heat loads, R_{LHP} does not depend on the fluid. It was expected because at these heat flux densities, the LHP operates at fixed conductance mode meaning that the reservoir temperature mainly depends on the global heat transfer coefficient at the condenser (Launay *et al.* [5]) itself depending on the heat transfer coefficient between the fluid and the condenser wall h_{cond} (by phase change) and on the heat transfer coefficient between the heat sink and the condenser wall h_{sink} (by convection). Since h_{sink} is very low compared to h_{cond} the main thermal resistance is due to the resistance between the heat sink and the condenser wall. Thus, R_{LHP} only slightly depends on the fluid.

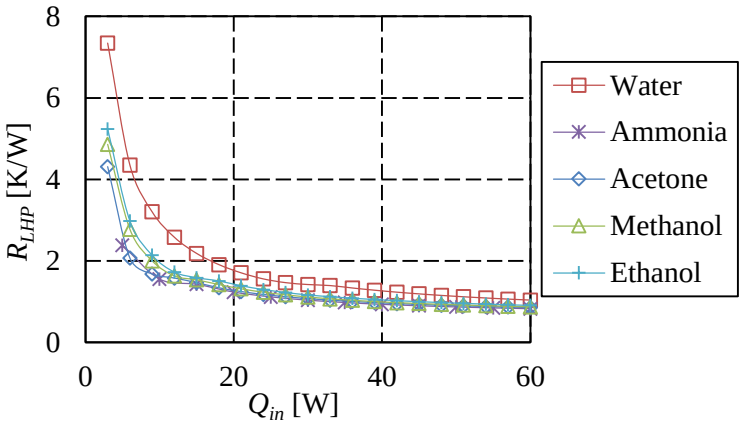

Figure II-22 : Influence of the working fluid on the global thermal resistance

Table II-4 details the operating limits obtained with each fluid. It is clear that water has an excellent behaviour. The boiling risk occurs at larger heat loads than any other fluid. Moreover, its capillary limit is high. This is due to its surface tension which is at least two times higher than any other fluid suitable for LHPs. In conclusion, for low heat loads (< 30 W), ammonia is the best fluid since its thermal

performance is good. However, at moderate and high heat loads, water is better as the boiling risk does not occur below 120 W.

Table II-4 : Maximum heat loads of various working fluids

Working fluid	Boiling limit		Capillary limit	
	[W]	[kW/m²]	[W]	[kW/m²]
Water	126	100	280	224
Ammonia	30	24	400	320
Acetone	27	21	72	57
Methanol	42	33	105	84
Ethanol	27	21	69	55

II.2.7 Conclusion

The main result obtained in this chapter is the determination of the optimum characteristics of a bi-layer wick. The top layer must act as a thermal barrier and enable the fluid to easily circulate through it. However, its pore radius must remain smaller than 10 µm in order to decrease the risk of boiling. The bottom layer must facilitate the heat transfer and thus, its thermal conductivity must be higher than 10 W/m.K. Its pore radius must be small enough to increase the capillary pumping force but not too small in in order to limit the pressure drops.

Table II-5 summarises all the results obtained during the parametric study and details the targets in terms of bi-layer wick characteristics. The results of the parametric analysis show that there is no strict optimum for the various parameters, but rather a trade-off between different considerations (thermal and hydrodynamic performance, mechanical strength, dimensions, etc). It is important to note that these results are only valid in the case of a specific LHP operating with water and having the characteristics described in Table II-3. These results will be used as specifications to manufacture an efficient wick in the following chapter.

Table II-5 : Optimum wick characteristics

Layer	e_w	λ_{mat}	ε	K	r_p
Top	5 - 10 mm	0.5 - 2 W/m.K	> 30 %	> 5.10^{-14} m²	5 - 10 µm
Bottom	1 - 5 mm	> 100 W/m.K	> 37 %	> 2.10^{-14} m²	2 - 10 µm

Chapter III Manufacturing of the wicks

This chapter presents the various manufacturing methods used in order to fabricate the wicks[6] with the specifications determined in the previous chapter. The influence of various manufacturing parameters on the wick properties for each method is also discussed.

This chapter starts with a state-of-the-art of the various methods enabling the manufacturing of a porous structure. The objective is to present the advantages and the drawbacks of these methods in order to correctly establish a procedure for the manufacturing of the porous structures studied in this thesis.

Then, the specific methods used to manufacture the bottom and the top layers are presented. All the protocols are described enabling to have a large view of the manufactured samples. Various solutions are proposed to obtain a two-layered wick. Indeed, the simulations performed above showed that this solution should provide the best performance.

Finally, the last section presents a first characterisation, especially in terms of architecture, geometry and topography. The objective is to characterise the wick in the following of the manufacturing process, independently of its thermal and hydrodynamic properties.

---

[6]Many porous structures have been manufactured during this thesis. Thus, a labelling system has been defined in order to name each protocol and each sample depending on its manufacturing process:

- The two first letters correspond to the material of the capillary structure. For example, it is ***Zi*** or ***Cu*** if the structure is made of zirconia or copper respectively.
- The three following letters correspond to the process used to manufacture the wick. For example, it is ***sin*** or ***frc*** if the structure is made by sintering or freeze casting respectively.
- The number corresponds to the specific protocol used to manufacture the capillary structure. The details of each protocol (powder used, sintering time…) are presented in Appendix D.
- The letters at the end of the label represents the number of the samples having been manufactured following exactly the same method (material, process and protocol).

III.1 Methods to manufacture porous structures

Several methods can be used order to manufacture LHP wicks. In the present section, the partial sintering and the freeze casting are deeply described. Especially, their characteristics, advantages and drawbacks are presented. This section ends with a study of different processing parameters, as a basis to enable the establishment of a robust manufacturing procedure leading to porous structures with expected characteristics.

III.1.1 Partial Sintering of powder

One of the most widespread methods to manufacture LHP wicks is the partial sintering. Sintering is the consolidation by thermal action of a granular agglomerate more or less compact, with or without fusion of one or more of its constituents (J. Peyssou [144]). According to Cizeron [145], sintering is the process by which a system constituted of individual particles (or a porous agglomerated) evolves by heat treatment below its melting point. This process assumes that at least one solid phase exists at any time.

III.1.1.1 Description of the sintering methods

At least two types of sintering exist: in solid phase and in liquid phase. Sintering in liquid phase involves the melting of some of the components (or a minor part of the main component). In solid phase, sintering process goes through two competitive mechanisms (Figure III-1): the grains growth decreases the number of grains and so, increases the grain size whereas the sintering creates a solid-solid interface by diffusion.

In both case, the system tends to decrease its internal energy by decreasing the solid-gas interfacial area and the curvature of the particles.

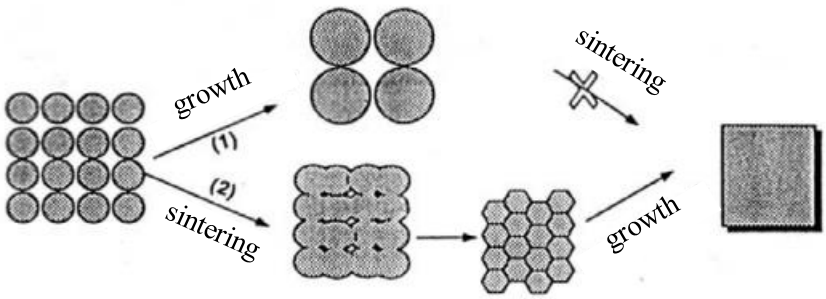

Figure III-1 : Competition between two mechanisms : Sintering and grain growth (adapted from Bernache-Assolant [146])

During a sintering process, a powder is slowly heated up to a targeted temperature lower than the material melting temperature. The atoms are diffusing to form necks between particles. It leads to a densification of the structure without any melting. Figure III-2 shows a schematic of a powder compact before and after sintering. Before sintering, the particles are touching each other and the compact is held together by weak forces (Van Der Waals or hydrogen bonds). The inter-particle necks formed at the contact points during sintering replace these weak bonds by strong chemical bonds (metallic, ionic or covalent bonds depending on the material) and thus largely increase the mechanical resistance of the compact.

The sintering implies a consolidation and sometimes a densification of the structure. It is divided in three steps:

- During the initial step, the porosity lies between 0.35 and 0.5. The porosity is open and the material gets a mechanical strength due to the formation of necks and bridges between particles.
- During the intermediate step, the porosity decreases from 0.35 to 0.1. The porosity becomes closed and the densification is important.
- During the final step, the porosity becomes lower than 0.1. Full density may be reached, but this step is sometimes difficult to complete.

It is important to note that, in order to obtain a porous structure suitable for LHPs, the last step must be avoided and even the intermediate step should not be completed. Indeed, a large permeability is required and it involves open porosity that cannot be obtained for porosity lower than 0.1.

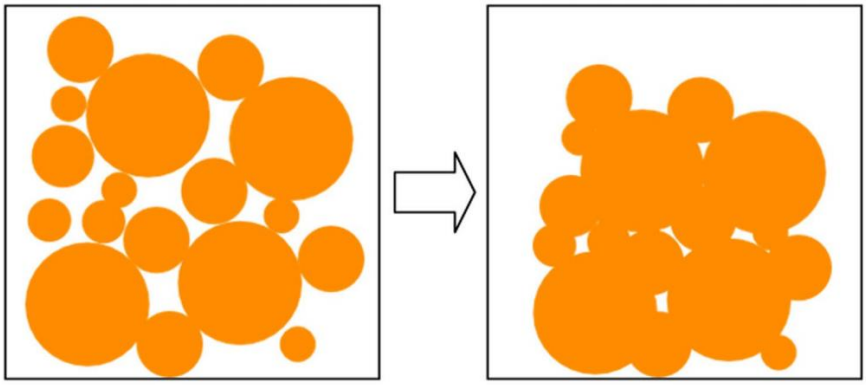

Figure III-2 : Schematic of the wick before (left) and after the sintering (right), Déjou [147]

Hammel *et al.* [65] explained that an increase of the porosity can be achieved by reducing the sintering time or the sintering temperature. Increasing the porosity reduces the mechanical strength but it enhances the heat transfer by convection because the pores are highly interconnected. This has to be taken into account depending on whether the porous structure is expected to have a low or a high thermal conductivity.

It is important to note that the sintering temperature depends on the considered material as the melting temperature is different from one material to another. Indeed, a sintering temperature of 800 °C will not affect in the same way a copper powder (melting temperature: 1083 °C) and a nickel powder (1450 °C). The sintering temperature has to be slightly lower than the melting temperature.

Most sintering thermal cycles are conducted in classical furnaces (natural sintering), in which the heat is transferred from the heating elements to the sample by radiation and convection. However it is possible to lower the sintering temperature by using field-assisted sintering. The assisting field can be a pressure or an electric field. In particular, sintering can be done at lower temperature with three different methods using a pulsed electrical current flowing through (or just around) the compact to sinter it. These techniques are called Spark Plasma Sintering (SPS), Pulsed Electrical Current Sintering (PECS) and flash sintering. Figure III-3 shows the operating principle of the SPS. Firstly (a), high current (~1000 A under a low tension of less than a kV) flows through the randomly packed particles. The extra Joule heating enables the elimination of micro-pores (b) and the spark plasma generates cracks or mass gap in the compact, resulting in evaporation-condensation mass transfer (c). If the sintering is not complete, bridges remain between the particles. For a given current, the longer the sintering time is, the smaller the porosity becomes since more mass melts. The PECS has a similar principle. The main difference is that the electrical current passes through the wall and not through the porous medium (in fact using the

same equipment one can refer to PECS for non-conductive materials and SPS for conductive ones). The flash sintering uses the same principle with a very high tension (several thousand volts).

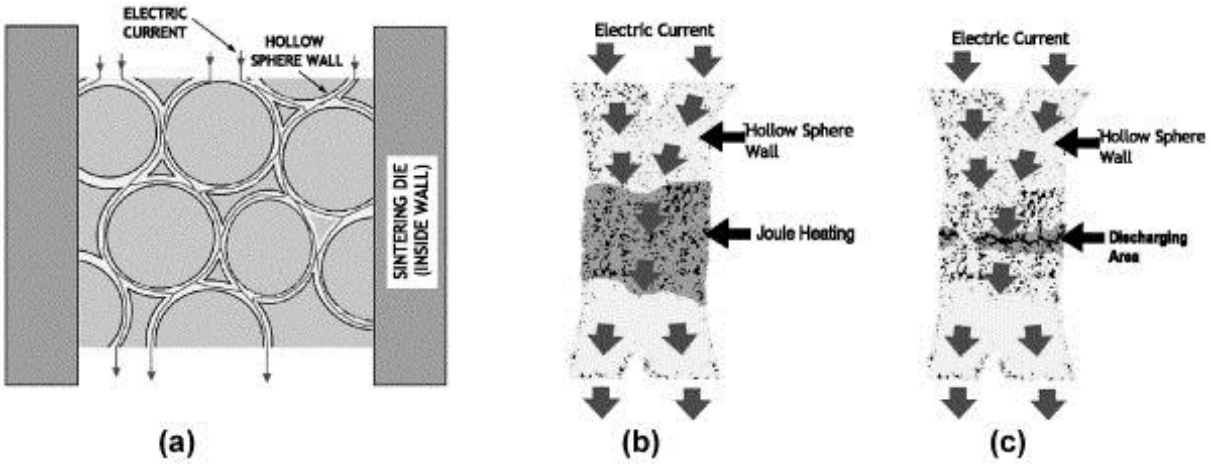

Figure III-3 : Schematic of Spark Plasma Sintering (Khor *et al.* [148]), illustrated on hollow spheres random compacts.

III.1.1.2 Sintering in the presence of a pore former agent

In order to change the porous medium characteristics, the sintering of the powder can be done in the presence of a pore former agent. For instance, Li and Xuan [149] used the slip casting technique. It consists in adding a binder, which acts as a pore former agent (PFA) to the powder. The binder is made of water, polyvininyl alcohol, sodium alginate and octanol. Several changes in the proportions were done to find the perfect viscosity. The water leaves the porous structure at moderate temperature and the rest of the binder is removed at the high sintering temperature. Qiang *et al.* [150] used the same technique to prepare sintered wicks in order to obtain high porosity and small pore size.

Wu *et al.* [151] used a similar method defined in one of their previous works [119]. They used a PFA made of Poly Methyl Methacrylate (PMMA) beads. Then, the mixture of PMMA and nickel is sintered. During the sintering, the PMMA is decomposed when its melting point is reached (140 °C). The decomposition of the PMMA beads creates large pores. In addition, using a low sintering temperature enabled to retain small pores at the contact points of two or more nickel particles, thus leading to porous samples with bimodal porosity.

Samanta *et al.* [152] used a binder to link a mixture made of polypropylene (PP) and nickel powder (Figure III-4 a). Then, the wicks were formed by Metal Injection Moulding (MIM). During the sintering, both the binder and the polypropylene are burnt leaving behind them big pores and interconnected porosity (Figure III-4 b).

Xu *et al.* [153] have manufactured biporous wicks with NaCl as a PFA. The wick is sintered with the PFA. Then, the wick is kept in a constant temperature bath at 90 °C during 4 h to dissolve the NaCl. This method is efficient and easy to implement. They also used microcrystalline cellulose as a PFA to compare the performance with the NaCl. Li *et al.* [106] used microcrystalline cellulose as a PFA. They cleaned the wicks by an ultrasonic cleaner with pure ethanol. Then, the wick are kept at 110 °C for 2 h.

The examples highlight the interest of PFA but, although the use of PFA enables increasing the overall porosity, it does not necessary lead to better permeability since the flow inside the porous structure will be controlled by the interconnections between the pores, potentially much smaller than the pores themselves. Thus generally speaking this method leads to the production of porous samples with

quite low mechanical properties (due to high porosity and large pore size) but also low permeability (due to small necks between particles). In the present study, the integration of PFA to the slurry is done only on few samples in order to confirm this trend.

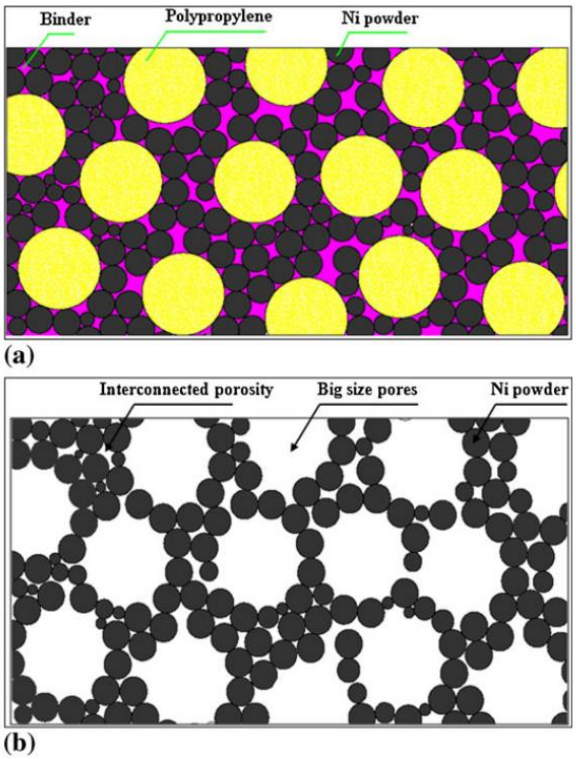

Figure III-4 : Distribution of the powder particles in the green compact (a) and interconnected porosity formed in the sintered wick (Samanta *et al.* [152])

III.1.1.3 Important sintering parameters

The partial sintering is the most used method to manufacture porous materials suitable for LHP wicks. Thus, this method profits from a large feedback on many experiment, enabling to perform an analysis of the most important parameters.

According to Chi [33], the pore radius of the wick mainly depends on the grain size. The higher is the grain size, the higher is the pore radius r_p after sintering. He proposed the following correlation:

$$r_p = 0.41 r_s \tag{III-1}$$

where r_s the powder particle radius. A literature review was done in order to validate this correlation. In Figure III-5, the pore radius of several wicks described in the literature are plotted as a function of the powder radius and compared to the Chi correlation. A relatively good agreement is observed. It means that it is possible to roughly estimate the pore radius of a wick if the size of the powder particles is known. Obviously this is valid if the material only goes through the first stage of sintering (second and third stages tend to diminish the pore size until the pores are removed).

Obviously, the sintering parameters also affects the wick properties. According to Hansen *et al.* [154], the parameters which determine the wick characteristics are:

- The sintering time t_{sin},
- The sintering temperature T_{sin},
- The sintering atmosphere

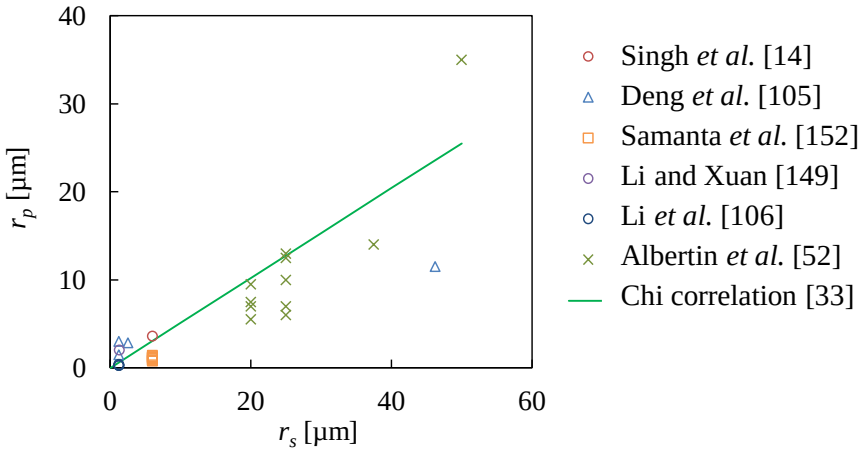

Figure III-5 : Pore radius (r_p) of experimental LHP wicks versus the powder radius (r_s)

- The type and amount of pore former (spacing agent),
- The pressure applied during sintering (forming pressure P_f).

Their results, confirmed by those of Singh *et al.* [7], show that long sintering time, high sintering temperature and high forming pressure provide wicks with low permeability, low porosity and small pore size but high mechanical strength. This result was expected due to the sintering mechanism detailed in a previous section. Figure III-6 presents the porosity of various nickel porous structures as a function of the sintering temperature. It clearly shows that the porosity decreases with an increasing sintering temperature.

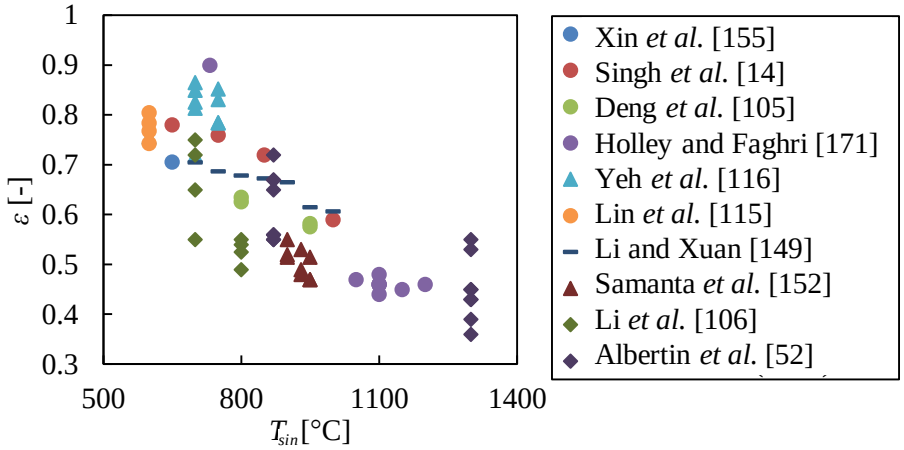

Figure III-6: Evolution of the porosity of nickel samples as a function of the sintering temperature

However, it is difficult to keep a high porosity with a small pore radius. Indeed, for a powder with given particle size distribution, a low sintering temperature and a short sintering time will give high porosity and large pore size whereas a high temperature and a long time will give low porosity and small pore size. Table III-1 summarises the effect (positive or negative) of the sintering parameters on the wick characteristics. It is clear that in each case, if the influence of a parameter is positive on the porosity, it is negative on the pore size and *vice versa*.

Table III-1 : Effect of the sintering parameters on the wick characteristics. A “plus”, for positive, means that the effect corresponds to the objective of the manufacturer (high porosity and small pore radius)

	Short sintering time	Long sintering time	Low sintering temperature	High sintering temperature
Effect on porosity	+	-	+	-
Effect on pore size	-	+	-	+

That is why a trade-off has to be found. Concerning the nickel, Samanta *et al.* [152] found that the best combination seemed to be 900 °C during 60 min. Concerning the copper, Albertin *et al.* [52] found 870 °C during 20 min was an interesting compromise to keep the porosity as high as possible with a small pore radius. Using a pore former agent enables to increase the porosity at the cost of relatively large pores, and may thus not be the optimum solution.

Li and Xuan [149] studied the influence of the forming pressure on the porous medium characteristics. They said that the pressing mould method may be not efficient to obtain high porosity and so, high permeability. Indeed, the high compacting pressure would reduce to a very small size the pore preventing the working fluid to flow through the wick. However, in specific cases, if the pressure is applied in the presence of a pore former agent, the porosity remains at an acceptable level.

The sintering atmosphere has a strong influence on the wick. Usually, the atmosphere is preferred to be not oxidant. Indeed, an oxidised wick surface can prevent a proper filtration of the working fluid through the absorbing face as explained by Singh *et al.* [7]. Usually, the wicks are sintered under vacuum, reducing or basic atmosphere as Nitrogen or Argon (Xin *et al.* [155]). However, it can be of interest to conserve an oxidant atmosphere when sintering copper as the oxidised copper has a better contact angle with water than pure copper. In the present study, sintering is used to manufacture both the top and bottom layers.

III.1.2 Freeze casting

The freeze casting is an innovative way to manufacture porous structures dedicated to LHPs. A freeze caster is composed of a cold and a hot source (Figure III-7). Usually, the cold source is made of a liquid nitrogen bath (around -200 °C) and is located at the bottom of the system. A metal finger is immersed in the bath. Above this bath, the heating element is placed around the finger in order to provide the heat flux to control the cooling rate of the suspension. At the top of the finger, a mould can receive the material suspension. This process uses the growth of ice in suspension to template the porous structure in a material.

Obtaining a material by freeze casting requires several steps summarised in Figure III-8 both by schematics and by a Clapeyron diagram:

(a): a ceramic suspension (slurry) is produced, constituted of well dispersed ceramic particles in an adequate liquid medium (generally water) and additives such as dispersing agents, binders, rheological modifiers…

(b): the suspension is frozen with a controlled ice front velocity. The solvent is then solidified in the shape of large plates with their long axis parallel to the freezing direction. The ceramic particles are ejected from the solvent and compressed between the laths of the frozen medium. The final structure mainly depends of the ice-front velocity, itself depending on the thermal gradient.

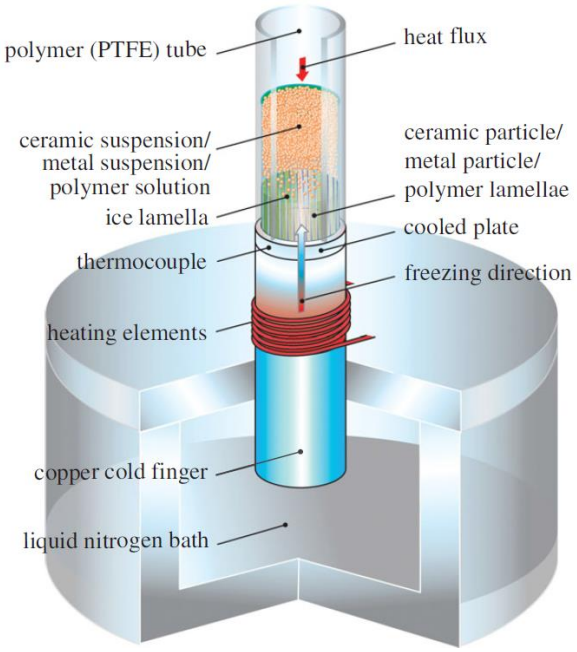

Figure III-7 : Schematic of a freeze casting system (Wegst *et al.* [156])

(c): the solvent is eliminated by freeze-drying. The solidified suspension is kept in vacuum in order to sublimate the solidified solvent.

(d): when all the solvent is sublimated, only ceramic and organic modifiers remain (forming a porous green ceramic body), the green body is heated up to the ambient temperature and pressurised up to the atmospheric pressure.

(e): the green body is solidified by sintering, retaining its lamellar structure.

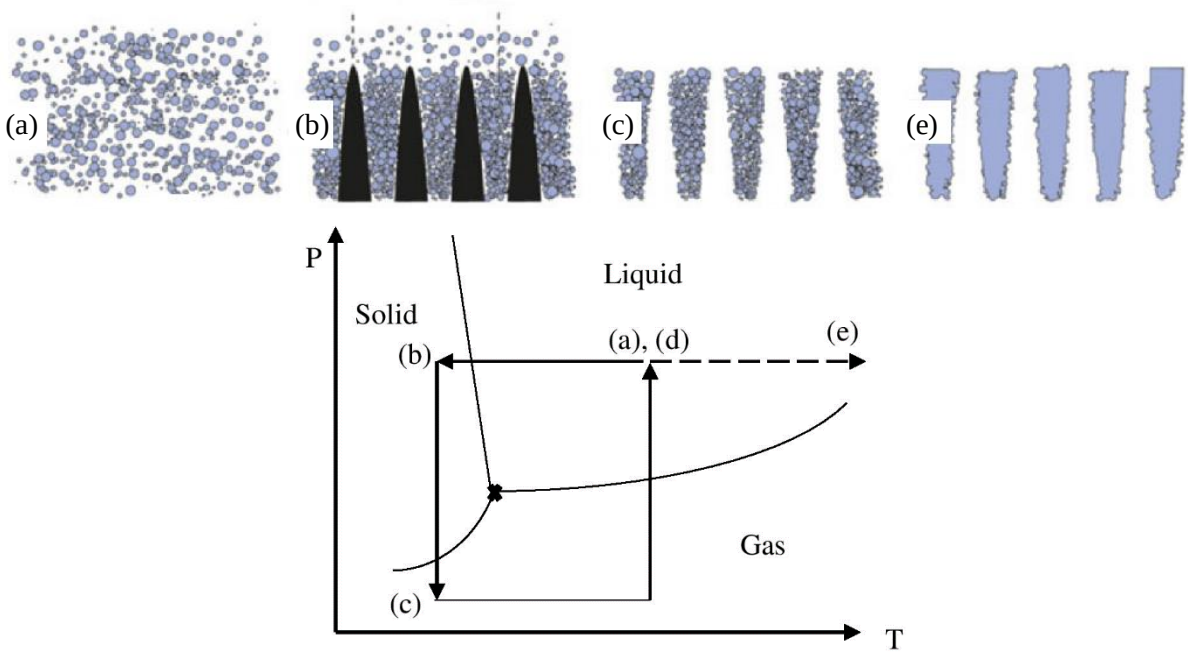

Figure III-8 : Schematic diagram of the ice templating process (adapted from Bouville [157])

Almost every material (polymers, metals, and ceramics) can be ice templated following this method, providing the particle size is lower than a dozen of microns, dispersed or soluble. Li and Li [158] and

Fukushima *et al.* [159] used the freeze casting method with Y_2SiO_5 and SiC respectively. The final material is constituted by every element present in the starting suspension (except the solvent and the components eliminated during sintering). Thereby this method is robust enough to mix or aggregate any constituents of a composite material.

This method gives low tortuosity channels as the crystals grow directionally inside the suspension. The thermal gradient has a strong influence on the porous structure characteristics, as well as the solid fraction in the starting suspension. An increasing volumetric fraction of ceramic in the initial suspension decreases the porosity. An increasing thermal gradient decreases the pore size. Experimentally, the thermal gradient is changed by changing the cooling rate. Since the temperature of the liquid nitrogen bath is constant, only the heat flux (provided by the heating element) can be modified in order to change the cooling rate of the suspension. The objective is to keep the ice front velocity between 5 and 80 µm/s. It roughly corresponds to a cooling rate lying between 0.5 K/min and 10 K/min. This process enables to obtain small pores. Mukai *et al.* [160] obtained porous structures with 10 µm-width unidirectional channels. Deville *et al.* [161] found that cooling rate lying between 0.5 K/min and 20 K/min leads to pore sizes between 100 µm and 4.5 µm respectively.

The porous structure can be adapted by changing the solvent For example, Deville *et al.* [161] studied the influence on the porous structure of the addition of zirconium acetate (ZRA) in an initial suspension made of ice crystals, and Bouville [157] tested ZRA, glycerol and acetic acid. The resulting microstructures are shown on Figure III-9. Different patterns are observed which may lead to various capillary forces and various pressure drops for the same size.

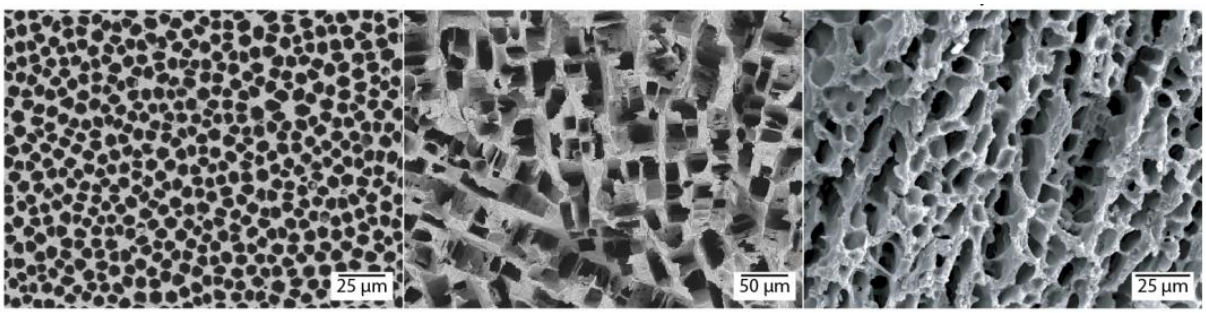

a) Zirconium acetate b) Acetic acid c) Glycerol

Figure III-9 : Cross sectional of ice templated ceramic samples including various additives (Bouville [157])

According to Hammel *et al.* [65], the freeze casting is the most effective method to manufacture a porous structure dedicated to thermal insulation. Moreover, a high mechanical strength is reached even for highly porous samples. The microstructure is well controlled and enables this method to meet the functional requirements in order to reduce the heat leaks when inserted in a LHP evaporator. In the present study, the freeze casting method is used to manufacture the top layer, but it could also be used to manufacture the bottom layer with a copper suspension.

III.1.3 Other methods

Many other methods can be used to create ceramic porous structures. They are briefly described in this section since they have not been used in this thesis. Saiz *et al.* [162] tested a new computer-driven technique to manufacture ceramic porous structures called robocasting. It enables to produce complex shapes, layer-by-layer, following a computer design. A ceramic suspension, called ceramic ink, is used to print the porous samples. It must be viscous enough and quickly settle to keep the designed shape. Figure III-10 shows the robocasting technique. The ink is extruded through a nozzle and the sample is

built layer-by-layer. It is possible to see that if the ceramic ink is not viscous enough, it is difficult to keep the expected shape and the pores may be smaller than in the computer design. The authors say that it is possible to decrease the pore size up to 150 µm.

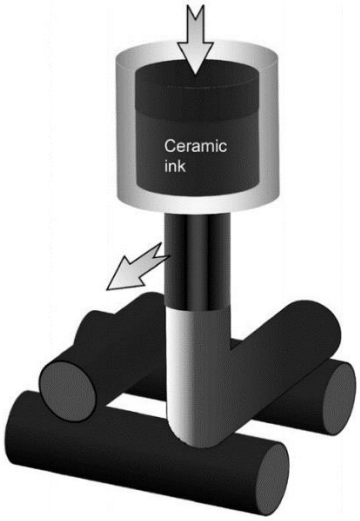

Figure III-10 : Schematic of robocasting technique (Saiz *et al.* [162])

Saiz *et al.* [162] investigate a more classical technique by infiltration of polymer foams. The ceramic slurry is put inside the foam and compressed to fill the pores. Then, the sample is burnt in order to remove the polymer. This process leaves empty pores instead of the polymer. The infiltration technique enables to obtain a pore size lying between 10 and 80 µm.

There are at least three other methods to manufacture a porous structure in ceramic. These methods are presented by Studart *et al.* [163] :

- The replica technique (Figure III-11 a): a synthetic or a natural template is immersed in a ceramic suspension. The excess suspension is evacuated. The suspension is dried and forms thin coating over the template. The template is removed, leaving a ceramic replica. The mechanical strength is usually low. However, very high porosities can be obtained (up to 95 %). It is possible to reach high porosities because the porous structure are reticulate. It means that the porosity is open and the pores very interconnected.
- The sacrificial template technique (Figure III-11 b): this method is comparable to the sintering with a pore former. A sacrificial material is incorporated in the ceramic and then dried or evaporated in order to create pores. The freeze casting is comparable to this technique as it uses growing ice crystals as pore former. The highest porosities obtained are around 70 %. It results in a high permeability in comparison to a structure with the same porosity but with closed pores
- The direct foaming technique (Figure III-11 c): gas bubbles are injected in the ceramic suspension. It is then dried and spherical pores are created. The direct foaming technique as well as the sacrificial method give reticulate structures when the porosity is high.

It is difficult with these methods to decrease the pore radius down to 10 µm. However, some of these techniques and especially the robocasting are recent and in continuous improvement. They could be able to decrease the pore size to the targeted value soon.

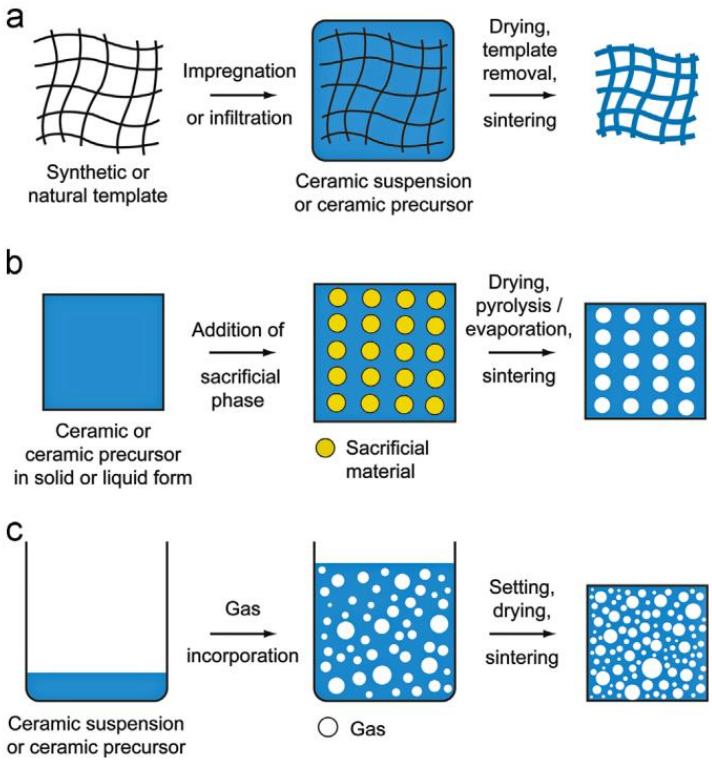

Figure III-11 : Typical processing methods for the production of macroporous ceramics (Studart *et al.* [163])

III.2 Manufacturing of the wick bottom layer

In the present chapter, the objective is to obtain a sample having characteristics similar to the optimum ones determined in the Chapter II. This section presents the manufacturing procedure of the bottom layer. As explained in the Section II.2, the aim of this layer is to ensure a high capillary pressure and to transfer the heat from the evaporator wall to the liquid-vapour interface. It must have small pore size and a high thermal conductivity. Several porous structures are manufactured in order to understand the effect of the manufacturing process parameters on the wick characteristics.

III.2.1 Pulsed Electric Current Sintering of copper wires

A possible bottom layer wick can consist in a consolidated array of copper wires, oriented in the direction of the liquid flow, in order to have both high thermal conductivity (thanks to the high thermal conductivity of copper), high permeability (thanks to high porosity, and long and smooth pores between the copper wires, thus oriented in the direction of the liquid flow) and high capillary pressure (due to the small diameter of the pores). Such an array of copper wires was assembled and heated by PECS in order to create bridges (by partial sintering) between the wires (Figure III-12). The wires have a diameter of 100 µm and a length of several centimetres. The electrical tension is around 800 V and the electrical current can reach several thousand of ampères. However, this method failed due to the large impurity of the copper wires which prevents the current to correctly pass from a wire to another. Moreover, it is not easy to keep the wires parallels and to form tubes. The risk is to create large pores and to reduce the capillary force. That is why, no sample manufactured following this method has been finally used. However this idea should not be eliminated in future works, having failed only for technical reasons and optimisation difficulties.

Figure III-12: Pictures of the porous structure after PECS

III.2.2 Partial sintering of copper powder

A more classical method to obtain a porous material is the partial sintering of powder particles. Copper is chosen in order to manufacture the bottom layer. Indeed, it has a high thermal conductivity. According to Chi [33], the pore radius depends on the powder diameter (Section III.1.1.3). The copper particles used in the present study have a dendritic structure and the following pore size distribution (illustrated in Figure III-13):

- 1st decile: 9.1 µm
- Median diameter: 28.2 µm
- 9th decile: 59.7 µm

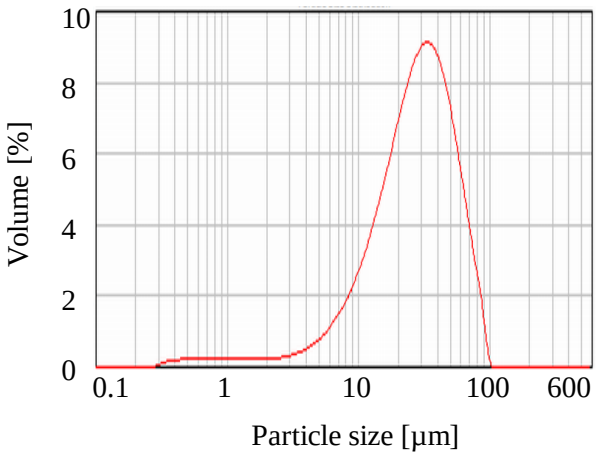

Figure III-13: Particle size distribution of the copper power used for sintering

It corresponds to an expected pore radius of about 6 µm. It is important to note that this estimation cannot be considered as accurate since Chi's equation (Eq. (III-1)) is derived for a powder made of spherical particles and not a powder made of dendritic particles. That is why, the Chi's correlation is only an indicator used to choose the appropriate powder for a specific application.

The wick fabrication process is divided in several steps. Firstly, the powder is mixed with a binder made of polyvinyl alcohol (PVA). The PVA helps the wick to keep its shape in the green compact state, after pressing and before the sintering step. The proportion of PVA in the slurry is kept constant (0.7 % of the copper mass). Indeed, a lower ratio would prevent the PVA to keep its binding role and a higher ratio would induce a too long debinding stage. The slurry dries during about a week. Then, it is crushed

in a porcelain mortar and pressed with two pistons in a floating cylindrical matrix in order to obtain its shape. The forming pressure is uniaxial (Figure III-14) and the matrix gives a flat-disk shape with a diameter of 40 mm.

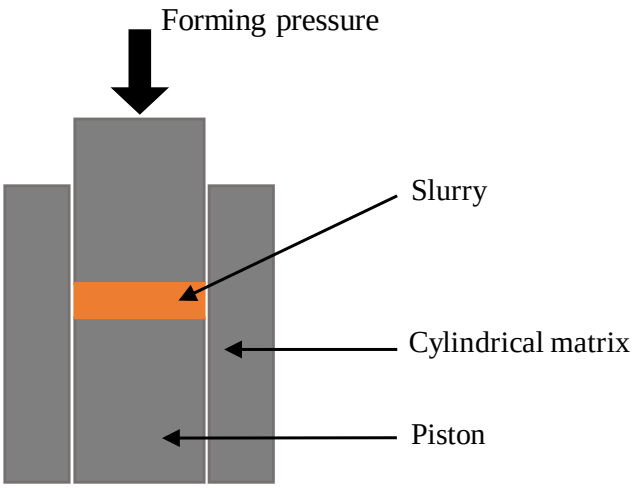

Figure III-14: Schematic of the method to obtain a flat disk shaped porous copper

The wick is then debinded and sintered in a muffle furnace *Nabertherm*. During the heating stage, the temperature increases at 1 K/min up to 600 °C (Figure III-15). The dwell time lies between 5 h and 10 h in order to remove all the PVA. Then, the temperature increases at 5 K/min up to the desired sintering temperature which is one of the parameters of the parametric study presented below.

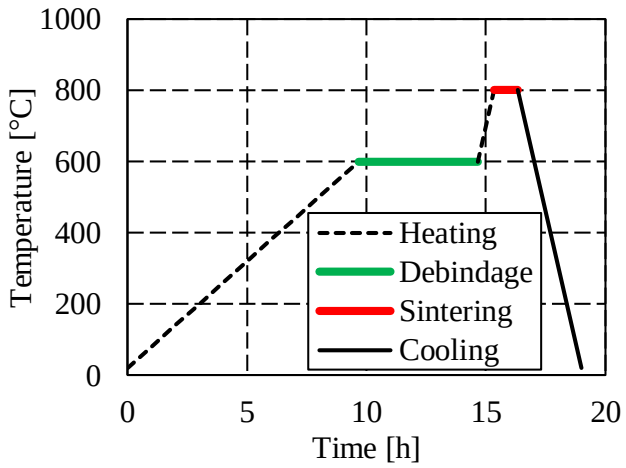

Figure III-15: Temperature profile of the muffle furnace during the copper powder sintering

Figure III-16 shows a picture of the final product as well as an XRD scan presenting its composition. The wick is black because it is completely oxidised. Indeed, the furnace works with the ambient atmosphere. The X-ray diffraction (XRD) scan confirms that there is probably no more metallic copper in the entire porous medium: it must be made of copper oxides (33 % cuprite (Cu_2O) and 67 % tenorite (CuO)). This information must be taken into account since it changes the contact angle as well as the thermal conductivity. Indeed, the thermal conductivity of the cuprite lies between 5 and 8 W/m.K (Touloukian [164]).

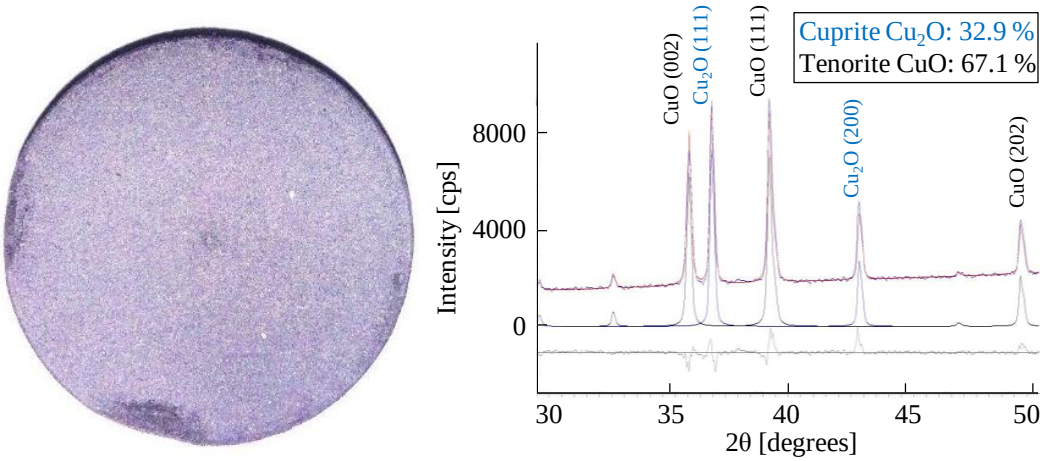

a) b)

Figure III-16: Picture of the bottom layer (a) and XRD scan (b)

The sintering has to be realised with the sample put on a bed of stainless steel spheres. Indeed, inside the furnace, the heat is not well transferred to the bottom surface of the sample if it is put directly on the furnace floor. Figure III-17 shows the picture of a sample sintered on the furnace floor. It is possible to observe that the sample core is not oxidised. It means that the temperature has not reached a high value and that the core is probably not sintered.

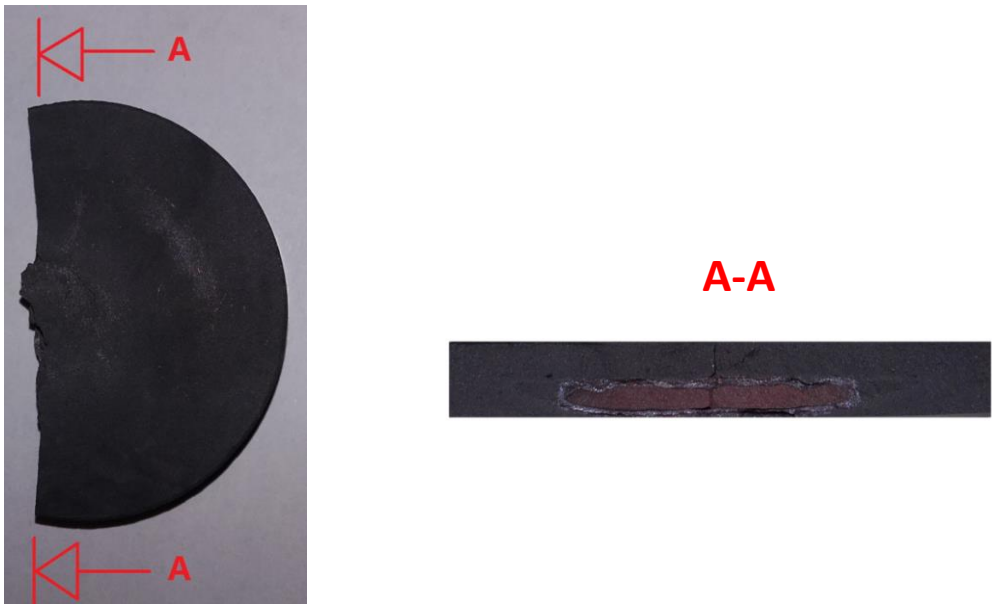

Figure III-17: Picture of a failed sintering process

In order to avoid any structural troubles, the sample must be manipulated with great care at any time. Indeed, the cracking risk is high. Even if the cracks are not observable, they can be revealed by the sintering process.

The bottom layer being very influent in terms of thermal performance, a 2-level fractional factorial design of experiment is conducted following the method of Montgomery [165] in order to optimise its characteristics. This method limits the number of samples to manufacture by avoiding trying all possible combinations of the parameters. The processing parameters optimised here are the pressure applied during uniaxial pressing, the copper mass, the sintering temperature and the sintering time. The maximum and minimum levels of each one are presented in Table III-2, as well as the eight different

sets of parameters. The hydrodynamic and thermal characteristics of the samples obtained with the design of experiment are studied in the Chapter IV and the Chapter V of this thesis.

Table III-2: Sintering parameters of the design of experiment

Level	P_f [MPa]	m_s [g]	T_{sin} [°C]	t_{sin} [min]
(-)	7	10	800	30
(+)	35	25	900	120

Protocol	P_f [MPa]	m_s [g]	T_{sin} [°C]	t_{sin} [min]
1	-	-	-	-
2	+	-	-	+
3	-	+	-	+
4	+	+	-	-
5	-	-	+	+
6	+	-	+	-
7	-	+	+	-
8	+	+	+	+

Other suitable sintering parameters have been used outside this design of experiment and are presented in Table III-3. In total, thirteen protocols have been tested leading to the manufacturing by sintering of twenty-three copper samples. Their characteristics are given in the Appendix D.

Table III-3: Manufacturing protocols of the copper samples obtained by sintering

	P_f [MPa]	m_s [g]	T_{sin} [°C]	t_{sin} [min]
9	100	-	900	15
10	35	25	800	60
11	35	25	800	120
12	18	25	800	90
13	18	10	800	90

III.3 Manufacturing of the wick top layer

In this section the various methods to manufacture the wick top layer are presented. As explained in the Chapter II, the role of this layer is to feed the bottom layer with liquid and to reduce the heat leaks from the evaporator to the reservoir. That is why it is manufactured with a material having a low thermal conductivity. Among this kind of materials, zirconia is chosen because it provides high mechanical resistance and has a thermal expansion coefficient quite close to the one of copper (10×10^{-6} K^{-1} for zirconia and 16×10^{-6} K^{-1} for copper). This condition must be respected in order to minimise the risk of cracks under thermal solicitation. Moreover, zirconia has a thermal conductivity of 2 W/m.K, which is in the range determined during the parametric study enabling to investigate the wick characteristics influence (Chapter II, Table II-5).

The two different methods chosen to manufacture the top layer are the freeze casting and partial sintering. They use the same zirconia powder whose particle size distribution is shown on Figure III-18 (note that it refers to agglomerate size, the individual crystallites being much smaller):

- 1st decile: 0.58 µm
- Median diameter : 5.42 µm
- 9th decile : 11.50 µm

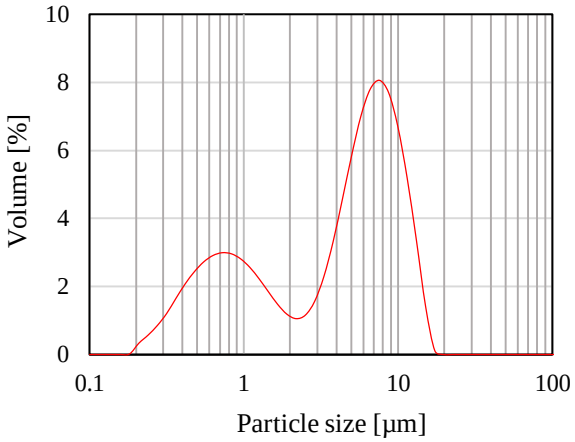

Figure III-18: Particle size distribution of the zirconia powder

This powder is a 12Ce-TZP (Tetragonal Zirconia Polycrystal stabilised with 12 mol.% CeO_2), chosen for its good trade-off between mechanical properties (high toughness in particular, up to 10 $MPa \cdot m^{1/2}$) and its resistance to hydrothermal ageing (indeed, at the temperatures used for the device and in the presence of water, the stronger Yttria-stabilised zirconia ceramics suffer from hydrothermal ageing resulting in a phase transformation that slowly degrade their mechanical properties until the device falls apart; this is not the case for Ce-TZP).

III.3.1 Freeze casting of zirconia powder

The freeze casting is an interesting method as it enables to create capillary tubes in the direction of the fluid flow (Section III.1.2). The freeze casting procedure is divided in three steps.

Firstly, a slurry is created, composed of 1.44 g of dispersing agent (*Darvan*), 1.2 g of polyethylene glycol (PEG) as a binder, 120 g of zirconia powder and 46 g of water. The dispersing agent enables to have PEG around each particle of zirconia. Two PEG with different molecular masses have been tested: 1500 and 4000 g/mol.

Secondly, the slurry is dispersed using ball milling (with zirconia balls) during two days to be perfectly homogeneous.

Thirdly, the slurry is poured inside a mould, the mould being put on the cold plate of the freeze caster (Figure III-19) in order to receive successive thermal treatments.

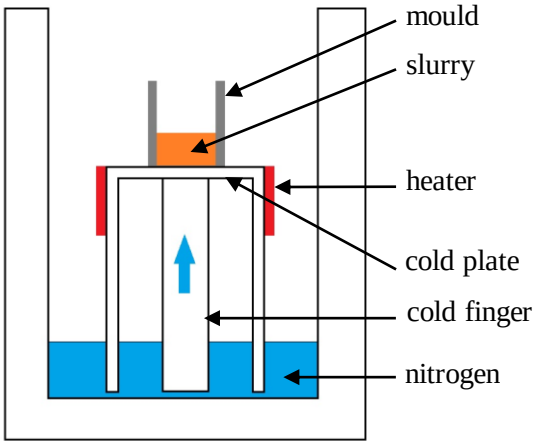

Figure III-19: Schematic of the freeze caster

Figure III-20 shows the profile of the thermal treatments:

- 1 to 2: after the temperature has been stabilised for a few minutes at 4 °C, the slurry is cooled at a frozen velocity of -10 °C/min down to the temperature of the liquid nitrogen.
- 2 to 3: the frozen slurry is put inside a sealed enclosure at -12 °C. Vacuum is created inside this enclosure in order to sublimate all the ice contained in the sample. This step is two days long.
- 3 to 4: the sample is put in a muffle furnace *Nabertherm* at 600 °C in order to remove all the PEG (debinding stage).
- 4 to 5: the temperature of the furnace is increased up to the sintering temperature in order to give a mechanical strength to the porous sample.

Note that, for a sake of clarity, the time scale is not respected in the Figure III-20.

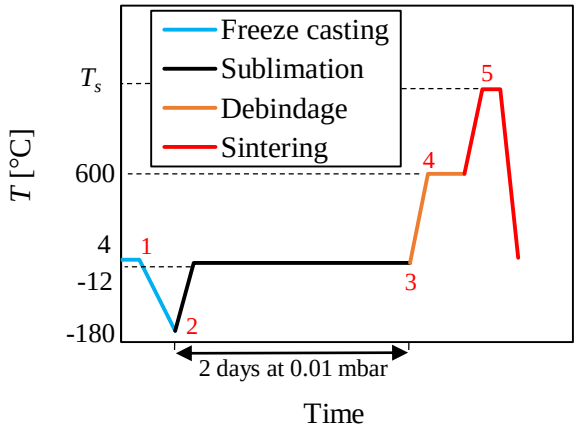

Figure III-20: Example of pressure and temperature profiles used for freeze casting

Figure III-21 shows SEM micrographs of one of the sample. It is possible to see that empty slices are created by the frozen front. It enables to reduce the tortuosity without increasing the channel size. Indeed, the tortuosity is close to one and the channel width is around 20 µm.

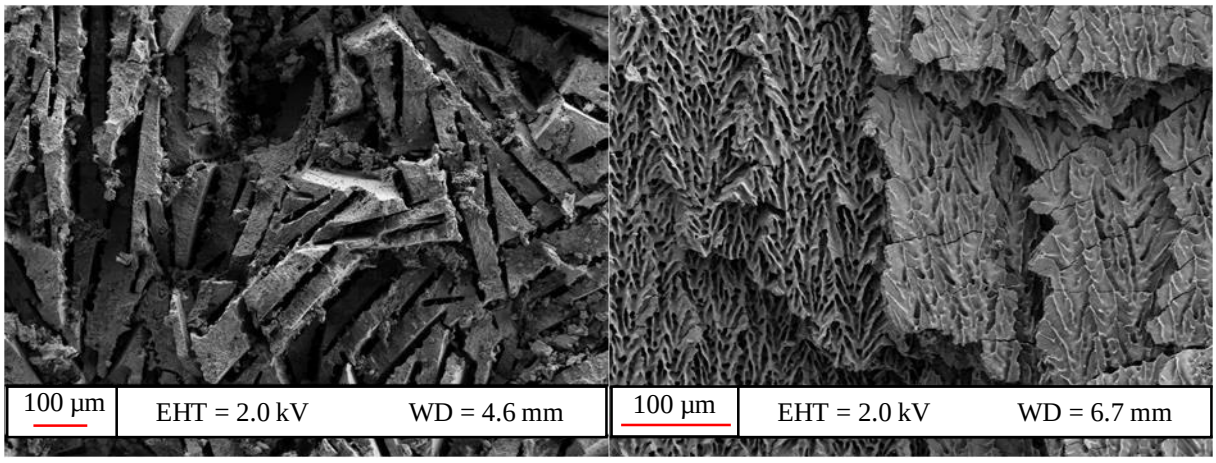

a) Top view of sample Zi-frc-2-b b) Side view of sample Zi-frc-2-a

Figure III-21: SEM pictures of a freeze casted samples

Table III-4 shows the four protocols tested in order to manufacture six porous media by freeze casting. The protocols are similar and mainly the temperature has been changed in order to obtain the suitable size and mechanical resistance. The characteristics of each sample is given in Appendix D.

Table III-4: Manufacturing protocols by freeze casting

	P_f [MPa]	m_s [g]	T_{sin} [°C]	t_{sin} [min]
1	-	60	1450	120
2	-	30	1280	120
3	-	30	1230	120
4	-	30	1250	120

Despite these obvious advantages, manufacturing of large pieces by freeze casting is not easy and often results in large cracks (sometimes larger than 500 µm in thickness) across the whole wick. This kind of channel drastically decreases the capillary pressure, thus prevents the porous structure to be used as a top layer.

These problems can be avoided by reducing the mass of zirconia slurry. Indeed, freezing of the slurry is more regular and with less distortion if the sample is thinner. However, it reduces the thickness lower than the range proposed in Table II-5 which is 6 to 10 mm. A trade-off should be found here, but an optimum could not be reached in the framework of this thesis.

III.3.2 Partial sintering of zirconia powder

The partial sintering of zirconia powder is the other method used to manufacture the top layer. The method is similar to the partial sintering of copper powder. A matrix larger than 40 mm must be used to press the dried and crushed suspension because a certain amount of shrinkage is necessary to maintain sufficient mechanical properties. The right microstructure and sufficient mechanical properties are reached with a 2 h long dwell and a sintering temperature of 1230 °C, leading to a 40 mm diameter sample when using a 48 mm diameter matrix. The debinding stage is exactly the same as for copper sintering (Figure III-22).

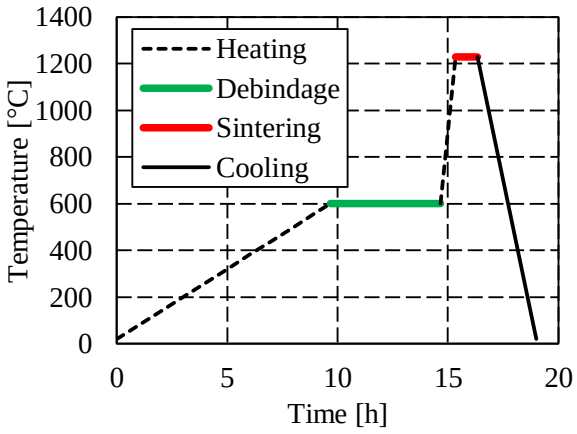

Figure III-22: Temperature profile of the muffle furnace during the zirconia powder sintering

On the SEM micrographs shown on Figure III-23, it is possible to see the pores as well as the necks created between the particles. Most pores are smaller than 1 µm, potentially leading to a too low permeability.

Since this layer must have a high permeability, nylon powder having a higher particle diameter than the zirconia can be added to the slurry as porogenic agent. The proportion of nylon in the slurry lies between 50 % and 65 % of the total volume. The pore size distribution of the nylon powder is shown in Figure III-24:

- 1st decile: 13.7 µm
- Median diameter : 19.7 µm
- 9th decile : 28.2 µm

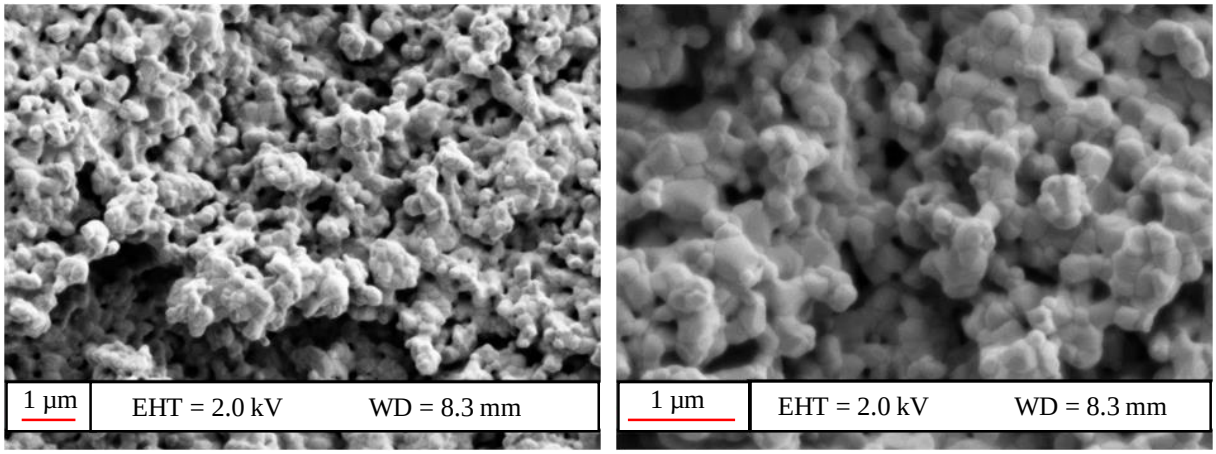

Figure III-23: SEM pictures of the sample Zi-sin-5-a

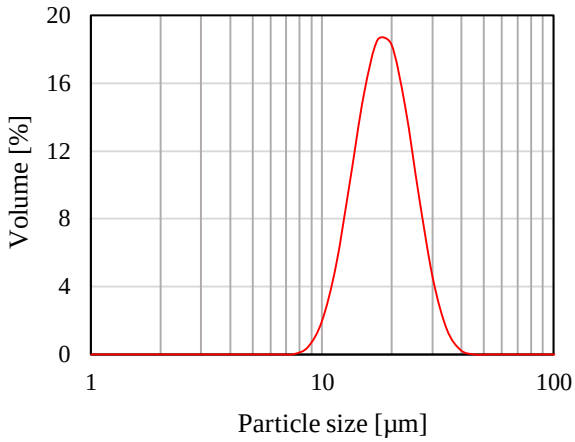

Figure III-24: Pore size distribution of the nylon powder

This method enables to increase the porosity up to 75 % if the proportion is 65 % of the total volume. However, it also increases the effective pore radius. Moreover, the samples are very fragile and sensitive to even small mechanical solicitation. Thus, this solution was finally not used in the following.

Table III-5 presents the eight manufacturing protocols used to obtain zirconia samples by sintering. Mainly the temperature and the pore former rate are changed. The characteristics of the eighteen zirconia samples manufactured by sintering are presented in Appendix D.

Table III-5: Manufacturing protocols of zirconia samples by sintering

	P_f [MPa]	m_s [g]	T_{sin} [°C]	t_{sin} [min]	Pore former [%]
1	35	20	1450	120	47.8
2	35	20	1280	120	47.8
3	35	20	1280	120	64.7
4	35	30	1320	120	47.8
5	35	30	1250	120	0
7	35	25	1230	120	0
8	35	20	1230	120	0
9	35	40	1230	120	0

III.4 Manufacturing of a bilayer wick

The aim of this section is the manufacturing of a wick having two different layers in order to increase the thermal and hydrodynamic performance of the LHP. Two methods were tested in this purpose.

III.4.1 Co-sintering of the two layers

The first method is the co-sintering of a zirconia layer on top of a copper layer. Firstly, the top layer (zirconia) is completely manufactured following the method presented in the Section III.3.2. Then, a copper slurry is made following the method presented in the Section III.2.2. This slurry is poured on the top layer which is located in the cylindrical matrix (Figure III-25) and dries during about a week. Then, it is pressed between the two pistons and the rest of the method is similar to the method used to manufacture a single bottom layer. Any protocol presented in Appendix D can be used to manufacture the top layer then the bottom layer. Generally speaking, the protocols having given the best results (See Chapter IV and Chapter V), for both the top and the bottom layers, have been used to co-sinter the two layers together.

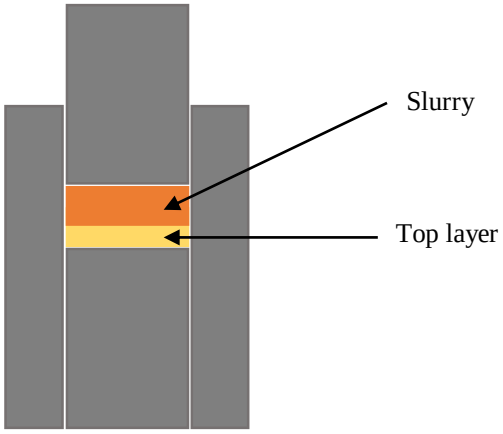

Figure III-25: Schematic of the method to obtain a bi-layer wick

The top layer is not affected by the second sintering because the temperature does not exceed 900 °C which is far below its own sintering temperature. The aim of this method is to assemble the two layers with an excellent contact. For this, the slurry should slightly penetrate the pores of the top layer which help the whole structure to be solid after the sintering of the copper particles. However, the bi-layer wick must be manipulated with great care because a weakness exists at the interface between the two layers. Indeed, the copper and zirconia have a slightly different thermal expansion coefficient (16×10^{-6} K^{-1} and 10×10^{-6} K^{-1} respectively), which can create cracks at the interface. An intermediate layer made of zirconia-copper composite and sintered at the sintering temperature adequate for zirconia, may strengthen this interface. However we could not test this solution in the framework of this thesis.

III.4.2 Coating of a gold film on the top layer

The second method used to manufacture a bilayer wick is the coating. A very thin gold layer is applied on the zirconia bottom surface of the top layer by sputtering. The top layer is located inside a metal coater where the air is removed. The pressure is decreased down to 4×10^{-2} mbar. Then, argon is added. A strong electric power is applied between a gold target (cathode) and the sample (anode). Under the effect of the electric power, the argon ions hit the gold target and eject gold atoms that are deposited in the whole chamber, and in particular on the sample. The operating principle of the system is shown in Figure III-26. For each coater, the thickness of the gold coating depends on the distance between the target and the top layer, on the electrical current and on the coating time. The tests have been conducted with a coater *BAL-TEC SCD*® and the following coating parameters: 60 mA during 200 s and at a distance of 50 mm. It leads to a theoretical gold coating thickness of 75 nm. It enables to drastically reduce the pressure losses through the bottom layer while keeping a high thermal conductance between the evaporator fins and the liquid-vapour interface.

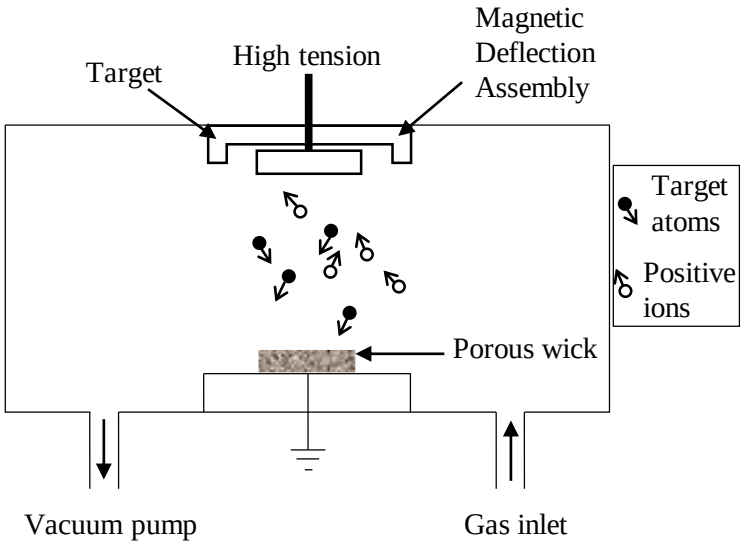

Figure III-26: Schematic arrangement of the gas ion and evaporation sources in a vacuum chamber

Finally, only five bi-layer wicks were manufactured. They are thermally characterised in the Chapter IV.

III.5 Geometrical characterisation of the manufactured samples

The geometrical and topographical characterisations of the porous samples are the first step of the whole characterisation. It enables to know if it is possible to work with a manufactured sample or if it must be removed from the study. For example, a sample having a diameter smaller than 39 mm cannot be kept as it is not suitable for the test benches presented hereafter. Moreover, a sample that would not be flat-disk-shaped or not porous would also be removed from the study. In this section, the methods to complete this characterisation are described.

III.5.1 Determination of the mass and the volume of the sample

The thickness of the samples as well as their diameter are important parameters. They are also necessary to determine the porosity. A calliper is used to measure these parameters. The uncertainty associated with each value is equal 0.3 mm. Indeed, the calliper is very accurate but the samples are not perfectly disk-shaped. The difference between the largest and the smallest diameters can reach up to 0.3 mm as well as the difference between the largest and the smallest thicknesses of the sample. These differences will affect the wick thermal characterisation, as it will be seen in Section V.5.1.1. The mass of the sample is determined with a precision balance *Mettler Toledo*. The accuracy is equal to 1 mg.

In order to determine the porosity, the large majority of the studies (Deng *et al.* [105], Adkins and Dykhuizen [24], Adkins *et al.* [166]…) reports a simple method. The volume and the mass of the sample being known, the Eq. (I-17) is used. However, Williams and Harris [167] used another method called imbibition proposed by Dullien [168]. The porous sample is saturated with highly wetting liquid after having been emptied in a vacuum chamber. The sample weight is recorded before (m_w) and after the wetting (m_{tot}). The following expression gives the porosity:

$$\varepsilon = \frac{\rho_{mat}(m_{tot} - m_w)}{\rho_l m_w + \rho_{mat}(m_{tot} - m_w)} \quad \text{(III-2)}$$

where ρ_{mat} is the wick material density. According to Williams and Harris [167], this method is not suitable to characterise every type of porosity. Indeed, in the case of a biporous wick, this method gives only the macroscopic and open porosity.

In the present study, the porosity is determined with the volume and mass measurements. Depending on the manufacturing process, the samples have a porosity lying between 20 and 60 %. Their diameter varies in a very thin range around 40 mm and their thickness varies from 1.6 to 16 mm. The mass, the thickness and the porosity of the all the manufactured samples are indicated in the Appendix D.

III.5.2 Topographical characterisation

The topographical characterisation of the samples is of interest because the flatness and the roughness of the samples can have an influence on the thermal performance (See Section I.2.2). Indeed, a gap between the evaporator and the porous wick can enhance the thermal performance up to a certain distance. The surface quality is investigated by scanning the sample faces with a confocal microscope *Stil*®. The microscope gives either the evolution of the altitude along a diameter or the topography of the complete surface. Moreover, a method exists enabling to characterise the quality of the contact between the grooved evaporator wall and the porous sample. It consists in setting between these two components a pressure paper provided by *Fujifilm*®. This paper becomes pink if it is submitted to high pressure.

Figure III-27 shows two different methods to characterise the topography of two samples, taken as examples (Cu-sin-7-c and Cu-sin-2-c). The profiles obtained with the confocal microscope (a, d) enables to estimate the roughness of the sample whereas the study of the complete surface (b, e) enables to investigate its flatness. The red areas are higher from a reference plane than the blue areas. Finally, the pressure paper characterises the contact between the porous sample and the evaporator (c, f). In these pictures, the pink areas indicate a higher contact pressure than the white ones.

The comparison of the pictures (b) and (e) with the pictures (c) and (f) show a correlation between the pink areas of the pressure papers and the red areas of the pictures obtained with the microscope. It confirms that the surface topography affects the quality of the contact between the evaporator wall and the wick.

The manufacturing process leads to differences of the surface topography between the samples. The profile (a) has a domed profile whereas the profile (b) is a cavity. This is due to the surface quality of the press. A flat side would lead to straight isocolour lines whereas the colour field is more heterogeneous if the sample is not flat. For each example, the pictures are in good accordance but they provide different information about the surface quality (roughness, flatness, contact). The type of surface profile (obtained with the 2D picture of the confocal microscope), the depth of the cavity or the dome and an estimation of the surface roughness are indicated for each sample sides. The depth or the height are determined by measuring the difference between the highest and the lowest points of the altitude profile. The roughness is determined by measuring on the profile the average height difference between the peaks and the off-peaks.

Moreover, the manufacturing process leads to difference between the two sides of the same sample. One side, called side A, is convex (a peak or a dome, as illustrated with the sample Cu-sin-7-c) whereas the other side, called side B, is concave, like a cavity (as illustrated with the sample Cu-sin-2-b).

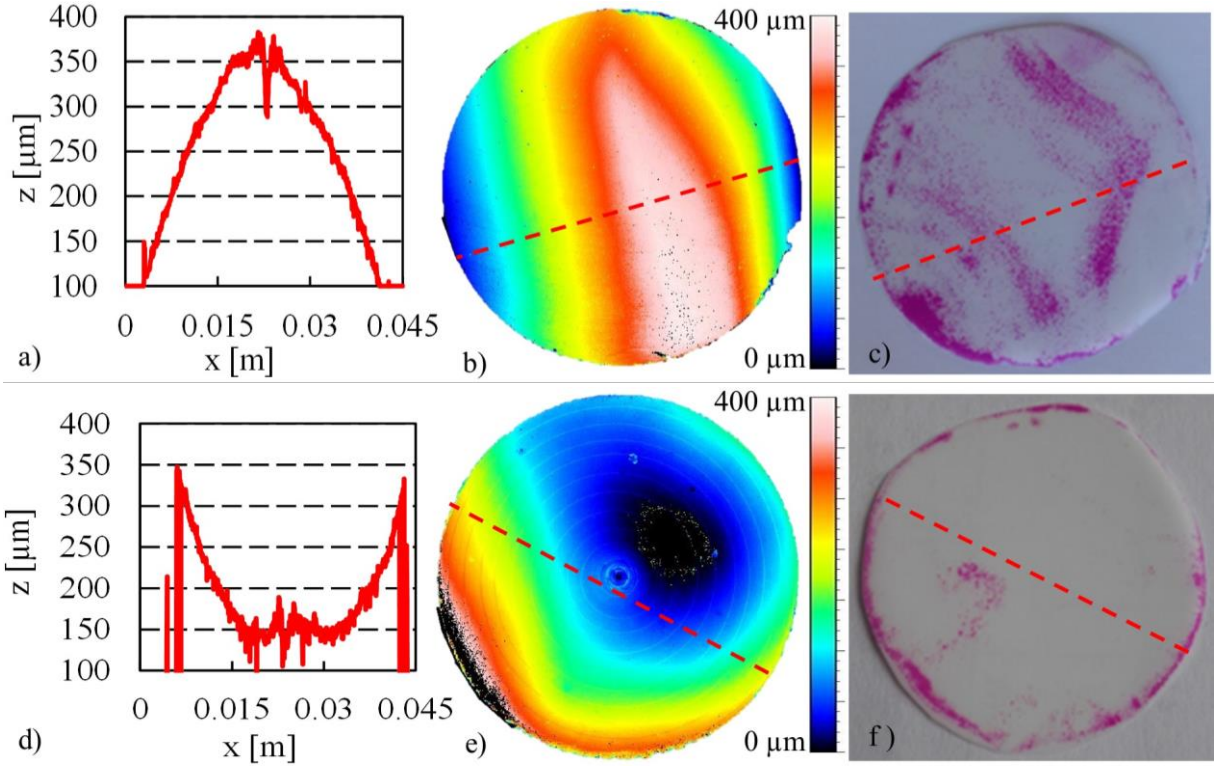

Figure III-27: Examples of topography analysis by confocal microscopy (profile (a, d) and complete surface (b, e)) and with pressure paper (c, f) of the side A of sample Cu-sin-7-c (a, b, c) and the side B of sample Cu-sin-2-c (d, e, f)

III.5.3 Microscopic characterisation

The samples can be microscopically characterised in order to investigate the pore radius and the porosity. The X-ray computed tomography (XRCT) enables to see if the pores are interconnected or not. An example of a picture obtained by XRCT is presented in Figure III-28 (a). It can be noted that the minimum resolution of such a device (0.7 µm per pixel) is not high enough to detect the smallest pores in the manufactured samples. However, it is an interesting method to detect large defects inside the porous wick, since it is the only one enabling a view of the inner structure of the porous wick.

The pore radius can also be determined by optical microscopy. It gives a large view of the porous sample surface (Figure III-28 b), from small to large pores. A maximum number of pore radii are measured on the microscopic view, from which the median radius r_p is calculated (Eq.(I-26)). The number of pores that can be measured with such pictures varies from 10 to 20. This method leads to a large uncertainty and provides only an order of magnitude of the pore size distribution since the number of pore radius measured is low and the perimeter of each pore is never perfectly circle-shaped.

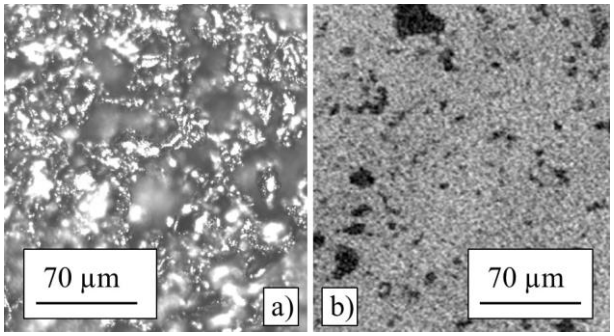

Figure III-28: XRCT of the sample Ni-sin-x (a) and microscopy of the sample Cu-sin-3-a (b)

In the case of a sample with large pores, the XRCT allows the investigation of its architecture. Figure III-29 shows a XRCT in 2D and 3D of a porous sample where the pores are interconnected. To estimate the porosity and the pore radius, a threshold is arbitrarily chosen in the degree of grey in order to change the original greyscale picture into a black and white picture. The pore radius is directly measured on the figure whereas the porosity is the ratio of the black area on the total area. The uncertainty of this method is due to the threshold choice. The XRCT is *a priori* a non-destructive method but the sample must be crossed by the X rays. Thus, it must be thin or made with a material having a low atomic number. The nickel, the copper and the zirconium have atomic numbers of 28, 29 and 40 respectively. It leads to a maximum sample volume of several mm^3 whereas the manufactured volume may reach several cm^3. Thus, to use the XRCT, the samples must be broken in small pieces. That's why, in the following, this method is not chosen to determine the characteristics.

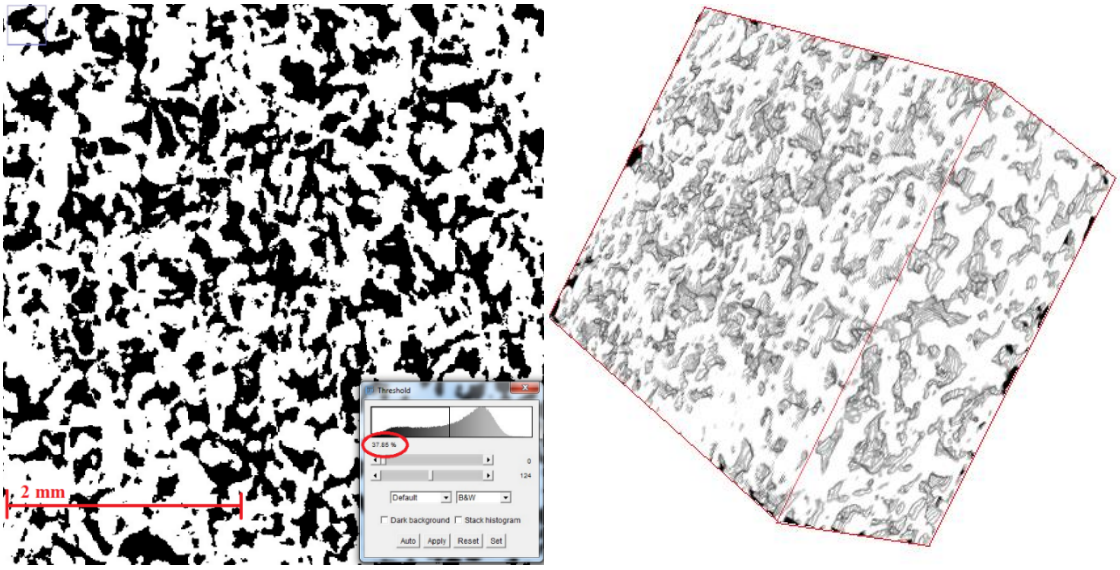

Figure III-29: XRCT of a sample with large pores (2D and 3D views of the sample Ni-sin-x)

Finally, the scanning electron microscope (SEM) can be used to measure the pore diameter and to estimate the interconnection of the pores. The very high resolution of this method compared to the optical microscopy or the XRCT, makes it a very good candidate to characterise the mesostructure as well as the microstructure of a porous structure (Figure III-30).

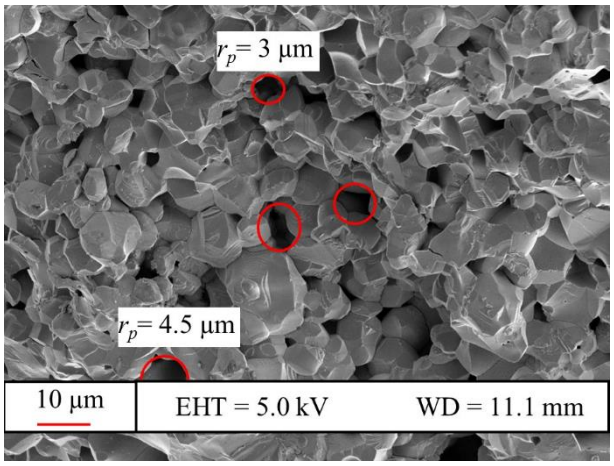

Figure III-30: SEM view of the sample Cu-sin-6-b

In this study, the pore radius is determined by means of optical microscopy and the results are given in Appendix D.

III.6 Conclusion

In this part, several methods have been proposed to manufacture a wick suitable for a flat-disk shaped evaporator, 40 mm in diameter, and mechanically resistant. The main investigated method, which is also the most usual one, is the partial sintering of powder. This technique can be used to manufacture both the copper layer and the zirconia layer of a bi-layer capillary structure. Moreover, the method of freeze casting of zirconia has been tested for the top layer. The procedures tested with the latter method have all led to cracks and mechanical weaknesses. However, it is promising if conducted for a relatively thin wick and with a binder having a high molecular mass. In total, forty-seven samples have been manufactured and some of them have been used to test the coating or the co-sintering.

The main challenge of this part is to obtain a bi-layer wick. Two methods, the co-sintering and the coating of a sintered layer with an ultra-thin gold layer, enable to correctly assemble two layers together. They do not exhibit any problem even if, concerning the co-sintering, it is impossible to know the quality of the contact between the two layers.

Geometrical, topographical and microscopic characterisations have been conducted on the sintered porous samples in order to determine their porosity, the median pore radius, the interconnectivity of the pores, and the surface flatness. In most cases, they are not flat and exhibit a concave side and a convex one. The hydrodynamic characterisation of the samples and the determination of their thermal performance is presented in the Chapter IV and Chapter V.

Chapter IV Hydrodynamic characterisation

The present chapter is dedicated to the hydrodynamic characterisation of the samples presented in the Chapter III. In a first part, a state-of-the-art of the hydrodynamic test benches used in the literature is presented. Then, several procedures are defined in order to characterise the hydrodynamic parameters of the samples and mainly their effective pore radius and their permeability. Indeed, these characteristics are expected to enable the understanding of the thermal behaviour of the porous structures that is presented in Chapter V of this thesis. Finally, the results are presented and discussed. The reproducibility of the hydrodynamic characteristics for the same manufacturing protocol is investigated. Then, the influence of the manufacturing parameters on the wick characteristics is studied. In the last section, the results are compared with the ones found in the literature.

IV.1 State-of-the-art of the hydrodynamic characterisation methods

This section gives a state-of-the-art of the existing test benches described in the literature by various authors in order to determine the hydrodynamic characteristics of porous samples. These test benches enable to determine the permeability and the effective pore radius with various methods. These methods are discussed in order to design a specific test bench dedicated to the characterisation of flat disk shaped LHP wicks.

IV.1.1 Determination of the permeability

Generally speaking the permeability of a porous medium is determined by means of the Darcy's law which mainly depends on the mass flow rate and on the pressure difference between the two sides of the porous medium. A system with a pressure sensor and a flow rate measurement would be suitable but some authors report other methods in the literature.

A variant of this method consists in creating a hydrostatic pressure difference and measuring the mass flow rate flowing through the wick. Singh *et al.* [169] proposed an experimental apparatus designed to this purpose, shown in Figure IV-1. A constant hydrostatic pressure is applied to the fluid while it flows through the wick. The volumetric flow rate is recorded with a mass balance. The Darcy's law enables to determine the permeability of the sample.

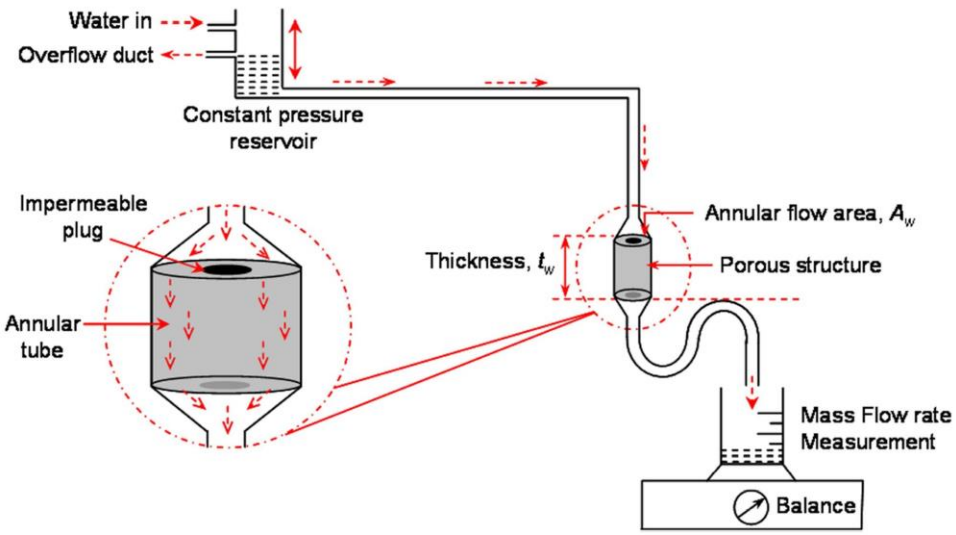

Figure IV-1: Experimental apparatus to measure the permeability using a constant pressure reservoir (Singh *et al.* [169])

Another method consists in applying a sinusoidal pressure signal by means of a shaker. Looyestijn *et al.* [170] used this method based on acoustic activation and detection with a nuclear magnetic resonance (NMR) technique. The outlet signal depends on the applied signal and on the permeability. The detection of the signal and the implementation of a complex theory underlying this method enables to determine the permeability. The experimental apparatus in shown in Figure IV-2. The major advantage of the NMR is that is doesn't require time to be accurate, contrarily to the previous test benches.

The most current method to determine the permeability is the rate-of-rise test (Holley and Faghri [171], Zhao and Liao [108]). The experimental apparatus consists of a porous medium inserted in a tube partially immersed in a reservoir (Figure IV-3). The liquid moves up by capillarity until reaching the equilibrium height H_{eq}. The same test can be done with the liquid moving down if the initial hydrostatic

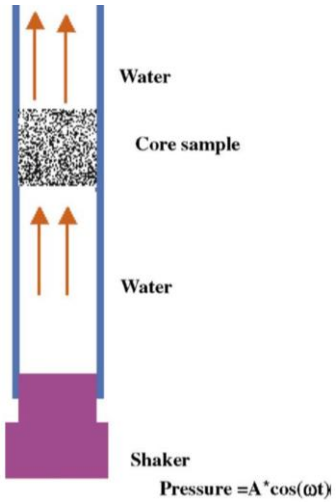

Figure IV-2: Experimental set up to measure the permeability by NMR (Looyestijn *et al.* [170])

force is greater than the capillary force. The pressure balance, in which the capillary pressure compensates the hydrostatic and frictional pressure losses, is written during the capillary rise process:

$$\frac{2\sigma}{r_{p,eff}} = \frac{\mu_l \varepsilon}{K} H \frac{dH}{dt} + \rho_l g H \qquad \text{(IV-1)}$$

where $r_{p,eff}$ is the effective pore radius and H the height of the liquid column. In this test, it can be difficult to distinguish the meniscus position in the porous sample. Moreover, the experimental measurements can suffer from several inaccuracies, for example the assumption of no evaporation and errors in the meniscus location (Adkins and Dykhuizen [24]). At last, this method requires to know the effective pore radius. That is why Deng *et al.* [105] as well as Adkins and Dykhuizen [24] used the same experimental set up to measure both the permeability and the effective pore radius, as explained in the next section.

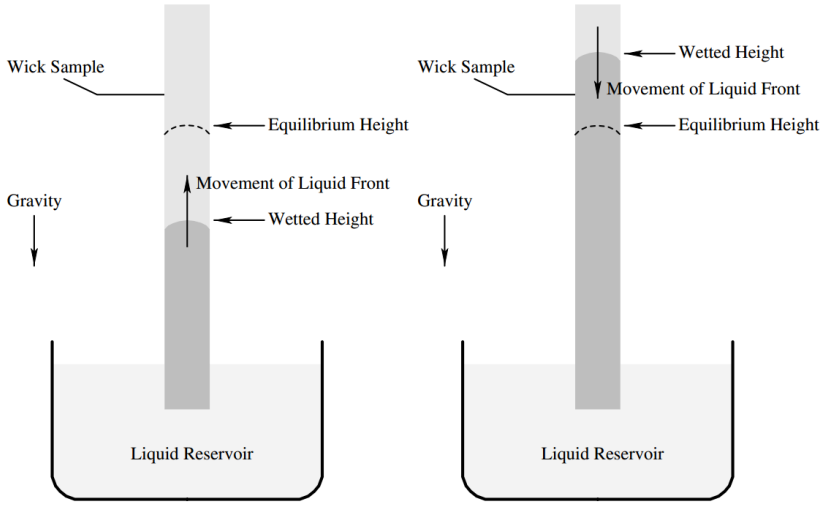

a) Rising meniscus b) Falling meniscus

Figure IV-3 : Schematic of the test benches for effective pore radius measurements (Holley and Faghri [171])

IV.1.2 Determination of the effective pore radius

The effective pore radius can be determined with the test bench shown in Figure IV-3. Indeed, if the rate-of-rise test is conducted until the meniscus reaches its equilibrium height H_{eq}, it is possible to

determine the effective pore radius. At the end of the test, the hydrostatic force compensates the capillary force, leading to:

$$\Delta P_{cap,max} = \rho_l g H_{eq} = \frac{2\sigma}{r_{p,eff}} \quad \text{(IV-2)}$$

The main sources of errors in this test are due to the assumption of a contact angle value (generally 0 °) leading to improperly write $r_{m,min} = r_{p,eff}$, and to the fact that the pore radius does not correspond to the maximum capillary pressure if the porous medium is heterogeneous.

Another test bench using the bubble point testing method is proposed by Singh *et al.* [7] (Figure IV-4). Air is injected with a syringe in the core of a wick sample shaped as a hollow cylindrical sleeve. The air pressure is progressively increased and recorded by a manometer. A bubble gets out of the wick external surface if the air pressure is higher than the maximum capillary pressure. The effective pore radius is then determined with Eq.(I-24).

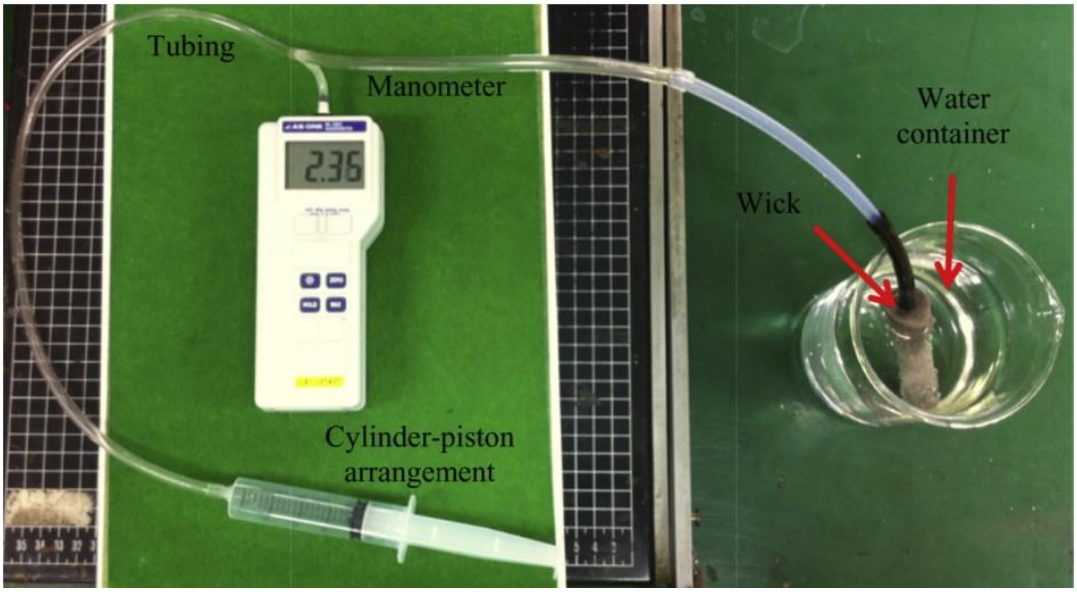

Figure IV-4: Experimental apparatus designed to perform the bubble point testing (Singh *et al.* [7])

A similar method can be conducted with a different experimental set up presented in Figure IV-5, proposed by Singh *et al.* [169]. The cylindrical wick sample is placed inside a glass U-tube with a water pool on the upper side and air on the lower side. Water is introduced in the tube branch opposite to the wick, creating a hydrostatic pressure on the air pocket at the back face of the wick. When this hydrostatic pressure is too high, the capillary pressure is not able to prevent the air to flow through the wick and a bubble appears in the water pool.

However, none of these tests is able to measure the pore size distribution. In order to obtain this data, the mercury injection method can be used (Leon [172]). Since the mercury is a non-wetting fluid, it can only penetrate the porous sample by applying a pressure. As the pressure increases step by step, smaller pores are progressively reached by the mercury. The Laplace-Young is applied for each pressure step enabling to obtain the pore size distribution. This method is used to measure the pore size distribution as well as the porosity (Adkins and Moss [173], Guyon *et al.* [174]).

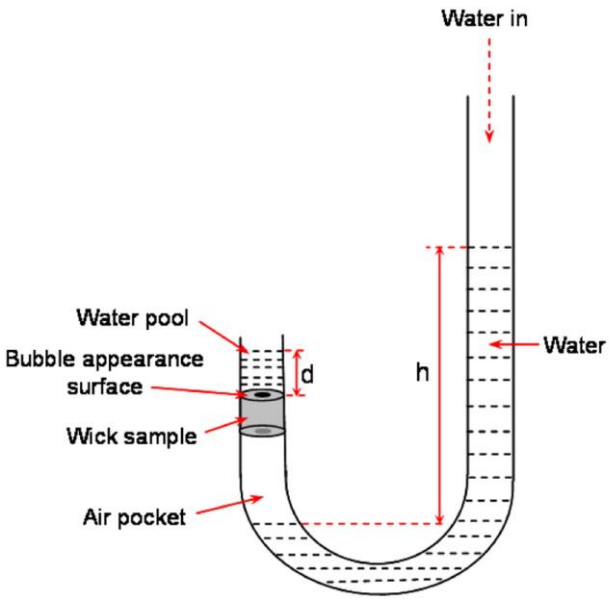

Figure IV-5: U-tube bubble point testing system (Singh *et al.* [169])

In the present work the mercury injection method was tested (it is described with more details in Appendix C), but not maintained because it is a pollutant, destructive method as the mercury is toxic. A specific test bench similar to the one of Singh *et al.* [169] was finally designed in order to determine the permeability and the effective pore radius of the manufactured wick samples. This method is selected due to its non-destructive character, enabling to perform reproducibility tests. The advantage of this method, compared to the rate-of-rise test, is that the position of the meniscus is more accurately defined. The experimental apparatus is described in the next section.

IV.2 Experimental apparatus and procedures

IV.2.1 Experimental apparatus

The experimental set up to measure the permeability and the effective pore radius, schematised in Figure IV-6, is constituted by:

- A reservoir made of a transparent tube with an internal diameter of 194 mm, an external diameter of 200 mm and a height of 2000 mm.
- A removable tube with an internal diameter of 44 mm, an external diameter of 50 mm and a height of 1800 mm. A wick carrier is inserted inside the tube. The top part of the wick carrier is screwed against the bottom part in order to ensure the sealing of the system. O-ring seals set in a throat, or at the contact between the wick and the carrier avoid the liquid leaks (Figure IV-6 b).
- A removable handling system by clamping ring to adjust the removable tube in the reservoir.
- A system enabling to empty the reservoir and to fill a drain pan with a butterfly valve. The drain pan has a volume greater than the reservoir one.

The wick can be set at the bottom of the test tube in order to measure the permeability (Section IV.2.3) or at the top of the test tube in order to measure the effective pore radius (Section IV.2.4). During the tests, the water levels in the test tube are measured with a tape measure having an uncertainty of about 5 mm. A stopwatch records the time.

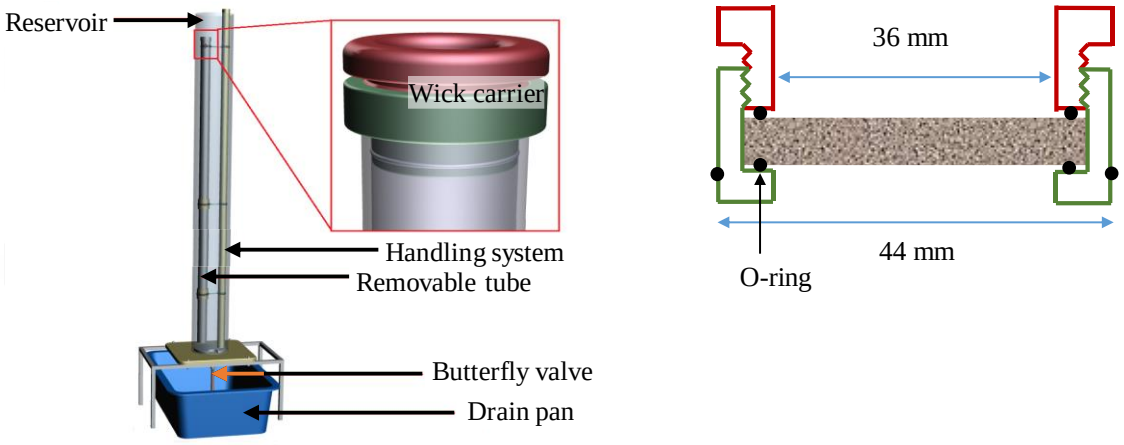

a) Global view b) Wick carrier dimensions

Figure IV-6: Schematic of the experimental setup

IV.2.2 Saturation of the wick

The determination of the hydrodynamic characteristics preliminarily requires to remove the air from the porous medium. The experimental procedure used to saturate the wick with liquid is the following (Figure IV-7):

- (a) The test tube and the reservoir are emptied.
- (b) The reservoir is filled.
- (c) The water level in the reservoir overcomes the wick carrier height. A pressure difference is created, expelling the air outside the porous medium.
- (d) The water penetrates the wick and saturates it.

Note that this procedure is efficient only for a fluid exhibiting a good wettability on the wick material. In the case of a non-wetting fluid, a higher hydrostatic pressure would be required to saturate the wick with the liquid.

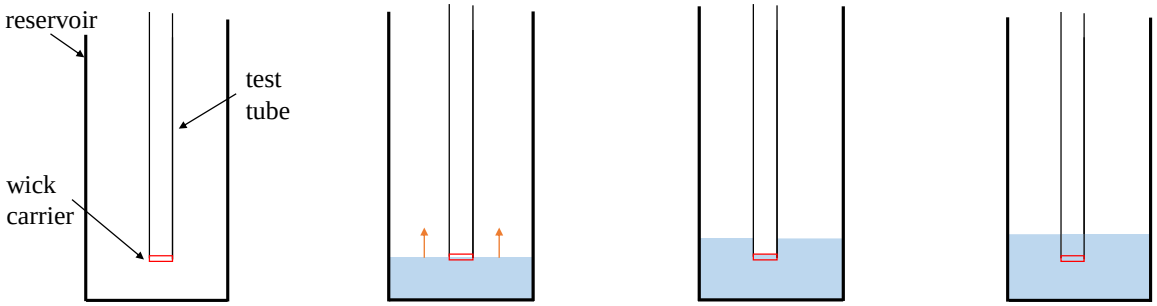

Figure IV-7: Schematic of the experimental procedure used to saturate the wick with liquid

IV.2.3 Determination of the permeability

A procedure has been developed in order to measure the permeability that directly follows the previous step of the wick saturation (Figure IV-8):

- (e) The test tube is completely filled and the liquid flows through the porous medium. The fluid velocity is maximum at the beginning of the experiment.
- (f) The fluid continues to flow through the wick with a decreasing velocity.
- (g) The water levels in the reservoir and in the test tube reach the same height H_∞.

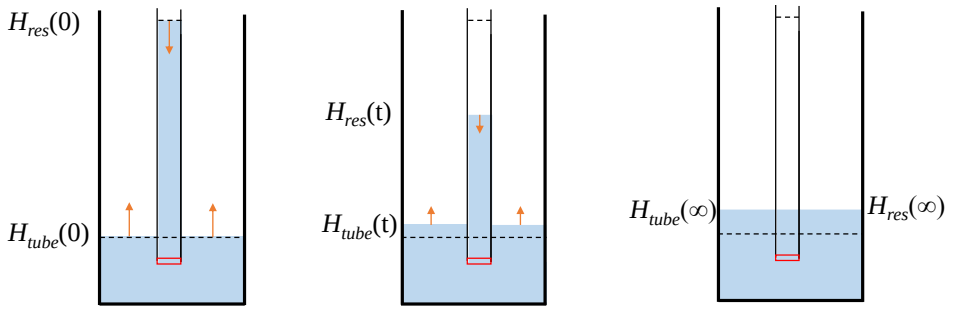

(e) t = 0 (f) t = t (g) t = ∞

Figure IV-8 : Schematic of the successive steps enabling to measure the permeability

When the liquid flows through the wick, the Darcy's law can be applied. It is expressed as follows:

$$\Delta P_w(t) = \frac{\mu_l \, e_w \, u_{Darcy}(t)}{K} \tag{IV-3}$$

with $\Delta P_w(t)$ the pressure difference across the porous medium and $u_{Darcy}(t)$ the Darcy's velocity. The Darcy's velocity can be written as follows:

$$u_{Darcy}(t) = \frac{\dot{V}(t)}{S_w} \tag{IV-4}$$

where $\dot{V}$ is the volumetric flow rate through the wick. Moreover, the volumetric flow rate can be defined by means of a mass balance inside the test tube:

$$\dot{V}(t) = -\frac{dH_{tube}(t)}{dt} S_{tube,i} \tag{IV-5}$$

where $H_{tube}(t)$ is the water level inside the tube and $S_{tube,i}$ the tube inner cross sectional area. Moreover, the pressure difference across the porous medium is also equal to the hydrostatic pressure of the liquid column:

$$\Delta P_w(t) = \rho_l g (H_{tube}(t) - H_{res}(t)) \tag{IV-6}$$

where $H_{res}(t)$ is the water level in the reservoir. Thereby, by combining equations (IV-3) to (IV-6), a differential equation is obtained:

$$\frac{dH_{tube}(t)}{dt} = -\frac{K \rho_l g (H_{tube}(t) - H_{res}(t))}{\mu_l \, e_w} \frac{S_w}{S_{tube,i}} \tag{IV-7}$$

At each time, a mass conservation equation expresses that the fluid which leaves the test tube through the porous medium flows entirely into the reservoir (Figure IV-8):

$$\big(H_{tube}(0) - H_{tube}(t)\big) S_{tube,i} = (H_{res}(t) - H_{res}(0))(S_{res,i} - S_{tube,o}) \tag{IV-8}$$

where $S_{res,i}$ and $S_{tube,o}$ are the inner cross sectional area of the reservoir and the outer cross sectional area of the test tube, respectively. At the end of the experiment, both levels are equals to H_∞. Thus, the mass conservation equation can be rewritten in the following form:

$$(H_\infty - H_{tube}(t)) S_{tube,i} = (H_{res}(t) - H_\infty)(S_{res,i} - S_{tube,o}) \tag{IV-9}$$

which leads to:

$$H_{res}(t) = H_{\infty}\left(1 + \frac{S_{tube,i}}{S_{res,i} - S_{tube,o}}\right) - H_{tube}(t)\frac{S_{tube,i}}{S_{res,i} - S_{tube,o}} \quad \text{(IV-10)}$$

Combining equations (IV-7) and (IV-10) leads to:

$$\frac{dH_{tube}(t)}{dt} = -\frac{(H_{tube}(t) - H_{\infty})}{\tau} \quad \text{(IV-11)}$$

with:

$$\tau = \frac{\mu_l \, e_w \, S_{tube,i}}{K\rho_l g \, S_w \left(1 + \frac{S_{tube,i}}{S_{res} - S_{tube,o}}\right)} \quad \text{(IV-12)}$$

the time constant of the differential equation (IV-11). Solving this equation leads to:

$$H_{tube}(t) = H_{tube}(0) - (H_{tube}(0) - H_{\infty}).\left(1 - \exp\left(-\frac{t}{\tau}\right)\right) \quad \text{(IV-13)}$$

and

$$H_{res}(t) = H_{res}(0) + (H_{tube}(0) - H_{\infty}).\left(1 - \exp\left(-\frac{t}{\tau}\right)\right)\frac{S_{tube,i}}{S_{res} - S_{tube,o}} \quad \text{(IV-14)}$$

During the experiment, both liquid levels are recorded as a function of time and are fitted by means of equations (IV-13) and (IV-14) with the least-squares method to determine τ, and thus the permeability by means of equation (IV-12). An example of experimental data points and the corresponding fitting curve is presented on Figure IV-9 (a). The evolution of the Darcy's velocity as a function of the pressure difference across the wick is plotted in Figure IV-9 (b). The linear shape of the curve confirms the validity of Darcy's law in the present configuration.

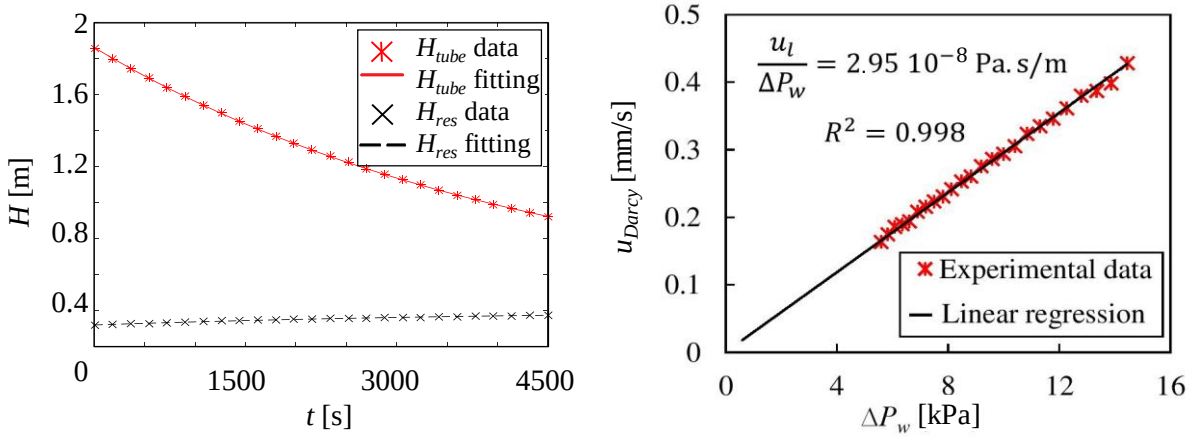

a) Measured and fitted curves of the water levels evolution

b) Liquid velocity as a function of the pressure difference during the test

Figure IV-9: Example of experimental data enabling to determine the permeability (Cu-sin-7-c)

Most tests have been performed with water. However, two tests were conducted with pentane in order to see if the permeability has the same value with both fluids. Indeed, the permeability is expected to be a characteristic of the porous medium only. The tests with pentane are conducted with the sample Cu-sin-1-c, having a high permeability with water, and with the sample Cu-sin-6-c, having a low

permeability with water. The results do not show a significant difference between water and pentane (Figure IV-10). Thus, the other tests are performed only with water, which is a low cost and non-toxic fluid.

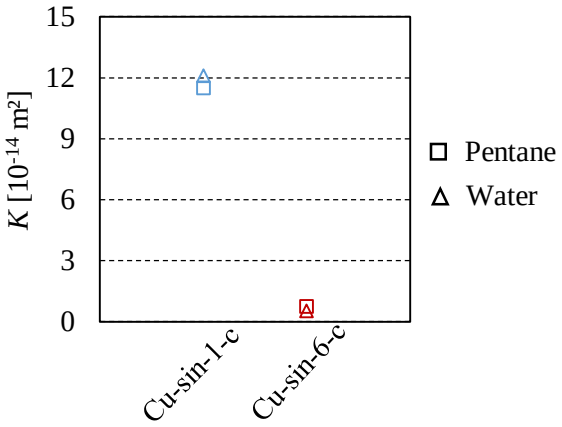

Figure IV-10: Comparison between the permeabilities measured with pentane and with water

IV.2.4 Determination of the effective pore radius

An experimental procedure was developed in order to measure the effective pore radius of the various samples. The wick must be saturated with liquid. Thus, the experiment starts with the steps (a) to (d) previously described to measure the permeability and goes on with the following steps (Figure IV-11):

- (h) The test tube and the reservoir are filled up to the top, then the wick carrier is set at the top of the test tube.
- (i) The test starts as the reservoir is slightly emptied. A hydrostatic pressure difference is created between the pool and the test tube. This pressure difference is compensated by the capillary force in the porous medium. The water level is decreased by steps of 5 cm until 20 cm and then, by steps of 10 cm until the wick depriming. Each step is twenty minutes long. This time is considered to be long enough to observe the wick depriming in case the hydrostatic pressure is higher than the capillary pressure.
- (j) The hydrostatic pressure overcomes the maximum capillary pressure and the wick deprimes. It is detected when an air bubble appears in the test tube below the wick. The test is stopped and the corresponding height is recorded.
-

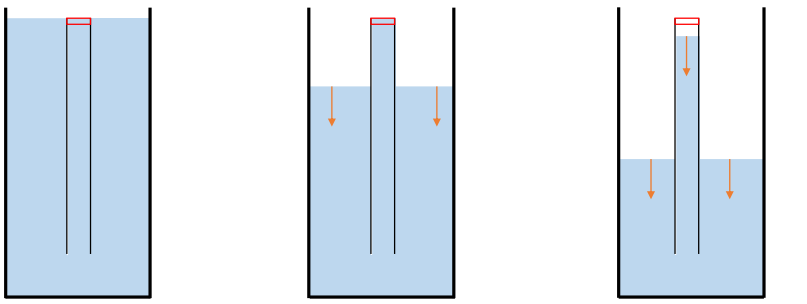

Figure IV-11 : Schematic of the successive steps enabling to measure the effective pore radius

An example of evolution of both liquid levels is shown in Figure IV-12. At the beginning, the liquid level in the reservoir decreases whereas the liquid remains inside the porous structure by capillarity.

Then, the wick depriming leads to a drop of the liquid level in the test tube. The minimum meniscus radius is determined with the Eq. (I-24):

$$r_{m,min} = \frac{2\sigma}{\Delta P_{cap,max}}$$

where $\Delta P_{cap,max}$ is the maximum sustainable capillary pressure corresponding, in the test, to the hydrostatic pressure of the liquid column:

$$\Delta P_{cap,max} = \rho_l g H_{max} \quad \text{(IV-15)}$$

where H_{max} is the maximum difference between both levels before the depriming of the wick. In the example shown in Figure IV-12, the sample Cu-sin-5-a is able to sustain a hydrostatic difference of 90 cm before the wick depriming, which corresponds to a minimum meniscus radius of 16.2 µm, in case of water used as the fluid.

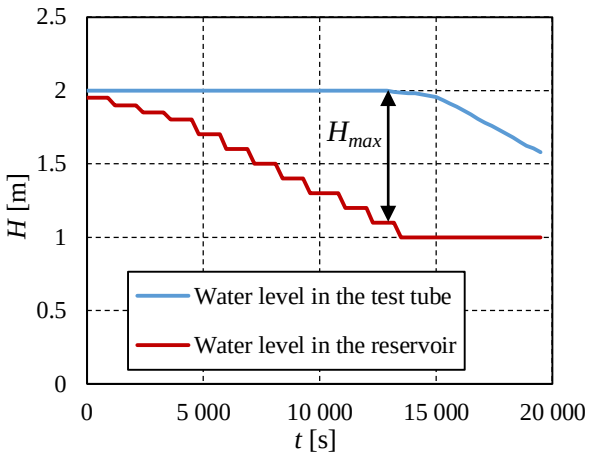

Figure IV-12: Example of minimum meniscus radius determination (sample Cu-sin-5-a).

A maximum height difference of 1.8 m can be measured with this bench. It prevents the measurement of a meniscus radius smaller than 8 µm when water is used.

All tests were performed with water. However, as explained in Section I.2.1, the contact angle between the wick material and the liquid has a significant influence on the minimum meniscus radius and thus, on the maximum capillary pressure. Indeed, an increasing contact angle of the working fluid on the pore wall decreases the capillary pressure (Eq. (I-1)). Moreover, a contact angle close to zero means an excellent wettability which may modify the heat transfer at the triple line. That will be studied in Chapter V.

A measure of the static contact angle has been performed by deposing a liquid droplet on an oxidised copper surface and a non-oxidised one and by taking a photograph. The angle was measured between the horizontal solid/liquid interface and the tangent of the droplet at the triple point (Figure IV-13). The results show that pentane has a better wettability than water, and both fluids have a better wettability on the non-oxidised surface.

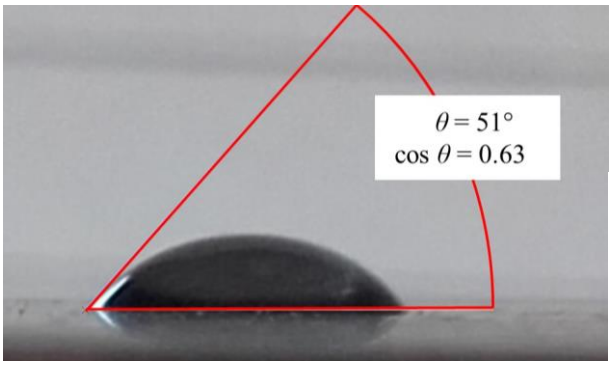

a) Water / Oxidised copper

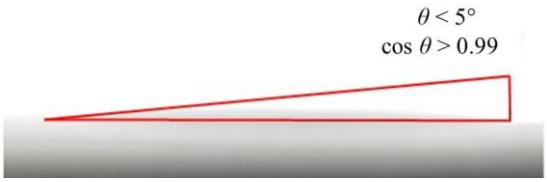

b) Pentane / Oxidised copper

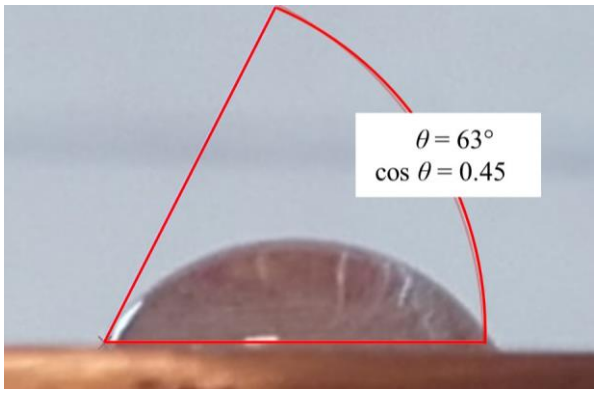

c) Water / Non-oxidised copper

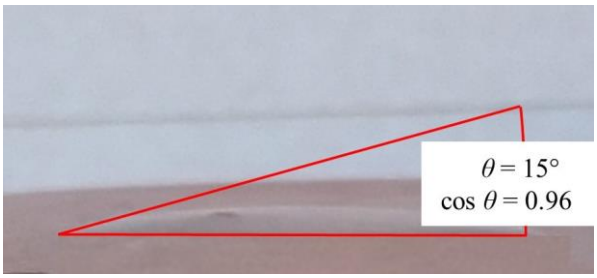

d) Pentane / Non-oxidised copper

Figure IV-13: Contact angle of water (a) and pentane (b) on oxidised copper, and water (c) and pentane on standard copper (c)

The knowledge of the minimum meniscus radius and of the contact angle enables to determine the effective pore radius $r_{p,eff}$, using equation (I-25). The effective pore radius with pentane as working fluid is equal to $r_{m,min}$ since cos θ is considered equal to 1 in this case. The contact angle between zirconia and water is taken in the literature. Gonzalez-Martin *et al.* [100] measured a contact angle of 71.8°.

The characterisation of the samples manufactured during this PhD work are presented in the following section.

IV.3 Results and discussions

IV.3.1 Reproducibility of the protocols

The study of the effect of the manufacturing parameters on the sample characteristics relies on the design of experiment presented in Section III.2.2. However, it is important to check that the same sintering parameters give the same sample characteristics. In this section, the results of various samples manufactured and characterised at least three times using the same protocols are studied.

Figure IV-14 presents the measurements of the thickness e_w, the porosity ε, the permeability K and the effective pore radius $r_{p,eff}$ obtained with these samples. There is a lack of results concerning the effective pore radius and the permeability because some manufacturing protocols have led to diameters incompatible with the experimental apparatus (Zi-sin-3) and because some samples were broken after the sintering due to their mechanical brittleness. It is possible to measure the porosity and the thickness of a broken sample, but not its effective pore radius and its permeability. Except the Zi-sin-6 protocol, the manufacturing protocols enable to obtain reproducible porosities and permeabilities. However, the effective pore radius is not reproducible. That can be explained because, contrarily to the other

characteristics, the effective pore radius is governed by local phenomena in the porous medium. Indeed, it represents the largest interconnection radius from the top of the wick to the bottom. As the structures are heterogeneous, this parameter is more likely to take different values from a sample to another one than the global characteristics as the permeability, the thickness or the porosity. To a less extent, the thickness is not reproducible either. That can be explained by the manufacturing procedure. The slurry is dried during about a week but the degree of humidity vary from a week to another. Thus, if water is not completely removed from the slurry, the real mass of copper decreases and thus, the thickness.

These conclusions are not valid for the Zi-sin-6 protocol. The thickness varies in a relatively small range (5.2 mm to 6.75 mm) but all the other characteristics are not reproducible, especially the permeability, which varies between 0.57×10^{-14} m² and 138×10^{-14} m². This can be due to the high sensitivity of the zirconia characteristics to the sintering temperature, much more than copper. A small change of temperature (in the order of 10 K) of the sintering temperature of zirconia may induce the shrinkage of the sample. The sintering furnace having an uncertainty of around 10 K, it is difficult to reproduce the sintering temperature and thus, the zirconia samples characteristics.

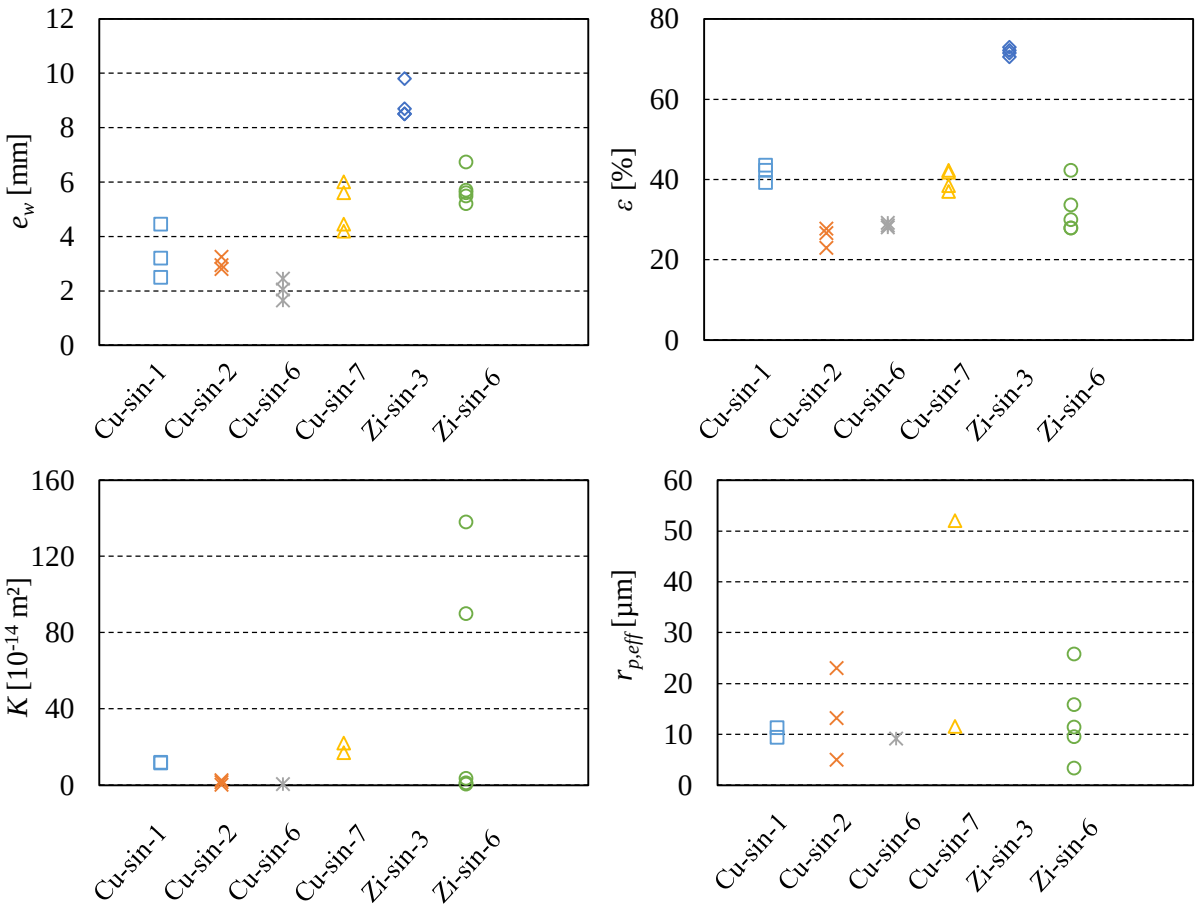

Figure IV-14: Hydrodynamic characteristics of samples obtained with the same protocol

In conclusion, the reproducibility of the manufacturing protocols is satisfactory for the copper samples and enables to investigate the influence of the manufacturing parameters on the wick characteristics. However, the discrepancy in terms of effective pore radius has to be kept in mind. In the following, when several samples were available with the same protocol used in the design of experiment, the one having the smallest pore radius was kept.

IV.3.2 Influence of the sintering parameters on the copper sample characteristics

The knowledge of the influence of the sintering parameters on the hydrodynamic characteristics of porous structures should help to manufacture samples with the expected characteristics. The main sintering parameters are the pressure applied on the sample, the mass of sintered powder, the sintering temperature and the sintering time. This study is only performed with the copper samples manufactured following the two-level fractional factorial design described by Montgomery [165] and presented in Table III-2 (See Section III.2.2 for further details).

Table IV-1 presents the thickness, measured with a calliper, the permeability and the effective pore radius $r_{p,eff}$, measured with the test benches developed in this thesis, and the mean pore radius r_p, obtained by microscopy, of the samples manufactured with eight different sets of parameters. It is important to remind that the test bench is not able to measure an effective pore radius smaller than 5 µm ($r_{m,min}$ = 8 µm) if water is used as a working fluid. The numbers are written in green if they correspond to the targeted range of the bottom layer characteristics detailed in Table II-5 (Chapter II), and in red otherwise.

Firstly, it can be noted that, for a given sample, the pore radius measured by microscopy is smaller than the effective pore radius. It means that, whatever the sample, there is at least one large interconnection pore which goes entirely through the wick and prevents a high capillary force. The pore radii observed by microscopy lie between 6.3 µm and 10.4 µm. These values are slightly above the pore radius predicted by the Chi correlation which is of 6 µm (Eq.(I-20)). The observed difference is satisfying since this correlation was developed for spherical powder particles, while the powder used in the present study is dendritic.

Secondly, it is observed that samples corresponding to the protocols 1 and 5 corresponds very well to the targeted characteristics. Indeed, their permeability and their porosity are higher than the minimum recommended values for this layer (2×10^{-14} m² and 37 % respectively). Their thickness is in the expected range and their pore radius corresponds to operating limits lying between 120 W and 250 W (i.e. to heat flux densities ranging between 10 W/cm² and 20 W/cm²), as shown in Figure II-21. Their effective pore radius is only slightly higher than 10 µm which is acceptable in terms of maximum capillary pressure.

Table IV-1: Hydrodynamic characteristics of the manufactured samples

Sample	Protocol	P_f	m_s	T_{sin}	t_{sin}	e_w [mm]	ε [%]	K [10^{-14} m²]	$r_{p,eff}$ [µm]	r_p [µm]
Cu-sin-1-b	1	-	-	-	-	3.2	39.3	11.6	11.3	8.4
Cu-sin-2-c	2	+	-	-	+	2.8	27.8	1.37	11.5	7.0
Cu-sin-3-a	3	-	+	-	+	5.2	40.6	10.1	18.3	10.4
Cu-sin-4-a	4	+	+	-	-	4.7	22.6	0.6	<5.0	8.1
Cu-sin-5-a	5	-	-	+	+	2.0	37.0	10.5	10.3	6.6
Cu-sin-6-c	6	+	-	+	-	2.45	28.6	0.52	9.3	6.3
Cu-sin-7-c	7	-	+	+	-	6	41.8	16.9	11.5	9.2
Cu-sin-8-a	8	+	+	+	+	5.45	22.5	0.56	11.3	8.9

Based on the results presented in Table IV-1, the design of experiment enables to quantify the influence of each sintering parameter on the thickness, the porosity, the permeability and the pore radii (Table IV-2). The values listed in Table IV-2 are the mean difference of a given characteristic for a given parameter at its high and low levels, respectively. For example, the four samples obtained with a high pressure applied before the sintering, have a permeability which is lower by 11.51×10^{-14} m² compared to the four samples obtained with a low pressure. Thus, the values must be compared to the average value given in the first line. For example, the median pore radius observed with the microscope

is reduced by 1.08 µm when changing the pressure, but it is not significant compared with the average value 8.11 µm.

Several conclusions can be drawn from this analysis: firstly, an increase of the mass of powder increases the thickness of the samples whereas an increasing forming pressure does not significantly reduce this characteristic. Secondly, the pressure has a significant influence on the porosity and on the permeability. Indeed, under a high pressure, the copper particles which have a dendritic structure can be interleaved or even broken. This phenomenon leads to a significant decrease of these characteristics. The pressure would not be so influent if the particles were spherical. Moreover, a large range of pressures is used (variation by a factor five). Similarly, an increasing forming pressure decreases the effective pore radius. Thirdly, the sintering time is also influent but to a less extent. An increasing sintering time increases the effective pore radius which is not in good accordance with the results proposed in the Section III.1.1.3. However, as explained in Section IV.3.1, this characteristic is governed by local phenomena making difficult any conclusion about it. Nonetheless, the sintering time has no influence on the pore radius r_p measured by microscopy. Finally, the temperature has a small influence but it is important to keep in mind that the investigated temperature range was narrow (800 to 900 °C). The results would probably be different with a larger range.

Table IV-2 also presents the influence of the interactions between the sintering parameters on the wick characteristics. A strong interaction between two parameters means that one of the parameter is very influential if the other parameter has a small value but not influent is the other parameter has a high value, and conversely. In other words, a high interaction value means that a parameter has a lot of influence especially for a certain value of the second parameter of the given couple. In this study, no strong interaction is found: interactions are always small compared to the values corresponding to a significant individual influence.

Table IV-2: Influence of the sintering parameters on the wick characteristics

Parameter	e_w **[mm]**	ε **[%]**	K **[10^{-14} m^2]**	$r_{p,\,eff}$ **[µm]**	r_p **[µm]**
Average	3.98	32.52	6.52	11.04	8.11
	Individual influence				
Forming pressure	-0.25	**-14.3**	**-11.51**	-3.55	-1.08
Mass of powder sintered	**2.73**	-1.3	1.04	0.94	2.08
Sintering temperature	0.00	-0.1	1.20	-0.94	-0.72
Sintering time	-0.23	-1.1	-1.77	3.55	0.23
		Interactions			
Press./Mass - Temp./Time	-0.28	-4.35	-1.41	-3.14	-0.23
Press./Temp. - Mass/Time	0.20	0.45	-1.65	2.95	0.78
Press./Time - Mass/Temp.	0.78	0.65	2.18	0.72	0.53

IV.3.3 Presentation of the hydrodynamic characteristics of the zirconia samples

The zirconia samples have been characterised in order to know if they had characteristics corresponding to the optimum top layer determined in the Chapter II. Eight different protocols have been tested (See Section III.3.2) and the porosity obtained with these protocols is shown in Figure IV-15 as a function of the percentage of pore former agent (PFA). A correct sample is in the green area since it has a sufficient porosity and a sufficient mechanical strength. Being in the brown, or red area, means that the sample have either a too small porosity or a too low mechanical strength, or both.

The protocols Zi-sin-1 to Zi-sin-4, with addition of nylon as a PFA (between 47.8 % and 64.7 %), results in samples with mechanical weaknesses. Moreover, even if the porosity is increased with addition

of PFA, the porosity of the samples obtained with 0 % PFA (protocol Zi-sin-5 to Zi-sin-8) is, in most cases, higher than the minimum value of 30 % (Table II-5). Thus, the manufacturing protocols with PFA are not maintained in the following.

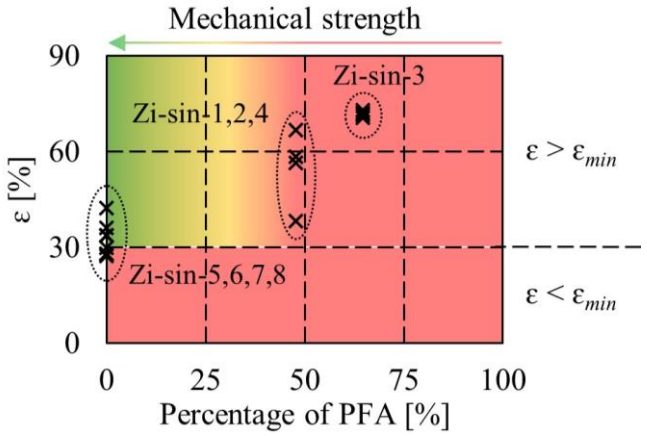

Figure IV-15: Porosity and mechanical resistance of the zirconia samples as a function of the percentage of PFA

The protocol 5 is not maintained because the sintering temperature being too high, the shrinkage is too important and the diameter is not suitable for the test bench. The characteristics of the samples manufactured with the protocols Zi-sin-6, 7 and 8 are presented in Table IV-3. The numbers are written in green if they correspond to the targeted range of the top layer characteristics detailed in Table II-5 (Chapter II), and in red otherwise. Note that the sample Zi-sin-6-b is not presented in this table since it has been used for co-sintering, preventing it to be characterised separately.

None of the samples displays all its characteristics in the optimum range proposed in Chapter II. However, samples Zi-sin-6-a and Zi-sin-8-a and to a less extent Zi-sin-6-e and Zi-sin-6-f have hydrodynamic characteristics suitable for LHPs even if they have only three characteristics included in the optimum range. The fourth one is outside the range and it leads to a reasonable reduction of the operating limits that must be taken into account, designing a LHP. The pore radius of the Zi-sin-6-a and Zi-sin-8-a (11.4 µm and 13.7 µm respectively) reduce the operating limit of 5.5 % and 16.7 % (see Figure II-20) respectively which is acceptable to be used in a LHP. The permeabilities of the samples Zi-sin-6-e and Zi-sin-6-f (1.33×10^{-14} m² and 0.57×10^{-14} m² respectively) reduce the operating limit of around 50 % and 70 % respectively (Figure II-16).

Table IV-3: Hydrodynamic characteristics of the zirconia samples

Sample	P_f [MPa]	m_s [g]	T_{sin} [°C]	t_{sin} [min]	e_w [mm]	ε [%]	K [10^{-14} m²]	$r_{p,eff}$ [µm]
Zi-sin-6-a	35	25	1230	120	6.75	42.3	90	11.4
Zi-sin-6-c	35	25	1230	120	5.7	27.9	138	25.8
Zi-sin-6-d	35	25	1230	120	5.2	27.9	3.7	15.9
Zi-sin-6-e	35	25	1230	120	5.6	33.7	1.33	9.5
Zi-sin-6-f	35	25	1230	120	5.5	30.0	0.57	3.4
Zi-sin-7-a	35	20	1230	120	3.7	33.7	0.2	6.0
Zi-sin-8-a	35	40	1230	120	8.2	33.7	38	13.7

To conclude, the influence of the sintering time and the forming pressure are not investigated since these parameters remain at the same level in each zirconia sintering protocol. The presence of PFA enables to increase the porosity (and probably the permeability) but it also increases the mechanical weaknesses and the risk of cracks. The sintering temperature has a significant influence on the shrinkage and thus, on the porous samples characteristics. However, this parameter is difficult to keep at the same level from one manufacturing to the other due to the uncertainties on the furnace temperature which may reach 15 K.

IV.3.4 Comparison with the literature

According to the literature review, the permeability of a sample is supposed to depend on its porosity and its pore radius (Section I.2.1). Figure IV-16 shows the experimental permeability as a function of the permeability predicted with the Kozeny-Carman correlation (Eq. (I-19)) as well as with the Rumpf-Gupte correlation (Eq. (I-21)). The experimental data are not compared with the correlations of Chi (Eq.(I-20)) and Du Plessis and Masliyah (Eq.(I-22)). Indeed, as explained in the Section I.2.1, these correlations give predictions with the same order of magnitude than the ones of Kozeny-Carman and Rumpf-Gupte correlations.

The major part of the samples manufactured during this work lies in the uncertainty range of the Kozeny-Carman correlation. Some of them are below this range due to the high forming pressure, which was applied to increase the mechanical resistance but which leads to a reduction of the permeability. Another reason that could explain the difference between the correlation and the experience is that the correlations don't take into account the tortuosity of the porous structure. However, a high tortuosity may reduce the permeability, for a given porosity and a given pore radius.

The Rumpf-Gupte correlation seems to better fit with the characterisations of the samples manufactured during this thesis. However, the model presented in the Chapter II uses the Kozeny-Carman correlation. In order to improve this model, the Rumpf-Gupte correlation could be used.

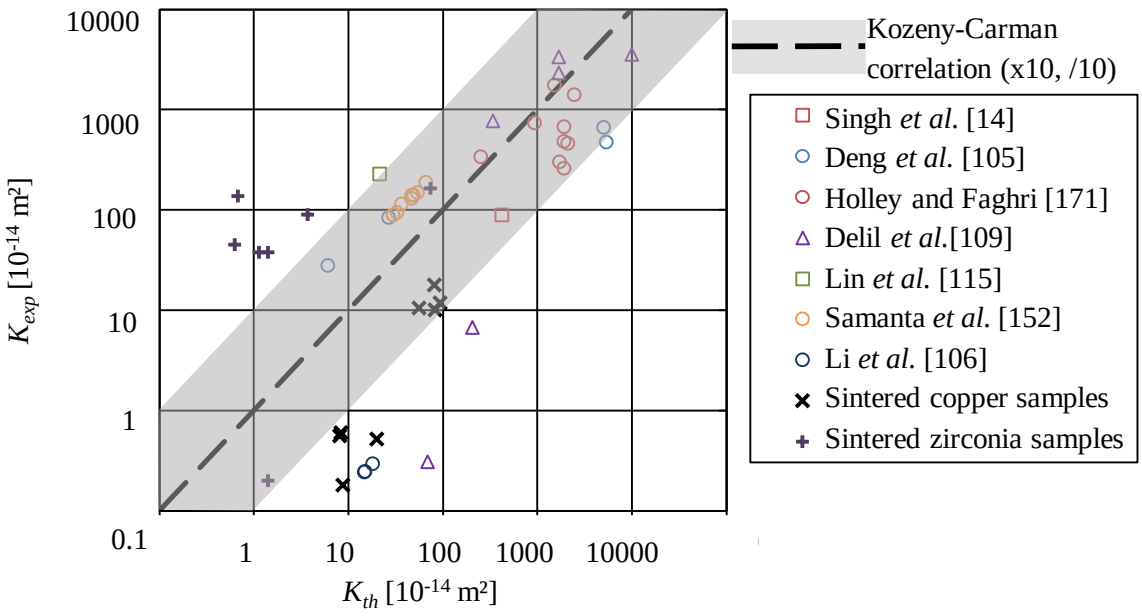

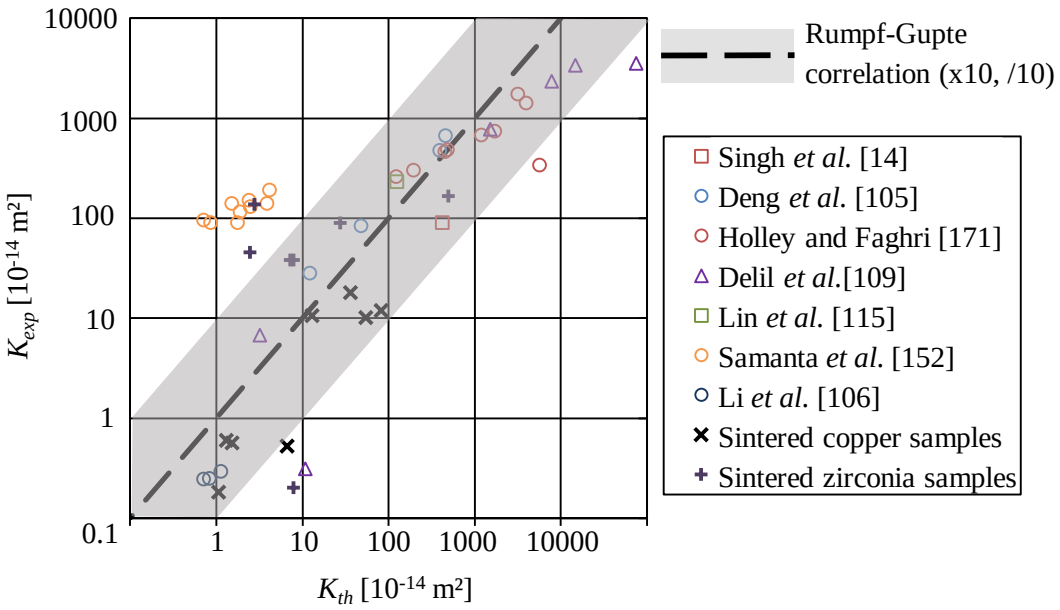

Figure IV-16: Experimental permeability versus theoretical permeability calculated with the Kozeny-Carman and Rumpf-Gupte correlations

In conclusion, this section shows that the samples manufactured during this thesis have characteristics comparable to previous studies. However, the trends are rough. A correlation taking into account the tortuosity may reduce the related uncertainties.

IV.4 Conclusion

A test bench enabling to characterise the permeability and the effective pore radius of many capillary structures made of sintered powder has been designed. The tests, partly performed following a design of experiment, aim at understanding the influence of the manufacturing procedures on the sample characteristics. The copper powder sintering protocols are reproducible regarding the permeability and the porosity, but not the effective pore radius and the thickness. The forming pressure applied on the porous structure before the sintering has an influence on the porosity and the permeability whereas the mass of powder used to manufacture a sample affects the thickness. The other sintering parameters have not a significant influence on any parameter. The zirconia sintering protocols are less reproducible than the copper ones, in terms of hydrodynamic characteristics, because the shrinkage is very sensitive to the sintering temperature. Zirconia and copper sintering protocols enabling to obtain suitable characteristics for a LHP wick with two layers have been proposed even if the zirconia samples do not fit perfectly with the expected characteristics.

Finally, the hydrodynamic characteristics of the copper and zirconia samples are compared with other porous structures of the literature. Their permeability is slightly lower than expected because of the forming pressure applied in order to increase the mechanical resistance of the samples.

The knowledge of characteristics such as the thickness, the porosity, the permeability or the different pore radii is of great interest in order to investigate the thermal behaviour of the manufactured samples, presented in the next Chapter.

Chapter V Thermal characterisation of the porous wick

This chapter presents the experimental characterisation of the thermal behaviour of the manufactured wicks.

A state-of-the-art of the various test benches encountered in the literature is firstly presented and discussed in order to enable the design of an efficient experimental apparatus dedicated to the LHP wicks manufactured during this thesis.

The various components of the test bench are described as well as the sensors, the measurement techniques and the procedures used to characterise the various samples. Then, the response of the system to various heat solicitations is presented in order to understand the phenomena acting inside a LHP evaporator. Water and pentane were used in order to study the influence of the fluid properties on the wick thermal behaviour.

Finally, these results are in-depth analysed in order to understand the influence of the manufacturing parameters and hydrodynamic characteristics on the wick thermal performance.

V.1 State-of-the-art of the test benches

Only few test benches enabling the thermal study of a LHP evaporator are presented in the literature. The benches are at atmospheric pressure or with a controlled ambiance, with or without visualisation and can reproduce the whole LHP evaporator or just a single fin of the evaporator wall.

Zhao and Liao ([38], [108]) as well as Khammar *et al.* [110] designed experimental test benches in order to study the heat transfer between the whole evaporator wall and the wick. Figure V-1 and Figure V-2 show that the system evaporator/wick/reservoir is similar to the one of a LHP. Contrarily to what happens in a whole LHP, the evaporator operating conditions are well controlled (elevation Δh, inlet temperature, heat load). Indeed, the wick is fed with liquid coming from a reservoir with a temperature controller. These benches enable the measurement of the heat transfer coefficient between the evaporator wall and the fluid under various conditions. The heat transfer coefficient is classically defined as the heat flux density divided by the difference between the saturation temperature and the mean wall temperature at the fin tips which was calculated by a heat conduction model using temperatures in the heating block. The test bench of Zhao and Liao ([38], [108]) enables a visualisation of the fluid behaviour at the vicinity of the fin, but the loop is open to the atmosphere preventing to adjust the pressure inside the bench and a digital scale enable to measure the mass flow rate. The test bench of Khammar *et al.* [110] enables to study the influence of a gap set between the fin and the wick on the fluid behaviour. No visualisation is possible with this bench but they also measure the mass flow rate coming from the reservoir.

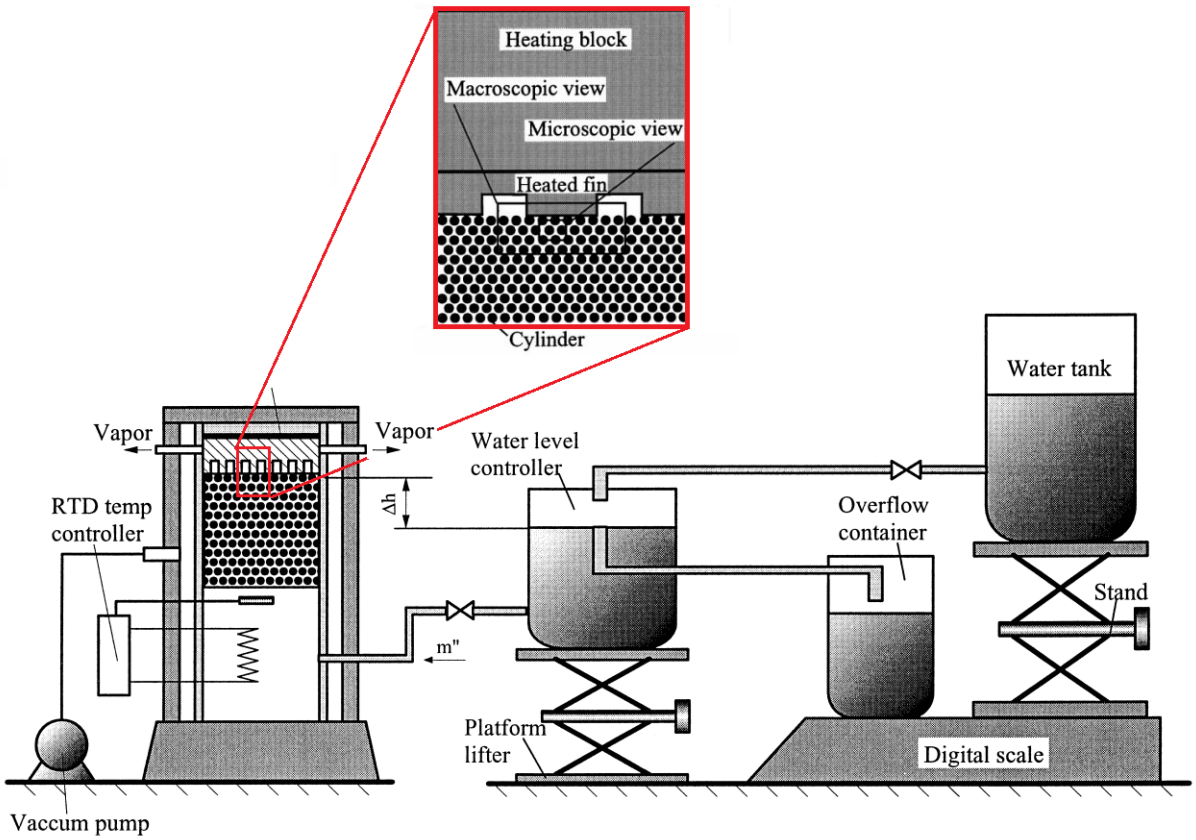

Figure V-1 : Schematic of the experimental set up used by Zhao and Liao ([38], [108])

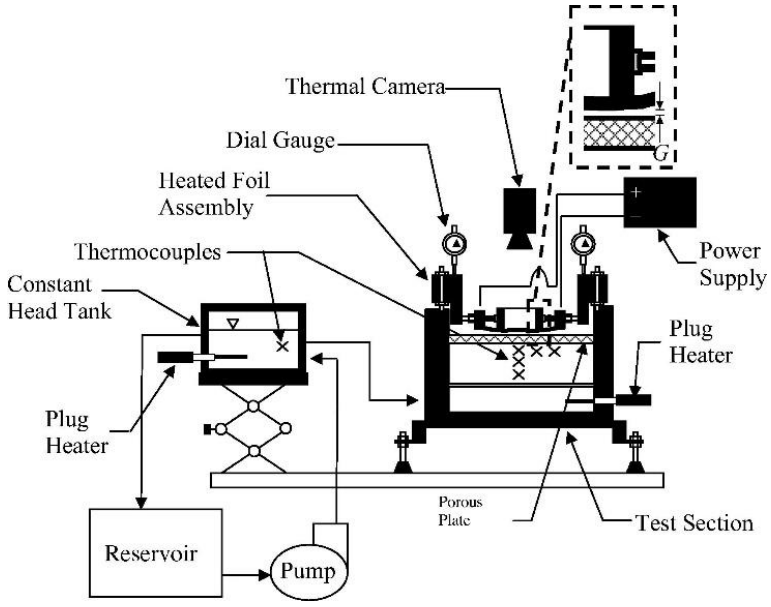

Figure V-2: Schematic of the experimental set up used by Khammar *et al.* [110]

Delil and Baturkin [109] designed a test bench reproducing a LHP without liquid line and where the condenser also plays the role of reservoir in order to reduce their influence on the evaporator behaviour (Figure V-3). The vapour directly flows from the grooves to the condenser then flows through the wick again. They do not measure the mass flow rate. However, since the system is closed and tight, it enables to easily modifying the saturation temperature. No visualisations are possible with this test bench and the study of the hydrostatic pressure influence is not enabled.

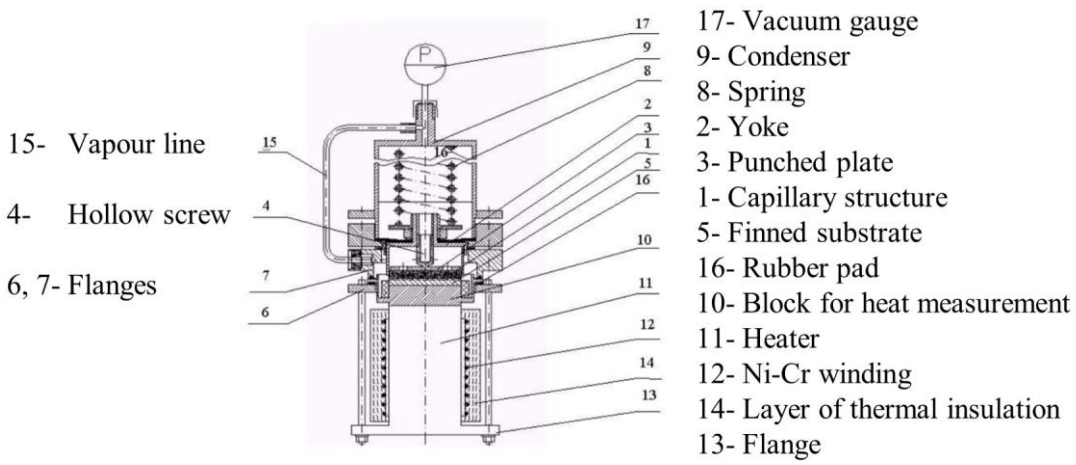

Figure V-3: Schematic of the experimental apparatus used by Delil and Baturkin [109]

Mottet *et al.* [29] designed another kind of test bench reproducing a single fin and a part of a wick (Figure V-4). Since the front face of the device is transparent, they observed experimentally the development of the vapour zone in quasi 2D conditions in order to validate the model discussed in Section I.3. The results are in good accordance with the model. On the successive pictures, it is possible to see the vapour zone growing until that a vapour finger (Figure V-4 e) completely flows through the wick. The breakthrough point is then reached (Figure V-4 f). For low and moderate heat fluxes a steady state can be reached even with a vapour pocket under the evaporator as predicted by Zhao and Liao [108]. With this test bench, it is not possible to estimate a heat transfer coefficient representative of the one of a porous wick for LHPs due to the simplified design (2D, one fin and one groove).

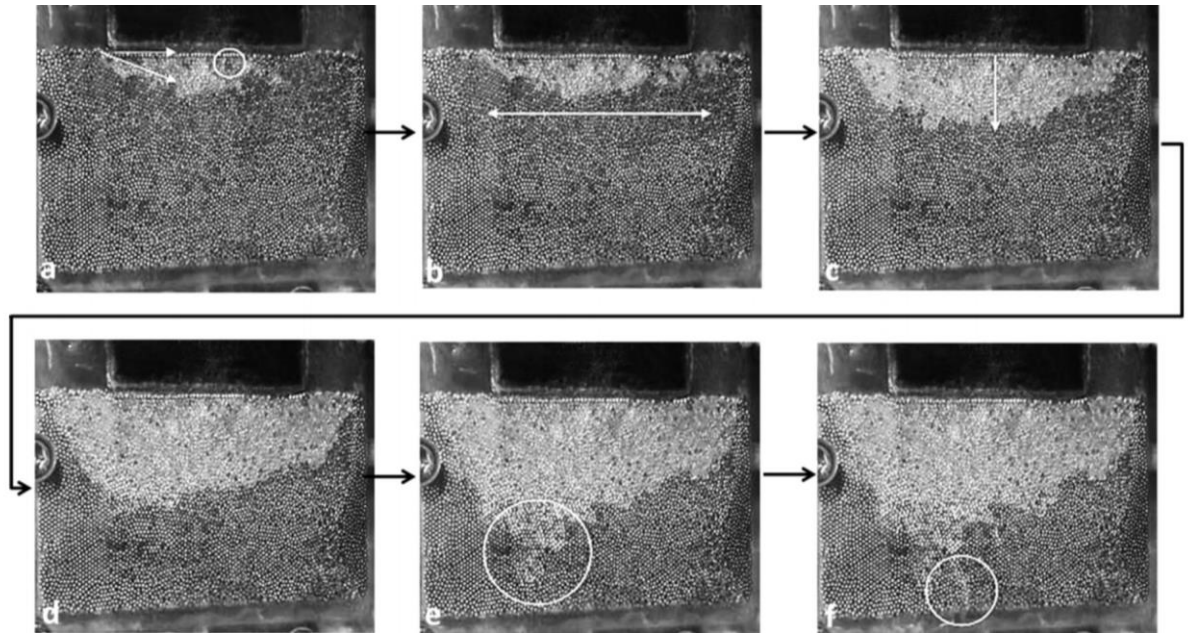

Figure V-4 : Evolution of the vapour zone up to the breakthrough (Mottet *et al.* [29])

The previous studies offer various possibilities in terms of thermal behaviour investigation. They enable to design a specific test bench to thermally characterise the manufactured wicks, depending on the specific objectives of this thesis. The determination of the heat transfer coefficient in order to improve the model presented in Chapter II is one of the major objective of this thesis. It means that the porous sample behaviour must be similar to the one of a LHP evaporator. That's why, a test bench similar to the one proposed by Delil and Baturkin [109] is preferred to the other ones because it enables to test a porous structure in the same conditions than in a LHP, even if it is not possible to observe the dry out within the capillary structure with such a system. Furthermore, this type of bench enables to adjust various parameters such as the saturation state and the hydrostatic pressure. The study of influence of the hydrostatic pressure on the wick thermal behaviour will also be simplified, compared to Zhao and Liao ([38], [108]) and Khammar *et al.* [110].

V.2 Description of the experimental apparatus and the procedures

V.2.1 Description of the experimental apparatus

The test bench designed in order to characterise the thermal behaviour of each manufactured sample aims at reproducing the configuration and the operation of an evaporator in a flat LHP, by decoupling it from the transport lines and the condenser (Figure V-5). It consists of a double-wall glass enclosure secured at the base by a clamping ring. A grooved evaporator and the wick are embedded into the cylindrical part of the base. The sealing is ensured by O-ring seals. An L-tube goes through the base wall to enable the vapour to flow from the grooves to the enclosure containing the fluid at liquid-vapour equilibrium.

The saturation temperature of the fluid is controlled by a cryogenic fluid flowing in the annular space of the enclosure from a thermostatic bath. The thermostatic bath operates from -50 °C to 120 °C. The water level H_l can be modified by opening the filling valve in order to adjust the hydrostatic pressure ΔP_{hs} applied on the wick. Two thermocouples enable to measure the saturation temperature: one in the liquid phase (T_l) and the other in the vapour phase (T_v). They are manufactured by *TC Direct* and are housed inside a sealed shell made of stainless steel in order to ensure the sealing of the system. They are as close as possible to the water level, enabling to detect the presence of NCGs if the temperatures are different.

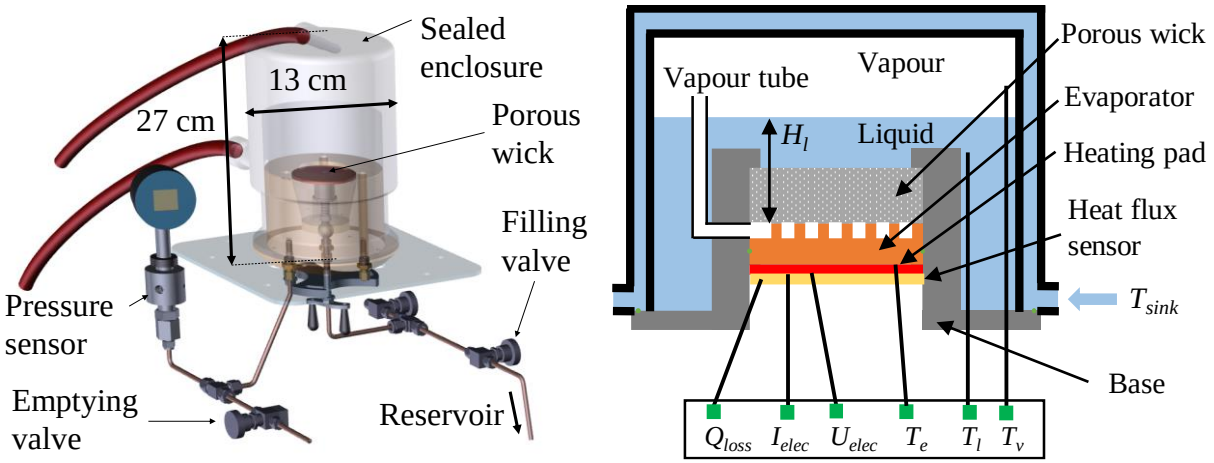

a) Global view b) Measurements

Figure V-5 : Schematic of the experimental apparatus

The evaporator, identical as the one used by Siedel [4], is composed by a flat disk-shaped copper block, of diameter 40 mm, where nine grooves, 2 mm wide and 1.5 mm deep, are engraved (Figure V-6) and separated by 1.5 mm thick fins, and by a wick located above the block. At the grooves outlet, a vapour collector having an increasing cross-sectional area is arranged to reduce the pressure drops. An exit vapour channel is machined at the copper block boundary at the centre of the collector. A thermocouple having a diameter of 80 µm is located inside a 0.8 mm thin groove engraved in the bottom surface of the evaporator in order to measure its temperature.

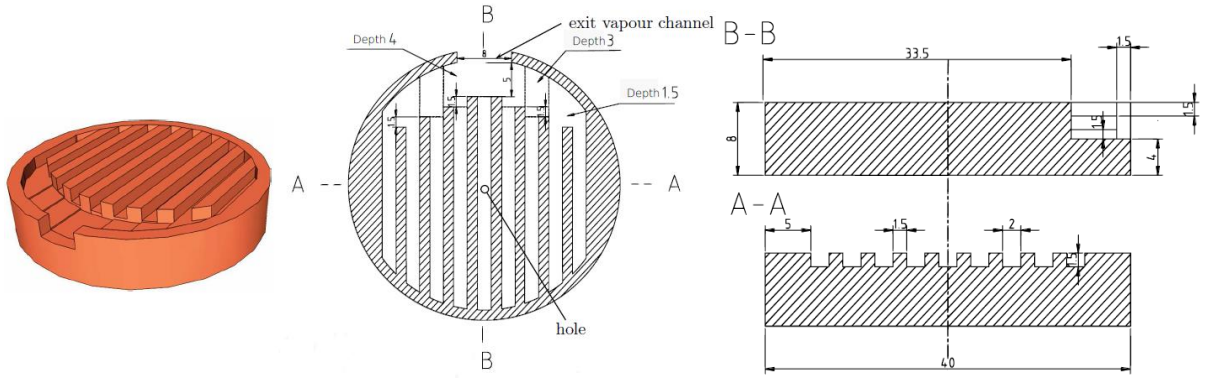

Figure V-6 : Evaporator design (Siedel [4])

The heat flux is provided by a heating pad manufactured by *Captec*. The heating pad is an electrical resistance of 10.0 Ω, with a maximum heat dissipation of 150 W (12 W/cm²), located between the evaporator wall and a heat flux sensor. This sensor measures the part of the heat flux lost through the back of the heat source.

A *Druck* absolute pressure sensor is used to record the saturation pressure inside the system. It has an accuracy of 10^{-4} bar in a range from 0 to 2 bars. As the saturation temperature is known, it is possible to determine the presence of non-condensable gas (NCGs): if the recorded pressure is higher than the pressure corresponding to the saturation temperature, it means that NCGs are present in the system.

The heat flux Q_{in} supplied to the evaporator is determined by measuring the electrical power Q_{elec} supplied to the resistance:

$$Q_{elec} = U.I \qquad \text{(V-1)}$$

where U is the tension and I the electrical current, and the heat losses Q_{hfs} at the back of the resistance:

$$Q_{hfs} = U_{hfs} \frac{S_w}{k_{hfs}} \tag{V-2}$$

where k_{hfs} is the heat flux sensor sensitivity equal to 11.1 µV / (W/m²) and U_{hfs} the tension provided by the heat flux sensor. Thus, the heat load effectively supplied to the evaporator is determined as follows:

$$Q_{in} = Q_{elec} - Q_{hfs} \tag{V-3}$$

The heat transfer coefficient is defined as follows:

$$h_e = \frac{Q_{in}}{S_w(T_e - T_{sat})} = \frac{Q_{in}}{S_w \Delta T_{sh}} \tag{V-4}$$

where T_e is the evaporator wall temperature and T_{sat} is assumed equal to the vapour temperature T_v. This last assumption is not totally exact since the temperature of the liquid is submitted to a slight subcooling. This is due to the sealed enclosure geometry which requires a strong cooling of the glass wall to evacuate by condensation the heat provided by the evaporator.

All the measured data are recorded by an acquisition system manufactured by *Keithley* connected to a *Labview* program enabling to follow the evolutions of the temperatures and the heat load applied to the evaporator wall.

The uncertainties are about 3 W on the heat fluxes, 5 % on the porous wick area and 1 K on the temperature difference. The uncertainty associated to the heat transfer coefficient can reach 30 % at low heat loads where the temperature difference between the evaporator and the vapour phase is small. At high heat loads, the uncertainty decreases down to 10 %. This relatively high uncertainty is explained by the estimation of the whole copper block temperature (thermocouple located at its bottom face) and by the subcooling of the liquid, making difficult the estimation of the saturation temperature.

V.2.2 Description of the experimental procedures

The procedures enabling the investigation of the thermal performance are described in this section. The first step is the filling of the sealed enclosure with the working fluid. It starts with the emptying of the sealed enclosure, to remove all the NCGs. Then, the filling valve is opened and the fluid is sucked into the enclosure up to the desired height H_l. It enables to easily control the hydrostatic pressure. The vacuum pump is maintained in operation during twenty minutes so that the fluid is correctly degassed. Indeed, even a small amount of NCGs may affect the heat transfer between the evaporator and the working fluid. Then, the saturation temperature is set at the desired level by means of the thermostatic bath. The temperature measurements of the vapour and the liquid phases are expected to be equal and to correspond to the saturation pressure recorded by a pressure sensor. If the temperature difference is higher than 3 K, it is considered that NCGs are present in the sealed enclosure. In this case, the sealing is reinforced by cleaning the O-rings and the filling procedure is conducted again.

Once the filling procedure is completed, the test can start. The heat load is increased step by step, a steady state being reached before applying the next step. The test is stopped when the evaporator temperature reaches 120 °C in order to protect the test bench materials against overheating.

Figure V-7 shows an example of thermal behaviour exhibited by a manufactured sample, in which the heat transfer coefficient h_e and the superheat ΔT_{sh} between the evaporator wall and the vapour phase are plotted as a function of the heat load. At low heat fluxes, the heat transfer coefficient remains

constant with an increasing heat load, up to a value called Q_{opt}. When Q_{opt} is reached, the heat transfer coefficient drastically decreases leading to a large increase of T_e. The heat transfer coefficient recorded at Q_{opt} is called the optimum heat transfer coefficient $h_{e,opt}$ and the temperature difference is called the maximum superheat $\Delta T_{sh,max}$. When the heat flux is greater than Q_{opt}, bubbles can sometimes be observed at the top surface of the porous structure. Clearly, an operating limit is reached at Q_{opt}, leading to a degradation of the heat transfer.

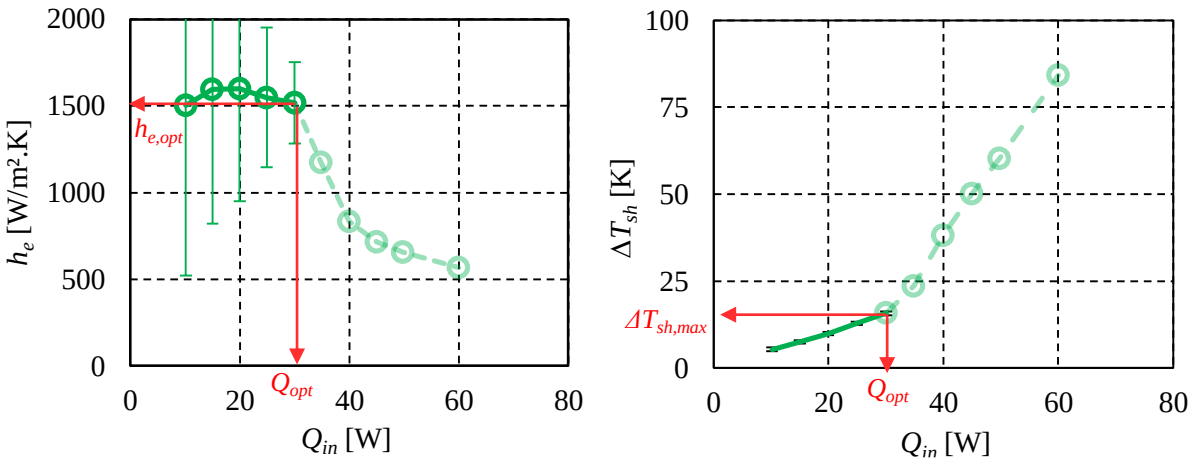

a) Heat transfer coefficient b) Evaporator superheat

Figure V-7: Example of thermal behaviour (sample Cu-sin4-a, water, 50 °C)

The measurements presented on Figure V-7 were performed for increasing heat fluxes. The possible existence of a hysteresis effect is studied on the sample Cu-sin-2-c. The evolution of the evaporator superheat as a function of the heat load is presented in Figure V-8 for water and pentane. Whatever the fluid, the heat load is increased step by step from 20 W up to the dry-out of the wick. Then, it is decreased up to 20 W and increased again. Figure V-8 shows that water (a) and pentane (b) have different behaviours when the heat load is decreased just after the dry out: the superheat of water is slightly higher than before the decrease whereas it gets back at the exact same level with pentane. When the heat load gets closer to 20 W, the superheat of water progressively comes back on the curve obtained at increasing heat load.

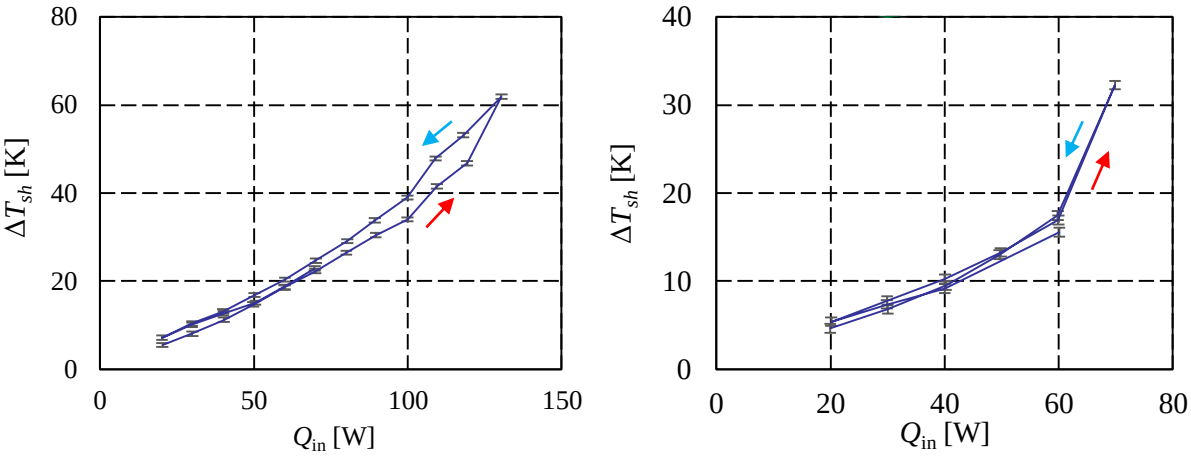

a) Water b) Pentane

Figure V-8: Evaporator superheat in the presence (a) and in the absence (b) of a hysteresis (Cu-sin-2-c)

This phenomenon can be due to the difference between the advancing and the receding contact angles of water on copper also called the contact angle hysteresis (Section I.1.6.2). Indeed, when the heat load increases up to the optimum heat load, the meniscus recedes inside the capillary structure (Figure V-9 a) whereas when the heat load decreases down to the optimum heat load, the meniscus advances inside the capillary structure (Figure V-9 b). Since the advancing contact angle is higher than the decreasing one, it needs more energy to rewet the wick than to dry it due to a lower capillary pumping.

Moreover, when the heat load is decreased, the liquid-vapour interface advances inside the capillary structure and needs to pass through a pore before reaching the next interconnection channel. Since the pore diameter is larger than the interconnection channel one, the capillary pressure decreases each time it reaches pore, making harder the complete rewetting of the wick.

The contact angle hysteresis is a complex phenomenon, depending on many parameters and among them, the contact line velocity. The higher the velocity, the larger is the hysteresis. When the heat flux increases, the menisci more rapidly in the pores, inducing a larger hysteresis as observed in Figure V-8 (a). The pentane being perfectly wetting, there is no hysteresis effect.

a) Increasing heat load: receding meniscus b) Decreasing heat load: advancing meniscus

Figure V-9: Schematic of the meniscus motion depending on the heat load

In the following, all experiments are performed at increasing heat fluxes in order to avoid hysteresis effects. For a sake of clarity, only the data points obtained with a heat flux lower than the optimal heat flux are presented. Indeed, the points beyond Q_{opt} are obtained with a dried wick which must be avoided in a normal operation.

V.3 Theoretical study of the wick operating limits

Various phenomena can lead to the dry-out of the evaporator. They must be investigated in order to understand the phenomena leading to the sudden drop of the heat transfer coefficient and the sharp increase of the evaporator temperature. If the phenomena leading to the wick limits were well understood, it would be possible to adjust the wick characteristics to improve its thermal performance. The operating limits of a LHP are presented in the Section I.1.3.3 of this thesis. The limits that the wick is likely to reach in the present test bench are the boiling limit and the capillary limit. The method used to predict the occurrence of one or the other limit is described in this section.

V.3.1 Prediction of the capillary limit

The capillary limit is reached when the pressure drops through the wick ΔP_w and the vapour tube ΔP_{vt} overcome the sum of the maximum capillary pressure and the hydrostatic pressure ΔP_{hs} of the liquid column of height H_l above the wick surface (Figure V-5). When the capillary limit is reached, the porous structure is not able to transport the liquid up to its surface anymore. A vapour blanket partially fills the

porous structure, leading to a decrease of the heat transfer coefficient and an increase of the evaporator wall temperature. The theoretical capillary limit $Q_{opt,th}$ is determined by equalising the pressure drops and the capillary force added to the hydrostatic pressure:

$$\Delta P_{cap,max} + \Delta P_{hs} = \Delta P_w|_{Qopt,th} + \Delta P_{vt}|_{Qopt,th} \quad \text{(V-5)}$$

The pressure drops along the vapour grooves are negligible. The hydrostatic pressure can be expressed as follows:

$$\Delta P_{hs} = (\rho_l - \rho_v) g H_l \quad \text{(V-6)}$$

The pressure drops through the wick can be expressed according to Darcy's law (Eq. (I-16)):

$$\Delta P_w = \mu_l e_w \frac{u_l}{K}$$

The pressure drops through the vapour tube can be expressed as follows:

$$\Delta P_{vt} = \frac{\left(\beta + \alpha \frac{L_{vt}}{d_{vt}}\right) \rho_v u_v^2}{2} \quad \text{(V-7)}$$

where β = 2.5, is the sum of the coefficients associated to singular pressure drops at the vapour tube entrance (equal to 0.5) and exit (equal to 1) as well as in the elbow (equal to 1). $\alpha = 64/Re$, is the friction coefficient associated to regular pressure drops along the vapour tube. L_{vt} and d_{vt} are the vapour tube length and diameter, respectively. The vapour and liquid velocities u_v and u_l are determined by calculating the mass flow rate in the circuit:

$$\dot{m} = \frac{Q_{in}}{h_{lv}} \quad \text{(V-8)}$$

This equation assumed that there is no heat leaks to the reservoir; the whole heat load is transferred to the fluid by evaporation. Combining equations (V-6) to (V-5) and (I-16) leads to:

$$\frac{2\sigma}{r_{m,min}} + (\rho_l - \rho_v) g H_l = \frac{\mu_l e_w}{K} \frac{Q_{opt}}{\rho_l S_w h_{lv}} + \frac{\left(\beta + \alpha \frac{L_{vt}}{d_{vt}}\right) \rho_v}{2} \left(\frac{Q_{opt}}{\rho_v S_{vt} h_{lv}}\right)^2 \quad \text{(V-9)}$$

where S_{vt} is the vapour tube cross section area. The resolution of this second degree equation enables to determine $Q_{opt,th}$. If the theoretical capillary limit is significantly higher than the experimental optimum heat load, another phenomenon is probably responsible of the dry-out.

V.3.2 Prediction of the boiling limit

The boiling limit, reached when the superheat between the evaporator wall and the saturation temperature of the fluid inside the porous sample is high enough so that nucleation can start, is here calculated using the Chi equation (I-13).

This equation depends on the nucleation radius r_n which must be known. Griffith and Wallis [175] carried out many nucleation experiments with water. They reported nucleation radius lying between 2.5 µm and 25 µm. However, Chi [33] explained that in absence of NCGs, in conventional heat pipes, the nucleation radius could be smaller and reach 0.25 µm. According to Lu and Peng [176], the nucleation radius is equal to:

$$r_n = -\frac{2\sigma}{\rho_v(g_v - g_l)} \quad \text{(V-10)}$$

where g_v and g_l are the specific free energies of the vapour and liquid phases respectively. These values are determined for water by Job and Herrmann [177]. It corresponds, at 20 °C, 50 °C and 70 °C, to a nucleation radius of 11.2 µm, 3.6 µm and 2.76 µm respectively, which lies in the experimental range previously presented. However, it is impossible to know exactly the nucleation radius as well as the radius of the pore where boiling starts. The nucleation radius and thus, the boiling limit are just estimated in this work.

V.4 Influence of the test bench parameters on the wick thermal behaviour

The experimental apparatus used to test the samples has many parameters that can be modified: the saturation temperature, the hydrostatic pressure, the oxidation of the evaporator and the pressure applied on the back face of the evaporator. It is important to perform a parametric study in order to see if a parameter has a strong influence on the results. In this case, it would mean that the parameter must be controlled very accurately.

V.4.1 Reproducibility of the thermal characterisation

To study the reproducibility of the thermal characterisation, the same test with sample Cu-sin-5-a is conducted three times a few days apart. Figure V-10 shows the heat transfer coefficient and the wall superheat obtained during these tests. The results are relatively similar from one test to another: the heat transfer coefficient and the superheat follow the same trends and the differences between each curve are lower than the uncertainty. However, in two tests the optimum heat flux is reached at 40 W whereas in the third one it is reached at 50 W. This can be due to the fact that the steps are too large. Maybe, the optimum heat flux would vary in a smaller range if the step between two heat fluxes would be of 2 W instead of 10 W. However, this difference is not significant at the scale of the whole study.

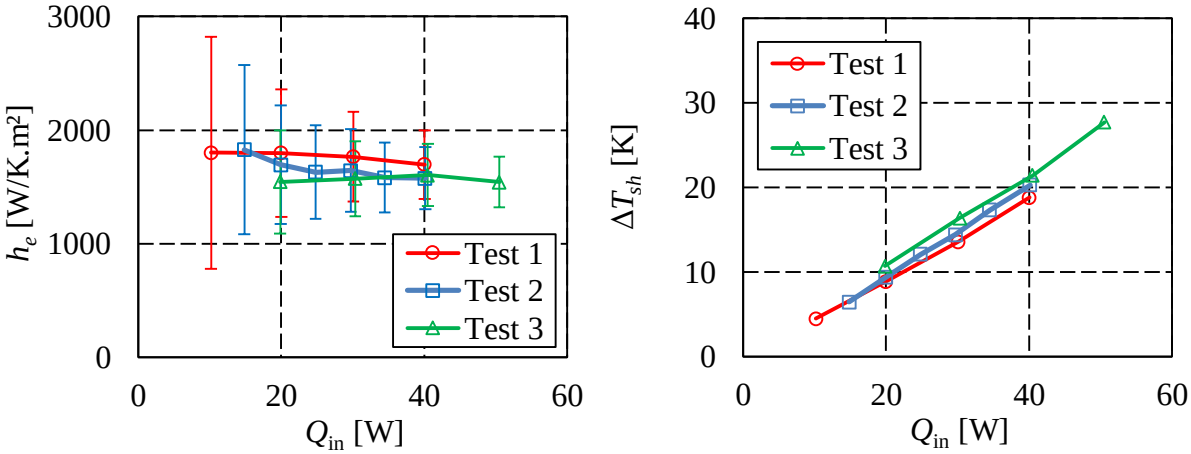

a) Heat transfer coefficient b) Evaporator wall superheat

Figure V-10: Test of reproducibility on the sample Cu-sin-5-a (water, T_{sat} = 50 °C)

V.4.2 Influence of the saturation temperature

The saturation temperature modifies the fluid properties. Thus, it is expected to modify the operation of the test bench. The investigation is conducted with the sample Cu-sin-3-a, tested with water at three different saturation temperatures. Figure V-11 shows the heat transfer coefficient and the evaporator wall superheat as a function of the heat load when water is used as a working fluid.

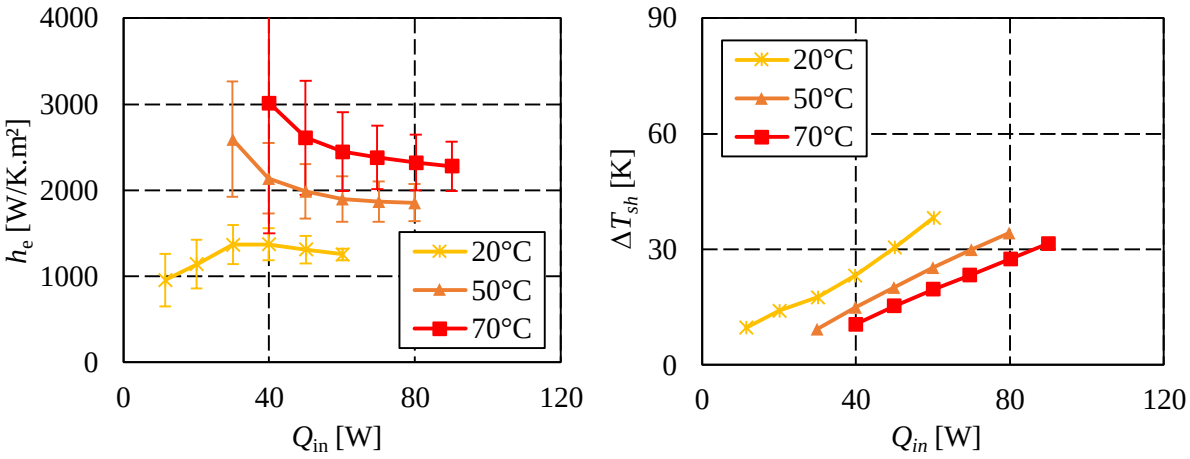

a) Heat transfer coefficient b) Evaporator wall superheat

Figure V-11: Influence of the saturation temperature on the thermal performance (Cu-sin-3-a, water)

An increasing saturation temperature increases Q_{opt} and decreases $\Delta T_{sh,max}$. In order to explain these results, the influence of the saturation temperature on the theoretical limits is done (Table V-1). An increasing saturation temperature increases the capillary limit. This result can be explained by the evolution of the fluid properties with the temperature and mainly its viscosity and its surface tension. The liquid viscosity is 2.48 times lower at 70 °C than at 20 °C whereas the surface tension is only 1.13 times lower at 70 °C than at 20 °C. Thus, the capillary limit increases with an increasing saturation temperature. However, since the measured optimum heat load is lower than the capillary limit, it is probably the boiling limit that firstly occurs. Indeed, the range of variation of the theoretical maximum superheat (30.4 K to 45.7 K) corresponds to the range of variation of the experimental superheat (31 K to 38 K). Since the heat transfer coefficient is higher at a high saturation temperature, the boiling limit is reached at lower heat loads at a low saturation temperature. Note that the theoretical maximum superheat increases from 31.8 K to 45.7 K then decreases to 30.4 K, for a saturation temperature increasing from 20 °C to 70 °C. Indeed, the nucleation radius decreases but the vapour density increases, leading to a maximum value of $\Delta T_{sh,max}$.

Table V-1: Influence of the saturation temperature on the theoretical limits (Cu-sin-3-a, water)

Temperature	$Q_{opt,th}$ (in case of the capillary limit)	$\Delta T_{sh,max,th}$ (in case of boiling limit)
20 °C	298 W	31.8 °C ($r_{n,th}$ = 11.2 µm)
50 °C	451 W	45.7 °C ($r_{n,th}$ = 3.6 µm)
70 °C	455 W	30.4 °C ($r_{n,th}$ = 2.76 µm)

An increasing saturation temperature increases the heat transfer coefficient (increase from 1250 W/m².K to 2300 W/m².K, for a saturation temperature increasing from 20 °C to 70 °C, respectively). That can be explained by a change of fluid properties. Indeed, the thermal conductivity of water increases for an increasing temperature, improving the heat transfer inside the wick. Moreover, the vapour viscosity decreases for an increasing temperature, reducing the pressure drops and leading to an increasing of the heat transfer. Indeed, rewetting the porous structure and feeding the liquid-vapour interface is easier if the viscosity is lower. Thus, the vapour blanket is expected to be thinner.

In conclusion, an increasing saturation temperature increases the performance of the test bench both in terms of hydrodynamic and thermal behaviours. In the following, the saturation temperature with water is set at 50 °C and at 40 °C with pentane.

V.4.3 Influence of the hydrostatic pressure

The hydrostatic pressure may have an influence on the test bench operation. Indeed, the hydrostatic pressure is added to the capillary pressure to enable the fluid to flow through the wick. Thus, this parameter must be investigated. It can be studied by modifying the liquid height in the enclosure. For instance, Figure V-12 presents the thermal behaviour of the sample Cu-sin-3-a with water for various liquid heights. The hydrostatic pressure has not a significant influence on the heat transfer coefficient. This is almost similar when investigating the optimal heat flux. Q_{opt} reaches 70 W for liquid heights of 2.3 cm and 3.1 cm and it reaches 80 W for 3.9 cm. This result was expected since the hydrostatic pressure varies between 225 Pa and 382 Pa, for 2.3 cm and 3.9 cm respectively, whereas the pressure losses through the wick in these conditions reaches 4700 Pa. It means that the hydrostatic pressure is not a preponderant parameter. In the following, H_l is set to 3.9 cm.

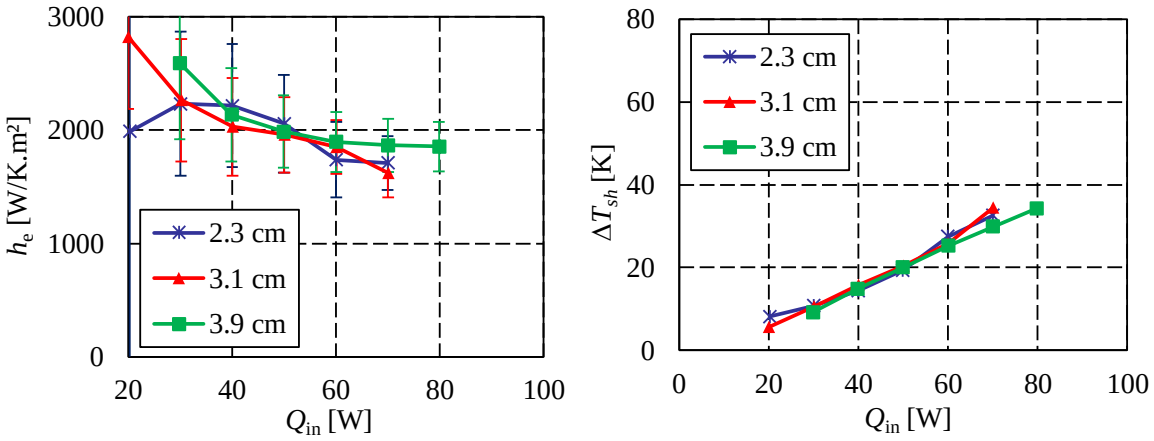

a) Heat transfer coefficient b) Evaporator wall superheat

Figure V-12: Influence of the hydrostatic pressure with sample Cu-sin-3-a (water, T_{sat} =50 °C)

V.4.4 Influence of the oxidation of the evaporator

The chemical surface quality of the evaporator wall may have an influence on the operation because the contact angle of water and pentane on oxidised copper is lower than on standard copper (see Section IV.2.4). Thus, the influence of this parameter is studied with the sample Cu-sin-6-c and water. The sample is firstly tested with the standard copper evaporator wall. Then, the evaporator wall is put in a furnace and the temperature is quickly increased up to 500 °C (increase of 5 K/min). It remains at this temperature during ten minutes and then it is cooled. After this operation, the copper is oxidised and the sample Cu-sin-6-c is tested in the same conditions than before. Figure V-13 shows the heat transfer coefficient and the wall superheat as a function of the heat load in both cases. The heat transfer coefficient as well as the optimum heat flux are not significantly affected by the change of chemical surface quality. In the following, the evaporator wall is not oxidised.

V.4.5 Influence of the pressure applied on the back face of the evaporator

The evaporator and the heating pad are pressed against each other with a spring in order to reduce as much as possible the thermal contact resistance between these two components and thus, to reduce the heat losses by the back face of the heating pad. The influence of the pressure applied by the spring is investigated on the sample Cu-sin-4-a operating with pentane. Figure V-14 shows the evolutions of the heat transfer coefficient and the wall superheat with the heat flux at pressures of around 5 kPa and around 30 kPa. This pressure is determined by measuring the force applied by the spring as a function of its length. The variation of the applied pressure does not significantly change neither the optimum heat flux nor the heat transfer coefficient. In the following, the pressure is set to about 30 kPa in order to reduce the thermal resistance between the heating pad and the evaporator and thus, reduce the heat losses by the back face of the heating pad.

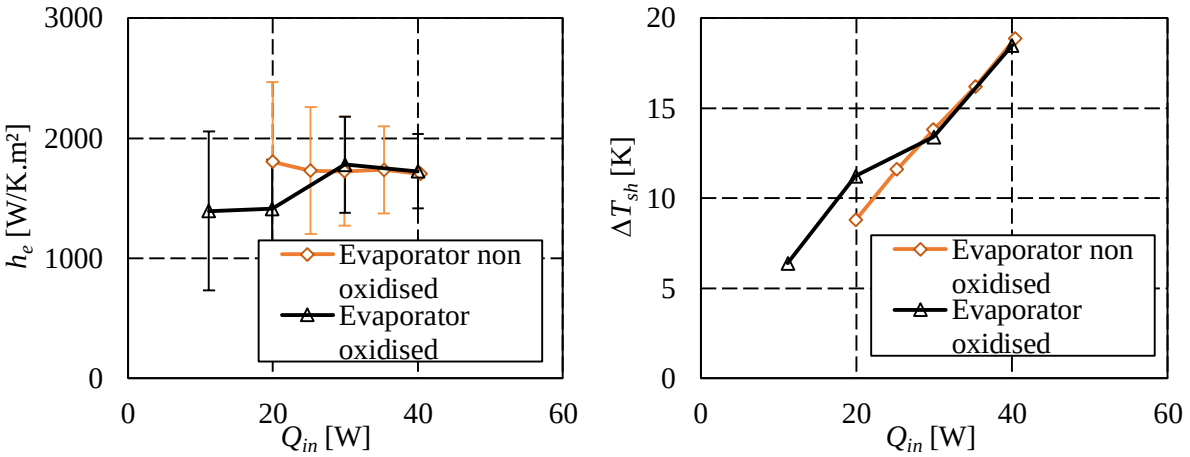

a) Heat transfer coefficient b) Evaporator wall superheat

Figure V-13: Influence of the chemical surface quality of the evaporator with sample Cu-sin-6-c (water, T_{sat} =50 °C)

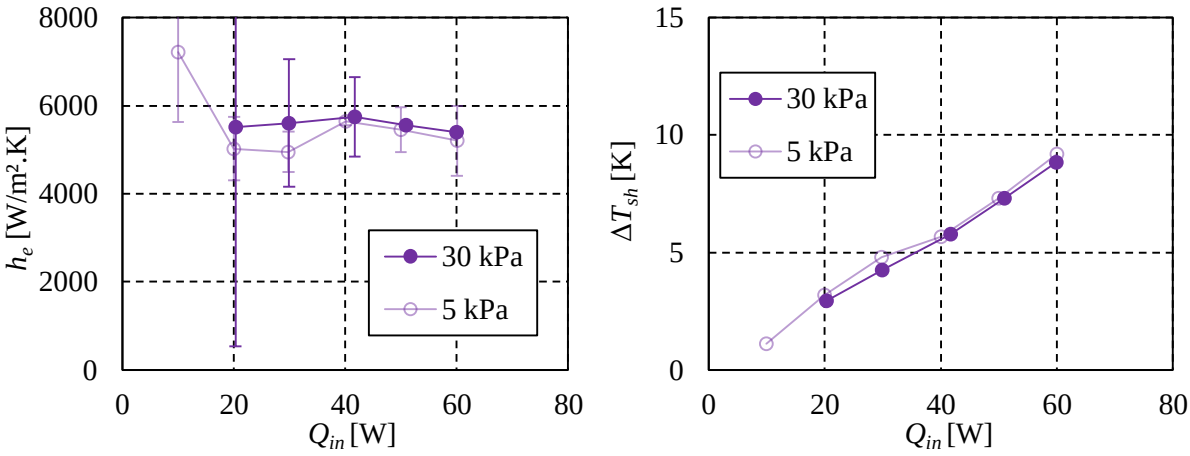

a) Heat transfer coefficient b) Evaporator wall superheat

Figure V-14: Influence of the pressure applied on the back face of the evaporator (sample Cu-sin-4-a, pentane, T_{sat} = 40 °C)

V.4.6 Influence of the addition of a top layer

This section investigates the influence of the addition of a zirconia top layer on the thermal behaviour of the copper bottom layer. Indeed, a top layer is expected to improve the thermal performance of a complete LHP.

The wick is manufactured by co-sintering a copper layer (Cu-sin-7-d) and a zirconia layer following the procedure detailed in Section III.4.1. The bi-layer wick is tested in the thermal test bench. Then, the two layers are separated and only the copper wick is tested. The separation stage creates strong mechanical solicitations so that the copper wick could only be tested inside the test bench of thermal characterisation. However, the reproducibility of the copper sintering protocol enables to estimate its hydrodynamic characteristics. They are deduced from the average value of the other samples manufactured with the same protocol, except the thickness which has been directly measured on this sample.

The results of the characterisation obtained with the bi-layer wick as well as with the copper layer alone are presented in Table V-2 and Figure V-15. First of all, due to the high permeabilities of the samples, the theoretical capillary limit reaches several hundreds of watts. It means that this is not the

limiting phenomenon. In contrast, the experimental superheat exceeds the theoretical value in both cases, meaning that the boiling limit may be reached.

The operation far from the capillary limit explains the similar behaviours of the copper layer and the bilayer wick. Indeed, the hydrodynamics characteristics, the surface quality and the material in contact with the evaporator fins are strictly similar since the copper layer is the bottom layer of the bi-layer wick. Moreover, since the zirconia top layer has a high permeability (90×10^{-14} m²), it only slightly affects the water mass flow rate. The thermal performance is not better with the bi-layer wick than with a single copper wick because the evaporator/reservoir is not coupled with the rest of the LHP (transport lines and condenser). That does not mean that the performance would not be better in a complete LHP equipped with the bi-layer wick: the low conductive top layer could play its role of thermal barrier to limit the heat leaks to the reservoir.

Table V-2: Results of thermal characterisation of the bilayer wick, and the copper layer alone (water, T_{sat} = 50 °C, H_l = 3.9 cm)

	e_w [mm]	K [10^{-14} m²]	$r_{p,eff}$ [µm]	$Q_{opt,exp}$ [W]	$Q_{opt,th}$ [W]	$\Delta T_{sh,max,exp}$ [K]	$\Delta T_{sh,max,th}$ [K]	$h_{e,opt}$ [kW/m².K]
Bi-layer wick	10.95	37.7	31.8	110	436	72.0	50.5	1220
Cu-sin-7-d	4.2	19.5	31.8	100	520	73.4	50.5	1083

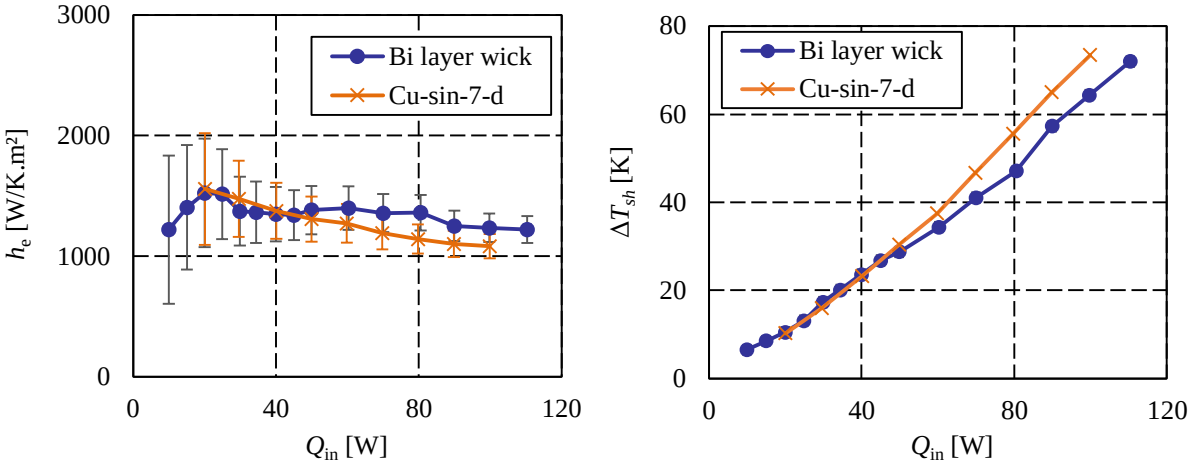

Figure V-15: Heat transfer coefficient as a function of the heat load applied to a bi-layer wick as well as to the copper layer alone

V.4.7 Conclusion

In conclusion, the complete investigation of the influence of the test bench parameters and the reproducibility of the measurements ensure the quality of the results proposed in the following sections. The saturation temperature is the only parameter affecting the thermal performance. Thus, this parameter is accurately controlled during the tests and is indicated for each result proposed in the following sections. Another conclusion is that the addition of a zirconia top layer has no significant influence on the thermal performance of a copper top layer inside this specific test bench. It is promising for future applications in a LHP since the role of the top layer is to be a thermal barrier, avoiding the heat leaks to the reservoir when coupled to the rest of the LHP, which is not the case here.

V.5 In-depth investigation of the thermal behaviour of wicks used as a bottom layer

The thermal behaviour of the copper wicks is more fully investigated than the zirconia ones. Indeed, the copper wick is designed to be the bottom layer, in contact with the evaporator fins, whereas the zirconia layer is designed to be the top layer, not in contact with the fins. The zirconia samples studied are only those coated with gold in order to study the change of behaviour due to this layer.

The investigation of the phenomena acting at the vicinity of the evaporator wall are expected to be the same if the wick is located in a real LHP evaporator. In this section, the influence of surface quality, the hydrodynamic characteristics and the fluid on the thermal performance are studied.

V.5.1 Influence of the surface quality

The influence of the surface quality on the thermal behaviour is investigated in this part. In particular, for a given material, the influence of a topographical modification is analysed and for a given topography, the influence of the modification of the material in contact with the evaporator fins is considered. The topography is modified by several mechanical surface treatments. Then, two zirconia samples are tested with and without a thin gold layer spread on the sample side in contact with the evaporator fins, without changing the topography of the sample.

V.5.1.1 Investigation with topographical modifications

The manufacturing process leads to difference between the two sides of the same sample, as highlighted in Section III.5.2. For instance, the surface quality of the samples manufactured following the design of experiment is summarised in Table V-3. Thus, it is necessary to investigate the influence of the surface quality on the thermal performance, for similar hydrodynamic characteristics.

Table V-3: Surface quality of the samples manufactured following the design of experiment

Sample	Protocol	Side A			Side B		
		Type	Depth	Roughness	Type	Depth	Roughness
Cu-sin-1-b	1	Peak	100 µm	15 µm	Cavity	50 µm	15 µm
Cu-sin-2-c	2	Dome	300 µm	15 µm	Cavity	200 µm	15 µm
Cu-sin-3-a	3	Peak	300 µm	10 µm	Cavity	200 µm	10 µm
Cu-sin-4-a	4	Dome	150 µm	15 µm	Cavity	100 µm	10 µm
Cu-sin-5-a	5	Peak	270 µm	5 µm	Cavity	60 µm	5 µm
Cu-sin-6-c	6	Peak	150 µm	10 µm	Cavity	60 µm	15 µm
Cu-sin-7-c	7	Dome	270 µm	5 µm	Cavity	150 µm	5 µm
Cu-sin-8-a	8	Peak	200 µm	5 µm	Cavity	80 µm	5 µm

In this section, various topographies are tested on the same copper sample. Variations of the flatness and the roughness are expected to modify the boiling dynamic and the fluid flow at the vicinity of the evaporator fins as explained by Platel *et al.* [113], Khammar *et al.* [110] and Schertzer *et al.* [111] (Section I.2.2).

Firstly, both sides of the sample Cu-sin-7-c are observed by confocal microscopy without any surface treatments. Figure V-16 (a) shows a large difference between the sides A and B: they have a similar roughness but the side A is convex whereas the side B is concave. Then, this sample is successively submitted to various surface treatments in order to change its flatness and its roughness:

- Firstly, the sample is machined by means of a turning machine. It enables to obtain a flat sample but it increases the roughness (Figure V-16 b).
- Secondly, the sample is sanded with two different papers (300 grains/cm² the first time, 600 grains/cm² the second time). It reduces the roughness but it creates a dome (Figure V-16 c).
- Finally, the sample is polished with a *Lamplan* flat polisher. It reduces the roughness and provides an excellent flatness but the sides of the sample are not parallel (Figure V-16 d).

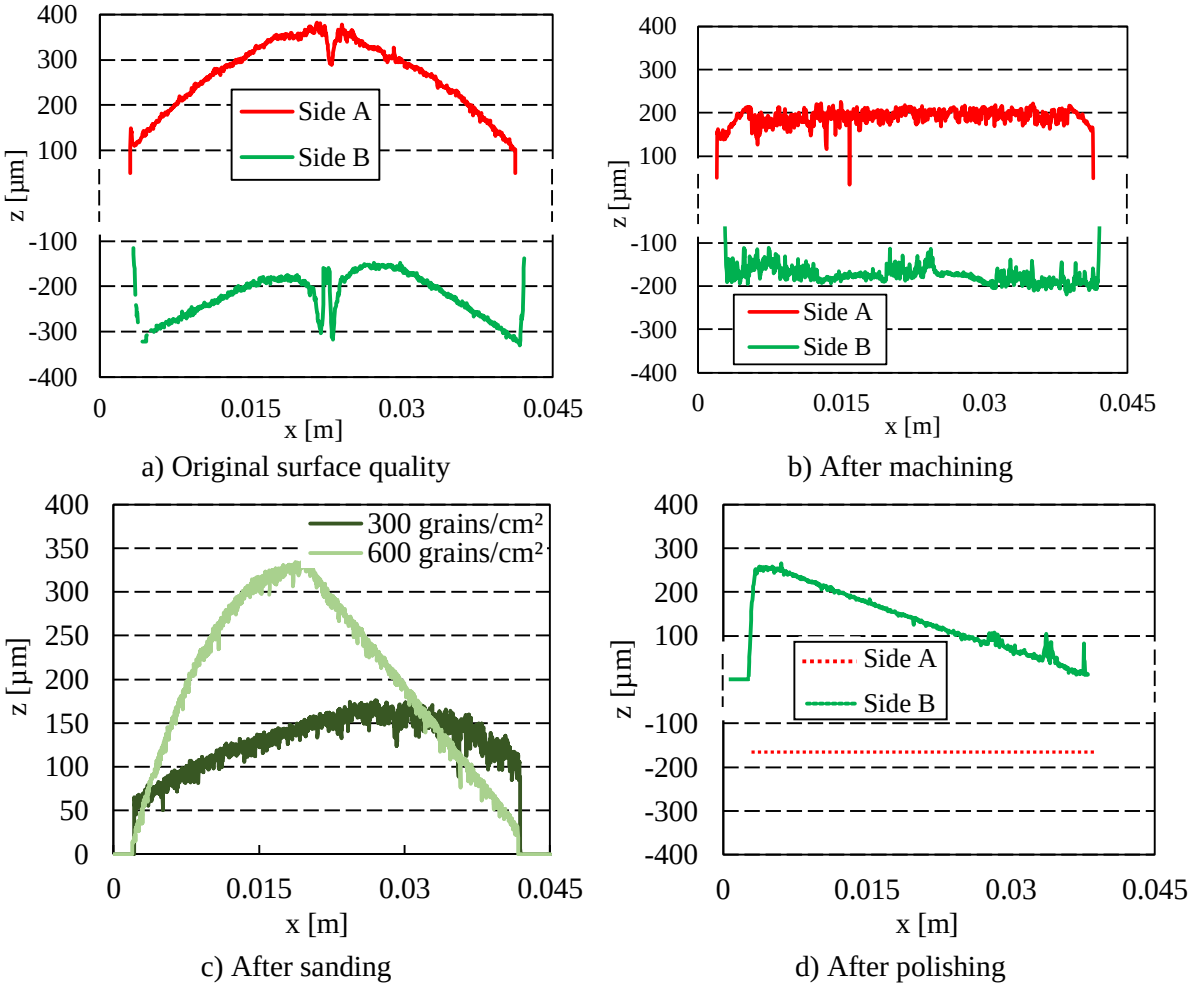

Figure V-16: Confocal microscopy of the sample Cu-sin-7-c

Table V-4 presents the hydrodynamic characteristics, the surface quality and the thermal performance of the sample Cu-sin-7-c after the various surface treatments. The thickness decreases after each treatment. After the last one, the sample is 35 % thinner than the original sample. The effective pore radius remains unchanged and the permeability varies in a small range except for the polished sample which has a very low permeability and a smaller effective pore radius than the other samples. The polishing may lead to an obstruction of the external face of the wick by the wasted copper. Thus, the sample is immersed in an acidic solution in order to dissolve the grains that may obstruct the smallest pores. However, this method has not a significant influence on the permeability. Thus, this sample is not taken into account in the following study, since only the influence of the surface quality is investigated.

Table V-4: Characteristics of the sample Cu-sin-7-c after each surface treatment (pentane, T_{sat} = 40 °C, H_l = 3.9 cm)

	e_w [mm]	K [10^{-14} m²]	$r_{p,eff}$ [µm]	Roughness [µm]	$Q_{opt,exp}$ [W]	$Q_{opt,th}$ [W]	$\Delta T_{sh,exp}$ [K]	$\Delta T_{sh,th}$ [K]	$h_{e,opt}$ [W/m².K]
No treatment (side A)	6.0	16.9	11.5	5	60	102	9.0	9.8	5310
No treatment (side B)				5	100		12.6		6280
Machined (side A)	5.5	19.5	11.5	40	40	128	12.6	9.8	2510
Machined (side B)				40	50		20.2		2020
Sanded (300 g/cm²)	4.2	18	11.5	20	40	153	9.6	9.8	3320
Sanded (600 g/cm²)	4.0	26.8	11.5	15	80	229	16.7	9.8	3810
Polished	3.9	0.43	7.1	5	50	-	16.8	-	2370

Figure V-17 shows the evolutions of the heat transfer coefficient (a) and the evaporator wall superheat (b) as a function of the head load after each surface treatment of the sample. The superheat, the heat transfer coefficient and the optimum heat flux are drastically affected by a variation of the surface quality, meaning that this parameter have a significant influence on the thermal behaviour since the hydrodynamic characteristics after each treatment are similar. Except the side B of the sample without surface treatment, for which the capillary limit may be reached, the boiling limit probably limits the operation of the surfaced sample. Indeed, the theoretical capillary limit varies from 102 W for this sample side to 229 W for the sample sanded with 600 grains/cm². These values are much higher than the experimental data: $Q_{opt,exp}$ is lower than 80 W, except for the side B without surface treatment for which it is of 100 W. On the contrary, the theoretical superheat to initiate boiling is of 9.8 K in these conditions, while $\Delta T_{sh,max,exp}$ almost reaches or exceeds this value in each test. It means that the boiling limit is more likely to be reached.

It can be observed that the flattest surfaces (side A and B of the machined sample and sample sanded with 300 grains/cm²) have the lowest heat transfer coefficient and optimum heat load whereas the concave side of the sample without treatment (side B) has the best performance. The samples with a domed surface (face A without treatment and sample sanded with 600 grains/cm²) have intermediate performance.

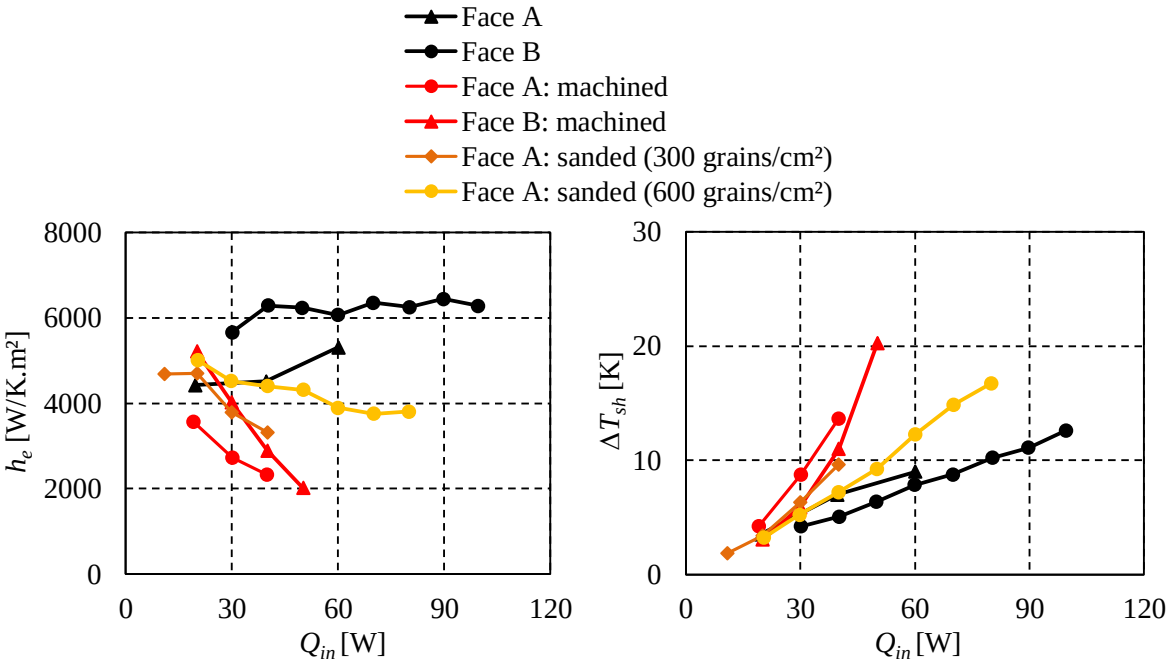

a) Heat transfer coefficient b) Evaporator wall superheat

Figure V-17: Influence of the surface quality on the thermal performance

The three observed levels of thermal performance can be explained by the modification of the contact between the porous wick and the evaporator wall. If the sample is not flat, a gap is created between these two components. Figure V-18 shows the three main configurations that can be encountered: a flat porous wick (a), a convex surface, creating a small gap (b), and a concave surface creating a large gap (c).

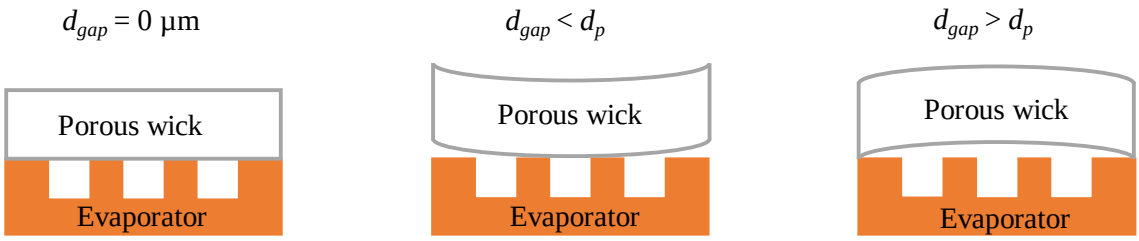

a) Flat surface b) Convex surface c) Concave surface

Figure V-18: Schematic of the contact configurations between the wick and the evaporator wall

It is of interest to understand how the gap size modifies the boiling dynamics and the fluid flow between the porous wick and the evaporator wall. At low heat loads, a liquid phase may exist between the porous wick and the evaporator fin. Moreover, the meniscus may be located between the fin and the porous wick as shown in Figure V-19 (a), as proposed by Demidov and Yatsenko [138]. When the heat load increases, a vapour phase can be located between the fin and the porous wick (Figure V-19 b). If the pore diameter is larger than the gap thickness, the vapour will be evacuated by the wick instead of the gap. Indeed, the meniscus remains at the place having the smallest diameter since the pressure difference is more difficult to overcome. This phenomena leads to a partial dry out of the wick and to a large increase of the thermal resistance. Thus, the evaporator temperature increases, decreasing $h_{e,opt}$, and if the heat load is increased, Q_{opt} is reached. This is even worse if the porous wick is flat and if there is no gap. At the contrary, if d_p is smaller than d_{gap}, the vapour is evacuated to the vapour grooves and the device operates correctly.

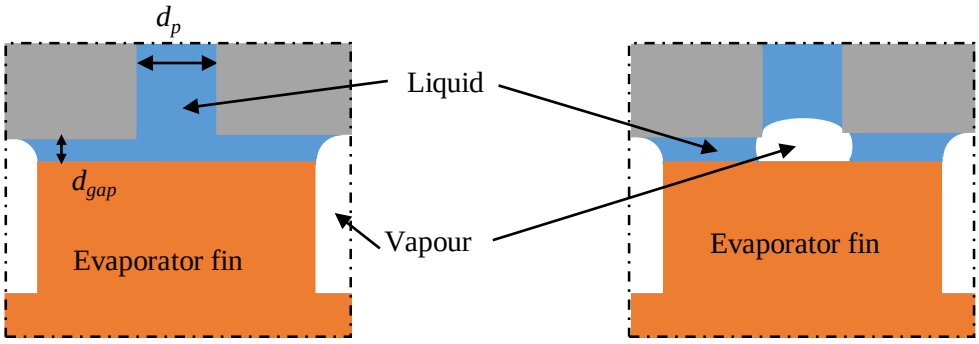

a) Low heat load b) High heat load

Figure V-19: Schematic of the boiling dynamics at the vicinity of an evaporator fin

These results tends to prove that it is important to conserve a gap larger than the pore diameter between an LHP evaporator and the porous wick. That was also demonstrated by Platel *et al.* [113] about the start up, but it can be extended to moderate and high heat loads. It increases both the optimum heat flux and the heat transfer coefficient. If the present experimental observations tend to confirm this behaviour, further experimental validations have to be performed, for instance by a direct visualisation of the bubble generation by means of an endoscope. Anyway, a surface treatment must be avoided since it seems to drastically decrease the thermal performance because of the reduction of the gap size.

V.5.1.2 Investigation with the addition of coating

This section investigates the influence of a thin gold layer (designed to be the bottom layer) added by coating on a zirconia sample (See Section III.4.2). The sample topography as well as the

hydrodynamic characteristics remain unchanged due to the low thickness of the gold layer (thinner than 0.1 µm). Two zirconia top layers are manufactured following the protocol Zi-sin-6 in order to test the effect of the coating on the concave side of one sample and on the convex side of the other. Indeed, the influence of the coating may be different depending on the sample topography. The characteristics of the two samples are described in Table V-5. There are differences between the two zirconia samples meaning that they cannot be compared together. Thus, only the comparison with and without coating is done for each sample. It enables to investigate the coating influence all other parameters being equal. The samples are placed in the thermal test bench with the coating against the evaporator wall.

Table V-5: Results of characterisation of the two zirconia samples used to test the coating

	e_w [mm]	K [10^{-14} m²]	$r_{p,eff}$ [µm]	Tested side
Zi-sin-6-e	5.6	1.33	18.4	B (concave)
Zi-sin-6-f	5.5	0.57	6.6	A (convex)

Figure V-20 (a) shows the thermal behaviour of the side B (concave) of the sample Zi-sin-6-e before and after the coating, with water. The heat transfer coefficient follows the same trend before and after the coating. The difference between the two curves is not significant compared to the uncertainties. It means that the gold coating has no influence on the evaporator temperature. However, the optimum heat load reaches 130 W with the coating whereas it reaches only 80 W without it. It means that the coating has a positive influence on the optimum heat load despite the poor contact between the concave wick surface and the evaporator, only at the periphery of the copper block. Indeed, due to the gold high thermal conductivity (315 W/m.K) the heat is better spread. It results, for the same evaporator temperature, in a more homogeneous temperature field at the surface of the wick. The maximum temperature being lower, the occurrence of the nucleation is delayed. That explains why the gold coating provides a higher optimum heat load without increasing the heat transfer coefficient.

Figure V-20 (b) shows the thermal behaviour of the side A (convex) of the sample Zi-sin-6-f before and after the coating, with water. The heat transfer coefficient is higher with coating as well as the optimum heat load (120 W compared to 110 W before coating). The maximum superheats are similar (68.9 K and 69.6 K after and before coating, respectively). In this case, there is no spreading effect since a larger part of the wick surface is in contact with the evaporator as shown in Figure V-18. Thus, the high thermal conductivity of the gold seems to just enable the decrease of the thermal contact resistance between the evaporator and the wick. Moreover, the low hardness of the gold could enable this layer to act as an interstitial material, decreasing also the thermal contact resistance. However, these conclusions still have to be confirmed by further experiments.

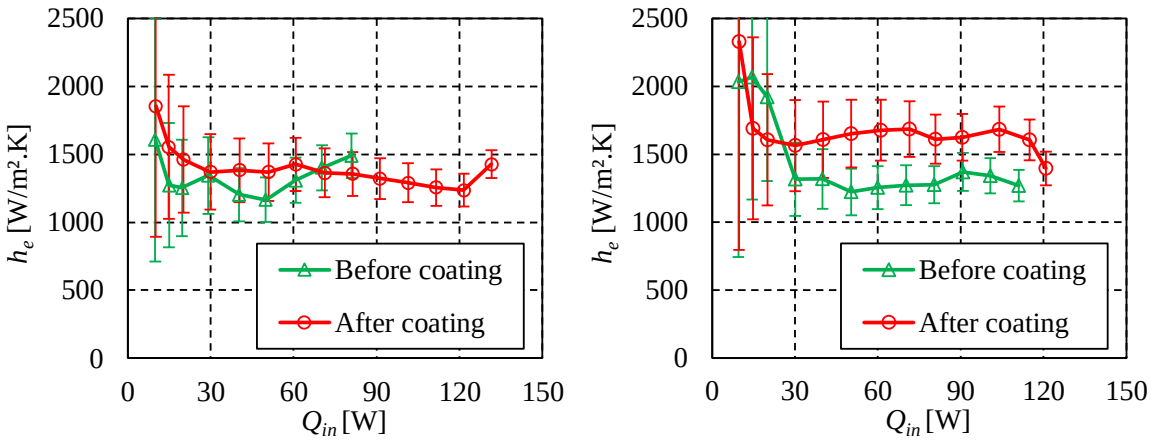

a) Zi-sin-6-e: Side B (concave) b) Zi-sin-6-f: Side A (convex)

Figure V-20: Comparison of the thermal performance before and after the coating

V.5.2 Influence of the hydrodynamic characteristics of the wick

The influence of the hydrodynamic characteristics on the thermal behaviour of the samples is investigated in this section. To this purpose, the samples manufactured with the design of experiment are tested with water, and then pentane as working fluids. Only the convex side of the samples are tested in order to avoid as much as possible the perturbation due to the difference of surface quality between both sides and to only study the influence of the hydrodynamic characteristics.

The evolution of the heat transfer coefficient is presented in Figure V-21 for each sample with water as the working fluid. It highlights the difference of behaviour of the various samples. Table V-6 summarises the thermal characterisation results of these tests. The wick parameters are coloured in green if they are in the range determined in Chapter II, in orange if they are close to this range and in red otherwise. In the three last columns, the tests results are coloured from green to red from high to low values of the heat transfer coefficient or the optimum heat flux respectively. The evaporator wall superheat is not coloured since it do not represent a performance indicator but it is only an information enabling the investigation of the phenomena. It is observed, on one hand, that only four samples (corresponding to the protocols 1, 2, 3 and 7) operate beyond 40 W, and these ones have permeabilities higher than 1.3×10^{-14} m². It could mean that in low-permeability samples (below 1.3×10^{-14} m²), the pressure losses are too high to supply liquid to the evaporator, leading to a dry out of the porous structure. Thus, a high permeability is necessary to ensure good thermal performance. However, this is not sufficient because sample Cu-sin-5-a has a high permeability but a low Q_{opt}.

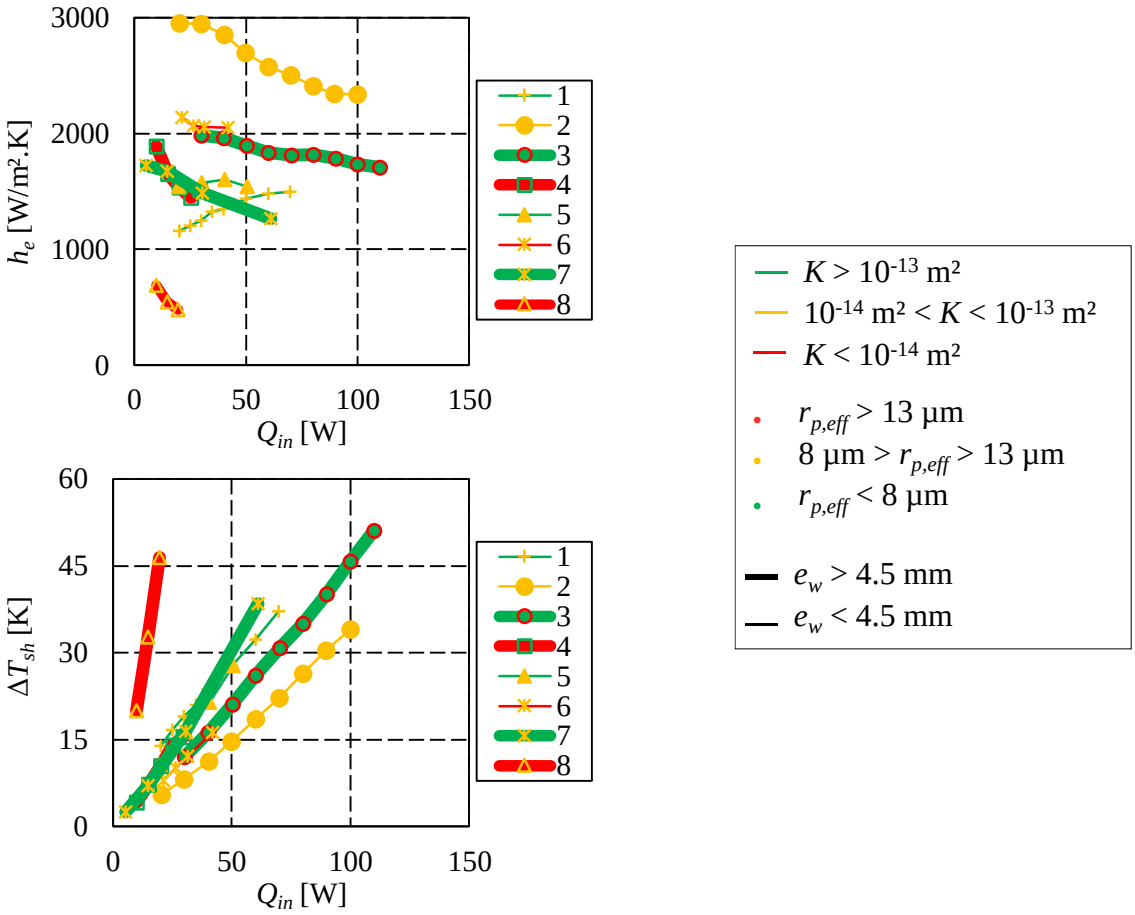

Figure V-21: Heat transfer coefficient as a function of the heat load for each sample with water

The heat transfer coefficient varies in a narrow range (from 1260 to 1950 W/m²K) except sample Cu-sin-8-a, which has much lower thermal performance, and sample Cu-sin-2-c which has a much

higher thermal performance. The variation of $h_{e,opt}$ can neither be explained by the permeability, nor by its thickness, and nor by the pore radius. Indeed, similar values of these characteristics can be found in other samples without the same consequences in terms of thermal performance. Thus, only the surface quality may be responsible of the difference of heat transfer coefficients between the various samples.

Table V-6: Results of thermal characterisation with water (T_{sat} = 50 °C, H_l = 3.9 cm, side A)

Sample	Protocol	e_w [mm]	K [10^{-14} m²]	$r_{p,eff}$ [µm]	Q_{opt} [W]	$h_{e,opt}$ [W/m²K]	$\Delta T_{sh,max}$ [K]
Cu-sin-1-b	1	3.2	11.6	11.3	70	1500	37.2
Cu-sin-2-c	2	2.8	1.37	11.5	100	2340	34.0
Cu-sin-3-a	3	5.2	10.1	18.3	110	1710	51.1
Cu-sin-4-a	4	4.7	0.6	<5.0	30	1520	15.5
Cu-sin-5-a	5	2.0	10.5	10.3	50	1540	27.7
Cu-sin-6-c	6	2.45	0.52	9.3	40	1950	16.3
Cu-sin-7-c	7	6	16.9	11.5	60	1260	38.5
Cu-sin-8-a	8	5.45	0.56	11.3	20	480	46.5

It is of interest to investigate the phenomena leading to the sudden drop of the thermal performance. Figure V-22 shows the experimental optimum heat flux $Q_{opt,exp}$ as a function of the theoretical capillary limit $Q_{opt,th}$, calculated by means of Eq. (V-9). The green marks correspond to samples having a high permeability, whereas the red ones correspond to samples having a low permeability. The samples of permeability lower than 10^{-13} m² probably reach the capillary limit since $Q_{opt,exp}$ varies between 25 and 50 % of the theoretical capillary limit. Even if it is lower than 100 %, it could mean that an early dry-out may occur at about 25 % of $Q_{opt,th}$. Instead, the samples having a permeability higher than 10^{-13} m² do not reach an optimum heat flux higher than 25 % of the capillary limit and even 10 % for the samples corresponding to the protocols 1, 5 and 7. Their permeabilities are so high that the capillary limit is not reached and another phenomenon might be responsible of the dry out.

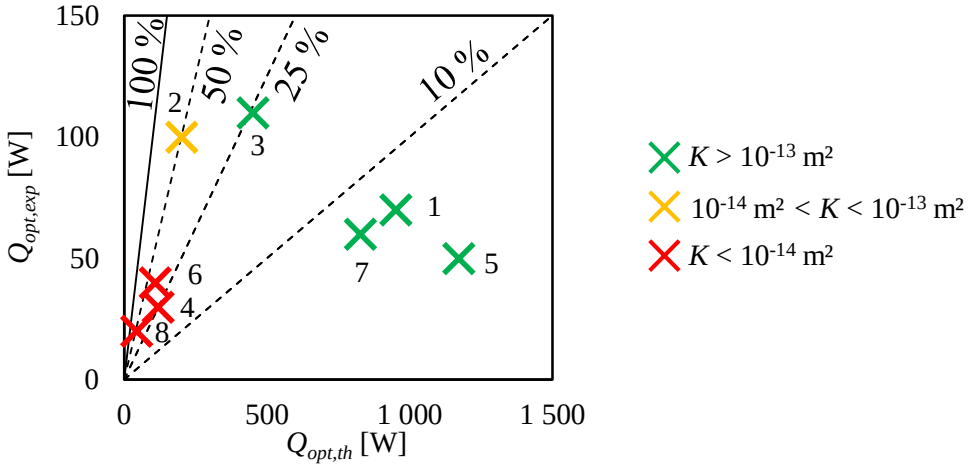

Figure V-22: $Q_{opt,exp}$ as a function of $Q_{opt,th}$ with water

In order to know if the boiling limit is reached, the same method is applied with the superheat. The theoretical maximum superheat $\Delta T_{sh,max,th}$ is determined with Eq.(I-13). Figure V-23 shows the experimental maximum superheat $\Delta T_{sh,max,exp}$ as a function of $\Delta T_{sh,max,th}$. The samples corresponding to the protocols 1, 3 and 7 probably reach the boiling limit since the superheat before the dry out is close to $\Delta T_{sh,max,th}$. It is important to note that the samples corresponding to the protocols 4 and 8 might be concerned by the boiling limit since they also reach the theoretical superheat.

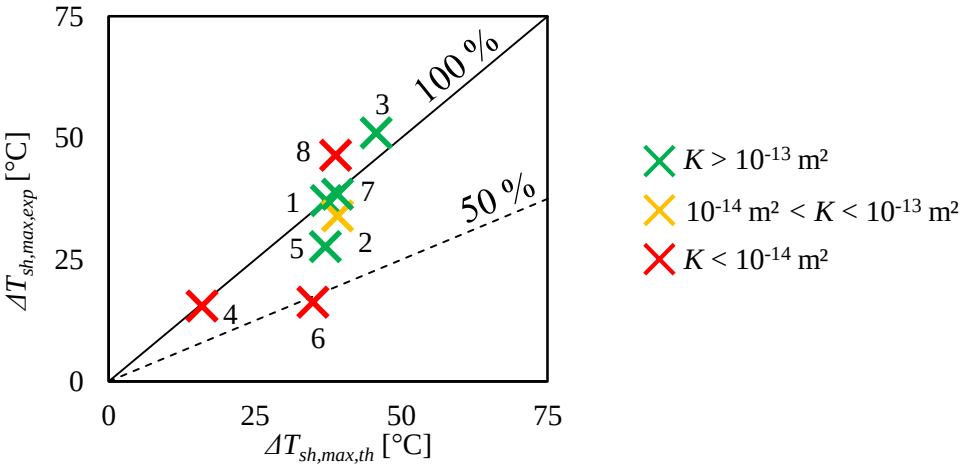

Figure V-23: $\Delta T_{sh,max,exp}$ as a function of $\Delta T_{sh,max,th}$ with water (r_n = 3.6 µm)

Except the sample Cu-sin-5-a which does neither reach $Q_{opt,th}$ nor $\Delta T_{sh,max,th}$, the previous results show that, in a capillary wick operating in the same conditions than a LHP wick, the capillary limit or the boiling limit can occur, preventing the system to operate at higher heat loads or higher superheats. A sample with a low permeability will probably reach the capillary limit since it prevents the fluid to easily flow through the wick. A sample with a high porosity (and thus a high permeability) will probably reach the boiling limit. The later has larger pores than samples of low porosity, as shown in Figure V-24. Considering that the saturation pressure of the liquid phase increases with an increasing pore radius, if it reaches the pressure of the liquid inside the capillary wick, boiling may occur.

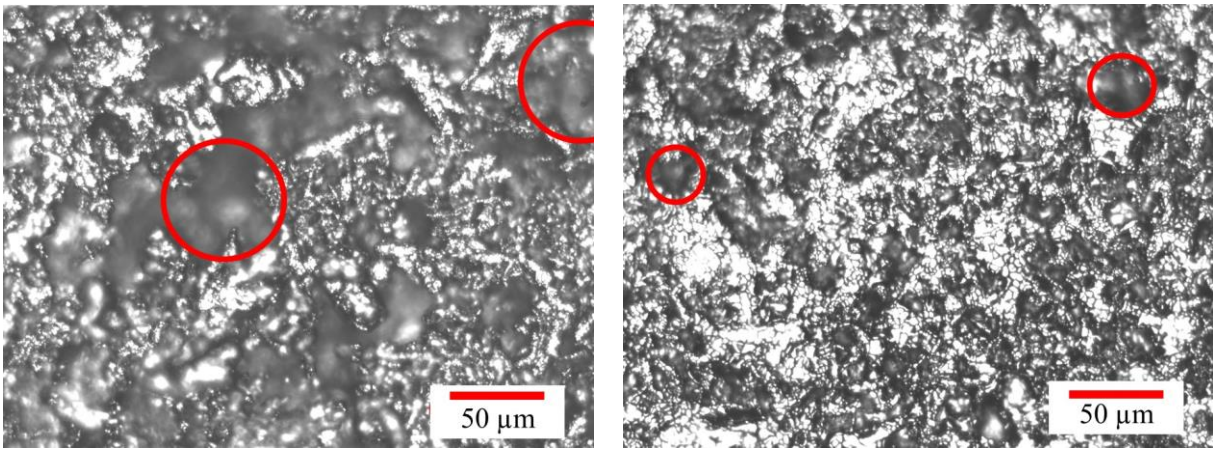

a) Sample Cu-sin-3-a ($K = 10.1\times10^{-14}$ m²) b) Sample Cu-sin-6-b ($K = 0.52\times10^{-14}$ m²)

Figure V-24: Pictures obtained with optical microscopy

The same study is conducted with another fluid, namely the pentane, in order to see if the previous conclusions remains valid. The results obtained with pentane (Figure V-25 and Table V-7) and water present many differences. Indeed, except the sample Cu-sin-8-a, all the samples have a Q_{opt} ranging from 50 to 70 W, no matter their permeability, as shown in Table V-7. Moreover, except the sample Cu-sin-3-a, the maximum superheat is much lower than with water. However, a similarity exists with the results obtained with water: the hydrodynamic characteristics still have no evident influence on $h_{e,opt}$. It varies between 2060 W/m².K and 5310 W/m².K. These values are higher than the heat transfer coefficients measured with water. This phenomena is discussed in the Section V.5.3.

Table V-7: Results of thermal characterisation with pentane (T_{sat} = 40 °C, H_l = 3.9 cm, side A)

Sample	Protocol	e_w [mm]	K [10^{-14} m²]	$r_{p,eff}$ [µm]	Q_{opt} [W]	$h_{e,opt}$ [W/m²K]	$\Delta T_{sh,max}$ [K]
Cu-sin-1-b	1	3.2	11.6	11.3	-	-	-
Cu-sin-2-c	2	2.8	1.37	11.5	50	3750	10.7
Cu-sin-3-a	3	5.2	10.1	18.3	70	2060	27.0
Cu-sin-4-a	4	4.7	0.6	<5.0	60	5200	9.2
Cu-sin-5-a	5	2.0	10.5	10.3	60	5030	9.5
Cu-sin-6-c	6	2.45	0.52	9.3	-	-	-
Cu-sin-7-c	7	6	16.9	11.5	60	5310	9.0
Cu-sin-8-a	8	5.45	0.56	11.3	20	4380	3.6

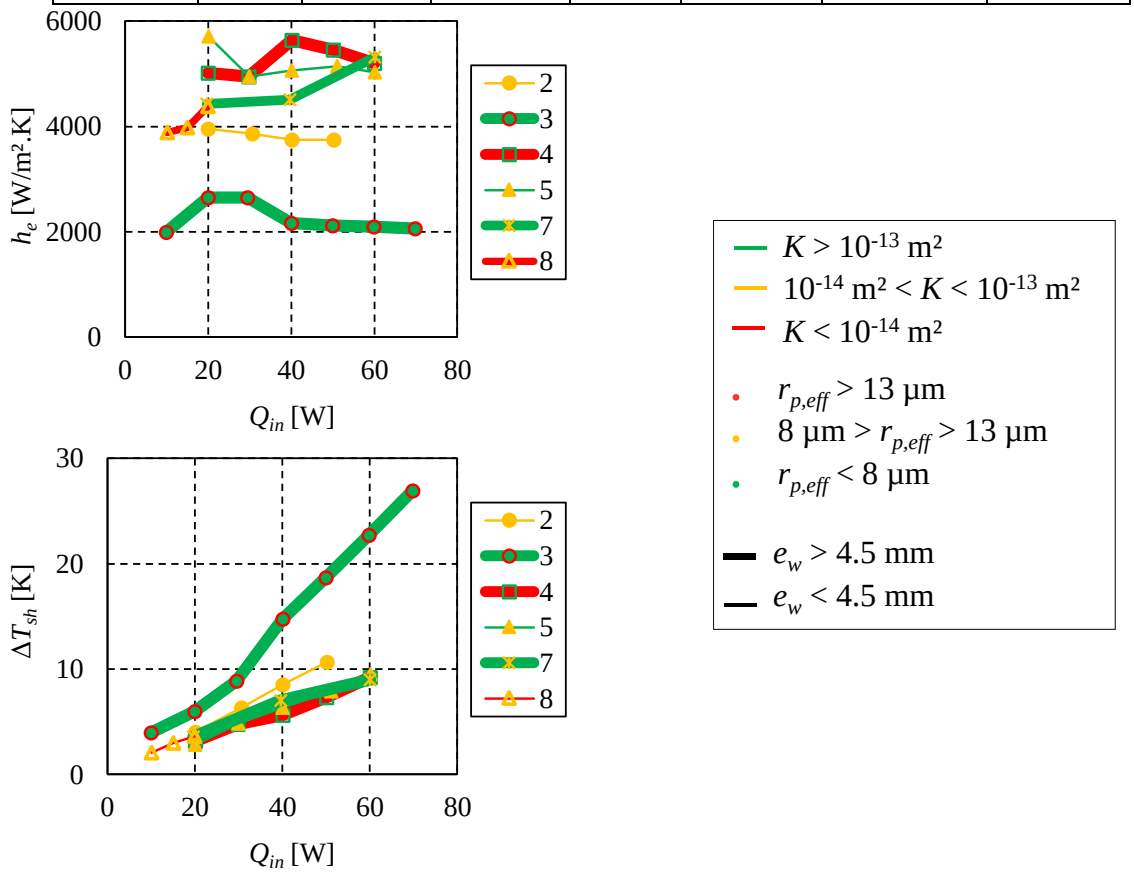

Figure V-25: Heat transfer coefficient as a function of the heat load for each sample with pentane

The pentane properties being different from water, it is of interest to investigate again the phenomena limiting the operation. Figure V-26 shows the experimental optimum heat load $Q_{opt,exp}$ as a function of the theoretical capillary limit Q_{opt}. The observed trend is roughly the same than with water. Indeed, the samples 5 and 7, having a high permeability, do not reach the capillary limit whereas the samples 2, 4 and 8, having a low permeability, operates beyond $Q_{opt,th}$. The difference with water is that four samples exceed the capillary limit. These surprising results may be explained by several phenomena. Firstly, the assumption of the absence of heat leaks cannot be confirmed. It is possible that a significant part of the heat load applied is evacuated by conduction to the reservoir. In this case, the mass flow rate would be drastically decreased and so, the pressure losses. Measuring the mass flow rate would be a major improvement of this test bench. Secondly, the static contact angle measured in the present study induces an uncertainty in the calculation of the theoretical capillary limit. Moreover, the minimum meniscus radius may be affected by the fluid evaporation itself. In this case, the minimum meniscus radius measured by the hydrodynamic test bench in adiabatic conditions may not be representative of the effective pore radius in the thermal test bench. Finally, a phenomenon of progressive dry-out could

happen inside the wick just after the capillary limit is reached, which does not hinder the evaporator operation but would lead to lower thermal performance. This phenomenon was also observed by Nagano and Ku [36] and Ku and Birur [178] in heat pipes. It means that the capillary limit would be exceeded for the samples corresponding to the protocols 2, 3, 4 and 8. This explanation can be confirmed when investigating the heat transfer coefficient of these samples. Their average value of $h_{e,opt}$ is only 3850 W/m².K, whereas it is 5170 W/m².K (34 % higher) for samples corresponding to the protocols 5 and 7 for which the capillary limit is supposed not to be reached.

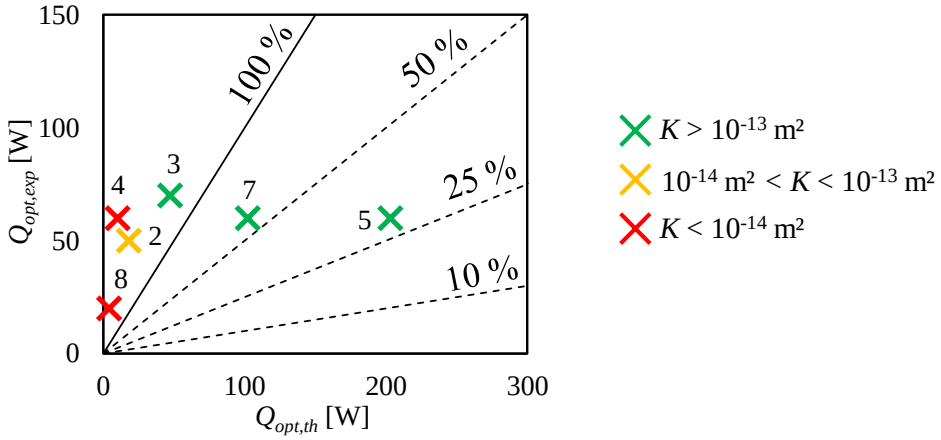

Figure V-26: $Q_{opt,exp}$ as a function of $Q_{opt,th}$ with pentane

Due to the lack of information about pentane, the nucleation radius cannot be determined by means of Eq. (V-10). In order to know if the boiling limit is reached, $\Delta T_{sh,max,exp}$ is plotted as a function of the effective pore radius (Figure V-27) for various nucleation radii. Samples corresponding to the protocols 2, 4, 5 and 7 reach a superheat that corresponds to a nucleation radius of around 0.7 µm. It is expected that the nucleation radius with pentane is lower than with water due to its lower surface tension and its higher vapour density. The superheat obtained with the sample Cu-sin-8-a is lower than expected but it is not surprising since it has probably reached the capillary limit. The sample Cu-sin-3-a operates with a superheat which greatly exceeds the theoretical superheat corresponding to a nucleation radius of 0.7 µm. It means that the first nucleation site is lately activated, or that the boiling phenomena does not prevent the operation of this specific sample. However, no specific property has been identified to explain this particular behaviour. As with water, the samples not concerned by the capillary limit (protocols 3, 5 and 7) reach an experimental superheat consistent with the occurrence of boiling. The samples corresponding to the protocols 2 and 4 might also be concerned by the boiling limit, since their experimental superheats are also consistent with the occurrence of boiling. However, for these samples, it cannot be decided if they have reached the capillary or the boiling limit.

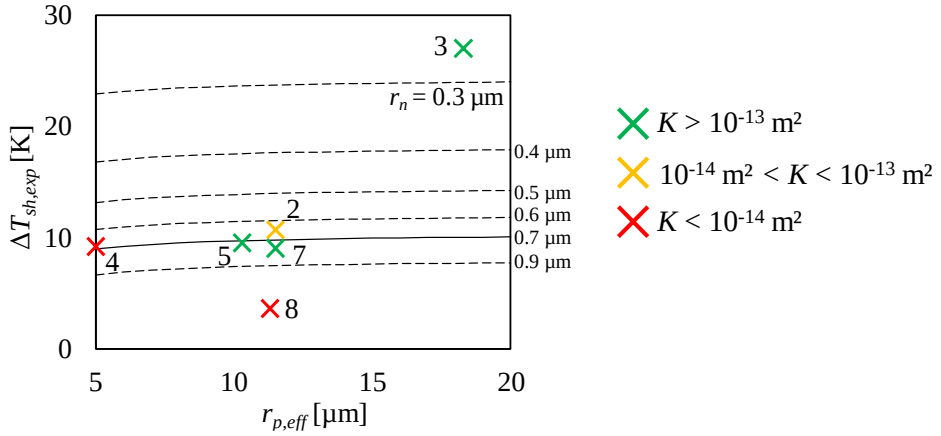

Figure V-27: Experimental maximum superheat as a function of the effective pore radius

The investigation of the hydrodynamic characteristics influence have shown that it is often possible, knowing the permeability, the thickness and the effective pore radius, to predict the operating limits. However, no direct relation has been established between these characteristics and the heat transfer coefficient.

V.5.3 Comparison of the results obtained with water and pentane

Figure V-28 presents a comparison of the optimum heat flux and optimum heat transfer coefficient of the sintered copper samples obtained when using pentane and water.

Firstly, the optimum heat flux measured with pentane varies in a narrower range than with water: except for the sample obtained with the protocol 8, the optimum heat flux varies between 50 W and 70 W with pentane whereas it varies between 30 W and 110 W with water. None of these two fluids leads to a higher optimum heat load than the other one: Q_{opt} is higher with pentane than with water for samples 4 and 5, identical for samples 7 and 8, lower for samples 2 and 3. As explained in Section V.5.2, the optimum heat load depends on the hydrodynamic characteristics with water whereas it is almost constant with pentane, since the boiling limit occurs at a very small nucleation radius compared to the pore radius. Thus, boiling always occurs approximately at the same heat load with pentane.

Secondly, the heat transfer coefficient is significantly higher with pentane than with water. This can be explained by the difference between the fluid properties of these two fluids. The wettability of the pentane being significantly higher than the water one on copper, it rewets more easily the wick in contact with the evaporator fins, reducing the thermal resistance.

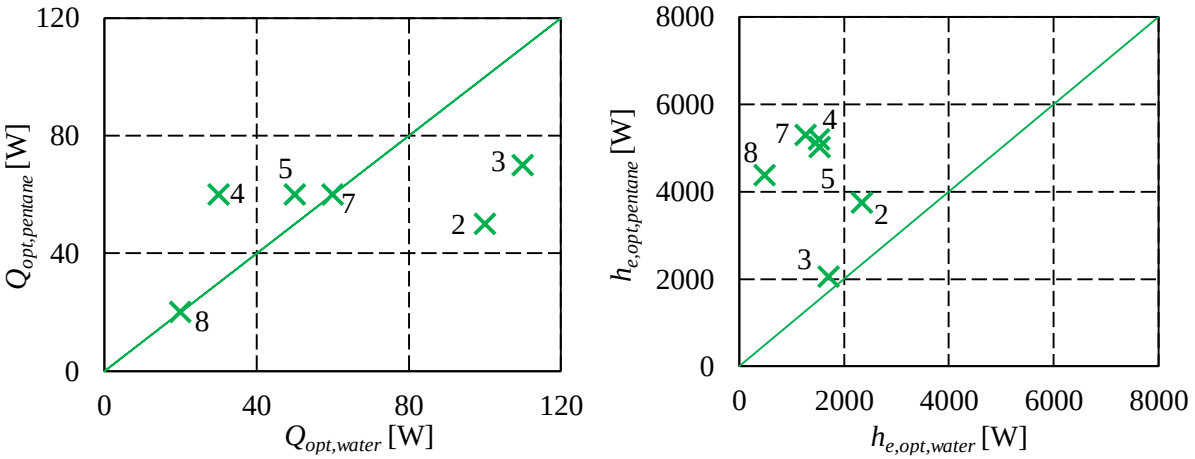

a) Optimum heat load b) Heat transfer coefficient

Figure V-28: Comparison of the thermal performance of the samples with water and pentane

V.5.4 Statistical analysis of the parameters influence on the heat transfer coefficient

The analysis performed with various porous samples, fluids, and surface qualities highlights the difficulty to understand the influence of the wick characteristics on the heat transfer coefficient. Despite the attempts to explain the observed tendencies, the coupled influence of numerous parameters and the experimental uncertainties make it difficult to provide strong conclusions.

Since a great number of tests results are available, a statistical analysis may help to differentiate the influent parameters from the non-influent ones. The selected method (called SPRINT[7]) is a decision-tree-based classification. The classification starts by the building of a table containing several tests

[7]Vasile-Marian Scuturici (LIRIS) is gratefully thanked for the help he gave to understand this method

(lines) and for each test, several parameters (columns) as well as the test results. The test results are assigned to a given level (high, medium and low) depending on thresholds. The algorithm starts with the whole data set. The data set is partitioned according to a splitting criterion into subsets. The procedure is repeated recursively for each subset until each subset contains only members belonging to the same level or is sufficiently small. Shafer *et al.* [179] present in more details this scalable parallel classifier for data mining.

Fifty-three test results are presented in Table V-8, obtained with the eight copper samples manufactured following the design of experiment, and other copper samples. The hydrodynamic characteristics of all the samples are also summarised in Table V-8. Twenty-nine tests were conducted with pentane and twenty-four with water. Thirty-nine tests were performed on samples without any surface treatments and fourteen tests with a surface treatment.

The tests are classified depending on the optimum heat transfer coefficient $h_{e,opt}$, and on the chosen thresholds: 3000 W/m².K and 5000 W/m².K. If $h_{e,opt}$ varies from 0 to 3000 W/m².K, the test performance is considered as LOW, if it varies from 3000 to 5000 W/m².K, it is considered as MEDIUM and if it is higher than 5000 W/m².K, the test performance is considered as HIGH. The test parameters are the sample, with its hydrodynamic characteristics and its surface quality (roughness, flatness), and the fluid. Note that the characteristics of a sample may vary from one test to another if a surface treatment has been brought to this sample between the two tests.

Figure V-29 shows the tree enabling to know what parameters give the highest heat transfer coefficient. The tree is built step by step. Firstly, the software finds the most discriminating parameter and creates two branches in which the tests are classified according to the three levels. One branch, with the tests leading to the major part of low heat transfer coefficients, is not studied. The other branch, with the tests leading to the major part of high heat transfer coefficients, is further investigated. The software finds another parameter that discriminates the remaining tests. Two more branches are built. At the end, the software is not able to find a discrimination of parameter anymore.

In our case, the fluid is the most discriminating parameter and the software builds a branch with the tests conducted with water and another one with the tests conducted with pentane. Indeed, all the tests giving a high $h_{e,opt}$ are obtained with pentane whereas twenty-three tests among the thirty-four giving a low $h_{e,opt}$ are obtained with water. This result was expected considering the explanations given in Section V.5.3. Secondly, the surface treatments are discriminating. Indeed, a surface treatment gives a low $h_{e,opt}$ in almost each test whereas it remains often at a high value without surface treatments. Again, this result was expected, because the gap created between the porous wick and the evaporator is larger if there is no surface treatment. Finally, the effective pore radius is the only hydrodynamic characteristic that is discriminating concerning the heat transfer coefficient. An effective pore radius lower than 15 µm leads to a high heat transfer coefficient.

It is confirmed that the surface quality is the wick characteristics with the highest influence on the thermal behaviour. Further investigations need to be conducted in order to improve the comprehension of this influence.

Table V-8: Test parameters enabling the estimation of the heat transfer coefficient

Sample	*ε (%)*	*K (10^{-14} m²)*	*$r_{p,eff}$ [µm]*	*e_w [mm]*	*Surface treatment*	*Flatness type*	*Flatness [µm]*	*Roughness [µm]*	*Fluid*	*$h_{w,opt}$ [kW/(m².K)]*
Cu-sin-1-b	39.3	11.6	11.3	3.2	WT	Convex	100	15	Water	1.17
Cu-sin-2-b	26.7	2.57	23.0	2.95	WT	Convex	250	30	Water	1.3
Cu-sin-2-c	27.1	1.37	11.5	2.8	WT	Convex	300	15	Water	1.83
Cu-sin-2-c	27.1	1.37	11.5	2.8	WT	Convex	300	15	Water	1.68
Cu-sin-2-c	27.1	1.37	11.5	2.8	WT	Convex	300	15	Pentane	3.2
Cu-sin-2-c	27.1	1.37	11.5	2.8	WT	Concave	-200	15	Pentane	3.08
Cu-sin-2-c	27.1	1.37	11.5	2.8	WT	Concave	-200	15	Pentane	3.75
Cu-sin-2-c	27.1	1.82	18.5	2.7	S300	Concave	-50	5	Pentane	3.45
Cu-sin-2-c	27.1	1.82	18.5	2.7	S300	Concave	-50	5	Pentane	2.42
Cu-sin-3-a	40.6	10.1	18.2	5.2	WT			10	Water	1.85
Cu-sin-3-a	40.6	10.1	18.2	5.2	WT			10	Water	1.7
Cu-sin-3-a	40.6	10.1	18.2	5.2	WT			10	Water	1.7
Cu-sin-3-a	40.6	10.1	18.2	5.2	WT			10	Water	1.62
Cu-sin-3-a	40.6	10.1	18.2	5.2	WT			10	Water	1.85
Cu-sin-3-a	40.6	10.1	18.2	5.2	WT			10	Water	2.28
Cu-sin-3-a	40.6	10.1	18.2	5.2	WT			10	Water	1.26
Cu-sin-3-a	40.6	10.1	18.2	5.2	WT	Concave	-200	10	Pentane	1.92
Cu-sin-3-a	40.6	10.1	18.2	5.2	WT	Convex	300	10	Pentane	2.06
Cu-sin-4-a	22.6	0.6	5.0	4.7	WT	Convex	160	10	Water	1.06
Cu-sin-4-a	22.6	0.6	5.0	4.7	WT	Convex	160	10	Water	2.4
Cu-sin-4-a	22.6	0.6	5.0	4.7	WT	Convex	160	10	Water	1.52
Cu-sin-4-a	22.6	0.6	5.0	4.7	WT	Convex	160	10	Pentane	5.4
Cu-sin-4-a	22.6	0.6	5.0	4.7	WT	Convex	160	10	Pentane	5.2
Cu-sin-4-a	22.6	0.12	5.0	4.45	P	Flat	50	5	Pentane	1.42
Cu-sin-4-a	22.6	0.12	5.0	4.45	P	Flat	50	5	Pentane	3.01
Cu-sin-5-a	37	10.5	10.2	2	WT	Concave	-60	5	Water	1.58
Cu-sin-5-a	37	10.5	10.2	2	WT	Concave	-60	5	Water	1.61
Cu-sin-5-a	37	10.5	10.2	2	WT	Concave	-60	5	Water	1.7
Cu-sin-5-a	37	10.5	10.2	2	WT	Concave	-60	5	Pentane	5.25
Cu-sin-5-a	37	10.5	10.2	2	WT	Convex	270	5	Pentane	5.03
Cu-sin-5-a	37	10.5	10.2	2	WT	Convex	270	5	Pentane	5.03
Cu-sin-5-a	37	10.5	10.2	2	WT	Convex	270	5	Pentane	4.77
Cu-sin-5-a	37	0.26	5.0	1.9	S300	Flat	0	10	Pentane	2.57
Cu-sin-5-a	37	0.26	5.0	1.9	S300	Flat	0	10	Pentane	2.59
Cu-sin-5-a	37	3.25	30.7	1.9	A	Flat	0	10	Pentane	5.84
Cu-sin-5-a	37	3.25	30.7	1.9	A	Flat	0	10	Pentane	2.3
Cu-sin-6-c	28.6	0.52	9.2	2.1	WT			10	Water	1.95
Cu-sin-7-b	37	18.8	52.1	5.6	WT				Water	0.84
Cu-sin-7-c	41.8	16.9	11.5	6	WT	Convex	350	5	Water	1.26
Cu-sin-7-c	41.8	16.9	11.5	6	WT	Concave	-150	5	Water	1.66
Cu-sin-7-c	41.8	16.9	11.5	6	WT	Concave	-150	5	Water	1.77
Cu-sin-7-c	41.8	16.9	11.5	6	WT	Convex	350	5	Pentane	7.05
Cu-sin-7-c	41.8	16.9	11.5	6	WT	Concave	-150	5	Pentane	6.28
Cu-sin-7-c	41.8	19.5	11.5	5.8	M	Flat	0	40	Pentane	2.51
Cu-sin-7-c	41.8	19.5	11.5	5.8	M	Flat	0	30	Pentane	2.02
Cu-sin-7-c	41.8	18	11.5	4.45	M	Convex	60	20	Pentane	3.32
Cu-sin-7-c	41.8	26.8	11.5	4.2	S600	Convex	320	15	Pentane	3.81
Cu-sin-7-c	41.8	0.43	7.1	4	P	Flat	0	5	Pentane	2.37
Cu-sin-7-c	41.8	0.43	7.1	4	P	Flat	0	5	Pentane	1.86
Cu-sin-8-a	22.4	0.56	11.3	5.45	WT	Convex	200	5	Pentane	4.38
Cu-sin-8-a	22.4	0.56	11.3	5.45	WT	Concave	-80	5	Pentane	3.75
Cu-sin-8-a	22.4	0.56	11.3	5.45	WT	Concave	-80	5	Water	2
Cu-sin-8-a	22.4	0.56	11.3	5.45	WT	Convex	200	5	Water	3

WT: Without surface treatment; S300/S600: Sanded with a grain density of 300/600 gr/cm²
P: Polished; M: Machined; A: Immersed in an acidic solution

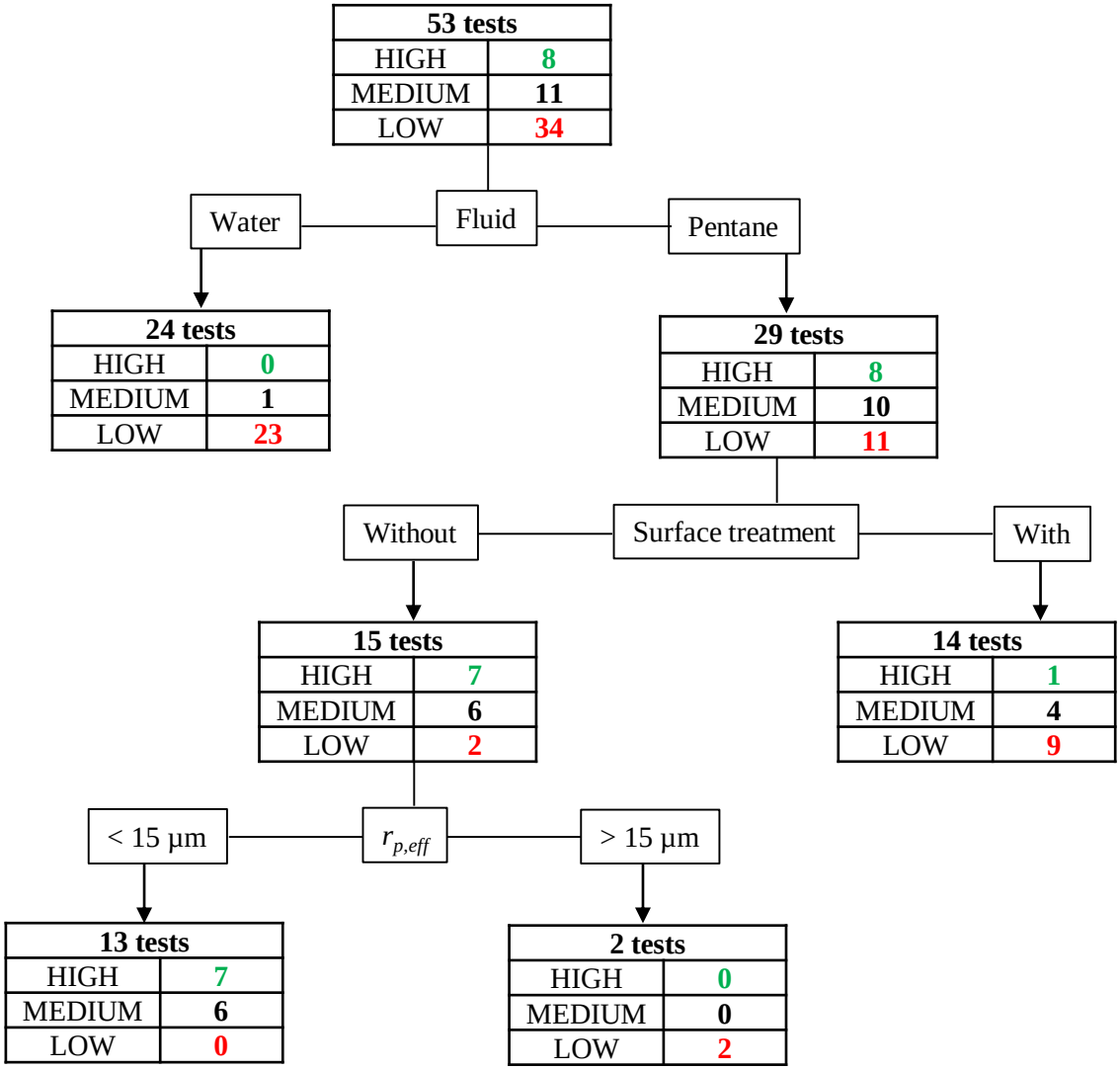

Figure V-29: Decision tree enabling the prediction of the heat transfer coefficient

This decision tree does not consider the tests obtained with water, since they were excluded at the first step. In order to also investigate these tests, the software is run without the tests obtained with pentane. Moreover, the thresholds are decreased from 3000 W/m².K and 5000 W/m².K to 1500 W/m².K and 1800 W/m².K. Surprisingly, a low permeability enables to obtain a high $h_{e,opt}$ (Figure V-30). However, only three tests are done with samples of this type whereas twenty-one tests are considered with a permeability higher than 0.6 10^{-14} m². Then, the flatness of the samples is the most discriminating parameter, according to the software results. However, it is not easy to analyse because the major part of the tests leading to poor performance is obtained with the flat samples (5 tests among 8), but the major part of the tests leading to the best performance is also obtained with these samples (3 tests among 5). The same problem is observed with the thickness. This is the limit of this type of data analysis. Indeed, if no parameter is significantly discriminating, the results are not exploitable. Thus, the prediction of $h_{e,opt}$ remains an issue if water is used as a working fluid.

As a conclusion, these decision trees must be seen as a tool enabling to predict the order of magnitude of the heat transfer coefficient depending on the hydrodynamic characteristics of the copper sample and on its surface quality. However, the results can be difficult to analyse. More experimental characterisation would be required to have a performant statistical analysis.

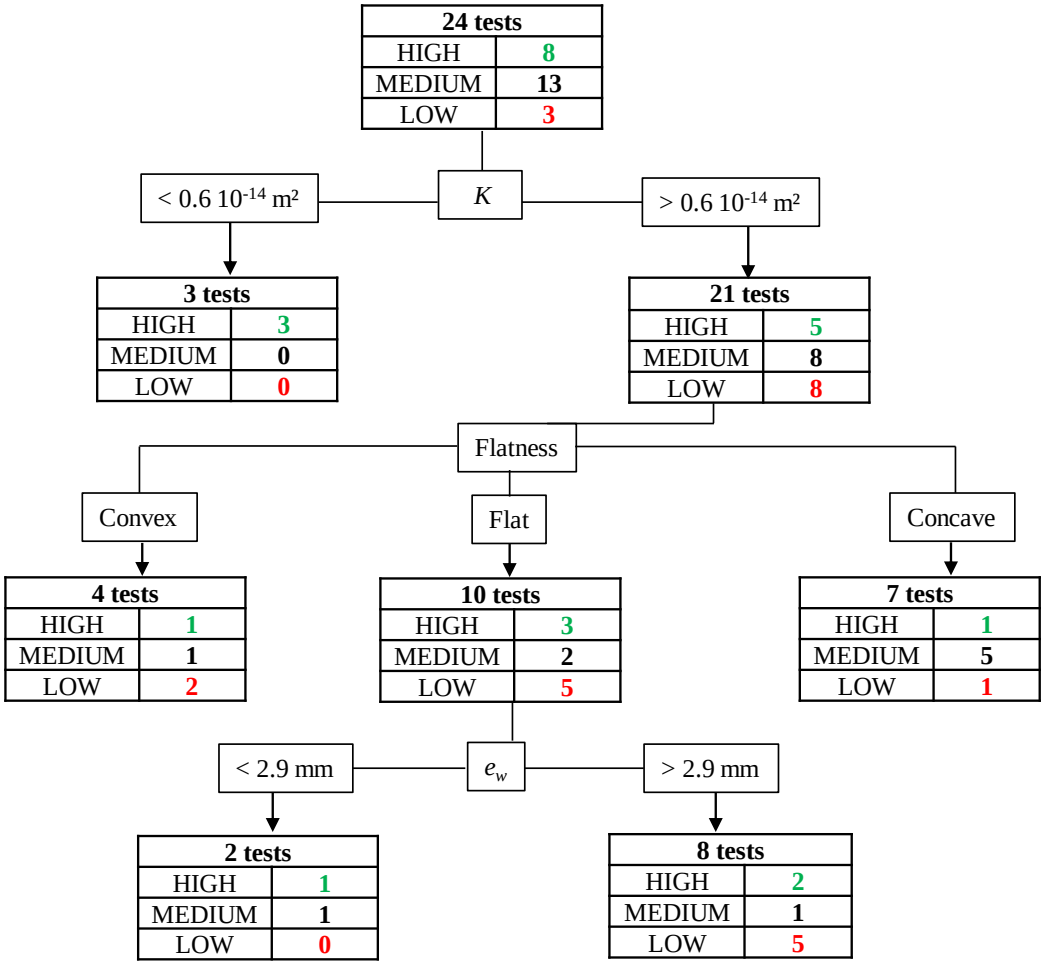

Figure V-30: Decision tree enabling the prediction of the heat transfer coefficient with water

V.6 Conclusion

A state-of-the-art is proposed in this chapter in order to review many different ways to study the thermal behaviour of a porous medium. It enables the design of a test bench specifically dedicated to this work. Then, the experimental apparatus is described as well as the procedures enabling the investigation of the thermal behaviour of the manufactured samples. The test bench reproduces an evaporator/reservoir of a LHP without the coupling with the rest of the loop. The study of the heat transfer coefficient as a function of the heat load applied shows the existence of operating limits. The theoretical operating limits are then investigated in order to enable the comprehension of the results obtained in the rest of this chapter.

The influence of the test bench parameters on the wick behaviour are discussed: hydrostatic pressure, oxidation of the evaporator, pressure applied on the back face of the evaporator, addition of a top layer, and saturation temperature. The saturation temperature has a significant influence on the thermal behaviour, contrarily to the other parameters. An increasing saturation temperature increases both the optimal heat flux and the heat transfer coefficient. However, the addition of a zirconia top layer to a copper layer has no significant effect on the thermal behaviour of the wick. That is promising for a future application since the bi-layer wick plays the role of thermal barrier only if coupled with the rest of the loop.

Then, the thermal behaviour of many porous structures used as bottom layer is discussed in order to study the influence of the surface quality and the hydrodynamic characteristics. It is shown that the surface quality has a significant influence on the fluid behaviour and on the thermal performance. A concave surface increases both the heat transfer coefficient and the optimal heat flux due to the presence of a gap larger than the pore size. A gold layer increases the optimum heat flux which confirms that a bi-layer wick may improve the thermal performance of a LHP. Moreover, it has been shown that both the boiling limit and the capillary limit are likely to be reached depending on the samples hydrodynamic characteristics and on the working fluid. A sample having a high permeability often reaches the boiling limit whereas a sample having a very low permeability may also reach the capillary limit.

The fluid has a significant influence on the heat transfer coefficient and on the optimum heat flux. Indeed, depending on the fluid properties, the boiling or the capillary limit is reached. Moreover, a small contact angle of the working fluid on the wick material increases the heat transfer coefficient by making easier the rewetting of the wick.

Finally, a statistical analysis on the heat transfer coefficient is done. Indeed, the large number of tests and parameters prevents a correct analysis without a specific tool. The interest of a gap between the wick and the evaporator fins in order to increase the heat transfer coefficient is confirmed as well as a small pore radius. Moreover, the heat transfer coefficient is almost always higher if pentane is used instead of water.

Conclusion

This thesis focuses on the heat and mass transfer in porous media specifically dedicated to LHPs. The major specificity of this work is to have joined material sciences and thermal sciences. The coupling of the different scientific skills of two laboratories, CETHIL and MATEIS, enabled to propose the approach summarised in Figure VI-1, from the theoretical design of the wick leading to the definition of its optimum characteristics, to the manufacturing, followed by the experimental characterisation and finally, the test of a complete LHP with the manufactured samples. A continuous improvement process was set up, since the knowledge of the manufacturing parameters effect on the wick characteristics enabled to adjust the procedures, to get closer to the targeted characteristics and to improve the LHP model.

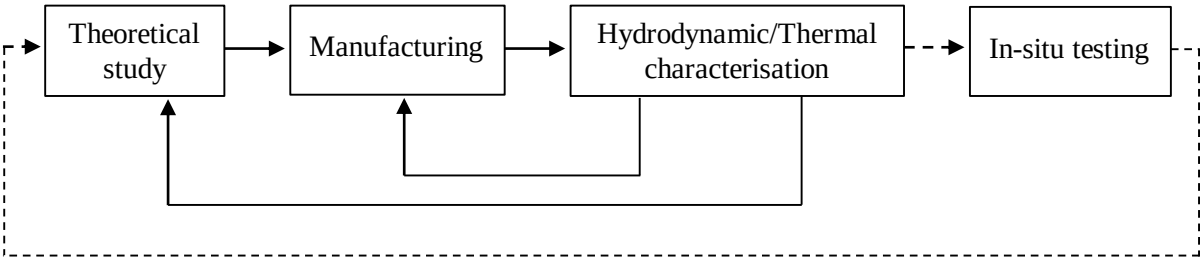

Figure VI-1: Scientific progress followed during the thesis

Firstly, an extensive literature review was undertaken in order to provide a better comprehension of the fundamental concepts of the LHP operation. The LHP operating principle was thoroughly described. The capillary structure, mostly made of mono porous sintered metallic powder, has to fulfil the functions of hydraulic and thermal barriers between the reservoir and the vapour line. However, its performance is limited by the development of dry-out phenomena at high heat fluxes, often associated to the appearance of the capillary limit. Advances capillary structures such as bi porous, bi dispersed structures or bi-layers wicks have proven their ability to delay the development of a dry-out zone.

Some LHP evaporator models identified in the literature assume a saturated wick whereas others assume a vapour zone inside the capillary structure. The objectives of these models are to understand the thermo-hydraulic phenomena governing the evaporator behaviour and to better understand the development of dry-out zones. Moreover, the models help to improve the properties of the porous structure. The probable interest of a two-layer capillary structure, including a material with a high thermal conductivity to transfer the heat to the liquid-vapour interface, and a material with a low thermal conductivity to limit the parasitic heat fluxes, was confirmed.

In the second chapter, an analytical model describing the thermo-hydraulic behaviour of a complete LHP having a flat disk-shaped evaporator (40 mm in diameter, 35 mm in thickness) equipped with a bi-layer wick was developed. This model was adapted from Siedel [4]. An extensive parametric study was performed in order to investigate the theoretical influence of the characteristics - thickness, thermal conductivity of the wick material, permeability, porosity and pore radius - of each layer. The layer in contact with the liquid of the reservoir should act as a thermal barrier and therefore, have a large thickness (5 to 10 mm) and a low thermal conductivity (< 2 W/m.K) whereas the layer in contact with the evaporator wall, which act as a capillary pump and a heat spreader, should have a small pore radius (2-10 µm) and a high thermal conductivity (> 100 W/m.K). The permeability of both layers should be higher than 30 to 37 % in order to decrease the pressure losses through the wick and delay the occurrence of the capillary limit. In order to avoid boiling inside the structure, small pore radii are required even in the layer close to the reservoir (5 to 10 µm).

In the third chapter, several manufacturing methods enabling to obtain porous media suitable for LHPs were presented; partial sintering of powder, PECS of wires and freeze casting. The main investigated method to manufacture flat disk shaped layers with a diameter of 40 mm is the partial sintering of copper, with or without pore former, and zirconia. Forty-seven samples were designed but the ones including a pore former in the sintering procedure and those resulting from freeze casting suffer from mechanical weaknesses. Bi-layer wicks were manufactured with two different methods: co-sintering and coating. Geometrical, topographical and microscopic characterisation was presented in this chapter enabling to determine the mass, the volume, the porosity, the topography and the global architecture of the wicks. It was observed that the wicks are porous and exhibit in most cases a concave and a convex side. A 2-level fractional factorial design of experiment was proposed for the sintering of copper powder in order to investigate the influence of the sintering parameters - forming pressure, mass of sintered powder, sintering time and sintering temperature - on the hydrodynamic characteristics.

The fourth chapter details typical test benches enabling the hydrodynamic characterisation of porous structures. A test bench for the determination of the effective pore radius and the permeability of a flat-disk shaped porous medium was specifically designed and fabricated. It is observed that the copper powder sintering protocols are reproducible regarding the permeability and the porosity, but not the effective pore radius and the thickness. The zirconia sintering protocols are less reproducible than the copper ones because the shrinkage is very sensitive to the sintering temperature. An increasing mass of sintered powder increases the wick thickness, whereas an increasing forming pressure decreases the permeability. A comparison of the results with the ones of the literature highlights that the permeability was slightly lower than expected due to a high forming pressure. The Rumpf-Gupte correlation seems to better fit the experiments than more usual ones (like the Kozeny-Carman correlation).

After a state-of-the-art of the test benches enabling the study of the thermal performance of LHP wicks, chapter V describes an experimental apparatus specifically designed to reproduce the evaporator/reservoir of a LHP decoupled from the rest of the loop and dedicated to the study of heat transfer in the flat-disk shaped wick. The analysis of the evolutions of the heat transfer coefficient h_e and the superheat ΔT_{sh} between the evaporator and the vapour phase as a function of the heat load shows that up to a value called Q_{opt}, h_e drastically decreases, leading to a large increase of the evaporator wall temperature. This phenomenon evidences a wick dry-out and the occurrence of an operating limit. The influence of the test bench parameters - saturation temperature, hydrostatic pressure, oxidation of the evaporator, pressure applied on the back face of the evaporator, number of wick layers - on the wick behaviour were discussed. The saturation temperature is the only parameter affecting the thermal performance: an increasing saturation temperature increases both Q_{opt} and h_e. The addition of a zirconia layer to a copper layer has no significant effect on the thermal behaviour of the wick.

The influence of the surface quality on the thermal behaviour was investigated by several mechanical surface treatments and by spreading a thin gold layer on a zirconia sample without changing the surface topography. It was shown that the concave shape of the wick surface in contact with the evaporator wall, creating a gap larger than the pore diameter, enables the vapour to flow along the grooves instead of penetrating the wick. A surface treatment must be avoided: it seems to drastically decrease the thermal performance because of the reduction of the gap size. The gold coating has a positive influence on the optimum heat load of a zirconia sample with a concave shaped surface, enabling to spread the heat over the whole surface and to delay the occurrence of boiling. This effect was not observed with a convex surface, for which the gold layer just enabled to decrease the thermal resistance between the evaporator wall and the wick.

The influence of the hydrodynamic characteristics on the thermal behaviour of the samples was investigated with two fluids, water and pentane, using only the convex surface of the wicks. The experimental optimum heat fluxes and maximum superheats were compared to the theoretical values predicted by usual correlations. Samples with a low permeability will probably reach the capillary limit since it prevents the fluid to easily flow through the wick whereas samples with a high porosity (and thus a high permeability) will probably reach the boiling limit first. The optimum heat flux obtained with pentane varies in a smaller range than with water, but none of these fluids is better than the other one concerning Q_{opt}. However, the heat transfer coefficient is significantly higher with pentane than with water, due to the higher wettability allowing the fluid to wet more easily the wick in contact with the evaporator fins.

A statistical analysis was proposed, based on a decision-tree classification, to facilitate the parametric study on the heat transfer coefficient. The results confirmed the major influence of the fluid, and thus of the wettability, on h_e. The surface quality is the second most influent parameter, showing the positive effect of a gap between the wick and the evaporator wall. At last, an effective pore radius lower than about 15 µm leads to a high heat transfer coefficient.

Despite these results, some improvements could be done on this work and many perspectives can be imagined in order to go further in the analysis performed all along this thesis.

As demonstrated, the Rumpf-Gupte correlation predictions fit better to the experimental permeabilities of the present manufactured samples than the Kozeny-Carman correlation ones. Since the present model uses the Kozeny-Carman correlation, it could be improved by changing the correlation or even by using the whole set of experimental wick characteristics.

The manufacturing of porous media has no limit but the imagination. Various manufacturing procedures have been imagined but not tested due to the lack of time. The most promising technique is probably the assembly of glass fibres. Indeed, they create capillary tubes in the fluid flow direction likely to reduce the pressure losses. Moreover, the glass has a low thermal conductivity and is really cheap compared to other materials. Nowadays, the robocasting (3D printing) has a too low definition to enable the manufacturing of porous structures suitable for LHPs but the progress concerning this technique must carefully be followed. This technique is promising since it enables to manufacture porous samples with a high level of control of their characteristics. The manufacturing by freeze casting is very sensitive to many parameters (initial and final temperature inside the mould, cooling rate, composition of the slurry, sintering time, sintering temperature, etc.) and time is required to find suitable procedures. Even if the tests performed in the present work failed due to the brittleness of the samples, skills were acquired and the results are encouraging for future works. These perspectives go hand in hand with the development of bi-layer wicks. Indeed, in this work, only preliminary results were presented. Since they showed the interest of focusing on this kind of porous medium for a LHP, a future work could go further in the design of manufacturing procedures enabling the development of porous media specifically dedicated for LHP.

When analysing the results obtained with the thermal test bench, the calculation of the fluid mass flow rate is based on the assumption that heat leaks are negligible and thus, the heat supply is used to evaporate the fluid. This assumption is probably not verified but it is very difficult to estimate to what extent. In order to improve the analysis of the results, measuring the mass flow rate would enable to better estimate the occurrence of the capillary limit and the heat flux distribution in the evaporator/wick system. The mass flow rate measurement requires a modification of the test bench in order to collect

and condensate the vapour and to determine its weight per unit of time. To this purpose the vapour tube needs to be extended so that its end is located outside and under the enclosure.

In a general way, the fluid behaviour at the vicinity of the evaporator fins remains a kind of mystery. In this thesis, the results enable to assume a dry-out in the wick or the occurrence of boiling depending on the heat load and on the evaporator wall temperature. However, no experimental observation has confirmed that the operation is exactly as assumed. In order to visualise the phenomena acting at this place, an endoscope inserted inside the evaporator wall could be used. This technique would enable to detect an eventual presence of vapour at the wick surface. Many analysis could be done based on such observations. This technique is promising but difficult to install while keeping a high sealing quality of the system.

Given the major effect of the surface quality on the operation, as highlighted during this thesis, it is important to further investigate this parameter, by modifying the wick surface flatness and/or the pattern of the evaporator fins. Moreover, to the authors' best knowledge, there is an absence of model taking into account a gap between the wick and the evaporator wall. Such a model could be developed in order to confirm the explanations proposed in this work.

To the same purpose, developing a statistical approach of the results is an opportunity to improve the comprehension of the physical mechanisms acting inside a porous medium. The software *KNIME* has shown that it was possible to go further in the analysis of the thermal behaviour of the tested samples. Since it is possible to increase the number of parameters, the decision-tree-base method is able to manage a very large number of tests, larger than in the present work.

Finally, the in-situ testing of the wick has not been performed in the framework of this PhD thesis. The laboratory LHP manufactured at the CETHIL by Siedel [4] could be used to test the manufactured wicks, and compare the LHP performance to the ones measured by Siedel [4] with a standard monolayer monoporous nickel wick. In-situ tests performed with bi-layer wicks is the only way to check the expected improvement of the LHP performance and to check if the wick thermal behaviour observed in the thermal test bench is a good image of its behaviour in a real LHP evaporator.

References

[1] G. E. Moore, 'Cramming more components onto integrated circuits', *Electronics*, vol. 38, no. 8, pp. 114–117, 1965.

[2] G. E. Moore and others, 'Progress in digital integrated electronics', *IEDM Tech Dig.*, vol. 11, 1975.

[3] J. Bonjour *et al.*, 'Systèmes diphasiques de contrôle thermique - thermosiphons et caloducs', *Les Techniques de l'Ingénieur. Traité de Génie energétique*. 2010.

[4] B. Siedel, 'Analysis of heat transfer and flow patterns in a LHP: modelling by analytical and numerical approaches and experimental observations. PhD thesis, INSA de Lyon'. 2014.

[5] S. Launay, V. Sartre, and J. Bonjour, 'An analytical Model for Characterization of Loop Heat Pipes', *J. Thermophys. Heat Transf.*, vol. 22, no. 4, pp. 623–631, 2008.

[6] R. Hodot, 'Modélisation et tests d'une boucle diphasique capillaire (LHP) pour applications avioniques civile et militaire', Thèse de doctorat, Université de Lyon, 2015.

[7] R. Singh, T. Nguyen, and M. Mochizuki, 'Capillary evaporator development and qualification for loop heat pipes', *Appl. Therm. Eng.*, vol. 63, no. 1, pp. 406–418, 2014.

[8] B. Siedel, V. Sartre, and F. Lefèvre, 'Numerical Investigation of the Thermohydraulic Behaviour of a Complete Loop Heat Pipe', *Appl. Therm. Eng.*, vol. 61, pp. 541–553, 2013.

[9] J. Ku, 'Operating Characteristics of Loop Heat Pipes', in *29th International Conference on Environmental System*, 1999, vol. 1999-01-2007, pp. 503–519.

[10] Y. F. Maydanik, 'Loop heat pipes', *Appl. Therm. Eng.*, vol. 25, pp. 635–657, 2005.

[11] T. Kaya and J. Goldak, 'Numerical analysis of heat and mass transfer in the capillary structure of a loop heat pipe', *Int. J. Heat Mass Transf.*, vol. 49, pp. 3211–3220, 2006.

[12] E. I. Altman, M. I. Mukminova, and H. F. Smirnov, 'The loop heat pipe evaporators theoretical analysis', in *12th International Heat Pipe Conference*, Moscow, Russia, 2002.

[13] D. Butler, J. Ku, and T. Swanson, 'Loop Heat Pipes and Capillary Pumped Loops: An Applications Perspective', presented at the 12th Halon Options Technical Working Conference, Albuquerque, New Mexico (USA), 2002, vol. 608, pp. 49–56.

[14] R. Singh, A. Akbarzadeh, C. Dixon, M. Mochizuki, and R. R. Riehl, 'Miniature Loop Heat Pipe With Flat Evaporator for Cooling Computer CPU', *IEEE Trans. Compon. Packag. Technol.*, vol. 30, no. 1, pp. 42–49, 2007.

[15] D. Wang, Z. Liu, S. He, J. Yang, and W. Liu, 'Operational characteristics of a loop heat pipe with a flat evaporator and two primary biporous wicks', *Int. J. Heat Mass Transf.*, vol. 89, pp. 33–41, 2015.

[16] P. Soler, 'Expérimentation et modélisation thermohydraulique des boucles à pompage capillaire de type Loop Heat Pipe (-LHP-): étude du lien entre la chambre de compensation et l'évaporateur', Thèse de doctorat, Université Aix-Marseille, 2009.

[17] J. M. Cimbala, J. S. J. Brenizer, A. P.-Y. Chuang, S. Hanna, C. T. Conroy, and D. R. R. A. A. El-Ganayni, 'Study of a loop heat pipe using neutron radiography', *Appl. Radiat. Isot.*, vol. 61, pp. 701–705, 2004.

[18] S. Launay and M. Vallée, 'State-of-the-Art Experimental Studies on Loop Heat Pipes', *Front. Heat Pipes*, vol. 2, no. 1, 2011.

[19] S. Launay, V. Sartre, and J. Bonjour, 'Parametric analysis of loop heat pipe operation: a literature review', *Int. J. Therm. Sci.*, vol. 46, no. 7, pp. 621–636, 2007.

[20] Y. F. Maydanik, 'Miniature loop heat pipes', in *13th International Heat Pipe Conference*, Shangai, China, 2004, pp. 23–35.

[21] Y. Chen, M. Groll, R. Mertz, Y. F. Maydanik, and S. V. Vershinin, 'Steady-state and transient performance of a miniature loop heat pipe', *Int. J. Therm. Sci.*, vol. 45, pp. 1084–1090, 2006.

[22] J. H. Boo and W. B. Chung, 'Experimental Study on the Thermal Performance of a Small-scale Loop Heat Pipe with Polypropylene Wick', *J. Mech. Sci. Technol.*, vol. 19, pp. 1052–1061, 2005.

[23] R. R. Riehl and T. Dutrab, 'Development of an experimental loop heat pipe for application in future space missions', *Appl. Therm. Eng.*, vol. 25, pp. 101–112, 2005.

[24] D. R. Adkins and R. C. Dykhuizen, 'Procedures for measuring the properties of heat-pipe wick materials', Sandia National Labs., Albuquerque, NM (United States), 1993.

[25] M. Hamdan *et al.*, 'Loop heat pipe (LHP) development by utilizing coherent porous silicon (CPS) wicks', in *The Eighth Intersociety Conference on Thermal and Thermomechanical Phenomena in Electronic Systems*, SanDiego (USA), 2002, pp. 457–465.
[26] P. Y. A. Chuang, 'An improved steady-state model of loop heat pipes based on experimental and theoretical analyses', PhD thesis, Pennsylvania State University, 2003.
[27] D. Mishkinis and J. Ochterbeck, 'Homogeneous Nucleation and the Heat-Pipe Boiling Limitation', *J. Eng. Phys. Thermophys.*, vol. 76, no. 4, pp. 813–818, 2003.
[28] S. Van Stralen, R. Cole, *Boiling Phenomena*, vol. 1. McGraw-Hill, 1979.
[29] L. Mottet, T. Coquard, and M. Prat, 'Three dimensional liquid and vapour distribution in the wick of capillary evaporators', *Int. J. Heat Mass Transf.*, vol. 83, pp. 636–651, 2015.
[30] V. Dhir, S. Kandlikar, Y. Fujita, Y. Iida, and R. Heist, 'Nucleate boiling', *Handb. Phase Change Boil. Condens.*, pp. 71–120, 1999.
[31] G. P. Peterson, *An introduction to heat pipes: modeling, testing, and applications*. Wiley-Interscience, 1994.
[32] P. D. Dunn and D. A. Reay, *Heat Pipes*. Pergamon Press, Oxford, 1982.
[33] S. W. Chi, *Heat pipe theory and practice: a sourcebook*. Washington DC: Hemisphere Pub. Corp., 1976.
[34] H. Y. Kwak and R. Panton, 'Tensile strength of simple liquids predicted by a model of molecular interactions', *J. Phys. Appl. Phys.*, vol. 18, p. 647, 1985.
[35] H. Y. Kwak and S. Lee, 'Homogenous bubble nucleation predicted by a molecular interaction model', *J. Heat Transf.*, vol. 113, pp. 714–721, Aug. 1991.
[36] H. Nagano and J. Ku, 'Capillary limit of a multiple-evaporator and multiple-condenser miniature loop heat pipe', *J. Thermophys. Heat Transf.*, vol. 21, no. 4, pp. 694–701, 2007.
[37] P. H. D. Santos, E. Bazzo, and A. A. M. Oliveira, 'Thermal performance and capillary limit of a ceramic wick applied to LHP and CPL', *Appl. Therm. Eng.*, vol. 41, pp. 92–103, 2012.
[38] Q. Liao and T. Zhao, 'A visual study of phase-change heat transfer in a two-dimensional porous structure with a partial heating boundary', *Int. J. Heat Mass Transf.*, vol. 43, no. 7, pp. 1089–1102, 2000.
[39] T. Hoang, T. O'Connell, and J. Ku, 'Management of parasitics in cryogenic advanced loop heat pipes', *Pap. No AIAA*, vol. 346, pp. 6–9, 2003.
[40] T. Kaya and J. Ku, 'A parametric study of performance characteristics of loop heat pipes', *SAE Tech. Pap.*, pp. 01–2006, 1999.
[41] T. Coquard, 'Transferts couplés de masse et de chaleur dans un élément d'évaporateur capillaire', Thèse de doctorat, Institut National Polytechnique de Toulouse, 2006.
[42] A. Faghri, *Heat Pipe Science And Technology*, 1st ed. Taylor & Francis, 1995.
[43] S. Launay, V. Sartre, and J. Bonjour, 'Selection criteria for fluidic and geometrical parameters of a LHP based on analytical approach.', in *15th International Heat Pipe Conference*, Clemson, USA, 2010.
[44] D. Mishkinis, P. Prado, R. Sanz, and A. Torres, 'Development of LHP for Intermediate Temperature Range', in *15th International Heat Pipe Conference*, 2010.
[45] J. Baumann and S. Rawal, 'Viability of Loop Heat Pipes for Space Solar Power Applications', in *35th AIAA Thermophysics Conference*, 2001.
[46] D. R. Lide, 'Handbook of chemistry and physics', *CRC Press*, 1992.
[47] Y. S. Touloukian, R. Powell, C. Ho, and P. Klemens, *Thermal Conductivity: Nonmetallic Solids, IFI*. Plenum, 1970.
[48] Y. S. Touloukian, R. W. Powell, C. Y. Ho, and P. G. Klemens, 'Thermophysical Properties of Matter-The TPRC Data Series. Volume 2. Thermal Conductivity-Nonmetallic Solids', Thermophysical and Electronic Properties Information Analysis Center Lafayette In, 1971.
[49] Y. S. Touloukian, 'Thermophysical Properties of High Temperature Solid Materials. Volume 3. Ferrous Alloys', Thermophysical and Electronic Properties Information Analysis Center Lafayette In, 1966.
[50] 'Prix des plastiques, www.emballagesmagazine.com/mediatheque/3/6/2/000014263.pdf', *www.industrie.com*. .
[51] 'Matières premières, investir.lesechos.fr/marches/matieres-premieres/', *Les Echos investir*. .

[52] T. Albertin, J.-F. Savard, and V. Sartre, 'Industrial manufacturing of loop heat pipe porous media', in *16th International Heat Pipe Conference*, Lyon, France, 2012.
[53] L. Bai, G. Lin, H. Zhang, and D. Wen, 'Mathematical modeling of steady-state operation of a loop heat pipe', *Appl. Therm. Eng.*, vol. 29, pp. 2643–2654, 2009.
[54] E. Bazzo and R. R. Riehl, 'Operation characteristics of a small-scale capillary pumped loop', *Appl. Therm. Eng.*, vol. 23, pp. 687–705, 2003.
[55] H. Nagano, F. Fukuyoshi, H. Ogawa, and H. Nagai, 'Development of an experimental small loop heat pipe with polytetrafluoroethylene wicks', *J. Thermophys. Heat Transf.*, vol. 25, no. 4, pp. 547–552, 2011.
[56] T. Kobayashi, T. Ogushi, S. Haga, E. Ozaki, and M. Fujii, 'Heat transfer performance of a flexible looped heat pipe using R134a as a working fluid: proposal for a method to predict the maximum heat transfer rate of FLHP', *Heat Transfer—Asian Res.*, vol. 32, no. 4, pp. 306–318, 2003.
[57] J. Xu, Y. Zou, D. Yang, and M. Fan, 'Development of biporous Ti 3 AlC 2 ceramic wicks for loop heat pipe', *Mater. Lett.*, vol. 91, pp. 121–124, 2013.
[58] L. F. Berti, P. H. D. Santos, E. Bazzo, R. Janssen, D. Hotza, and C. R. Rambo, 'Evaluation of permeability of ceramic wick structures for two phase heat transfer devices', *Appl. Therm. Eng.*, vol. 31, no. 6–7, pp. 1076–1081, 2011.
[59] E. A. Silk and D. Myre, 'Fractal loop heat pipe heat flux and operational performance testing', in *ASME 2009 Heat Transfer Summer Conference collocated with the InterPACK09 and 3rd Energy Sustainability Conferences*, 2009, pp. 221–229.
[60] E. A. Silk and D. Myre, 'Fractal loop heat pipe performance testing with a compressed carbon foam wick structure', *Appl. Therm. Eng.*, vol. 59, no. 1–2, pp. 290–297, 2013.
[61] B. Weisenseel, P. Greil, and T. Fey, 'Biomorphous Silicon Carbide as Novel Loop Heat Pipe Wicks', *Adv. Eng. Mater.*, vol. 19, no. 1, 2017.
[62] Y. F. Maidanik and V. G. Pastukhov, 'Loop heat pipes-recent developments, test results and applications', SAE Technical Paper, 1999.
[63] P. H. D. Santos, E. Bazzo, S. Becker, R. Kulenovic, and R. Mertz, 'Development of LHPs with ceramic wick', *Appl. Therm. Eng.*, vol. 30, no. 13, pp. 1784–1789, Sep. 2010.
[64] E. G. Reimbrecht, 'Manufacturing, geometric characterization and determination of hydraulic properties of porous wicks for using in capillary pumps', Ph. D. thesis, Federal University of Santa Catarina, 2004.
[65] E. C. Hammel, O.-R. Ighodaro, and O. I. Okoli, 'Processing and properties of advanced porous ceramics: An application based review', *Ceram. Int.*, vol. 40, no. 10, pp. 15351–15370, 2014.
[66] N. Putra, R. Saleh, W. N. Septiadi, A. Okta, and Z. Hamid, 'Thermal performance of biomaterial wick loop heat pipes with water-base Al 2 O 3 nanofluids', *Int. J. Therm. Sci.*, vol. 76, pp. 128–136, 2014.
[67] M. Groll, M. Schneider, V. Sartre, M. C. Zaghdoudi, and M. Lallemand, 'Thermal control of electronic equipment by heat pipes', *Rev. Générale Therm.*, vol. 37, no. 5, pp. 323–352, 1998.
[68] W. G. Anderson, P. Chow, and K. Yerkes, 'Loop Heat Pipes for Anti Icing of Gas Turbine Inlets', in *Proceedings of the IX International Heat Pipe Conference, New Mexico, USA*, 1995.
[69] Cat pumps, 'Chemical Compatibility Guide', 2011.
[70] Cole-Parmer, 'Chemical Compatibility Database', *www.coleparmer.com/chemical-resistance*. .
[71] Franklin-electric, 'Chemical Compatibility Database', *http://www.franklin-electric.com/media/documents/17-2-995516.pdf*. .
[72] FMC Technologies, 'Compatibility Manual', 1996.
[73] Techniques des fluides, 'Chemical Compatibility Database', *http://www.techniquesfluides.fr/download/Guide de compatibilite chimique.pdf*. .
[74] P. J. Brennan and E. J. Kroliczek, *Heat pipe design handbook*. NASA Goddard Space Flight Center, 1979.
[75] D. Reay, R. McGlen, and P. Kew, *Heat Pipes: Theory, Design and Applications*, 6th ed. Amsterdam: Butterworth-Heinemann, 2013.
[76] H. Loesch and P. Pawlowski, 'Heat pipe and phase changing material/PCM/sounding rocket experiment', in *8th Thermophysics Conference*, Palm SPrings, USA, 1973, p. 759.
[77] N. Gernert, 'Heat Pipe Reliability Documentation', *Thermacore Intern. Doc.*, 1999.

[78] D. D. Kenney and K. T. Feldman Jr, ‘Heat pipe life tests at temperatures up to 400 C’, in *13th Intersociety Energy Conversion Engineering Conference*, 1978, vol. 1, pp. 1056–1059.
[79] W. B. Kaufman and L. K. Tower, ‘Evaluation of Commercially Available Spacecraft-Type Heat Pipes’, *J. Spacecr. Rockets*, vol. 16, no. 2, pp. 98–103, 1979.
[80] A. S. Reyes, J. R. Brown, W. S. Chang, and R. Ponnappan, ‘Gas generation test data and life tests of low temperature heat pipes’, in *5th Joint Thermophysics and Heat Transfer Conference*, 1990.
[81] A. Basiulis, C. M. Eallonardo, and B. M. Kendall, ‘Heat-pipe system for space shuttle traveling wave tube amplifier’, in *8th Thermophysics Conference*, Palm SPrings, USA, 1973, pp. 431–444.
[82] W. G. Anderson, M. C. Ellis, J. R. Hartenstine, C. J. Peters, C. Tarau, and K. L. Walker, ‘Variable Conductance Heat Pipes for Variable Thermal Links’, in *42nd International Conference on Environmental Systems*, San Diego, USA, 2012.
[83] W. M. Rohsenow, J. P. Hartnett, Y. I. Cho, and others, *Handbook of heat transfer*, vol. 3. McGraw-Hill New York, 1998.
[84] V. M. Kiseev, ‘Heat and Mass Transfer and Phase Change in Fine Pore Capillary Structures’, Ph. D. thesis, Ural State University, Ekaterinburg, Russia (in Russian), 2001.
[85] A. D. Lobanov, A. A. Yatsenko, M. D. Parfentiev, and L. V. Barkova, ‘Life tests of aluminium axial groove heat pipes with acetone as a working fluid’, in *4th European Symposium on Space Environmental Control Systems*, Florence, Italy, 1991, vol. 1, pp. 583–586.
[86] Air liquide, ‘Chemical Compatibility Database’, *encyclopedia.airliquide.com*. .
[87] W. G. Anderson, J. H. Rosenfeld, D. Angirasa, and Y. Mi, ‘Evaluation of heat pipe working fluids in the temperature range 450 to 700 K’, in *AIP Conference*, 2004, vol. 699, pp. 20–27.
[88] W. T. Anderson and others, *Hydrogen evolution in nickel-water heat pipes*. American Institute of Aeronautics and Astronautics, 1973.
[89] L. R. Grzyll, ‘Investigation of heat pipe working fluids for thermal control of the sodium/sulfur battery’, in *26th Intersociety Energy Conversion Engineering Conference*, Boston, USA, 1991, vol. 3, pp. 390–394.
[90] W. G. Anderson, D. Sarraf, P. M. Dussinger, T. Stern, and J. Barth, ‘Development of a high temperature water heat pipe radiator’, in *3rd International Energy Conversion Engineering Conference*, San Francisco, USA, 2005, pp. 15–18.
[91] R. Ponnappan, J. E. Leland, and J. E. Beam, ‘Comparison of performance results for water and methanol rotating heat pipes’, *Am. Inst. Aeronaut. Astronaut.*, no. 96-0477, 1996.
[92] W. B. Bienert *et al.*, ‘Proof-of-feasibility of multiple evaporator loop heat pipes’, in *6th European Symposium on Space Environmental Control Systems*, 1997, vol. 400, p. 393.
[93] C. W. Extrand and Y. Kumagai, ‘An experimental study of contact angle hysteresis’, *J. Colloid Interface Sci.*, vol. 191, no. 2, pp. 378–383, 1997.
[94] A. Faghri and Y. Zhang, *Transport phenomena in multiphase systems*. Academic Press, 2006.
[95] J. Rafiee *et al.*, ‘Wetting transparency of graphene’, *Nat. Mater.*, vol. 11, no. 3, pp. 217–222, 2012.
[96] D. Y. Kwok and A. W. Neumann, ‘Contact angle measurement and contact angle interpretation’, *Adv Coll Int Sci*, vol. 81, pp. 167–249, 1999.
[97] H. Y. Erbil, G. Mchale, S. M. Rowan, and M. I. Newton, ‘Determination of the receding contact angle of sessile drops on polymer surfaces by evaporation’, *Langmuir*, pp. 7378–7385, 1999.
[98] Majeed, M. H., ‘Static Contact Angle and Large Water Droplet Thickness Measurements with the Change of Water Temperature’, p. pp.114-128, 2014.
[99] Espagon, L., Longeard, N., and Ménager, C, ‘Les morphologies de surface’. Université de Nice Sophia-Antipolis, 2015.
[100] M. L. Gonzalez-Martin, L. Labajos-Broncano, B. Jańczuk, and J. M. Bruque, ‘Wettability and surface free energy of zirconia ceramics and their constituents’, *J. Mater. Sci.*, vol. 34, no. 23, pp. 5923–5926, 1999.
[101] P. C. Carman, *Flow of gases through porous media*. Academic press, 1956.
[102] J. L. Poiseuille, *Recherches expérimentales sur le mouvement des liquides dans les tubes de très-petits diamètres*. Imprimerie Royale, 1844.
[103] H. Rumpf and A. R. Gupte, ‘The influence of porosity and grain size distribution on the permeability equation of porous flow’, *NASA STIRecon Tech. Rep. N*, vol. 75, p. 30484, 1975.

[104] J. P. Plessis and J. H. Masliyah, ‘Mathematical modelling of flow through consolidated isotropic porous media’, *Transp. Porous Media*, vol. 3, no. 2, pp. 145–161, 1988.
[105] D. Deng, D. Liang, Y. Tang, J. Peng, X. Han, and M. Pan, ‘Evaluation of capillary performance of sintered porous wicks for loop heat pipe’, *Exp. Therm. Fluid Sci.*, vol. 50, pp. 1–9, 2013.
[106] J. Li, Y. Zou, L. Cheng, R. Singh, and A. Akbarzadeh, ‘Effect of fabricating parameters on properties of sintered porous wicks for loop heat pipe’, *Powder Technol.*, vol. 204, no. 2–3, pp. 241–248, 2010.
[107] T. T. Hoang, T. A. O’Conne, J. Ku, C. D. Butler, and T. D. Swanson, ‘Miniature loop heat pipes for electronic cooling’, in *International Electronic Packaging Technical Conference and Exhibition*, Maui, Hawaii, USA, 2003.
[108] T. Zhao and Q. Liao, ‘On capillary-driven flow and phase-change heat transfer in a porous structure heated by a finned surface: measurements and modeling’, *Int. J. Heat Mass Transf.*, vol. 43, no. 7, pp. 1141–1155, avril 2000.
[109] A. Delil, V. Baturkin, Y. Friedrichson, Y. Khmelev, and S. Zhuk, ‘Experimental results of heat transfer phenomena in a miniature loop heat pipe with a flat evaporator’, presented at the 12th International Heat Pipe Conference, Moscow, Russia, 2002, vol. 19, p. 8.
[110] M. Khammar, D. Ewing, C. Y. Ching, and J. S. Chang, ‘Heat transfer from a surface into a confined gap over a saturated porous plate’, *Int. J. Heat Mass Transf.*, vol. 76, pp. 144–152, 2014.
[111] M. J. Schertzer, D. Ewing, and C. Y. Ching, ‘The effect of gap distance on the heat transfer between a heated finned surface and a saturated porous plate’, *Int. J. Heat Mass Transf.*, vol. 49, no. 21–22, pp. 4200–4208, 2006.
[112] J. Choi, B. Sung, C. Kim, and D.-A. Borca-Tasciuc, ‘Interface engineering to enhance thermal contact conductance of evaporators in miniature loop heat pipe systems’, *Appl. Therm. Eng.*, vol. 60, no. 1–2, pp. 371–378, 2013.
[113] V. Platel, O. Fudym, C. Butto, and P. Briend, ‘Coefficient de transfert, à l’interface de vaporisation, d’une boucle fluide diphasique à pompage thermocapillaire’, *Rev Gén Therm*, vol. 35, pp. 592–598, 1996.
[114] C. Figus, Y. Le Bray, S. Bories, and M. Prat, ‘Heat and mass transfer with phase change in a porous structure partially heated: continuum model and pore network simulations’, *Int. J. Heat Mass Transf.*, vol. 42, pp. 1446–1458, 1999.
[115] F.-C. Lin, B.-H. Liu, C.-C. Juan, and Y.-M. Chen, ‘Effect of pore size distribution in bidisperse wick on heat transfer in a loop heat pipe’, *Heat Mass Transf.*, vol. 47, no. 8, pp. 933–940, 2011.
[116] C. C. Yeh, B. H. Liu, and Y. M. Chen, ‘A study of loop heat pipe with biporous wicks’, *Heat Mass Transf.*, vol. 44, no. 12, pp. 1537–1547, 2008.
[117] C. C. Yeh, C. N. Chen, and Y. M. Chen, ‘Heat transfer analysis of a loop heat pipe with biporous wicks’, *Int. J. Heat Mass Transf.*, vol. 52, no. 19, pp. 4426–4434, 2009.
[118] H. Li, Z. Liu, B. Chen, W. Liu, C. Li, and J. Yang, ‘Development of biporous wicks for flat-plate loop heat pipe’, *Exp. Therm. Fluid Sci.*, vol. 37, pp. 91–97, 2012.
[119] S.-C. Wu, C.-J. Huang, S.-H. Chen, and Y.-M. Chen, ‘Manufacturing and testing of the double-layer wick structure in a loop heat pipe’, *Int. J. Heat Mass Transf.*, vol. 56, no. 1–2, pp. 709–714, 2013.
[120] L. Mottet and M. Prat, ‘Numerical simulation of heat and mass transfer in bidispersed capillary structures: Application to the evaporator of a loop heat pipe’, *Appl. Therm. Eng.*, vol. 102, pp. 770–784, 2016.
[121] N. S. Rasor and J. L. Desplat, ‘K-max: a material with exceptional heat transfer properties’, in *24th Intersociety Energy Conversion Engineering Conference*, Washington, USA, 1989, pp. 2847–2852.
[122] B. Yu and P. Cheng, ‘A fractal permeability model for bi-dispersed porous media’, *Int. J. Heat Mass Transf.*, vol. 45, no. 14, pp. 2983–2993, 2002.
[123] Z. Q. Chen, P. Cheng, and T. S. Zhao, ‘An experimental study of two phase flow and boiling heat transfer in bi-dispersed porous channels’, *Int. Commun. Heat Mass Transf.*, vol. 27, no. 3, pp. 293–302, 2000.
[124] V. G. Pastukhov, Y. F. Maidanik, and M. A. Chernyshova, ‘Development and investigation of miniature loop heat pipes’, SAE Technical Paper, 1999.

[125] S. Van Oost, B. Mullender, G. Bekaert, and J. C. Legros, 'Secondary wick operation principle and performance mapping in LHP and FLHP evaporators', in *AIP Conference*, New York, USA, 2002, vol. 608, p. 94.
[126] T. Ogushi, A. Yao, J. J. Xu, H. Masumoto, and M. Kawaji, 'Heat transport characteristics of flexible looped heat pipe under micro-gravity condition', *Heat Transf. Asian Res.*, vol. 32, no. 5, pp. 381–390, 2003.
[127] Y. G. Fershtater and Y. F. Maidanik, 'Analysis of the temperature field in the capillary structure of an "antigravity" heat pipe', *J. Eng. Phys. Thermophys.*, vol. 51, no. 2, pp. 897–900, 1986.
[128] J. Xu, X. Ji, W. Yang, and Z. Zhao, 'Modulated porous wick evaporator for loop heat pipes: Experiment', *Int. J. Heat Mass Transf.*, vol. 72, pp. 163–176, 2014.
[129] E. G. Alexander, 'Structure-property relationships in heat pipe wicking materials', Ph. D. Thesis, Departement of Chemical Engineering, North Carolina State University, 1972.
[130] R. Singh, A. Akbarzadeh, and M. Mochizuki, 'Effect of Wick Characteristics on the Thermal Performance of the Miniature Loop Heat Pipe', *J. Heat Transf.*, vol. 131, no. 8, p. 082601, 2009.
[131] C. Li and G. P. Peterson, 'The effective thermal conductivity of wire screen', *Int. J. Heat Mass Transf.*, vol. 49, no. 21–22, pp. 4095–4105, 2006.
[132] M. Hamdan, F. M. Gerner, and H. T. Henderson, 'Steady state model of a loop heat pipe (LHP) with coherent porous silicon (CPS) wick in the evaporator', presented at the 19th Annual IEEE Symposium , Semiconductor Thermal Measurement and Management, 2003, pp. 88–96.
[133] V. P. Carey, *Liquid-vapor phase-change phenomena*. Hemisphere, New York, 1992.
[134] S. Morooka, T. Kuroki, and T. Waki, 'Study on the Heat Pipe: 3rd Report, Heat Transfer Mechanism in the Evaporator of Heat Pipe with Screen Mesh Wick', *Bull. JSME*, vol. 24, no. 196, pp. 1811–1819, 1981.
[135] I. W. Eames, N. J. Marr, and H. Sabir, 'The evaporation coefficient of water: a review', *Int. J. Heat Mass Transf.*, vol. 40, no. 12, pp. 2963–2973, 1997.
[136] Y. Cao and A. Faghri, 'Analytical solutions of flow and heat transfer in a porous structure with partial heating and evaporation on the upper surface', *Int. J. Heat Mass Transf.*, vol. 37, no. 10, pp. 1525–1533, 1994.
[137] Y. Cao and A. Faghri, 'Conjugate analysis of a flat-plate type evaporator for capillary pumped loops with three-dimensional vapor flow in the groove', *Int. J. Heat Mass Transf.*, vol. 37, no. 3, pp. 401–409, 1994.
[138] A. S. Demidov and E. S. Yatsenko, 'Investigation of heat and mass transfer in the evaporation zone of a heat pipe operating by the inverted meniscus' principle', *Int. J. Heat Mass Transf.*, vol. 37, no. 14, pp. 2155–2163, 1994.
[139] L. Mottet, 'Simulation tridimensionnelle des échanges de masse et de chaleur dans les évaporateurs capillaires', Thèse de doctorat, Université de Toulouse, 2016.
[140] B. Siedel, V. Sartre, and F. Lefèvre, 'Literature review: Steady-state modelling of loop heat pipes', *Appl. Therm. Eng.*, vol. 75, pp. 709–723, 2015.
[141] B. Siedel, V. Sartre, and F. Lefevre, 'Steady-state analytical model of a loop heat pipe', in *17th International Heat Pipe Conference*, Kanpur, India, 2013.
[142] S. Becker, S. Vershinin, V. Sartre, E. Laurien, J. Bonjour, and Y. F. Maydanik, 'Steady state operation of a copper–water LHP with a flat-oval evaporator', *Appl. Therm. Eng.*, vol. 31, no. 5, pp. 686–695, 2011.
[143] K. Stephan, *Heat transfer in condensation and boiling*. Springer, 1992.
[144] J. Peyssou, 'Le frittage'. Ecole Nationale Supérieure de Céramique Industrielle de Sèvres, 1977.
[145] G. Cizeron, 'Le frittage sous son aspect physico-chimique', *L'industrie Céramique*, vol. 611, no. 10, pp. 713–729, 1968.
[146] D. Bernache-Assollant, 'Le frittage des céramiques et des métaux (1ère partie)-le frittage en phase solide', *Ind. Céramique Verrière*, no. 925, pp. 257–274, 1997.
[147] J. Déjou, 'Les céramiques', Société Française de Biomatériaux dentaires, 2009.
[148] K. A. Khor, L. G. Yu, O. Andersen, and G. Stephani, 'Effect of spark plasma sintering (SPS) on the microstructure and mechanical properties of randomly packed hollow sphere (RHS) cell wall', *Mater. Sci. Eng. A*, vol. 356, no. 1, pp. 130–135, 2003.
[149] Q. Li and Y. Xuan, 'Development of High Performance Sintered Wicks for CPLs', in *7th International Heat Pipe Symposium*, Jeju, Korea, 2003.

[150] L. Qiang, X. Yimin, and C. Xiaobo, ‘Development of high performance sintered wicks for miniature CPLs’, *Powder Metall. Technol.*, vol. 5, p. 002, 2005.
[151] S.-C. Wu, D. Wang, and Y.-M. Chen, ‘Investigating the effect of double-layer wick thickness ratio on heat transfer performance of loop heat pipe’, *Int. J. Therm. Sci.*, vol. 86, pp. 292–298, 2014.
[152] S. K. Samanta, P. R. DAS, A. K. Lohar, H. Roy, S. Kumar, and A. K. Chowdhury, ‘A novel approach of manufacturing Nickel Wicks for loop heat pipes using Metal Injection Moulding (MIM)’, *Sadhana*, vol. 38, no. 2, pp. 281–296, 2013.
[153] J. Xu, Y. Zou, M. Fan, and L. Cheng, ‘Effect of pore parameters on thermal conductivity of sintered LHP wicks’, *Int. J. Heat Mass Transf.*, vol. 55, no. 9–10, pp. 2702–2706, 2012.
[154] G. Hansen, E. Naess, and K. Kristjansson, ‘Sintered nickel powder wicks for flat vertical heat pipes’, *Energies*, vol. 8, no. 4, pp. 2337–2357, 2015.
[155] G. Xin, K. Cui, Y. Zou, and L. Cheng, ‘Reduction of effective thermal conductivity for sintered LHP wicks’, *Int. J. Heat Mass Transf.*, vol. 53, no. 13, pp. 2932–2934, 2010.
[156] U. G. Wegst, M. Schecter, A. E. Donius, and P. M. Hunger, ‘Biomaterials by freeze casting’, *Philos. Trans. R. Soc. Lond. Math. Phys. Eng. Sci.*, vol. 368, no. 1917, pp. 2099–2121, 2010.
[157] F. Bouville, ‘Self-assembly of anisotropic particles driven by ice growth: Mechanisms, applications and bioinspiration’, Thèse de doctorat, INSA de Lyon, 2013.
[158] D. Li and M. Li, ‘Porous Y 2 SiO 5 Ceramic with Low Thermal Conductivity’, *J. Mater. Sci. Technol.*, vol. 28, no. 9, pp. 799–802, 2012.
[159] M. Fukushima, M. Nakata, Y. Zhou, T. Ohji, and Y. Yoshizawa, ‘Fabrication and properties of ultra highly porous silicon carbide by the gelation–freezing method’, *J. Eur. Ceram. Soc.*, vol. 30, no. 14, pp. 2889–2896, 2010.
[160] S. R. Mukai, H. Nishihara, and H. Tamon, ‘Formation of monolithic silica gel microhoneycombs (SMHs) using pseudosteady state growth of microstructural ice crystals’, *Chem Commun*, no. 7, pp. 874–875, 2004.
[161] S. Deville *et al.*, ‘Ice shaping properties, similar to that of antifreeze proteins, of a zirconium acetate complex’, *PloS One*, vol. 6, no. 10, pp. e26474–e26474, 2011.
[162] E. Saiz, L. Gremillard, G. Menendez, P. Miranda, K. Gryn, and A. P. Tomsia, ‘Preparation of porous hydroxyapatite scaffolds’, *Mater. Sci. Eng. C*, vol. 27, no. 3, pp. 546–550, 2007.
[163] A. R. Studart, U. T. Gonzenbach, E. Tervoort, and L. J. Gauckler, ‘Processing routes to macroporous ceramics: a review’, *J. Am. Ceram. Soc.*, vol. 89, no. 6, pp. 1771–1789, 2006.
[164] Y. S. Touloukian, R. W. Powell, C. Y. Ho, and M. C. Nicolaou, ‘Thermophysical Properties of Matter-The TPRC Data Series. Volume 10. Thermal Diffusivity’, DTIC Document, 1974.
[165] D. C. Montgomery, *Design and analysis of experiments*. John Wiley & Sons, 2008.
[166] D. R. Adkins, T. A. Moss, C. E. Andraka, N. H. Andreas, and H. M. Cole, ‘An examination of metal felt wicks for heat-pipe applications’, Sandia National Labs., Albuquerque, NM (United States), 1994.
[167] R. R. Williams and D. K. Harris, ‘Cross-plane and in-plane porous properties measurements of thin metal felts: applications in heat pipes’, *Exp. Therm. Fluid Sci.*, vol. 27, no. 3, pp. 227–235, 2003.
[168] F. A. Dullien, *Porous media: fluid transport and pore structure*. New-York: Academic press, 2012.
[169] R. Singh, A. Akbarzadeh, and M. Mochizuki, ‘Experimental determination of wick properties for loop heat pipe applications’, *J. Porous Media*, vol. 12, no. 8, pp. 759–776, 2009.
[170] W. J. Looyestijn, R. M. Smits, I. Abu-Shiekah, B. Kuvshinov, J. P. Hofman, and A. Schwing, ‘Permeability determination through NMR detection of acoustically induced fluid oscillation’, *Magn. Reson. Imaging*, vol. 24, no. 9, pp. 1187–1201, 2006.
[171] B. Holley and A. Faghri, ‘Permeability and effective pore radius measurements for heat pipe and fuel cell applications’, *Appl. Therm. Eng.*, vol. 26, no. 4, pp. 448–462, 2006.
[172] C. A. L. y Leon, ‘New perspectives in mercury porosimetry’, *Adv. Colloid Interface Sci.*, vol. 76, pp. 341–372, 1998.
[173] D. R. Adkins and T. Moss, ‘Measuring flow properties of wicks for heat pipe solar receivers’, Sandia National Labs., Albuquerque, NM (USA), 1990.

[174] E. Guyon, L. Oger, and T. J. Plona, ‘Transport properties in sintered porous media composed of two particle sizes’, *J. Phys. Appl. Phys.*, vol. 20, no. 12, p. 1637, 1987.
[175] P. Griffith and J. D. Wallis, ‘The role of surface conditions in nucleate boiling’, Cambridge Massachusetts Institute of Technology, Division of Industrial Cooperation, 1958.
[176] J. Lu and X. F. Peng, ‘Dynamical evolution of heterogeneous nucleation on surfaces with ideal cavities’, *Heat Mass Transf.*, vol. 43, no. 7, pp. 659–667, 2007.
[177] G. Job and F. Herrmann, ‘Chemical potential—a quantity in search of recognition’, *Eur. J. Phys.*, vol. 27, no. 2, p. 353, 2006.
[178] J. Ku and G. Birur, ‘Capillary Limit in a Loop Heat Pipe with Dual Evaporators’, SAE Technical Paper, 2002.
[179] J. Shafer, R. Agrawal, and M. Mehta, ‘SPRINT: A scalable parallel classi er for data mining’, in *22th Int. Conf. Very Large Data Bases*, Bombay, India, 1996, pp. 544–555.
[180] I. H. Tavman, ‘Effective thermal conductivity of granular porous materials’, *Int. Commun. Heat Mass Transf.*, vol. 23, no. 2, pp. 169–176, 1996.
[181] D. R. Chaudhary and R. C. Bhandari, ‘Heat transfer through a three-phase porous medium’, *J. Phys. Appl. Phys.*, vol. 1, no. 6, p. 815, 1968.
[182] Z. Živcová, E. Gregorová, W. Pabst, D. S. Smith, A. Michot, and C. Poulier, ‘Thermal conductivity of porous alumina ceramics prepared using starch as a pore-forming agent’, *J. Eur. Ceram. Soc.*, vol. 29, no. 3, pp. 347–353, 2009.
[183] L. Rayleigh, ‘On the influence of obstacles arranged in rectangular order upon the properties of a medium’, *Phil Mag*, vol. 34, no. 481–502, p. 205, 1892.
[184] J. K. Carson, S. J. Lovatt, D. J. Tanner, and A. C. Cleland, ‘Thermal conductivity bounds for isotropic, porous materials’, *Int. J. Heat Mass Transf.*, vol. 48, no. 11, pp. 2150–2158, 2005.
[185] Y. Asaad, *A study of the thermal conductivity of fluid-bearing porous rocks*. University of California, Berkeley, 1955.
[186] J. Maxwell, *A Treatise on Electricity and Magnetism*, 3rd ed., vol. 1. New York, 1891.
[187] H. Russell, ‘Principles of heat flow in porous insulators’, *J. Am. Ceram. Soc.*, vol. 18, no. 1–12, pp. 1–5, 1935.
[188] A. Eucken, ‘Forsh. Gebiete Ingenieur’, *B3*, vol. 353, pp. 6–21, 1932.
[189] P. Zehner and S. EU, ‘Thermal conductivity of packings at moderate temperatures’, *Chem. Ing. Tech.*, vol. 42, no. 14, p. 933, 1970.
[190] S. Mo, P. Hu, J. Cao, Z. Chen, H. Fan, and F. Yu, ‘Effective Thermal Conductivity of Moist Porous Sintered Nickel Material’, *Int. J. Thermophys.*, vol. 27, no. 1, pp. 304–313, 2006.
[191] J. Koh and A. Fortini, ‘Prediction of thermal conductivity and electrical resistivity of porous metallic materials’, *Int. J. Heat Mass Transf.*, vol. 16, no. 11, pp. 2013–2022, 1973.
[192] M. Aivazov and I. Domashnev, ‘Influence of porosity on the conductivity of hot-pressed titanium-nitride specimens’, *Powder Metall. Met. Ceram.*, vol. 7, no. 9, pp. 708–710, 1968.

Appendix A Effective thermal conductivity correlations

Authors	Correlation	Validity
Alexander [129]	$\lambda_{eff} = \lambda_l \left(\frac{\lambda_{mat}}{\lambda_l}\right)^{(1-\varepsilon)^{0,59}}$	Layer of sintered wick screens
Parallel [180]	$\lambda_{eff} = \varepsilon\lambda_l + (1-\varepsilon)\lambda_{mat}$	All geometries
Series [180]	$\lambda_{eff} = \frac{\lambda_l \lambda_{mat}}{\varepsilon\lambda_l + (1-\varepsilon)\lambda_{mat}}$	All geometries
Chaudhary and Bhandari [181]	$\lambda_{eff} = (\varepsilon\lambda_l + (1-\varepsilon)\lambda_{mat})^n \left(\frac{\lambda_l \lambda_{mat}}{\varepsilon\lambda_{mat} + (1-\varepsilon)\lambda_l}\right)^{n-1}$	0.42 < n < 0.51
Zivcova *et al.* [182]	$\lambda_{eff} = \lambda_{mat} \exp\left(-\frac{1.5\varepsilon}{1-\varepsilon}\right)$	microstructure
Rayleigh [183]	$\lambda_{eff} = \lambda_l \frac{[\lambda_l + \lambda_{mat} - (1-\varepsilon)(\lambda_l - \lambda_{mat})]}{\lambda_l + \lambda_{mat} + (1-\varepsilon)(\lambda_l - \lambda_{mat})}$	For isotropic porous material, not really for a layer of screen mesh, problem of prediction of the contact
Carson *et al.* [184]	$\lambda_{eff} = \frac{1}{4}\left((3\epsilon-1)\lambda_l + [3(1-\epsilon)-1]\lambda_{mat} + \sqrt{((3\epsilon-1)\lambda_l + [3(1-\epsilon)-1]\lambda_{mat})^2 + 8\lambda_l\lambda_{mat}}\right)$	All geometries
Asaad [185]	$\lambda_{eff} = \lambda_{mat} \left(\frac{\lambda_l}{\lambda_{mat}}\right)^{c\varepsilon}$	C=1 for unconsolidated solids
Krupiczka [180]	$\lambda_{eff} = \lambda_l \left(\frac{\lambda_{mat}}{\lambda_l}\right)^{[0.28-0.757log\varepsilon-0.057log\left(\frac{\lambda_{mat}}{\lambda_l}\right)]}$	
Maxwell [186]	$\lambda_{eff} = \frac{\lambda_l[2\lambda_l+\lambda_{mat}-2\varepsilon(\lambda_l-\lambda_{mat})]}{2\lambda_l+\lambda_{mat}+\varepsilon(\lambda_l-\lambda_{mat})}$	
Russell [187]	$\lambda_{eff} = \lambda_{mat}\left[\frac{\varepsilon^{2/3}+\left(\frac{\lambda_{mat}}{\lambda_l}\right)(1-\varepsilon^{2/3})}{\varepsilon^{2/3}-\varepsilon+\left(\frac{\lambda_{mat}}{\lambda_l}\right)(1-\varepsilon^{2/3}+\varepsilon)}\right]$	
Eucken [188]	$\lambda_{eff} = \lambda_{mat}\left[\frac{1+2\varepsilon\left(1-\frac{\lambda_{mat}}{\lambda_l}\right)/\left(2\frac{\lambda_{mat}}{\lambda_l}+1\right)}{1-\varepsilon\left(1-\frac{\lambda_{mat}}{\lambda_l}\right)/\left(2\frac{\lambda_{mat}}{\lambda_l}+1\right)}\right]$	Development of Maxwell's model

Zehner and Schlunder [189]	$\lambda_{eff} = \lambda_l \left\{ 1 - (1-\varepsilon)^2 + \frac{2(1-\varepsilon)^{1/2}}{1-\frac{\lambda_l}{\lambda_{mat}}B} \left[\frac{\left(1-\frac{\lambda_l}{\lambda_{mat}}\right)B}{\left(1-\frac{\lambda_l}{\lambda_{mat}}B\right)^2} ln\left(\frac{1}{\frac{\lambda_l}{\lambda_{mat}}B}\right) - \frac{B+1}{2} - \frac{B-1}{1-\frac{\lambda_l}{\lambda_{mat}}B} \right] \right\}$	B=1.25((1-ε)/ε)$^{10/9}$
Mo *et al.* [190]	$\lambda_{eff} = 5.759 + 5.565\lambda_l - 3.094\lambda_l^2$	Experimentally determined for nickel wicks with a certain porosity
Koh and Fortini [191] Aivazov and Domashnev [192]	$\lambda_{eff} = \frac{1-\varepsilon}{1+11\varepsilon}\lambda_{mat}$	Fluid conductivity neglected
Peterson [31]	$\lambda_{eff} = \frac{\lambda_l[2\lambda_l+\lambda_{mat}-2\varepsilon(\lambda_l-\lambda_{mat})]}{2\lambda_l+\lambda_{mat}+\varepsilon(\lambda_l-\lambda_{mat})}$	Non truncated packed spheres
Chi [82]	$\lambda_{eff} = \frac{\lambda_l[2\lambda_l+\lambda_{mat}-2\varepsilon(\lambda_l-\lambda_{mat})]}{(2\lambda_l+\lambda_{mat})+(1-\varepsilon)(\lambda_l-\lambda_{mat})}$	packed spheres

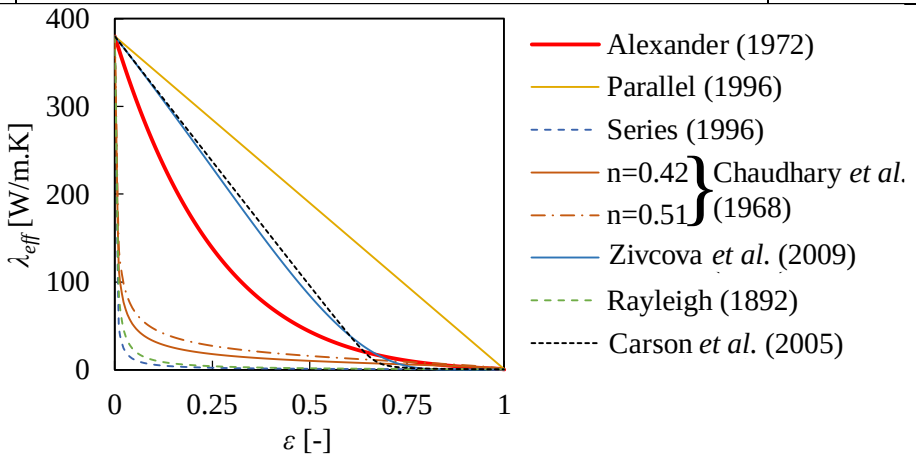

Figure A-1: Effective thermal conductivities calculated with λ_l = 0.6 W/m.K and λ_{mat} = 380 W/m.K

Appendix B Detailed expression of the coefficients defined in the Siedel analytical study

The equations detailed in the Chapter II depend on k_n coefficients (Table B-1), resulting of the analytical description of the heat transfer inside the wick and the evaporator body. The present analytical model considers a 1-D thermal resistance in the top layer of the wick. It means that the upper boundary condition of the bottom layer becomes a fixed temperature equal to T_{cont} instead of T_r (Figure B-1). The bottom boundary conditions are similar to the previous model: the wick temperature close to the evaporator wall is fixed to T_{we} at the left of the domain and the one in contact with the vapour groove is fixed to the vapour temperature T_v at the right of the domain. Between a_0 and a_1, the temperature linearly decreases from T_{we} to T_v.

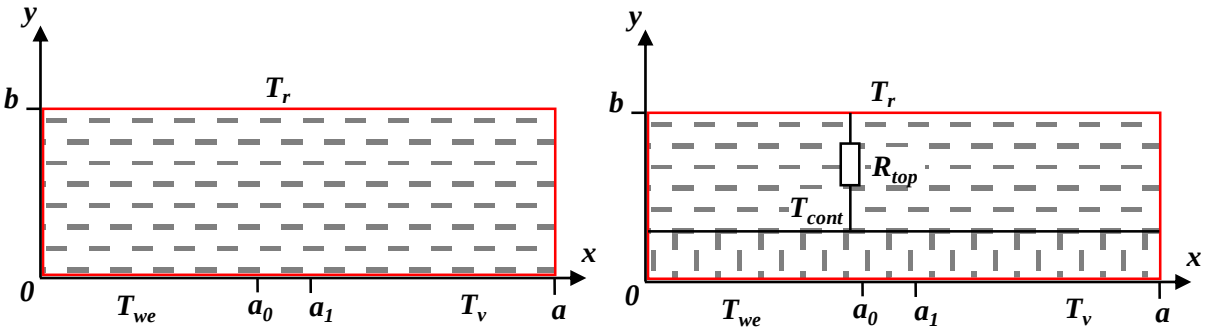

Figure B-1: Schematic of the 2D analytical model domain and boundary conditions

The values of a_0 and a_1 depend on the heat transfer coefficient of evaporation h_{ev} and on the effective thermal conductivity λ_{eff} :

$$h_{ev} = \frac{\lambda_{eff}}{a_1 - a_0} \tag{B-1}$$

Where the heat transfer coefficient is determined using the kinetic gas theory (Carey [133]):

$$h_{ev} = \frac{2a_{ev}}{2 - a_{ev}} \frac{\rho_v h_{lv}^2}{T_{sat}} \left(\frac{2\pi \bar{R} T_{sat}}{\bar{M}} \right)^{-0.5} \left(1 - \frac{P_{sat}}{2\rho_v h_{lv}} \right)$$

These two equations enable to determine a_0 and a_1. The other geometrical parameters enabling the determination of the k_n coefficients are presented in Figure B-2.

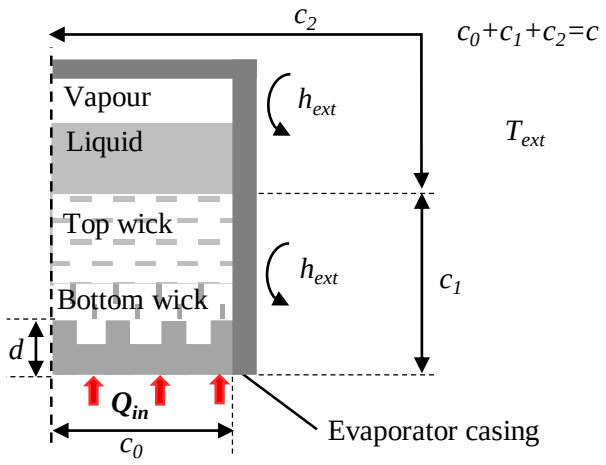

Figure B-2: Geometrical parameters enabling the resolution of the analytical model

Finally:

$$B = \frac{b}{a} \qquad D = \frac{d}{c}$$

The k_n coefficients are presented in Table B-1.

Table B-1: k_n coefficients (Siedel [4])

$k_1 = S_w \frac{a_0+a_1}{2a}\left(-\frac{\lambda_{eff}}{b} + \dot{m}C_{p,l}\frac{6}{\pi d_w^2}\right)$	(B-2)
$k_2 = S_w \left[\sum_{m=1}^{\infty}\left(2\frac{\lambda_{eff}}{a_1-a_0}\frac{1}{m^2\pi^2} sin\left(m\pi\frac{a_0+a_1}{2a}\right)\left(cos\left(\frac{m\pi a_0}{a}\right) - cos\left(\frac{m\pi a_1}{a}\right)\right)((1 - e^{2m\pi B})^{-1} - (1 - e^{-2m\pi B})^{-1}) + \frac{a_0+a_1}{2a}\left(\frac{\lambda_{eff}}{b}\left(1-\frac{a_0+a_1}{2a}\right) - \dot{m}C_{p,l}\frac{6}{\pi d_w^2}\right)\right)\right]$	(B-3)
$k_3 = -S_w \left[\sum_{m=1}^{\infty}\left(2\frac{\lambda_{eff}}{a_1-a_0}\frac{1}{m^2\pi^2} sin\left(m\pi\frac{a_0+a_1}{2a}\right)\left(cos\left(\frac{m\pi a_0}{a}\right) - cos\left(\frac{m\pi a_1}{a}\right)\right)((1 - e^{2m\pi B})^{-1} - (1 - e^{-2m\pi B})^{-1}) - \frac{\lambda_{eff}}{b}\left(\frac{a_0+a_1}{2a}\right)^2\right)\right]$	(B-4)
$k_4 = S_w\left(1-\frac{a_0+a_1}{2a}\right)\left(\frac{\lambda_{eff}}{b} - \dot{m}C_{p,l}\frac{6}{\pi d_w^2}\right)$	(B-5)
$k_5 = S_w \left[\sum_{m=1}^{\infty}\left(2\frac{\lambda_{eff}}{a_1-a_0}\frac{1}{m^2\pi^2} sin\left(m\pi\frac{a_0+a_1}{2a}\right)\left(cos\left(\frac{m\pi a_0}{a}\right) - cos\left(\frac{m\pi a_1}{a}\right)\right)((1 - e^{2m\pi B})^{-1} - (1 - e^{-2m\pi B})^{-1}) - \left(1-\frac{a_0+a_1}{2a}\right)\left(\frac{\lambda_{eff}}{b}\left(1-\frac{a_0+a_1}{2a}\right) - \dot{m}C_{p,l}\frac{6}{\pi d_w^2}\right)\right)\right]$	(B-6)
$k_6 = -S_w \left[\sum_{m=1}^{\infty}\left(2\frac{\lambda_{eff}}{a_1-a_0}\frac{1}{m^2\pi^2} sin\left(m\pi\frac{a_0+a_1}{2a}\right)\left(cos\left(\frac{m\pi a_0}{a}\right) - cos\left(\frac{m\pi a_1}{a}\right)\right)((1 - e^{2m\pi B})^{-1} - (1 - e^{-2m\pi B})^{-1}) + \frac{\lambda_{eff}}{b}\frac{a_0+a_1}{2a}\left(1-\frac{a_0+a_1}{2a}\right)\right)\right]$	(B-7)

$$k_7 = h_{ext}\pi\frac{c_1^2}{2}\left(\frac{-\frac{c_0+c_1}{2c}+1}{Bi_b+1}\right) - \sum_{m=1}^{\infty}\left(2\lambda_b\frac{c}{c_1-c_0}\frac{1}{m^2\pi^2}\left(cos\left(\frac{m\pi c_0}{c}\right) - cos\left(\frac{m\pi c_1}{c}\right)\right)\left[\left(c_0\pi sin\left(\frac{m\pi c_1}{c}\right)(e^{m\pi D}-1) + \frac{\pi h_{ext}}{\lambda_b}\left(-\frac{c^2}{m^2\pi^2}+\frac{c^2}{m^2\pi^2}cos\left(\frac{m\pi c_1}{c}\right) + \frac{c_1 c}{m\pi}sin\left(\frac{m\pi c_1}{c}\right)\right)\right)\left(e^{m\pi D}+e^{-m\pi D}\frac{m\pi D+Bi_b}{m\pi D-Bi_b}\right)^{-1} + \left(-c_0\pi sin\left(\frac{m\pi c_1}{c}\right)(e^{-m\pi D}-1) + \frac{\pi h_{ext}}{\lambda_b}\left(-\frac{c^2}{m^2\pi^2}+\frac{c^2}{m^2\pi^2}cos\left(\frac{m\pi c_1}{c}\right)+\frac{c_1 c}{m\pi}sin\left(\frac{m\pi c_1}{c}\right)\right)\right)\left(e^{-m\pi D}+e^{+m\pi D}\frac{m\pi D-Bi_b}{m\pi D+Bi_b}\right)^{-1}\right]\right)$$	(B-8)
$$k_8 = h_{ext}\pi\frac{c_1^2}{2}\left(\frac{c_0+c_1}{2c}\frac{1}{Bi_b+1}\right) + \sum_{m=1}^{\infty}\left(2\lambda_b\frac{c}{c_1-c_0}\frac{1}{m^2\pi^2}\left(cos\left(\frac{m\pi c_0}{c}\right) - cos\left(\frac{m\pi c_1}{c}\right)\right)\left[\left(c_0\pi sin\left(\frac{m\pi c_1}{c}\right)(e^{m\pi D}-1) + \frac{\pi h_{ext}}{\lambda_b}\left(-\frac{c^2}{m^2\pi^2}+\frac{c^2}{m^2\pi^2}cos\left(\frac{m\pi c_1}{c}\right) + \frac{c_1 c}{m\pi}sin\left(\frac{m\pi c_1}{c}\right)\right)\right)\left(e^{m\pi D}+e^{-m\pi D}\frac{m\pi D+Bi_b}{m\pi D-Bi_b}\right)^{-1} + \left(c_0\pi sin\left(\frac{m\pi c_1}{c}\right)(e^{-m\pi D}-1) + \frac{\pi h_{ext}}{\lambda_b}\left(-\frac{c^2}{m^2\pi^2}+\frac{c^2}{m^2\pi^2}cos\left(\frac{m\pi c_1}{c}\right)+\frac{c_1 c}{m\pi}sin\left(\frac{m\pi c_1}{c}\right)\right)\right)\left(e^{-m\pi D}+e^{+m\pi D}\frac{m\pi D-Bi_b}{m\pi D+Bi_b}\right)^{-1}\right]\right)$$	(B-9)
$$k_9 = h_{ext}\pi\frac{c_1^2}{2}\left(\frac{\Phi_0 d}{\lambda_b}\frac{c_0\Phi_{in}}{c\Phi_0} - \frac{1}{Bi_b+1}T_{ext}\right) + \sum_{m=1}^{\infty}\left(2\Phi_{in}\frac{1}{m^2\pi^2}sin\left(\frac{m\pi c_0}{c}\right)\left[\left(-c_0\pi sin\left(\frac{m\pi c_1}{c}\right)(e^{m\pi D}-1) - \frac{\pi h_{ext}}{\lambda_b}\left(-\frac{c^2}{m^2\pi^2}+\frac{c^2}{m^2\pi^2}cos\left(\frac{m\pi c_1}{c}\right)+\frac{c_1 c}{m\pi}sin\left(\frac{m\pi c_1}{c}\right)\right)\right)((1+e^{2m\pi D})^{-1}) + \left(-c_0\pi sin\left(\frac{m\pi c_1}{c}\right)(e^{-m\pi D}-1) + \frac{\pi h_{ext}}{\lambda_b}\left(-\frac{c^2}{m^2\pi^2}+\frac{c^2}{m^2\pi^2}cos\left(\frac{m\pi c_1}{c}\right)+\frac{c_1 c}{m\pi}sin\left(\frac{m\pi c_1}{c}\right)\right)\right)(1+e^{-2m\pi D})^{-1}\right]\right)$$	(B-10)
$$k_{10} = h_{ext}\pi\frac{c_1^2}{2}\left(\frac{-\frac{c_0+c_1}{2c}+1}{Bi_b+1}\right) - \sum_{m=1}^{\infty}\left(2\lambda_b\frac{c}{c_1-c_0}\frac{1}{m^2\pi^2}\left(cos\left(\frac{m\pi c_0}{c}\right) - cos\left(\frac{m\pi c_1}{c}\right)\right)\frac{\pi h_{ext}}{\lambda_b}\left(-\frac{c^2}{m^2\pi^2}+\frac{c^2}{m^2\pi^2}cos\left(\frac{m\pi c_1}{c}\right)+\frac{c_1 c}{m\pi}sin\left(\frac{m\pi c_1}{c}\right)\right)\left[\left(e^{m\pi D}+e^{-m\pi D}\frac{m\pi D+Bi_b}{m\pi D-Bi_b}\right)^{-1} + \left(e^{-m\pi D}+e^{+m\pi D}\frac{m\pi D-Bi_b}{m\pi D+Bi_b}\right)^{-1}\right]\right)$$	(B-11)
$$k_{11} = h_{ext}\pi\frac{c_1^2}{2}\left(\frac{c_0+c_1}{2c}\frac{1}{Bi_b+1}\right) + \sum_{m=1}^{\infty}\left(2\lambda_b\frac{c}{c_1-c_0}\frac{1}{m^2\pi^2}\left(cos\left(\frac{m\pi c_0}{c}\right) - cos\left(\frac{m\pi c_1}{c}\right)\right)\frac{\pi h_{ext}}{\lambda_b}\left(-\frac{c^2}{m^2\pi^2}+\frac{c^2}{m^2\pi^2}cos\left(\frac{m\pi c_1}{c}\right)+\frac{c_1 c}{m\pi}sin\left(\frac{m\pi c_1}{c}\right)\right)\left[\left(e^{m\pi D}+e^{-m\pi D}\frac{m\pi D+Bi_b}{m\pi D-Bi_b}\right)^{-1} + \left(e^{-m\pi D}+e^{+m\pi D}\frac{m\pi D-Bi_b}{m\pi D+Bi_b}\right)^{-1}\right]\right)$$	(B-12)

$k_{12} = h_{ext}\pi\frac{c_1^2}{2}\left(\frac{\Phi_0 d}{\lambda_b}\frac{c_0\Phi_{in}}{c\Phi_0} - \frac{1}{Bi_b+1}T_{ext}\right) - \sum_{m=1}^{\infty}\left(2\Phi_{in}\frac{1}{m^2\pi^2}sin\left(\frac{m\pi c_0}{c}\right)\frac{\pi h_{ext}}{\lambda_b}\left(-\frac{c^2}{m^2\pi^2}+\frac{c^2}{m^2\pi^2}cos\left(\frac{m\pi c_1}{c}\right)+\frac{c_1 c}{m\pi}sin\left(\frac{m\pi c_1}{c}\right)\right)[(1+e^{2m\pi D})^{-1}-(1+e^{-2m\pi D})^{-1}]\right)$	(B-13)
$k_{13} = exp\left(\frac{-\pi(L_c-L_{2\varphi})}{\dot{m}_l C_{p,l}\left(\frac{1}{(D_{c,i}h_l)}+\frac{1}{(h_{sink}D_{c,o})}+\frac{\ln\left(\frac{D_{co}}{D_c}\right)}{2\lambda_L}\right)}\right).exp\left(\frac{-\pi d_{L,i}L_L}{\dot{m}_l C_{p,l}\left(1/h_l+D_{L,i}/(h_{ext}D_{L,o})+\frac{\ln\left(\frac{D_{co}}{D_c}\right)}{2\lambda_L}\right)}\right)$	(B-14)
$k_{14} = exp\left(\frac{-\pi d_{L,i}L_L}{\dot{m}_l C_{p,l}\left(1/h_l+d_{L,i}/(h_{ext}d_{L,o})+\frac{\ln\left(\frac{d_{c,o}}{d_c}\right)}{2\lambda_L}\right)}\right).\left[1-exp\left(\frac{-\pi(L_c-L_{2\varphi})}{\dot{m}_l C_{p,l}\left(\frac{1}{(D_{c,i}h_l)}+\frac{1}{(h_{sink}D_{c,o})}+\frac{\ln\left(\frac{d_{c,o}}{d_c}\right)}{2\lambda_L}\right)}\right)\right].T_{sink} + \left[1-exp\left(\frac{-\pi d_{L,i}L_L}{\dot{m}_l C_{p,l}\left(\frac{1}{h_l}+\frac{d_{L,i}}{(h_{ext}d_{L,o})}+\frac{\ln\left(\frac{d_{c,o}}{d_c}\right)}{2\lambda_L}\right)}\right)\right]T_{ext}$	(B-15)

Appendix C Characterisation by mercury intrusion

This appendix presents some results obtained by mercury intrusion and compares these results with the ones obtained with the test bench described in the Chapter IV. The mercury intrusion requires the use of a small sample (less than 1 cm^3). It means that the sample has to be divided in small pieces and thus, it is destroyed. One of the small pieces is put in a reservoir. The mercury is introduced in the reservoir by increasing step by step the pressure. There are 50 steps from 3.5 kPa to 200 MPa. At the beginning, the pores are empty since a vacuum pump has removed the air. However, the pressure is not low enough to evaporate the liquid mercury since, at 20 °C, its saturation pressure is very low (0.0016 mbar). The mercury does not penetrate the porous medium as it is a non-wetting fluid. At each pressure step, only the largest pores which was still empty are filled with mercury. The last step enables to fill pore having a diameter of 6.3 nm. The cumulative mercury intrusion is recorded for each step in the case of the sample Cu-sin-11-a (Figure C-1 a). The derivative of this curve results in the curve of Figure C-1 (b), showing a pore distribution centred on 4.3 µm. A statistical investigation of these curves enables to obtain the porosity, the permeability and the tortuosity.

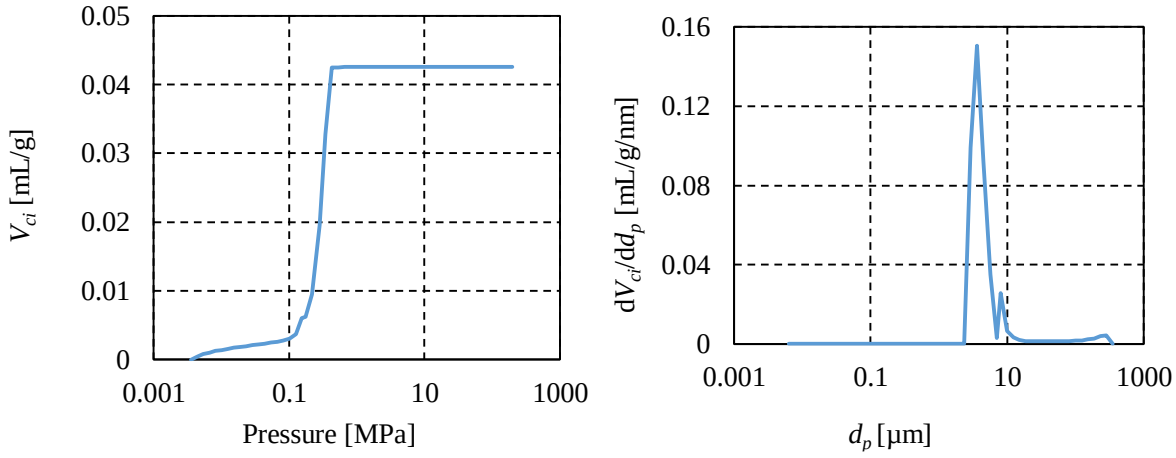

a) Cumulative intrusion b) Derivative of the cumulative intrusion

Figure C-1: Example of curves enabling the determination of the porous medium characteristics

Table C-1 details the porosity and the permeability of four samples. It presents the values obtained with the mercury intrusion method and with the test benches used in this thesis. Both the porosity and the permeability largely differ between the two methods. The differences can be explained as follows. The sample volumes vary from 4.1 cm^3 to 7.5 cm^3 whereas only 1 cm^3 is studied with the mercury intrusion. If the sample characteristics are not heterogeneous, the measures are not representative of the whole volume. Moreover, in the permeability measurement method proposed in the Chapter IV, the fluid flows in one direction whereas with the mercury intrusion method, the fluid randomly circulates inside the porous medium. That is why, this method has not been used in the thesis.

Table C-1: Comparison between the porosity and permeability obtained with mercury intrusion and with the test benches used in this thesis

Sample	ε [%]		K [10^{-14} m²]	
	Mercury intrusion	Test bench	Mercury intrusion	Test bench
Ni-sin-x	30.7	33.5	8.95	50
Cu-sin-10-a	19.6	15.0	0.038	-
Cu-sin-11-a	18.2	34.3	0.23	8.0
Cu-sin-2-a	14.5	22.9	8.5	0.18

Appendix D Characteristics of the capillary structures

Table D-1: Characteristics of the manufactured porous samples

Nomenclature	Material	r_s [µm]	d_w [mm]	e_w [mm]	m_w [g]	ε [%]	r_p [µm]	$r_{p,eff}$ [µm]	K [10^{-14} m²]
Cu-sin-1-a	Copper	28 µm	40.0	2.5	11.19	43.6	6.3 to 17.5		-
Cu-sin-1-b	Copper	28 µm	39.4	3.2	14.95	39.3	2.8 to 14	11.3	11.6
Cu-sin-1-c	Copper	28 µm	40.0	4.45	20.37	42.3	4 to 13.3	9.4	12.1
Cu-sin-2-a	Copper	28 µm	39.9	3.25	19.76	22.9	1.7 to 12.3	<5	0.18
Cu-sin-2-b	Copper	28 µm	40.0	2.95	17.15	26.7		23	2.57
Cu-sin-2-c	Copper	28 µm	40.0	2.8	16.04	27.8		11.5	1.37
Cu-sin-3-a	Copper	28 µm	39.5	5.2	23.88	40.6	4.8 to 16	18.2	10
Cu-sin-4-a	Copper	28 µm	39.8	4.65	28.26	22.6	3.3 to 12.9	<5	0.6
Cu-sin-5-a	Copper	28 µm	39.4	2	9.69	37	2.6 to 10.5	10.2	10.5
Cu-sin-6-a	Copper	28 µm	39.7	2.05	11.52	28.1	3.6 to 15.4	9.2	-
Cu-sin-6-b	Copper	28 µm	40.1	1.65	9.31	29.2	2.8 to 9.8		-
Cu-sin-6-c	Copper	28 µm	39.5	2.45	13.52	28.6		9.2	0.52
Cu-sin-7-a	Copper	28 µm	39.4	4.45	19.7	42.5	3.6 to 13.6		-
Cu-sin-7-b	Copper	28 µm	38.9	5.6	26.45	37	3.7 to 14.7	52.1	22
Cu-sin-7-c	Copper	28 µm	39.8	6	27.42	41.8		11.5	16.9
Cu-sin-7-d	Copper	28 µm	40.1	4.2	20.6	38.5			250
Cu-sin-8-a	Copper	28 µm	39.9	5.45	33.33	22.5	3.3 to 14.5	11.3	0.56
Cu-sin-9-a	Copper	4 µm	22.0			37	2 to 10		38
Cu-sin-10-a	Copper	28 µm	40.2	5.2	35.42	15	3 to 7		-
Cu-sin-11-a	Copper	28 µm	39.8	5.15	26.57	34.3	1.7 to 19.3	21.4	8
Cu-sin-12-a	Copper	28 µm	40.2	5.25	29.29	30.2		<5	2.2
Cu-sin-13-a	Copper	28 µm	39.8	2.5	15.37	21.5			-
Cu-sin-13-b	Copper	28 µm	39.6	2.45	12.66	33.5		5.7	-
Zi-sin-1-a	Zircone	5.4 µm	29.6	7.1	18.79	38.2	4.5 to 35		-
Zi-sin-2-a	Zircone	5.4 µm	33.4	10	22.61	58.4	up to 50		
Zi-sin-2-b	Zircone	5.4 µm	35.1	9.3	18.58	66.8			
Zi-sin-3-a	Zircone	5.4 µm	33.8	8.7	13.8	71.6			165
Zi-sin-3-b	Zircone	5.4 µm	34.7	8.5	14.66	70.6	19.3 to 50		
Zi-sin-3-c	Zircone	5.4 µm	34.1	9.8	15.07	73			
Zi-sin-3-d	Zircone	5.4 µm	34.0	8.5	13.35	72.2			
Zi-sin-4-a	Zircone	5.4 µm	38.7	9.2	29.3	56.5			
Zi-sin-5-a	Zircone	5.4 µm	37.8	6.5	29.01	36.1	0.2 to 0.5		
Zi-sin-5-b	Zircone	5.4 µm	37.6	5.5	27.73	27.3			45.2
Zi-sin-6-a	Zircone	5.4 µm	39.9	6.75	30.33	42.3		22	90
Zi-sin-6-c	Zircone	5.4 µm	38.1	5.7	29.3	27.9		49.8	138
Zi-sin-6-d	Zircone	5.4 µm	37.9	5.2	26.45	27.9		30.7	3.7
Zi-sin-6-e	Zircone	5.4 µm	39.0	5.6	27.72	33.7		18.4	1.33
Zi-sin-6-f	Zircone	5.4 µm	38.4	5.5	27.91	30		6.6	0.57
Zi-sin-7-a	Zircone	5.4 µm	39.0	3.7	18.26	33.7		11.5	0.2
Zi-sin-8-a	Zircone	5.4 µm	38.9	8.2	40.23	33.7		26.4	38
Zi-frc-1-a	Zircone	5.4 µm	37.4	12.6	56.23	34.8			
Zi-frc-1-b	Zircone	5.4 µm	38.0	17.6	73.39	41			
Zi-frc-2-a	Zircone	5.4 µm	42.5	5	24.54	44.4			
Zi-frc-3-a	Zircone	5.4 µm	42.1	6.1	22.79	56.9			
Zi-frc-3-b	Zircone	5.4 µm	42.1	6.4	24.65	55.6			
Zi-frc-4-a	Zircone	5.4 µm	41.2	6.9	25.63	55.4			
Ni-sin-x	Nickel	-	40.0	6		33.5		44	50
Zi-sin-6-b	**Zi** + Cu	5.4 µm	39.5	~ 9	48.38	60.5			
Cu-sin-7-e	Zi + **Cu**	28 µm		~ 7					

FOLIO ADMINISTRATIF

THESE DE L'UNIVERSITE DE LYON OPEREE AU SEIN DE L'INSA LYON

NOM : GIRAUDON DATE de SOUTENANCE : 15/01/2018

Prénoms : Rémi

TITRE : Contribution à la fabrication et à la compréhension du comportement thermique des structures capillaires optimales pour les boucles diphasiques à pompage thermo-capillaire

NATURE : Doctorat Numéro d'ordre :

Ecole doctorale : MEGA

Spécialité : Thermique et Energétique

RESUME : Les boucles diphasiques à pompage thermo-capillaire de type LHP permettent un transfert de chaleur particulièrement efficace et entièrement. Ce transfert s'effectue au moyen d'un fluide diphasique, mû grâce à la force motrice capillaire générée par un matériau poreux contenu dans l'évaporateur/réservoir de la LHP. L'aptitude du matériau à remplir sa fonction de barrière thermique et hydraulique dépend de sa microstructure, liée à la méthode de fabrication. L'objectif de la thèse est donc d'associer la science des matériaux et de la thermique, pour améliorer les méthodes de fabrication de structures capillaires existantes. Au cours de ce travail, un modèle analytique est développé afin de simuler le comportement thermo-hydraulique d'une LHP munie de structures poreuses mono- et bicouches. Une étude paramétrique est menée afin de connaître l'influence des caractéristiques hydrauliques et thermiques (conductivité thermique, perméabilité, porosité, rayon de pore) de chaque couche sur les performance de la LHP, et de déterminer les valeurs optimales de ces caractéristiques. Sur la base de ces résultats, de nombreux échantillons poreux en cuivre et en zircone ont été fabriqués, par frittage de poudres ou par une technique de freeze casting. Des structures bicouches ont également été réalisées, par dépôt d'une fine couche d'or sur certains échantillons en zircone, ou par superposition d'une couche de zircone et d'une couche de cuivre. Un premier banc d'essais a été conçu et réalisé, qui permet de mesurer successivement le rayon de pore effectif et la perméabilité des structures capillaires obtenues. Les résultats obtenus montrent que la pression de formation de la pastille poreuse est le paramètre le plus influent sur la perméabilité et le rayon de pores tandis que la masse de poudre frittée a une influence significative sur l'épaisseur de la pastille. Un second banc d'essais, dont la géométrie et le fonctionnement reproduisent ceux d'un évaporateur/réservoir de LHP permet de mesurer le coefficient d'échange thermique de l'évaporateur et de détecter le flux thermique maximal. Il s'avère que ces valeurs dépendent fortement de l'état de surface, de la perméabilité et du rayon de pores de la structure. L'existence d'un interstice entre la surface de l'échantillon et la paroi ailetée de l'évaporateur favorise l'évacuation de la vapeur et retarde ainsi l'apparition de l'assèchement. Un matériau poreux perméable permet la dissipation de fortes densités de flux thermiques, car le liquide percole plus facilement à travers lui. L'étude des limites de fonctionnement théoriques montre qu'un échantillon peu perméable est susceptible d'atteindre la limite capillaire alors qu'un échantillon très perméable atteindrait la limite d'ébullition. Toutefois, les tendances observées différent fortement selon le fluide utilisé (eau ou pentane). Le pentane permet d'obtenir des coefficients d'échanges plus élevés que l'eau grâce à sa forte mouillabilité. Le nombre de tests et de paramètres étant très élevé, une approche statistique par arbre de décision a été mise en œuvre. Elle confirme la forte influence du fluide, de l'état de surface et du rayon des pores sur le coefficient d'échange thermique.

MOTS-CLÉS: loop heat pipe, structure capillaire, frittage, freeze casting, caractérisation hydrodynamique, caractérisation thermique

Laboratoire (s) de recherche : CETHIL - MATEIS

Directeur de these: Valérie Sartre, Laurent GREMILLARD, Stéphane LIPS

Président de Jury:

Composition du jury: Ghislaine BERTRAND, Marc PRAT, Yves BERTIN, Stéphane LAUNAY, Laurent GREMILLARD, Valérie Sartre, Laurent GREMILLARD, Stéphane LIPS